



**HAL**  
open science

# Stability and ageing studies of praseodymium-based nickelates as cathodes for Solid Oxide Fuel Cells

Vaibhav Vibhu

► **To cite this version:**

Vaibhav Vibhu. Stability and ageing studies of praseodymium-based nickelates as cathodes for Solid Oxide Fuel Cells. Material chemistry. Université de Bordeaux, 2016. English. NNT: 2016BORD0017. tel-01424845

**HAL Id: tel-01424845**

**<https://theses.hal.science/tel-01424845>**

Submitted on 3 Jan 2017

**HAL** is a multi-disciplinary open access archive for the deposit and dissemination of scientific research documents, whether they are published or not. The documents may come from teaching and research institutions in France or abroad, or from public or private research centers.

L'archive ouverte pluridisciplinaire **HAL**, est destinée au dépôt et à la diffusion de documents scientifiques de niveau recherche, publiés ou non, émanant des établissements d'enseignement et de recherche français ou étrangers, des laboratoires publics ou privés.

# THÈSE

PRÉSENTÉE

POUR OBTENIR LE GRADE DE

**DOCTEUR DE**

**L'UNIVERSITÉ DE BORDEAUX**

ÉCOLE DOCTORALE DES SCIENCES CHIMIQUES

SPÉCIALITÉ : Physico-Chimie de la Matière Condensée

Par **Vaibhav VIBHU**

---

## **Stability and ageing studies of Praseodymium-based nickelates as cathodes for Solid Oxide Fuel Cells**

---

Sous la co-direction de : Jean-Marc BASSAT et Aline ROUGIER

Soutenance: 12 Février 2016

Membres du jury :

<b>Mme Le gal la salle Annie</b>	<b>CR (HDR) – IMN, Nantes</b>	<b>Rapporteur</b>
<b>M. Skinner Stephen</b>	<b>Prof – Imperial College London</b>	<b>Rapporteur</b>
<b>Mme Vannier Rose-Noëlle</b>	<b>Prof – UCCS, Lille</b>	<b>Examineur</b>
<b>M. Grenier Jean-Claude</b>	<b>DR (Emer) – ICMCB, Bordeaux</b>	<b>Invité</b>
<b>M. Bassat Jean-Marc</b>	<b>DR – ICMCB, Bordeaux</b>	<b>Directeur</b>
<b>Mme Rougier Aline</b>	<b>DR – ICMCB, Bordeaux</b>	<b>Directeur</b>
<b>M. Maglione Mario</b>	<b>DR – ICMCB, Bordeaux</b>	<b>Président</b>



**This thesis is dedicated to my Parents....**

(यह पीएचडी मेरी पूजनीय माँ श्रीमती प्रेमशीला देवी और मेरे पूजनीय पिता श्री रामानन्द भक्त के अथक प्रयास के द्वारा मुझे शिक्षा के सबसे अहम मुकाम पर पहुंचाने के लिए समर्पित हैं।)

In science one tries to tell people, in such a way as to be understood by everyone, something that no one ever knew before. But in poetry, it's the exact opposite.

.....Paul Dirac



## Acknowledgements

I have had the great pleasure to work in these four years and would like to express my sincere gratitude to each and every people who helped me directly or indirectly to achieve my doctorate degree. The list is although huge and not possible to name everyone. I hope the following lines will make justice to the efforts of those who supported me and those who are not specifically acknowledged are already aware of my appreciation.

First and foremost, I would like to express my sincere gratitude and great appreciation to my supervisors, Dr. Jean-Marc Bassat and Dr. Aline Rougier who gave me this golden opportunity to work in their research group. Many thanks to both of them for their great guidance and encouragements!! The results of this thesis would not have been possible without their support. Their enthusiasm and ability to find solutions to all aspects of materials research make them a fantastic supervisors and role models for a young scientist. Whenever I needed their help they were listening to my queries and doubts. They always took time from their busy schedule to listen my words. I could not find a proper word to express my appreciation for the assistances received from both of you on a personal level. Jean-Marc, first of all I would say your research ideas were really amazing. You are guide cum friend, with whom I learned that basics of scientific thinking, planning and implementing my ideas in a focused manner. Heartiest thanks to you for long scientific discussion and anecdote about French cuisine, soccer games and many more things. Aline, I have learned a lot of things from you. Your scientific approach, energy and enthusiasm were astounding. Your positivity and patience towards research always inspired me. A warm thanks to you for all these things.

I am truly grateful to Dr. Jean-Claude Grenier for their continuous research motivation and support during my stay in Bordeaux. Despite his busy schedule, we often found time for interesting scientific discussion and exploring French wines. You have been a constant source of knowledge and inspiration for me.

I would like to address my sincere thanks to Dr. Mario Maglione, Director of the Laboratory, for giving me the opportunity to work in ICMCB and for agreeing to become the president of jury of my thesis.

I would like to thank all my jury members, Prof. Stephen Skinner at Imperial College London, Dr. Annie Le Gal La Salle at Institut des Matériaux de Nantes (IMN) and Prof. Rose

Noëlle Vannier at Unite de Catalyse et Chimie du Solid (UCCS) Lille, for their valuable time in reading this thesis and their comments.

I would like to thank Dr. Matthew Suchomel, Dr. Nicolas Penin and Dr. François Weill for helping me in deep structural analysis and proper understanding.

I would like to thank my office-mates Clément and Aurélien with whom I shared my office during these years. Both of you are amazing; we had very nice scientific discussion and personal chit-chats all together more especially some interesting jokes and mimicry, which have made the workdays so much enjoyable. I would like to thank Sébastien for his technical help throughout my work. I want to thank Dr. Michel Pouchard for nice discussion and enthusiasm, Dr. Michael Pollet and Dr. Olivier Toulemonde for interesting discussions. I thank all my colleagues Alexandre, Mathias, Quentin, David, Thomas, Giljoo, Lucile, Alice, Sourav, Madhu and all other..... for providing an excellent environment both on a professional and personal level. I want to thank all members of Group 1 of ICMCB for their support and friendly gesture which made my stay wonderful and joyous.

I thank to all people from collective services and resource centers, especially, Mr. Eric Lebraud and Mr. Stanislav Pechev for X-ray diffraction measurements, Mr. Dominique Denux for thermal measurements, Mr. Rodolph Decourt for electrical measurements, Mrs. Laetitia Etienne for chemical analysis, Mr. Stéphane Toulin for library and documentation, Mr. Fabien Palencia for IT help. I want to thank Mrs. Frédérique Bonnet, Mrs. Virginie Cosseron Da Costa and Mrs. Sylvie Letard for their great help in administration work.

I would like to thank Dr. Jean Etourneau for funding sources. I want to thank PEREN and ENDURANCE project for giving me additional funding support by which I successfully achieved my work.

I would like to thank Prof. Elisabeth Djurado, LEPMI Grenoble for giving me inspiration to work in this research field. You are the first person who told me what scientific research is actually.

I want to thanks my entire friends more especially Abhishek for giving me motivation, support and constant assistance throughout my stay in France. I can't forget your helps especially in the difficult moments. I want to thanks Ravi, Sumit and Surendra for their great company, which made my life full of pleasure in the past few years.

I am highly thankful to my parents and my family members for all their love, support, encouragement and for being my strength. More especially from my parents, despite of distance between us, I always got their support from the beginning of this adventure. Thanks mom for being there every single day to give me your love, you made me feel at home. Thanks dad for encourage me to believe in my dreams and taught me the meaning of being persistent and strong. Last but not the least, I want to thank my wife Srishti for her unconditional love, trust and encouragement. You have blossomed my life with pleasure and fun sweetheart, which always absorb my professional stress. Thank you all for being always there and believe in me, I love you all guys.!

Finally, I want to thank my God, because of their blessing it was possible to achieve such a nice work.



Résumé du mémoire de thèse de M<sup>r</sup> Vaibhav VIBHU,  
soutenu le 12 février 2016 à l'Université de Bordeaux

## **Introduction**

Ce travail concerne le développement de nouveaux matériaux de cathode pour pile à combustible haute température (SOFC pour Solid Oxide Fuel Cell), qui constituent une source de production d'énergie dite « propre ». La dernière génération de piles SOFC, dite à Métal Support (MSC), est moins coûteuse tout en permettant de travailler à température réduite. Du côté cathodique, outre la nécessité de travailler sur des matériaux à conductivité mixte (ions oxydes /électrons), il est ici impératif d'employer des oxydes stables sous pression partielle d'oxygène réduite, de manière à pouvoir les déposer puis fritter dans des conditions acceptables par le métal.

Vis-à-vis de l'ensemble de ces contraintes, ce travail de thèse s'est concentré sur des oxydes de praséodyme et de nickel substitués partiellement voire totalement par le lanthane. Il débute par une revue bibliographique relative aux matériaux classiques de SOFC ainsi qu'aux différents designs incluant les piles de type MSC (chapitre 1). Les propriétés physico-chimiques des nickelates de formulation générale  $\text{La}_{2-x}\text{Pr}_x\text{NiO}_{4+\delta}$  (LPNO) ont été examinées dans le but de trouver le meilleur compromis entre stabilité chimique et performances électrochimiques (chapitre 2). Les analyses structurales initiales ont montré l'existence de trois domaines cristallographiques qui dépendent de la valeur de x. Le chapitre 3 se focalise sur une étude structurale complète des nickelates LPNO en mettant en œuvre des mesures de diffraction Synchrotron et neutronique, ainsi que des analyses HR-TEM. Après les premières mesures électrochimiques effectuées à « t = 0 », des études de vieillissement ont été conduites, à la fois sans et sous polarisation. En parallèle, la stabilité chimique des matériaux a été étudiée, et ce comme pour la partie précédente sur des temps longs, soit un mois, et ce entre 600 et 800°C. L'ensemble de ces travaux est présenté au chapitre 4. Une conclusion issue de celui-ci est que, du côté riche en Pr de la solution solide, les matériaux se décomposent en perovskite  $(\text{La}, \text{Pr})\text{NiO}_{3-\delta}$ ,  $(\text{La}, \text{Pr})_4\text{Ni}_3\text{O}_{10+d}$  et  $\text{Pr}_6\text{O}_{11}$ . Les propriétés physico-chimiques et électrochimiques de  $\text{PrNiO}_{3-\delta}$  et  $\text{Pr}_4\text{Ni}_3\text{O}_{10+\delta}$  sont étudiées aux chapitres 5 et 6, respectivement. Enfin, les performances électrochimiques d'une cellule de type anode supportée (Ni-YSZ//YSZ) incluant la cathode ont été mesurées à 700 et 800°C.

## **Chapitre 1 – Revue bibliographique**

Dans une première partie, cette revue se concentre sur les piles à combustible au sens large : après un historique de leur développement, les différents types, avantages et applications sont présentés. L'accent est mis sur la problématique des pertes de potentiel qui caractérisent les courbes tension-densité de courant enregistrées sur les piles.

La seconde partie se focalise sur les piles SOFC, en présentant tout d'abord très rapidement la problématique rencontrée à l'anode. Puis l'électrolyte et ses caractéristiques sont présentés plus en détails, en insistant uniquement sur les matériaux les plus classiques. Enfin, l'accent est mis sur la présentation du matériau de cathode, depuis les conducteurs purement électroniques jusqu'aux matériaux à conductivité mixte ( $\text{O}^{2-}/\text{e}^-$ ). Au sein de cette dernière catégorie, on peut distinguer très principalement les matériaux de structure perovskite, les perovskites doubles et les matériaux de la série de Ruddlesden-Popper  $\text{A}_{n+1}\text{M}_n\text{O}_{3n+1}$ . Les nickelates correspondant au terme n=1 de cette série ( $\text{Ln}_2\text{NiO}_{4+\delta}$  avec Ln = La ou Pr) constituent la base de ce travail.

La troisième partie de cette revue porte sur les développements, assez récents, des piles de type MSC. Les différents designs sont présentés, ainsi que les métaux potentiels de support et la fenêtre de température acceptable pour un bon fonctionnement des cellules.

## Chapitre 2 – Les phases $\text{La}_{2-x}\text{Pr}_x\text{NiO}_{4+\delta}$ comme cathodes de piles à combustible à Métal support

Les phases  $\text{La}_{2-x}\text{Pr}_x\text{NiO}_{4+\delta}$  ont été synthétisées par la voie citrate-nitrate à partir des précurseurs  $\text{Pr}_6\text{O}_{11}$ ,  $\text{La}_2\text{O}_3$  et  $\text{Ni}(\text{NO}_3)_2 \cdot 6\text{H}_2\text{O}$  traités thermiquement à  $1200\text{ °C}$  sous air pendant 12 h. Suivant la composition (i.e. la valeur de  $x$ ), l'analyse en diffraction des rayons X met en évidence, l'existence de trois domaines structuraux. Pour  $x < 0,5$  et  $x > 1,0$ , les phases de structure orthorhombique cristallisent en groupe d'espace  $Fmmm$  et  $Bmab$  respectivement, tandis que les compositions intermédiaires ( $0,5 < x < 1$ ) correspondent à un domaine biphasé.

L'écart à la stoechiométrie ( $\delta$ ), évalué par analyse thermogravimétrique, augmente de 0,16 à 0,24 en fonction de la teneur en Pr. De plus, quelle que soit l'atmosphère de recuit ( $T \leq 1000\text{ °C}$ , sous air ou argon), les nickelates restent sur-stoechiométriques en oxygène. Les bonnes propriétés de conduction électrique, sont illustrées par une conductivité maximum de  $110\text{ S.cm}^{-1}$  à  $600\text{ °C}$  pour les compositions riches en Pr ( $x \geq 1$ ). Les coefficients de diffusion,  $D^*$ , et d'échange de surface de l'oxygène,  $k^*$ , des phases  $\text{La}_{2-x}\text{Pr}_x\text{NiO}_{4+\delta}$ , augmentent avec la teneur en Pr. Les valeurs de  $D^*$  sont comprises entre celle de LNO ( $1,5 \cdot 10^{-8}\text{ cm}^2\text{s}^{-1}$ ) et celle de PNO ( $2,5 \cdot 10^{-8}\text{ cm}^2\text{s}^{-1}$ ). Les valeurs de  $k^*$  sont légèrement supérieures aux valeurs de LNO et PNO. Les bonnes propriétés de conduction électrique et ionique laissent présager des propriétés électrocatalytiques intéressantes.

Les propriétés électrochimiques ont été évaluées par spectroscopie d'impédance sur des cellules symétriques LPNO/GDC/8YSZ/GDC/LPNO, pour des électrodes frittées à  $1150\text{ °C}$  sous  $\text{N}_2$  pendant 1 heure. Les diagrammes d'impédance, représentés dans le plan de Nyquist sur la Figure 1, ont été affinés par un Gerisher classique pour LNO et à partir de deux circuits R//CPE pour les phases LPNO (Exemple  $x = 1$  sur la Figure 1b). L'évolution de la résistance de polarisation,  $R_p$ , calculée à partir de l'intersection de la partie réelle de l'impédance, en fonction de  $x$ , montre une diminution de  $R_p$  lorsque  $x$  augmente (Fig. 2). Par exemple, à  $600\text{ °C}$ , la valeur de  $R_p$  diminue de  $0,93\ \Omega\text{.cm}^2$  pour LNO à  $0,29\ \Omega\text{.cm}^2$  pour LPNO ( $x = 1,0$ ) et  $0,15\ \Omega\text{.cm}^2$  pour PNO.

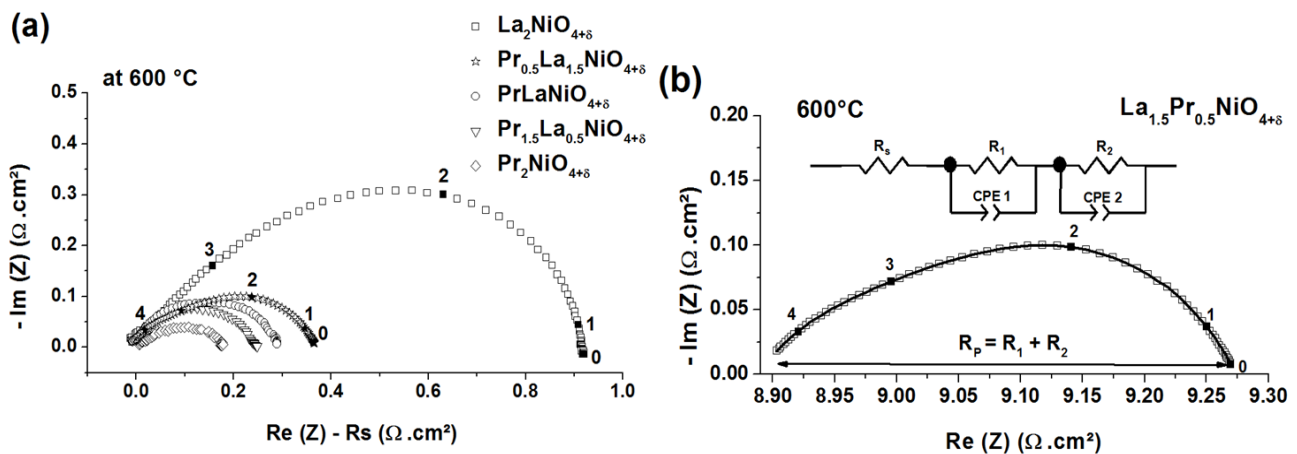
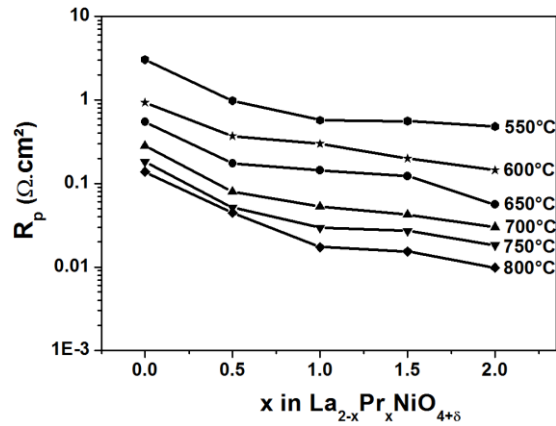


Figure 1 : a) Diagramme d'impédance dans le plan de Nyquist, mesurés à  $600\text{ °C}$ , sur des cellules symétriques, LPNO/GDC/8YSZ/GDC/LPNO, et b) exemple de simulation de diagramme d'impédance pour la phase  $\text{La}_{1.5}\text{Pr}_{0.5}\text{NiO}_{4+\delta}$  (i.e.  $x = 0.5$ ) avec deux éléments R//CPE (Constant Phase Element).



*Figure 2* : Variation de  $R_p$  en fonction du temps pour des cellules symétriques, LPNO/GDC/8YSZ/GDC/LPNO dans une gamme de température de 500 à 800 °C.

L'étude préliminaire des phases  $\text{La}_{2-x}\text{Pr}_x\text{NiO}_{4+\delta}$  a mis en évidence leurs bonnes propriétés électrocatalytiques comme électrodes à oxygène pour piles à combustible. Dans le chapitre suivant, une étude structurale plus approfondie sera présentée (chapitre 3) tandis que le comportement en vieillissement thermique et en fonctionnement sera détaillé dans le chapitre 4.

### **Chapitre 3 – Détermination structurale avancée par étude couplée en diffraction de neutron et synchrotron des phases $\text{La}_{2-x}\text{Pr}_x\text{NiO}_{4+\delta}$**

L'analyse par diffraction des rayons X de laboratoire ayant laissé plusieurs zones d'ombre quant à (i) la présence de raies de diffraction dédoublée, affinée incorrectement en symétrie orthorhombique, de la phase PNO et (ii) la détermination des limites du domaine biphasé ( $0,5 < x < 1$ ) et de sa nature, une étude structurale couplant diffraction synchrotron (HR-SPD) et diffraction de neutrons (NPD) a été menée.

Dans le cas de PNO, l'analyse couplée HR-SPD et NPD confirme la présence d'une distorsion monoclinique d'une maille orthorhombique (Groupe d'Espace : C2/m) résultant d'une perte de symétrie associée à deux positions équivalentes pour Pr, Ni, O1 et O2. La détermination structurale semble toutefois plus complexe avec la présence de raies de diffraction non indexées dont l'origine pourrait être liée une modulation de la structure comme identifié sur les clichés de microscopie électronique haute résolution enregistrés à température ambiante et à 100 K.

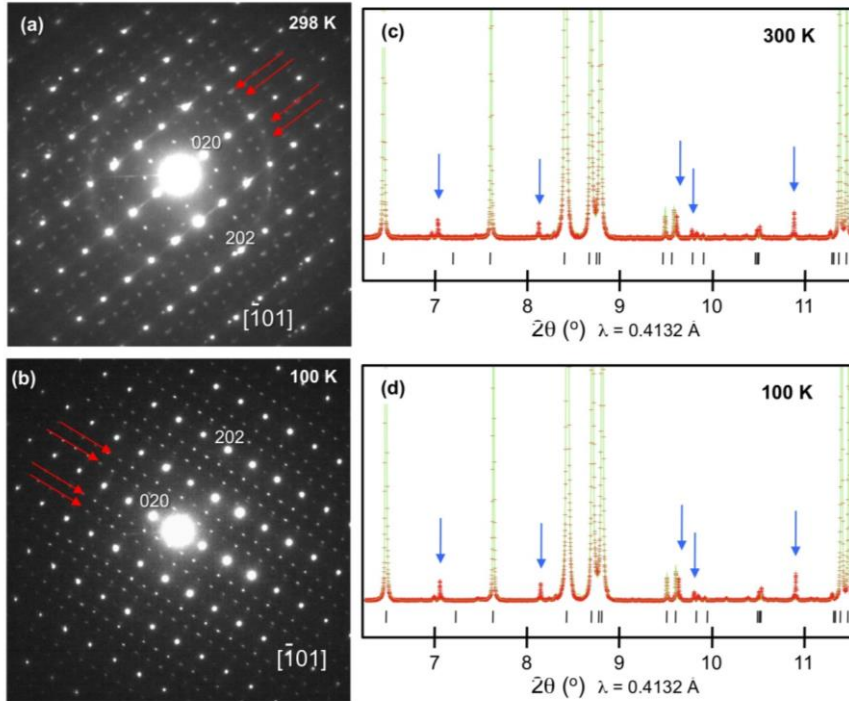


**Figure 3** : Clichés de diffraction électronique haute résolution et de diffraction synchrotron haute résolution pour la phase PNO à  $T_{amb.}$  et à 100 K. Les flèches bleues en HR-SPD et en rouge en HR-TEM correspondent aux raies non indexées.

L'étude couplée HR-SPD et NPD des phases LPNO, confirme la structure monoclinique jusqu'à une valeur en Pr de  $x = 1,1$ . Dans le domaine biphasé, borné à  $0,5 < x < 1,15$ , coexiste deux phases de structure monoclinique et de structure orthorhombique, dont les proportions et compositions restent à affiner. Dans le domaine riche en Pr ( $x > 1,15$ ), la distorsion monoclinique semble dépendre plus fortement du rapport La/Pr que de l'écart à la stoechiométrie  $\delta$  (Fig. 4). En effet, pour PNO, une diminution de l'écart à la stoechiométrie  $\delta$  est associée à une faible modification de l'angle  $\beta$  tandis que les variations de volume et d'angle sont nettement plus marquées pour les phases La/Pr.

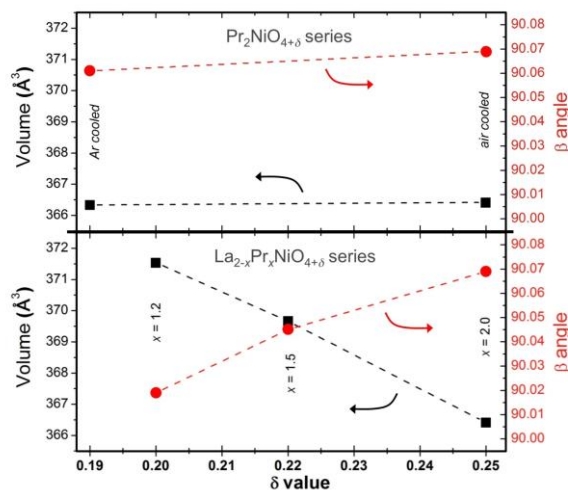


**Figure 4** : Variations des volumes de maille monoclinique et de l'angle  $\beta$  pour PNO, traité sous air et sous argon, et pour les phases  $La_{2-x}Pr_xNiO_{4+\delta}$  riches en Pr ( $1.2 \leq x \leq 2.0$ ).

Afin de préciser l'origine des pics supplémentaires, des études sur monocristal seraient à envisager.

#### **Chapitre 4 – Etude du vieillissement des matériaux de la famille $\text{La}_{2-x}\text{Pr}_x\text{NiO}_{4+\delta}$ (LPNO)**

Dans le but de trouver le meilleur compromis entre performances électrochimiques ( $\text{Pr}_2\text{NiO}_{4+\delta}$ ) et stabilité chimique ( $\text{La}_2\text{NiO}_{4+\delta}$ ), l'étude de la famille  $\text{La}_{2-x}\text{Pr}_x\text{NiO}_{4+\delta}$  a donc été entreprise. Dans cette partie de la thèse, l'attention a été portée sur deux points principaux : 1) l'étude de la stabilité chimique des matériaux (poudres) sous air à la température de travail, et 2) la mesure de l'évolution des résistances de polarisation ( $R_p$ ) des électrodes correspondantes au cours de leur vieillissement thermique (pendant un mois) conduit soit sans courant, soit sous polarisation. En effet, les mécanismes de dégradation affectent directement les différentes étapes composant la réaction globale de réduction de l'oxygène (notée ORR). La spectroscopie d'impédance est donc bien adaptée à de telles études.

Le vieillissement thermique des poudres a été effectué sous air, pendant des durées comprises entre une semaine et un mois, à 600, 700 et 800°C. L'analyse par diffraction des rayons X après le vieillissement a conduit aux conclusions suivantes : 1) Les matériaux riches en lanthane ( $x \leq 0.5$ ) sont stables ; 2) au contraire, les matériaux contenant un taux de praséodyme plus élevé ( $x \geq 1$ ) se décomposent partiellement en différents termes de la série de Ruddlesden-Popper :  $(\text{La,Pr})\text{NiO}_{3-\delta}$  et  $(\text{La,Pr})_4\text{Ni}_3\text{O}_{10+\delta}$ , plus l'oxyde simple  $\text{Pr}_6\text{O}_{11}$ . La quantité de chaque matériau formé dépend de la température et du taux de praséodyme comme le montre un tableau exhaustif présenté dans le manuscrit. Il est à noter par exemple que  $\text{Pr}_2\text{NiO}_{4+\delta}$  est totalement décomposé en  $\text{PrNiO}_{3-\delta}$  et  $\text{Pr}_6\text{O}_{11}$  à 600°C, alors qu'à 700 et 800°C  $\text{Pr}_4\text{Ni}_3\text{O}_{10+\delta}$  est également présent.

Les études électrochimiques ont été conduites sur des cellules symétriques de type LPNO//GDC//8YSZ//GDC//LPNO en fonction de la température et sous air. Avant vieillissement, les résistances de polarisation décroissent progressivement, à température fixe, lorsque le taux de praséodyme augmente. Dans un second temps les cellules ont été maintenues pendant un mois à 600 et 700°C, et les mesures électrochimiques enregistrées sans courant ( $i=0$ ). Pour toutes les compositions LPNO la résistance de polarisation n'évolue pas. En particulier la forme des diagrammes d'impédance n'est pas modifiée. Le résultat est très intéressant, puisque les résistances de polarisation ne sont pas modifiées après le vieillissement, et ce en dépit de la décomposition au moins partielle des matériaux, observées également sur les électrodes et correspondant au descriptif précédent. A ce stade de l'étude, une conclusion partielle est que certaines des phases formées pourraient également être électro-chimiquement actives. Pour  $\text{Pr}_2\text{NiO}_{4+\delta}$ , la résistance de polarisation augmente légèrement avec le vieillissement et la forme des diagrammes évolue aussi. Ensuite, les cellules de type LPNO ont subi un vieillissement thermique du même type que précédemment, mais sous polarisation ( $i = \pm 300 \text{ mA.cm}^{-2}$ ). A cet effet, une électrode de référence a été ajoutée sur toute la tranche de l'électrolyte. Ainsi, le fonctionnement de l'électrode ayant fonctionné en cathode peut-il être distingué de celui de l'électrode ayant fonctionné en anode. A la suite du vieillissement, les mesures électrochimiques sont effectuées sans courant comme précédemment. Le résultat principal de cette étude est qu'en mode cathodique la résistance de polarisation des électrodes de type LPNO augmente avec le vieillissement, alors qu'elle reste stable en mode anodique. Pour arriver à ces conclusions, une déconvolution minutieuse des diagrammes, en particulier du côté anodique, a dû être employée. La figure 1 montre l'évolution de la résistance de polarisation en fonction du temps, enregistrée sur chacune des deux électrodes après vieillissement sous polarisation.

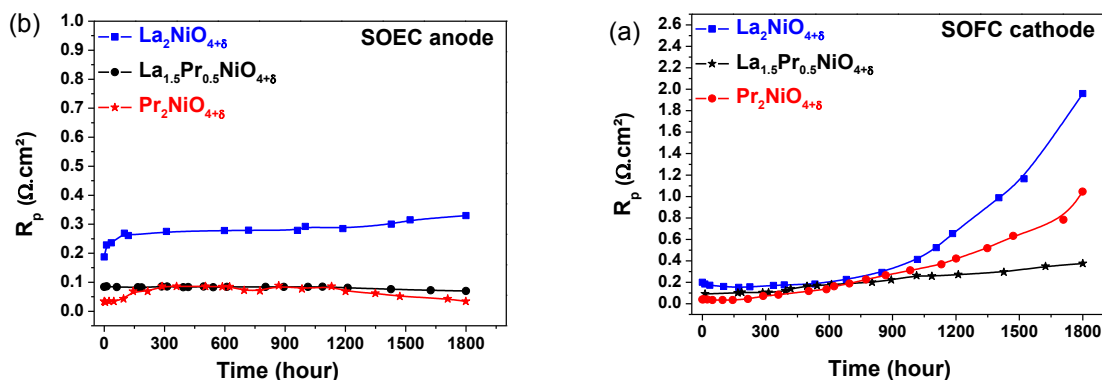


Figure 5 : Variation de  $R_p$  en fonction du temps pour les 3 électrodes LNO, PNO et  $La_{1.5}Pr_{0.5}NiO_{4+\delta}$  vieilles sous courant ( $i_{dc} = -300 \text{ mA.cm}^{-2}$ ) à  $700^\circ\text{C}$  pendant 1800h, (a) mode SOFC et (b) mode SOEC

Des analyses *post-mortem* ont ensuite été entreprises sur les cellules vieilles. Les mesures de DRX confirment les conclusions déjà établies après le vieillissement des poudres et aucune différence n'est notée entre les côtés anodique et cathodique. Ainsi, l'origine de l'augmentation de  $R_p$  côté cathodique pourrait provenir d'une modification chimique de l'interface entre l'électrode et la couche barrière de CGO. Pour pouvoir conclure en ce sens des analyses de cette interface ont été menées par FIB-SEM. La diffusion partielle de praséodyme dans la couche barrière est directement visible par un changement de couleur caractéristique (orange). Dans le cas de  $La_2NiO_{4+\delta}$ , une interphase (composition chimique non déterminée contenant à la fois du cérium et du lanthane, *a minima*) est bien présente entre les deux couches concernées.

Finalement, une discussion a été construite conduisant à formuler l'hypothèse selon laquelle certaines interfaces pourraient être électro-chimiquement actives alors que d'autres pourraient bloquer au moins partiellement la réaction de réduction de l'oxygène.

## Chapitre 5 – Etude du matériau $PrNiO_{3+\delta}$

L'étude des phases, en vieillissement thermique et en fonctionnement, a montré une décomposition de la phase PNO en  $Pr_6O_{11}$ ,  $Pr_4Ni_3O_{10+\delta}$  et  $PrNiO_{3-\delta}$ , associée toutefois à une stabilité des performances électrochimiques. Afin, de comprendre, l'origine de cette stabilité, les propriétés des phases  $PrNiO_{3-\delta}$  et  $Pr_4Ni_3O_{10+\delta}$  ont été caractérisées séparément. Le chapitre 5 est dédié à la caractérisation de la phase perovskite  $PrNiO_{3-\delta}$ .

La phase  $PrNiO_{3-\delta}$  a été synthétisée par voie citrate-nitrate, à partir des précurseurs  $Pr_6O_{11}$ , et  $Ni(NO_3)_2 \cdot 6H_2O$ , recuit à  $850^\circ\text{C}$  sous flux d'oxygène pendant 48 h. Huit recuits successifs ont conduit à l'obtention d'une phase bien cristallisée, de structure orthorhombique (G.E. : *Pbnm*). Une étude en diffraction des rayons x haute température a mis en évidence une transition orthorhombique-rhomboédrique aux alentours de  $600^\circ\text{C}$ . Afin de déterminer les conditions de frittage les plus appropriées pour la préparation d'électrode, la stabilité thermique de  $PrNiO_{3-\delta}$  a été étudiée sous différentes atmosphères, argon, air et oxygène. Quelle que soit l'atmosphère considérée,  $PrNiO_{3-\delta}$  se décompose en  $Pr_2NiO_{4+\delta}$  (+ NiO), soit en une seule étape sous Ar au dessus de  $800^\circ\text{C}$ , soit en passant par la formation de  $Pr_4Ni_3O_{10+\delta}$  sous air ( $1000^\circ\text{C}$ ) et sous oxygène ( $1040^\circ\text{C}$ ). En parallèle, une étude de stabilité thermique, en conditions de fonctionnement ( $600^\circ\text{C}$ ,  $700^\circ\text{C}$ ,  $800^\circ\text{C}$  sous air) par diffraction des rayons X démontre que la phase  $PrNiO_{3+\delta}$  est stable dans ces conditions.

La conductivité électrique de  $PrNiO_{3-\delta}$  présente un comportement de type métallique diminuant de  $180 \text{ S.cm}^{-1}$  à température ambiante à  $120 \text{ S.cm}^{-1}$  à  $600^\circ\text{C}$ .

Les propriétés électrochimiques ont été évaluées par spectroscopie d'impédance sur des cellules symétriques  $\text{PrNiO}_{3-\delta}/\text{GDC}/8\text{YSZ}/\text{GDC}/\text{PrNiO}_{3-\delta}$ . La première étape de notre travail a consisté à optimiser les conditions de frittage de l'électrode en relation avec l'étude de stabilité précédente. Un frittage à 950 °C sous air pendant 2 heures conduit à une valeur de résistance de polarisation très élevée de l'ordre de 4,5  $\Omega\text{cm}^2$ . Une élévation de la température de frittage à 1050 et 1150 °C sous air, suivi d'un recuit additionnel à 800 °C sous oxygène de 24 h, permet de diminuer la valeur de la résistance de polarisation à des valeurs de  $R_p$  de 0,44  $\Omega\text{cm}^2$ . Cependant pour ces conditions de frittage, l'électrode correspond à un mélange de  $\text{PrNiO}_{3-\delta}$  et  $\text{Pr}_6\text{O}_{11}$ . Une électrode de  $\text{PrNiO}_{3-\delta}$  « pure » a été obtenue en co-frittant à 950 °C pendant 2 heures les couches  $\text{PrNiO}_{3-\delta}$  et GDC. Le co-frittage conduit à une valeur de polarisation  $R_p$  de 0,91  $\Omega\text{cm}^2$  supérieure à celle enregistrée pour  $\text{Pr}_2\text{NiO}_{4+\delta}$  suggérant qu'une compréhension plus poussée du mécanisme de dégradation nécessite l'étude de la phase  $\text{Pr}_4\text{Ni}_3\text{O}_{10+\delta}$ . De plus, des premières simulations des diagrammes d'impédance démontre la présence de deux ou trois contributions pour les électrodes frittées séparément et co-frittées ; L'origine de la contribution supplémentaire dans le cas du frittage en deux étapes reste à expliciter.

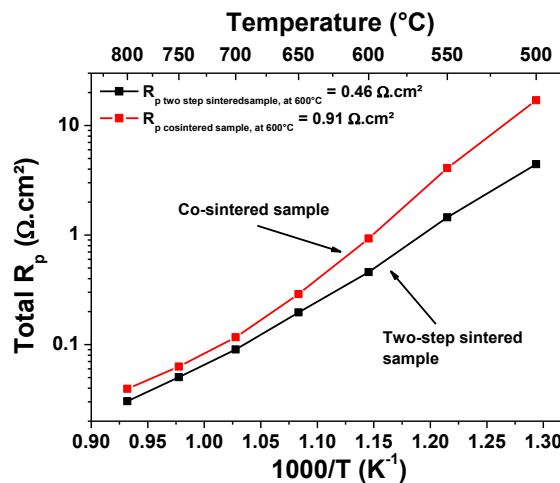


Figure 6 : Variation de  $R_p$  en fonction de la température pour les demi-cellules frittées en deux étapes ou cofrittées  $\text{PrNiO}_{3-\delta}/\text{GDC}/8\text{YSZ}/\text{GDC}/\text{PrNiO}_{3-\delta}$

## Chapitre 6 – Etude du matériau $\text{Pr}_4\text{Ni}_3\text{O}_{10+\delta}$

Cette thèse a déjà permis de bien mettre en évidence la décomposition de  $\text{Pr}_2\text{NiO}_{4+\delta}$  en  $\text{PrNiO}_{3-\delta}$ ,  $\text{Pr}_6\text{O}_{11}$  et  $\text{Pr}_4\text{Ni}_3\text{O}_{10+\delta}$ , lors de chauffages en température longs conduits entre 600 et 800°C. Un point très intéressant, cependant, est qu'en dépit de cette décomposition quasi-totale les performances électrochimiques, au moins à l'OCV, ne changent pas ou très peu comparativement à celles enregistrées sur le matériau initial. L'objectif de cette partie du travail était d'apporter des éléments de réponse à cette interrogation via une étude détaillée du matériau  $\text{Pr}_4\text{Ni}_3\text{O}_{10+\delta}$ .

Le matériau a été préparé par voie glycine-nitrate, et les recuits ultimes réalisés à 1000°C pendant 48h sous flux d'oxygène ont permis d'obtenir une phase pure. Le matériau cristallise dans une structure orthorhombique de groupe d'espace  $Fmmm$ . Cette structure est conservée lors de chauffages effectués sous air jusqu'à 1000°C. Ces études de DRX en fonction de la température ont également permis de déterminer un coefficient d'expansion thermique de l'ordre de  $10 \times 10^{-6} \text{ } ^\circ\text{C}^{-1}$ , qui est du même ordre de grandeur que celui des autres composants céramiques de la pile SOFC. La détermination du taux de sur-stœchiométrie en oxygène  $\delta$  (via des ATG conduites sous atmosphère réductrice) a conduit à la valeur  $\delta = 0,1$  à température ambiante.

Des analyses thermogravimétriques effectuées sous air et oxygène dans le but de déterminer à la fois le domaine de stabilité chimique et de trouver la température adéquate pour le frittage des électrodes sur les supports de YSZ recouverts d'une couche de cérine substituée. Sous air  $\text{Pr}_4\text{Ni}_3\text{O}_{10+\delta}$  est stable jusqu'à 1050°C, température au-delà de laquelle il se décompose en  $\text{Pr}_2\text{NiO}_{4+\delta}$  et NiO. Cette décomposition est irréversible sous air. Sous oxygène, la stabilité chimique est améliorée, la décomposition précédente se produisant à plus haute température. Par ailleurs, la décomposition est partiellement réversible sous oxygène, en accord avec les résultats précédents de la littérature (une faible quantité de  $\text{PrO}_x$ , NiO et  $\text{Pr}_2\text{NiO}_{4+\delta}$  reste présente). La variation thermique du taux initial de sur-stœchiométrie en oxygène a ensuite été suivie sous air et sous oxygène, jusqu'à 1000°C. Des cycles réversibles au chauffage et refroidissement sont observés dans les deux cas, à condition d'avoir au préalable équilibrés les matériaux sous l'atmosphère considérée. La conclusion principale est que quelles que soient les conditions et la température le matériau conserve une sur-stœchiométrie en oxygène, laissant à penser qu'il conserve ses propriétés de conductivité mixte.

La suite du travail a consisté à étudier la stabilité thermique du matériau à la température de travail de la pile SOFC, soit entre 600 et 800°C et sous air, mais sur des durées longues (1 mois). Les mesures par DRX après ces traitements permettent de conclure à la bonne stabilité thermique du matériau dans ces conditions.

La mesure de la conductivité totale a été effectuée par la méthode des 4 points, sous air et jusqu'à 800°C. Le comportement est de type métallique. La valeur de conductivité maximale est de l'ordre de  $\sigma = 200 \text{ S.cm}^{-1}$  à température ambiante, qui est une des plus élevées enregistrées pour un matériau nickelate. Elle diminue ensuite pour atteindre environ  $\sigma = 85 \text{ S.cm}^{-1}$  à 800°C, valeur qui dépasse le seuil minimal fixé pour un matériau de cathode. Des mesures de conductivité ionique ont ensuite été entreprises via la méthode dite IEDP (Isotopic Exchange Depth Profiling). Cependant, dans ce cas un prérequis est de pouvoir disposer de pastilles parfaitement denses (compacité > 95%), condition qu'il fût très difficile d'atteindre avec ce matériau. Néanmoins, quelques pastilles denses ont été obtenues et des mesures réalisées. Les coefficients de diffusion de l'oxygène et d'échange de surface semblent, selon ces mesures préliminaires, proches de ceux déterminés pour  $\text{Pr}_2\text{NiO}_{4+\delta}$ , qui figurent parmi les plus élevés de la littérature parmi ceux des matériaux à conductivité mixte. Par ailleurs, ils ne semblent pas dépendre de la pression partielle d'oxygène maintenue dans l'enceinte qui, rappelons-le, détermine le taux de sur-stœchiométrie en oxygène.

Préalablement aux études électrochimiques, un travail a consisté à optimiser le dépôt de l'encre contenant le matériau et utilisée pour la sérigraphie. La taille moyenne des grains de la poudre est de l'ordre de 600 nm. Une première méthode a consisté à réaliser le dépôt de l'électrode en deux étapes, c'est-à-dire après le dépôt/recuit préalable de la couche barrière de CGO. Le dépôt de l'électrode a été effectué à haute température sous air, étape suivie d'un refroidissement lent (1°C/min) conduit sous flux d'oxygène depuis la température maximale jusqu'à 950°C, température maintenue pendant 6h de manière à favoriser au maximum la formation de  $\text{Pr}_4\text{Ni}_3\text{O}_{10+\delta}$ . Il est à noter que porte le matériau à 1150°C sous air avant le cycle de refroidissement décrit ci-dessus permet de minimiser les résistances de polarisation ( $R_p$ ) des électrodes, qui est bien entendu le but recherché. La seconde méthode de mise en forme des électrodes, toujours conduite par sérigraphie, a consisté à effectuer un cofrittage de la couche de  $\text{Pr}_4\text{Ni}_3\text{O}_{10+\delta}$  avec celle de la couche barrière de CGO. Un cycle conduit à 950°C pendant 2h sous air a été optimisé.

La figure 2 montre la variation de la résistance de polarisation en fonction de la température, et ce pour les deux méthodes de mises en forme, résistances déduites des mesures menées par spectroscopie d'impédance complexe. Les valeurs de  $R_p$  sont un peu plus faibles, à température identique, pour les électrodes cofrittées comparativement aux électrodes déposées selon le processus en deux étapes. A 600°C et pour les électrodes cofrittées, la valeur est très proche de celle mesurée dans notre groupe pour  $\text{Pr}_2\text{NiO}_{4+\delta}$ , qui constitue un matériau de référence. La différence,

examinée au travers des différentes composantes des diagrammes d'impédance, pourrait provenir soit de la présence (même faible) de phases additionnelles, soit d'une morphologie d'électrode différente, cette seconde hypothèse semblant privilégiée à la suite d'études MEB conduites sur les cellules après les mesures.

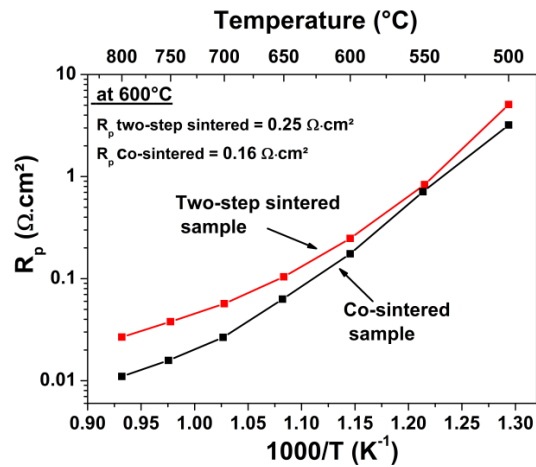


*Figure 7 : Variation de  $R_p$  en fonction de la température pour les demi-cellules frittées en deux étapes ou cofrittées.*

Enfin, des mesures en cellules complètes (anode/électrolyte/couche CGO/électrode) ont été conduites (Figure 3). Les performances sont très élevées à 700 et 800 $^\circ\text{C}$ , avec par exemple un maximum de densité de puissance de 1.6  $\text{W} \cdot \text{cm}^{-2}$  à 800 $^\circ\text{C}$ . Par ailleurs, les cellules ont été maintenues en température et sous courant pendant des durées longues (500h), et aucun vieillissement notable n'a été mis en évidence.

Au final, le comportement électrochimique de  $\text{Pr}_4\text{Ni}_3\text{O}_{10+\delta}$  est très proche de celui de  $\text{Pr}_2\text{NiO}_{4+\delta}$ , mais sa stabilité chimique et électrochimique bien supérieure dans les conditions de fonctionnement de la pile SOFC.

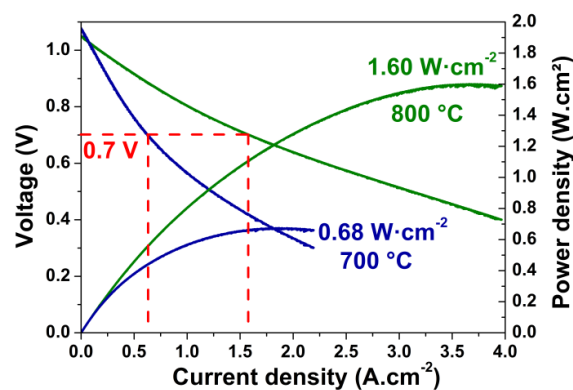


*Figure 8 : courbes  $i$ - $V$  et densités de puissance mesurées sur une mono-cellule constituée d'une demi-cellule commerciale et d'une cathode de  $\text{Pr}_4\text{Ni}_3\text{O}_{10+\delta}$ .*

## **Conclusion**

En conclusion, l'objectif de cette thèse était double. D'une part identifier des matériaux susceptibles d'être utilisés comme électrodes à oxygène dans des cellules à métal support, impliquant des conditions de frittage sous faible  $PO_2$ , et d'autre part d'étudier leur stabilité chimique et thermique en conditions de fonctionnement. Ainsi les phases  $La_{2-x}Pr_xNiO_{4+\delta}$  ont été choisies dans le but de trouver un compromis entre la stabilité électrochimique du  $La_2NiO_{4+\delta}$  et les bonnes performances du  $Pr_2NiO_{4+\delta}$ . Une étude structurale couplant diffraction de laboratoire, diffraction synchrotron et neutrons a démontré l'existence de trois domaines structuraux en fonction de x. Un des résultats majeurs de ce travail a été l'identification d'une structure monoclinique pour les phases riches en Pr. La caractérisation des propriétés physico-chimiques et électrochimiques des phases  $La_{2-x}Pr_xNiO_{4+\delta}$  a permis de démontrer leur bonnes performances. En particulier, la phase  $La_{1,5}Pr_{0,5}NiO_{4+\delta}$  a été déterminée comme le meilleur compromis entre performance et stabilité. Par ailleurs, cette dernière est fortement dépendante non pas de la stabilité chimique des matériaux mais majoritairement de l'interface/interphase entre l'électrode à oxygène et la couche barrière GDC. Pour finir, ce travail de thèse a mis en évidence le comportement très prometteur du nickelate  $Pr_4Ni_3O_{10+\delta}$ , de performance très proche de  $Pr_2NiO_{4+\delta}$  mais de stabilité plus élevée et ceci en cellule complète.

# Content

<b>Introduction</b> .....	<b>5</b>
<b>Chapter 1: Literature Survey</b> .....	<b>11</b>
<b>1. Fuel cells</b> .....	<b>12</b>
1.1. Historical Background .....	12
1.2. Various types of Fuel Cells .....	13
1.3. Advantages and applications of Fuel Cells .....	13
1.4. Working principle of Fuel Cell .....	16
1.5. Losses.....	18
1.5.1. Activation over-potential .....	18
1.5.2. Ohmic losses (ohmic overpotential/overvoltage).....	19
1.5.3. Concentration or diffusion losses (concentration overpotential/overvoltage): .....	19
<b>2. Solid Oxide Fuel Cells (SOFCs)</b> .....	<b>20</b>
2.1. Anode.....	20
2.2. Electrolyte .....	21
2.2.1. Ytria Stabilized Zirconia (YSZ).....	21
2.2.2. Doped Ceria .....	23
2.3. Cathode .....	24
2.3.1. General requirements – electronic conductors .....	24
2.3.2. MIEC Materials.....	26
2.4. Interconnects .....	32
2.5. IT-SOFCs .....	32
2.6. Metal Supported Cells (MSCs).....	33
2.6.1. Different SOFC designs .....	33
2.6.2. Early MSC development.....	34
2.6.3. Choice of metal for support .....	35
2.6.4. Suitable operation temperature window.....	36
<b>References</b> .....	<b>37</b>
<b>Chapter 2: <math>\text{La}_{2-x}\text{Pr}_x\text{NiO}_{4+\delta}</math> as suitable cathodes for Metal Supported SOFCs</b> .....	<b>43</b>
<b>1. Introduction</b> .....	<b>44</b>
<b>2. Experimental</b> .....	<b>46</b>
<b>3. Results and Discussion</b> .....	<b>48</b>

3.1.	XRD characterizations .....	48
3.2.	Thermogravimetry analyses .....	50
3.3.	Electrical Conductivity Measurements .....	53
3.4.	Dilatometry Measurements .....	54
3.5.	Oxygen diffusion and surface exchange coefficients ( $D^*$ , $k^*$ ) .....	54
3.6.	Electrochemical Measurements .....	56
<b>4.</b>	<b>Conclusions.....</b>	<b>59</b>
	<b>References.....</b>	<b>60</b>
	<b>Additional Information: Chapter 2.....</b>	<b>62</b>

### **Chapter 3: Structural Characterization of Pr-rich phases in $\text{La}_{2-x}\text{Pr}_x\text{NiO}_{4+\delta}$ series using Synchrotron and Neutron Powder Diffraction.....65**

<b>1.</b>	<b>Introduction.....</b>	<b>66</b>
<b>2.</b>	<b>Experimental .....</b>	<b>68</b>
<b>3.</b>	<b>Results and Discussion.....</b>	<b>69</b>
3.1.	Initial structural characterizations .....	69
3.2.	Structure of $\text{Pr}_2\text{NiO}_{4+\delta}$ .....	71
3.2.1.	Joint synchrotron and neutron data refinement of $\text{Pr}_2\text{NiO}_{4+\delta}$ .....	71
3.2.2.	Discussion of distortion details in PNO structures .....	76
3.2.3.	Variation of extra peaks .....	78
3.2.4.	Synchrotron diffraction vs. Temperature for $\text{Pr}_2\text{NiO}_{4.25}$ from 450 K to 100 K.....	80
3.3.	Pr-rich LPNO mixed nickelates .....	82
3.3.1.	Joint synchrotron and neutron data refinement of $\text{La}_{0.5}\text{Pr}_{1.5}\text{NiO}_{4+\delta}$ .....	83
3.3.2.	$\text{La}_{0.8}\text{Pr}_{1.2}\text{NiO}_{4+\delta}$ joint refinement .....	86
3.3.3.	Variation of $\beta$ –angle for Pr-rich phases .....	87
3.3.4.	Determination of biphasic zone .....	88
3.3.5.	$\text{La}_{1.4}\text{Pr}_{0.6}\text{NiO}_{4+\delta}$ joint refinement .....	89
3.3.6.	Variation of lattice parameters .....	92
3.3.7.	Variation of extra peaks with A-site cation substitution .....	94
3.3.8.	Effect of $\delta$ -value and A-site cation substitution.....	95
<b>4.</b>	<b>Conclusions.....</b>	<b>96</b>
	<b>References.....</b>	<b>97</b>

### **Chapter 4: Ageing Study of Praseodymium-Lanthanum Nickelates $\text{La}_{2-x}\text{Pr}_x\text{NiO}_{4+\delta}$ as scathodes for MS-SOFCs.....99**

<b>1. Introduction.....</b>	<b>101</b>
<b>2. Experimental .....</b>	<b>103</b>
<b>3. Results and discussion .....</b>	<b>104</b>
3.1. Thermal ageing of the mixed nickelates: powders.....	105
3.2. Symmetrical Half-Cell Characterization.....	107
3.3. Ageing of half cells under $i_{dc} = 0$ .....	108
3.4. Ageing of half cells under $i_{dc} \neq 0$ up to 1800 h .....	110
3.4.1. Behavior of the electrode in SOFC mode during ageing .....	111
3.4.2. Behaviour under cathodic current .....	112
3.4.3. Behaviour under anodic current .....	114
3.4.4. Discussion about the inductive loop .....	116
3.4.5. Determination of the “true” $R_p$ in SOFC and SOEC modes .....	117
3.4.6. Variation of polarization resistance with time .....	123
3.4.7. Postmortem analyses.....	124
<b>4. Conclusion .....</b>	<b>131</b>
<b>References.....</b>	<b>132</b>
<b>Additional Information: Chapter 4.....</b>	<b>134</b>

## **Chapter 5: Structural and stability studies of $\text{PrNiO}_{3-\delta}$ and characterization as oxygen electrode in SOFCs .....**

<b>1. Introduction.....</b>	<b>138</b>
<b>2. Experimental .....</b>	<b>140</b>
<b>3. Results and discussion .....</b>	<b>142</b>
3.1. XRD Analysis .....	142
3.1.1. Stability with Temperature (XRD vs. T).....	143
3.1.2. Variation of lattice parameters and TECs .....	143
3.2. TGA .....	147
3.2.1. Determination of $\delta$ .....	147
3.2.2. Thermal stability under argon, air and oxygen .....	148
3.2.3. Variation of oxygen content under argon, air and oxygen .....	152
3.2.4. Stability above 950 °C and in operating SOFCs condition.....	153
3.3. Long term chemical stability of $\text{PrNiO}_{3-\delta}$ powder under air at operating conditions.....	155
3.4. Electrical Conductivity .....	156
3.5. Electrochemical measurements.....	157
3.5.1. Optimization of the sintering two-step process .....	157
3.5.2. Co-sintering of GDC and $\text{PrNiO}_{3-\delta}$ half cell .....	158
3.5.3. Discussion.....	160

<b>4. Conclusion .....</b>	<b>163</b>
<b>References.....</b>	<b>164</b>
<b>Additional Information: Chapter 5.....</b>	<b>166</b>
<b>Chapter 6: Pr<sub>4</sub>Ni<sub>3</sub>O<sub>10+δ</sub>: a new promising oxygen electrode material for Solid Oxide Fuel cells.....</b>	<b>169</b>
<b>1. Introduction.....</b>	<b>170</b>
<b>2. Experimental .....</b>	<b>172</b>
<b>3. Results and discussion .....</b>	<b>175</b>
3.1. XRD analysis .....	175
3.1.1. Thermal behaviour of the material with temperature under air (XRD vs. T) .....	176
3.1.2. Variation of lattice parameters with temperature: determination of TEC.....	178
3.2. TG analyses.....	178
3.2.1. Determination of δ of material equilibrated under air .....	178
3.2.2. Behavior under air and oxygen .....	179
3.2.3. Variation of the oxygen content (δ value) under air and oxygen.....	181
3.2.4. Long term chemical stability at operating temperatures .....	183
3.3. Electrical Conductivity .....	183
3.4. Electrochemical studies.....	185
3.4.1. Morphology of as-prepared powder.....	185
3.4.2. EIS characterization: symmetrical cell.....	186
3.4.3. Optimization of the two-step sintering process.....	186
3.4.4. Co-sintering of GDC and Pr <sub>4</sub> Ni <sub>3</sub> O <sub>10+δ</sub> half cell .....	188
3.4.5. Discussion .....	189
3.4.6. Morphology of half cells after EIS measurements.....	192
3.4.7. Single cell measurements.....	193
<b>4. Conclusion .....</b>	<b>195</b>
<b>References.....</b>	<b>196</b>
<b>Additional Information: Chapter 6.....</b>	<b>198</b>
<b>Conclusion.....</b>	<b>205</b>
<b>Annexure.....</b>	<b>211</b>
<b>Annex 1 .....</b>	<b>212</b>
<b>Annex 2 .....</b>	<b>216</b>

# Introduction

---

## Introduction

The sustainable sources of energy are mandatory for maintaining the quality of life in developed countries and improving the standard of living in emerging ones. The conventional ways of generating energy especially from coal and petroleum suffer from their limited source and contamination of environments caused by them. The striking example is the rise in the average sea level as a consequence of global warming threatening the low lying land masses. The very recent COP21 conference helps to convince everybody about the need for solutions. It is for instance urgently required to look for clean and long-lasting sources of energy with minimum environmental impact. Among various alternative clean sources, fuel cells based energy production appears highly promising. *A fuel cell is a device that generates electricity by an electrochemical reaction without combustion.*

There are several kinds of fuel cells, each operating a bit differently. Out of them, Solid Oxide Fuel Cell (SOFC) has proved to be the most efficient, with more than 80% output efficiency. Nevertheless, this technology is still not used at large scale because of problems related to the use of hydrogen, lack of durability and high expenses involved. One of the challenging issues for the development of economically competitive SOFCs include lowering the operating temperature from above 1000 °C down to Intermediate Temperature 600–700 °C (*i.e.* IT-SOFCs) in order to reduce the overall cost and increase their lifetime. Lowering the operating temperature below 800 °C extend material selection as well as cell reliability. Indeed it allows the use of low-cost component materials, improvement of sealing capability, reduction of the interfacial reaction and limitation of chromium poisoning during the cell operation. Aiming at lower cost devices, the last generation of SOFC concerns the Metal Supported Cells (MSCs). However, it is generally recognized that the performance of SOFCs deteriorate at lower temperature, mainly due to the overpotentials generated at the cathode interface and to the decrease in ionic conductivity of the electrolyte. At the lowered temperatures, polarization resistance of the cathode becomes dominant in determining overall performance of the cell due to high activation energy of oxygen reduction reaction (ORR) taking place at the cathode and consequently cathode materials with improved properties are needed.

Current efforts aimed at finding oxides that have fast oxygen diffusion and surface exchange kinetics. Among them, the cobalt-containing oxides with perovskite-type structure such as  $\text{La}_{0.6}\text{Sr}_{0.4}\text{Co}_{0.2}\text{F}_{0.8}\text{O}_{3-\delta}$  (LSCF) and  $\text{La}_{0.8}\text{Sr}_{0.2}\text{CoO}_{3-\delta}$  (LSC) are extensively used as IT-SOFC cathode materials due to their Mixed Ionic and Electronic Conducting (MIEC)

properties and catalytic activity. However, they suffer from four main disadvantages namely (i) their high values of thermal expansion coefficients (TECs) in comparison with the other parts of the cell, (ii) their reactivity with zirconia electrolyte to form  $\text{SrZrO}_3$  insulating phase, (iii) the easy formation of  $\text{SrSO}_4$  insulating phase in the presence of sulphur, (iv) the Sr-segregation at the electrode electrolyte interface, leading to a degradation of the cell performance.

Therefore, there is a strong need for MIEC cathode materials which are stable at operating temperature, very efficient for oxygen reduction reaction with no or less interface modification with time and temperature. In this respect, nickelates belonging to the Ruddlesden-Popper series are good candidates. They have been studied in our group since about 2003<sup>1</sup>.

This PhD work concerns the study of praseodymium based nickelates as cathode materials for IT-SOFCs.

Chapter 1 deals with a short literature review regarding fuel cells and more especially Solid Oxide Fuel Cells. In particular the description of the various SOFC designs including the Metal Supported Cells is done. The starting point of our study was the following one: in the  $\text{Ln}_2\text{NiO}_{4+\delta}$  ( $\text{Ln} = \text{La}, \text{Pr}$ ) compounds with the  $\text{K}_2\text{NiF}_4$ -type structure,  $\text{Pr}_2\text{NiO}_{4+\delta}$  shows excellent electrochemical performance at intermediate temperature with limited thermal stability range, while  $\text{La}_2\text{NiO}_{4+\delta}$  exhibits good chemical stability but lower electrochemical performance. The properties of  $\text{La}_{2-x}\text{Pr}_x\text{NiO}_{4+\delta}$  (hereafter labelled LPNO) mixed nickelates are thus investigated with the aim to find the best compromise between chemical stability and electrochemical performance. The synthesis and several physico-chemical characterizations of these LPNO mixed nickelates are reported in Chapter 2. More precisely, preliminary structural characterizations, mixed ionic and electronic conducting (MIEC) properties investigated through the evolution of the oxygen over-stoichiometry,  $\delta$ , measured as a function of temperature and oxygen pressure  $p\text{O}_2$ , are discussed. The electrochemical performance measured in symmetrical cells using LPNO materials sintered under low  $p\text{O}_2$  ( $\sim 10^{-4} - 10^{-5}$  atm), as requested in Metal Supported Cells are presented.

---

<sup>1</sup> E. BOEHM, J.M. BASSAT, C. STEIL, P. DORDOR, F. MAUVY and J.C. GRENIER, "Oxygen transport properties of  $\text{La}_2\text{Ni}_{1-x}\text{Cu}_x\text{O}_{4+\delta}$  mixed conducting oxides", *Solid State Science* 5, 973 – 981 (2003).

Initial structural analysis of LPNO nickelates indicates the existence of three domains depending on  $x$  value (*i.e.* Pr content). In between the La-rich and Pr-rich parts, a third one consisting of a biphasic domain is observed.

Chapter 3 focuses on an in-depth structural study of the LPNO nickelates using Synchrotron and Neutron diffraction as well as HR-TEM analysis. Some of the synchrotron diffraction experiments were performed at low temperature.

With the aim to find the best compromise between chemical stability and electrochemical performance, the chemical stability of the  $\text{La}_{2-x}\text{Pr}_x\text{NiO}_{4+\delta}$  mixed nickelates under air at operating temperatures as well as the evolution of the polarization resistances during ageing (recorded under air at  $i_{dc} = 0$  and  $i_{dc} \neq 0$  conditions) were studied for duration up to one month (at 600, 700 and 800 °C). The results are summarized in Chapter 4.

Upon ageing Pr-rich phases (and in particular  $\text{Pr}_2\text{NiO}_{4+\delta}$ ) decompose into the perovskite  $(\text{La}, \text{Pr})\text{NiO}_{3-\delta}$ , the Ruddlesden-Popper  $(\text{La}, \text{Pr})_4\text{Ni}_3\text{O}_{10+\delta}$  and  $\text{Pr}_6\text{O}_{11}$ . The properties of  $\text{PrNiO}_{3-\delta}$  and  $\text{Pr}_4\text{Ni}_3\text{O}_{10+\delta}$  as possible active cathodes for SOFCs are presented in Chapter 5 and Chapter 6, respectively. In Chapter 5, prior to the electrochemical measurements, the thermal stability of  $\text{PrNiO}_{3-\delta}$ , coupling thermal gravimetric analysis (TGA) and X-ray diffraction (XRD) is carefully investigated at high temperature (up to 1200 °C) as well as in various atmospheres (air, oxygen and argon).

The structural stability of  $\text{Pr}_4\text{Ni}_3\text{O}_{10+\delta}$  in temperature up to 1000 °C under air and oxygen is discussed in Chapter 6 in relation with the variation of oxygen content ( $10+\delta$ ). The polarization resistance ( $R_p$ ) of  $\text{Pr}_4\text{Ni}_3\text{O}_{10+\delta}$  electrode is measured both for GDC/co-sintered and two-step sintered half cells. Finally, the electrochemical performance of an anode supported (Ni-YSZ//YSZ) single cell including GDC// $\text{Pr}_4\text{Ni}_3\text{O}_{10+\delta}$  co-sintered electrode were measured at 700 and 800°C.

## **Note to the reader on the “Structure of the thesis”**

*Except for Chapter 1 which concerns Literature Survey, this manuscript gathers articles either already published (Chapter 2, Solid State Ionics, 278 (2015) 23 -27), submitted (Chapter 5, Journal of Solid State Electrochemistry and Chapter 6, Journal of Power Sources) or in preparation (Chapters 3 and 4). Thus, I do apologize for some repetitions in paragraph of introductions and experimental descriptions. Additional information and experiments have been added at the end of Chapters 2, 4, 5 and 6.*

*The annex1 describes the principle of the impedance spectroscopy measurements; the annex 2 gathers the list of articles in which I am co-author, additional proceedings and list of my presentations in several conferences.*



# Chapter 1: Literature Survey

---

---

# Chapter 1

## Literature Survey

---

### Abstract

A short general introduction is given on fuel cells. The history, advantages, description of different types, working principle as well as applications of fuel cells are discussed. The second part of this chapter concerns the Solid Oxide Fuel Cell (SOFC), its main components and used materials. Particular attention is devoted to the presently available knowledge on the Metal Supported Cells (MSCs) and to a description of nickelates oxides, which are MIEC materials possibly used as cathodes for IT-SOFCs, especially in MSCs conditions.

### 1. Fuel cells

A fuel cell is a device that converts electrochemical energy into electrical energy (dc current). Typically, a direct process of electricity generation from fuels involves several energy conversion steps, namely:

1. The combustion of fuel converts chemical energy of fuel into heat,
2. The heat is then used to boil water and generates steam,
3. The steam is used to run a turbine in a process that converts thermal energy into mechanical energy, and finally
4. The mechanical energy is used to run a generator that generates electricity.

A fuel cell avoids all these processes and generates electricity in a single step with high efficiency.

#### 1.1. Historical Background

The principle of the fuel cell (FC) was discovered in 1839 by Swiss scientist Christian Friedrich Schoenbein. Simultaneously, the English scientist William Robert Grove [1] built the first practical fuel cell. By this time, he demonstrated that the reaction between oxygen and hydrogen is used to produce electricity and water through a reverse reaction of the electrolysis. The first cell was thus built with porous platinum electrodes in an electrolytic

solution of sulfuric acid. However, competition with other types of power generators having greater powers and the difficulty to achieve effective and inexpensive electrodes impeded the development of this technology for over a century. In 1953, Francis Thomas Bacon revives the studies and generated a 1 kW prototype as a model to the stack used in the Apollo space missions [2]. Over the past twenty years, this technology and associated research experienced a new craze in a general context of finding new sources of clean energy.

## **1.2. Various types of Fuel Cells**

There are currently almost six types of fuel cells, depending on the type of membrane (electrolyte) they used, i.e. AFC: Alkaline Fuel Cell, PEMFC: Polymer Electrolyte Membrane Fuel Cell, DMFC: Direct Methanol Fuel Cell, PAFC: Phosphoric Acid Fuel Cell, MCFC: Molten Carbonate Fuel Cell, SOFC: Solid Oxide Fuel Cell. The working principle of all these fuel cells is the same but the operating temperature ranges, electrolytes as well as the used fuels largely differ from one to the other. Moreover, the efficiencies differ. Some characteristics of various fuel cells, including the possible applications, are presented in **Table 1**.

## **1.3. Advantages and applications of Fuel Cells**

**Figure 1** summarizes the main advantages of fuel cells with respect to their type. The advantages and drawbacks of fuel cells systems are different depending on the kind of fuel cell and are related to their operating temperatures, having direct consequences on the trends for their respective commercial applications.

For instance, low temperature fuel cells (PEMFC, AFC) are characterised by their rapid start-up and are thus competitive in mobile applications. However, they need a good quality of hydrogen supply with a low CO content in the fuel. On the contrary, thanks to their high operating temperatures, SOFC and MCFC are able to operate on fuels containing large fractions of carbon monoxide, and can thus run either with an external or internal reformer without extensive gas cleaning.

**Table 1: Various types of fuel cells**

Type of Fuel Cells	Typical electrolyte	Ion diffusing through the electrolyte	Operating Temperature (°C)	Fuel	Efficiency (%)	Applications
Alkaline Fuel Cell (AFC)	KOH solution	OH <sup>-</sup>	60-80	Pure H <sub>2</sub>	60-70	Buses and Spaceships
Proton Exchange Membrane Fuel Cell (PEMFC)	Polymer membrane (Perfluoro Sulfonic acid)	H <sup>+</sup>	50-220	Pure or reformed H <sub>2</sub>	40-60	Vehicles mobile and stationary
Direct Methanol Fuel Cell (DMFC)	Polymer membrane (Nafion, sulfonated <u>tetrafluoro ethylene</u> )	H <sup>+</sup>	50-120	methanol	40-60	Vehicles mobile and stationary
Phosphoric Acid Fuel Cell (PAFC)	Phosphoric acid	H <sup>+</sup>	150-200	Pure or reformed H <sub>2</sub>	55	Stationary
Molten Carbonate Fuel Cell (MCFC)	Solution of Lithium, Sodium and/ or Potassium Carbonates	CO <sub>3</sub> <sup>2-</sup>	500-650	Pure or reformed H <sub>2</sub>	55	Stationary and heavy vehicle
Solid Oxide Fuel Cell (SOFC)	Ytria Stabilized Zirconia (YSZ)	O <sup>2-</sup>	550-1000	Pure or reformed H <sub>2</sub>	60-80	Stationary and heavy vehicle

The main advantages of fuel cells are listed below:

(1) *High energy conversion efficiency.* Because of the direct conversion of electrochemical energy to electrical energy, the usual losses linked to the combustion (related to the Carnot cycle), due to the conversion of fuel to heat, heat to mechanical energy and mechanical energy to electrical energy, are avoided. The efficiency is further improved when the by-product heat is fully retrieved.

(2) *Environmental compatibility.* Fuel cells mainly use hydrogen as energy source, thus with minor environmental impacts (almost no CO<sub>2</sub> and NO<sub>x</sub> produced per kWatt of power).

(3) *Modularity.* The size of a fuel cell can be easily increased or decreased in order to adapt it to the targeted application. The electric efficiency is relatively independent of size.

(4) *Sitting flexibility.* Because fuel cells can be made in a large variety of sizes, they can be placed at different locations with minimum sitting restrictions. Consequently fuel cells can be easily located near points of use.

(5) *Silence.* Fuel cells are quiet because they have no moving parts, even those with extensive extra fuel processing equipment.

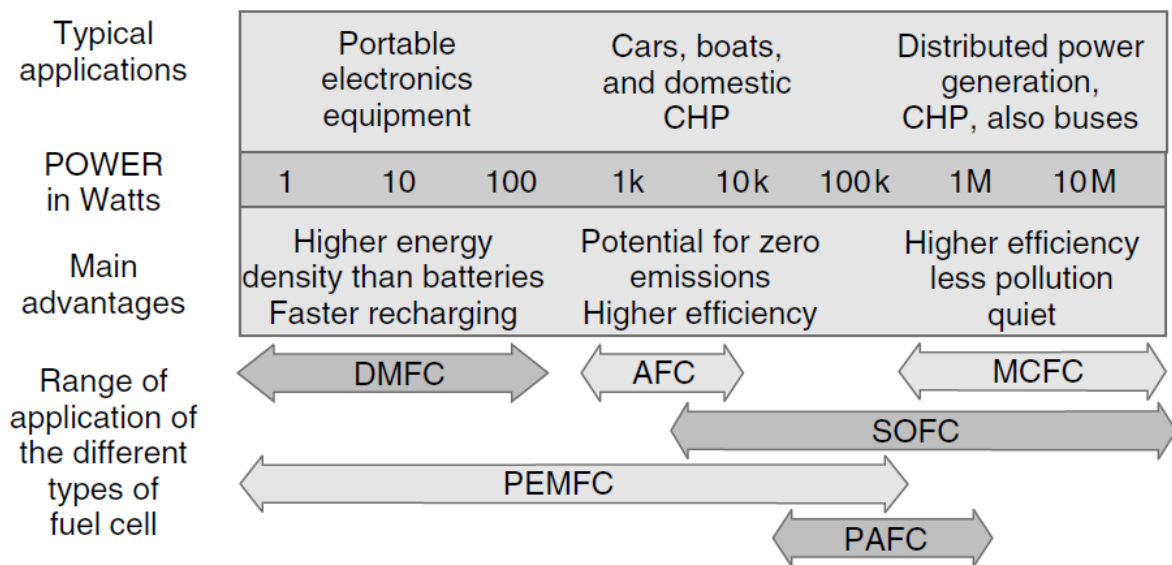


**Figure 1: Chart summarizing the applications and main advantages of fuel cells of different types, and in various applications [3].**

Applications of fuel cells are mainly related to *combined heat and power* systems (for both large- and small-scale applications), and to *mobile power systems*, especially for *vehicles* and electronic equipment such as *portable computers, mobile phones, and military communications equipment* (**Figure 1**). More specifically, low temperature fuel cells (PEMFC, AFC) can be used in mobile applications. On the contrary, high temperature fuel cells (MCFC, SOFC) are competitive in stationary applications. A key point is the wide range of applications of fuel cell power, from systems ranging from few watts up to megawatts. In this respect, fuel cells are quite unique as energy converters; their range of application far exceeds all other types of energy production/conversion.

## 1.4. Working principle of the Fuel Cell

The working principle of the fuel cell is here illustrated in the case of the SOFC, which will be considered in this work (**Figure 2**). Air (oxygen) flows along the cathode. The cathode is also called oxygen electrode. When oxygen molecule gets to the reaction site, it catalytically acquires two electrons from the cathode and splits into oxygen ions  $O^{2-}$ . The oxide ions diffuse into the dense electrolyte layer and migrate to the other side of the cell, where they encounter the anode. The anode is also called fuel electrode. The oxygen ions encounter the fuel at the anode/electrolyte interface and reacts catalytically to produce water, heat and electrons. The balance equations of the electrochemical reactions are:

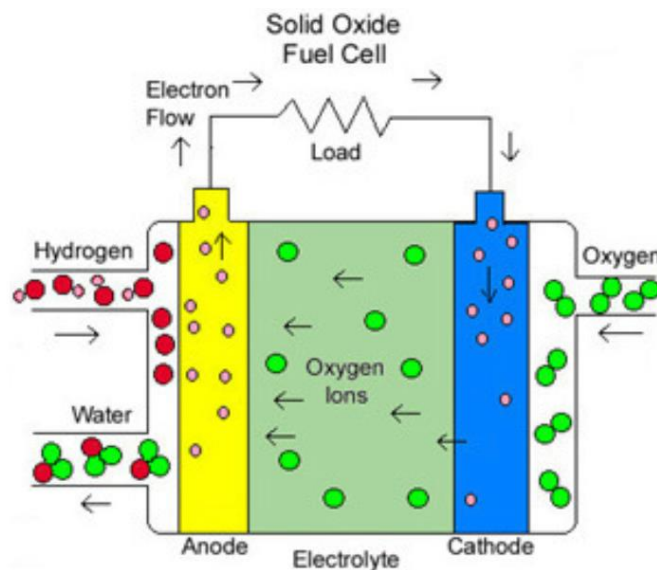
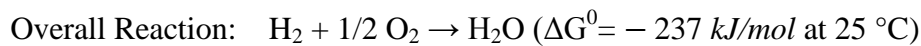
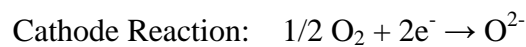


**Figure 2: Working principle of the Solid Oxide Fuel Cell (SOFC).**

The electrons are transported through the anode to the external circuit and return to the cathode, providing electricity in the external circuit.

In practice, a fuel cell consists of several single cells (labelled as SRU for Single Repeat Unit) separated by interconnects forming a "stack". The power of a cell therefore depends on the number of SRU constituting the stack. The thermodynamic efficiency, also called conversion factor, is defined by the ratio between the energy which can be recovered in the form of electrical work and the total amount of energy theoretically available.

Interestingly, the system performance is not limited by Carnot's principle, unlike thermal machines, since the power generation is carried out without thermal combustion. However, part of the energy appears in the form of heat of which portion can be recovered by working at high temperatures, for cogeneration (electricity and heat) type of application.

The performance of the fuel cell is linked to the Nernst potential relationship:

$$E_{i=0} = E^0 + \frac{RT}{2F} \ln \left( \frac{P_{H_2} \cdot P_{O_2}^{1/2}}{P_{H_2O}} \right)$$

Where,  $E_{i=0}$  = thermodynamic potential at equilibrium or Open Circuit Voltage (OCV)

$E^0$  = Standard potential

R= gas constant

T=Temperature

2= electrons number exchanged in the reaction

F= Faraday constant

The electric power density is the product of voltage by current density at each point of the current/voltage curve (**Figure 3**). At OCV, no power is produced. The power then increases with increasing current density up to a maximum. Beyond the maximum, the drop in cell voltage is stronger than the increase in current density.

The voltage across the cell ( $E_{cell}$ ,  $i \neq 0$ ) in operation is lower than the thermodynamic one ( $i=0$ ) because of losses from polarization effects appearing when applying the current. The cell potential is then modified as follows:

$$E_{cell} = E_{i=0} - \left| \eta_{cathode} \right| - \eta_{anode} - \eta_{ohmic}$$

$E_{i=0}$  = potential at zero current, called open circuit voltage (OCV)

$\eta_{cathode} (<0)$  = cathodic overpotential;  $\eta_{anode} (>0)$  = anodic overpotential

$\eta_{ohmic} = R_i$  = ohmic losses due to electrolyte as well as contact resistances (the resistances due to anode and cathode are negligible)

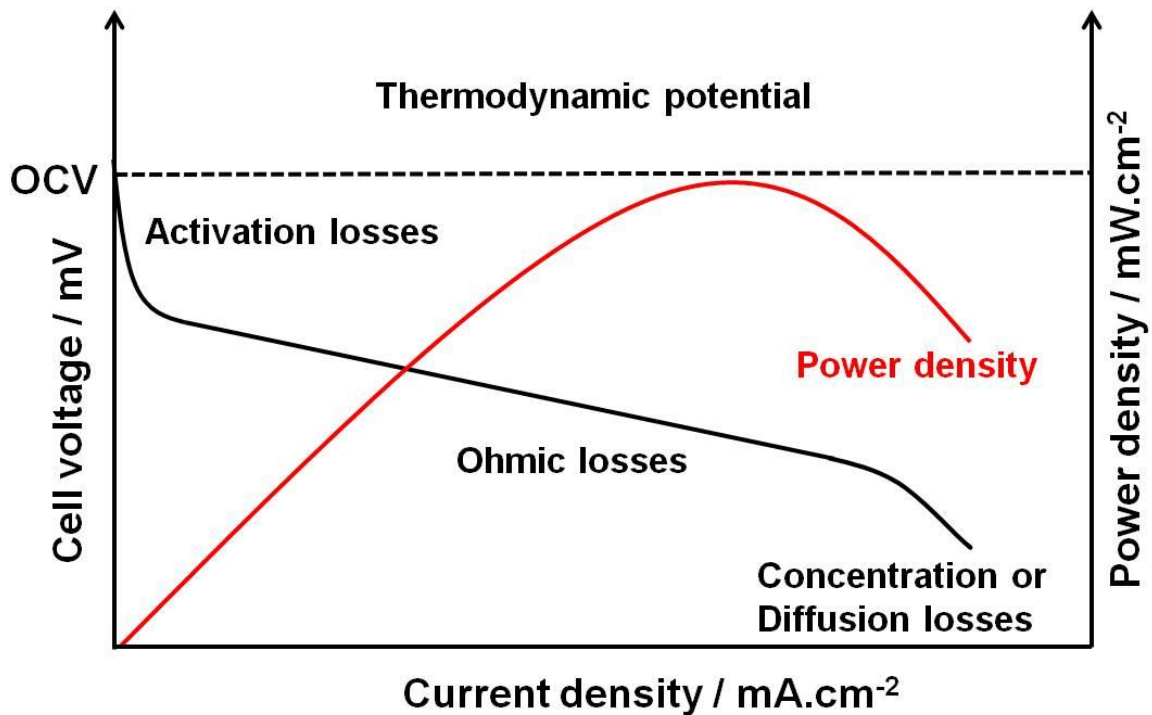


**Figure 3:**  $E = f(i)$  characteristic of a fuel cell.

## 1.5. Losses

The evolution of the cell voltage against current density expressed by the polarization curve (**Figure 3**) can be separated into three parts:

- The rapid initial drop in voltage.
- The voltage then falls less rapidly, and more linearly.
- The voltage falls again rapidly at higher current density.

Three main mechanisms of voltage losses exist in polarization curve, namely activation, ohmic and concentration over-potentials which lead to the decrease of performance of the cell. The dependency of these losses versus the temperature, current density and species concentrations mainly determine the characteristics of the fuel cell.

### 1.5.1. Activation over-potential

The activation overpotential losses are limiting at low current density. They are caused by the slowness of the reactions taking place on the surface of the two electrodes. A proportion of the voltage generated is lost in driving the chemical reaction that transfers the electrons to or from the electrodes. The activation overpotential of the electrodes (labelled  $\eta_{\text{anodic}}$  and  $\eta_{\text{cathodic}}$ ) is thermally activated and kinetically controlled. This effect is increased by a decrease in temperature. To reduce the activation overpotential, it is needed to improve

the electrode material and microstructure, by preparing electrodes having a larger area active towards electrochemical reactions. As shown in **Figure 3**, the voltage drop is highly non-linear. The voltage drop increases at low reaction rates and after a certain level it becomes almost constant. Activation over-potential is the dominant source of losses for low temperature fuel cells, while its influence is in principle smaller for SOFCs.

### **1.5.2. Ohmic losses (ohmic overpotential/overvoltage)**

The ohmic (resistive) losses are mainly caused by the resistance of the conducting ions (mainly through the electrolyte) and contact resistances between the cell components. The effects of these losses are mostly limiting at intermediate current densities. This voltage drop is linearly proportional to the current density.

The ohmic polarisation,  $\eta_{ohmic}$ , is expressed as:

$$\eta_{ohmic} = R_i$$

$R$  represents the total ohmic cell resistance, including both ionic and electronic resistances.

### **1.5.3. Concentration or diffusion losses (concentration overpotential/overvoltage):**

The concentration or diffusion losses mostly limit the cell voltage at high current densities and result from the change in concentration of the reactants at the surface of the electrodes as the fuel is used. Reactants must flow through the porous electrodes to the Triple Phase Boundaries TPBs (see part 2.3.1.), and product must be evacuated, driven by diffusion. As the current increases, the amount of reactant available at the reaction sites decreases. In the meantime, the amount of water produced increases and limits the reactants access to the reaction sites. These two phenomena imply that the concentration of reactants at the reaction sites becomes lower, which creates a potential drop called *diffusion or concentration overpotential*. The voltage drop increases with increasing current toward an asymptotic maximum current. At this point, the concentration of one of the reactants at the TPB is close to zero and no further current increase is possible. An improvement can be done when changing the microstructure and increasing flow rate of the gas.

## 2. Solid Oxide Fuel Cells (SOFCs)

The SOFC, which operates at high temperature, is built with solid (ceramic) components (anode, electrolyte, and cathode). There are two main designs, planar and tubular. The main advantages of SOFCs are the following ones: 1) SOFC can retrieve heat from the reaction (combined heat and power (CHP)), allowing to increase the maximum efficiency up to around 85 %, and 2) SOFCs show a great versatility in terms of fuels which can be possibly used, moreover without poisoning by carbon monoxide. The main drawbacks are related to: 1) the fabrication cost of the SRUs and interconnects, 2) the chemical reactivity between the cell components, linked to the high operating temperature. The different components of a SOFC cell, *i.e.* anode, electrolyte, cathode and interconnect are described below.

### 2.1. Anode

The chemical reaction occurring at the anode is the oxidation of gaseous fuel with the release of electrons and formation of water vapour by using the oxide ions that migrated through the electrolyte. Physically, this reaction takes place at the TPB where the fuel gas, electrolyte and anode material meet.

The activity of the anode is improved when the surface of the anode, then the TPBs number, increases. Accordingly, the anode is generally made of a porous cermet (30-40% porosity) combining ceramic and metal phases, providing the ion and electron conduction respectively. The fuels most likely used in SOFCs are hydrogen (possibly obtained from reformed natural gas), hydrocarbons, oil or coal gasification. The most common anode material is Ni/Yttria stabilized zirconia (YSZ, see electrolyte part) cermet [4]. About 30% by volume of nickel is required to ensure the electronic percolation. Nickel is cheap and has good catalytic properties for the oxidation of fuel (hydrogen). Copper could also be considered as a replacement for nickel [5, 6], but has a higher propensity for carbon deposition and sulphur poisoning at lower temperature. Even if the anode does not limit the cell performance as much as the electrolyte and the cathode, research is still conducted on the particular problems of anodic degradation [7], as well as possible new materials with MIEC (mixed ionic and electronic conductivity) properties.

## 2.2. Electrolyte

The SOFC electrolyte is a dense layer of ceramic that conducts oxygen ions  $O^{2-}$ . For ensuring such ionic conduction, the cell has to be heated above  $T > 600^\circ\text{C}$ . The transportation of oxide ions takes place from the cathode to the anode through the electrolyte, which has to be a dense membrane (density  $> 95\%$ ). The electrolyte must retain its properties of chemical stability and ion transport in the presence of oxidizing and reducing atmospheres, as well as possess thermal expansion coefficients compatible with the other components of the stack. It is mostly the electrolyte that defines the TEC of all other cell components.

While a quite large number of recent studies in the SOFC field concern possible new chemical compositions, we focused here only on the presentation of doped zirconia and ceria, which are by far the most used electrolytes.

### 2.2.1. Yttria Stabilized Zirconia (YSZ)

The most widely used electrolyte material is Yttria Stabilized Zirconia (YSZ):  $ZrO_2$ - $Y_2O_3$  [8, 9]. YSZ has good mechanical properties and excellent chemical stability over a wide range of temperatures and oxygen partial pressures ( $10^{-22} < p_{O_2} \text{ (atm)} < 0.2$ ). The cubic structure of  $ZrO_2$  can be stabilized using  $Y_2O_3$ , as well as other divalent and trivalent dopants such as  $MgO$ ,  $CaO$ ,  $Sc_2O_3$  and  $Yb_2O_3$  for example, providing oxygen vacancies, which amount depend on the nature of dopants and on the substitution level [9, 10]. The oxygen vacancies are responsible for the ion conduction for this type of material provided there are sufficiently mobile, a characteristic that increases with temperature. The radius of the dopant ion should be as close as possible to that of the host  $Zr^{4+}$  ion ( $r_{Zr^{4+}} = 0.84 \text{ \AA}$  [11]) to avoid high mechanical stresses which reduce the ionic mobility [12, 13].

The most used dopants are yttrium ( $r_{Y^{3+}} = 1.02 \text{ \AA}$  [11]) and scandium ( $r_{Sc^{3+}} = 0.87 \text{ \AA}$  [11]), allowing to obtain materials having the highest ionic conductivity [14-17]. For instance, at  $800^\circ\text{C}$ , the ionic conductivity of 8-10 mol%  $Sc_2O_3$ - $ZrO_2$  is  $0.12 \text{ S.cm}^{-1}$ , while it is  $0.052 \text{ S.cm}^{-1}$  for 8-8.5 mol%  $Y_2O_3$ - $ZrO_2$  (YSZ) [15]. Substitution with scandium is less used for cost reasons and also because of the presence of a phase transition (rhombohedral-quadratic) at  $650^\circ\text{C}$ .

A maximum of conductivity values is observed for a doping rate of about 8 mol%  $Y_2O_3$  doping in  $ZrO_2$  (8YSZ) (**Figure 4**), which also stabilizes the cubic phase. A material is

considered as a pure ionic conductor when the transport number ( $t_i$ ) is greater than or equal to 0.99. The number of ion transport is defined as follows:

$$t_i = \sigma_{ionic} / \sigma_{total}$$

The ion transport number of 8YSZ is very close to 1, between 500 and 1000 ° C, for oxygen partial pressures ranging from 0.1 atm (oxidizing atmosphere) to  $10^{-22}$  atm (reducing atmosphere). Therefore 8YSZ is a pure ionic conductor in this pressure range, compatible with its use in SOFC [14].

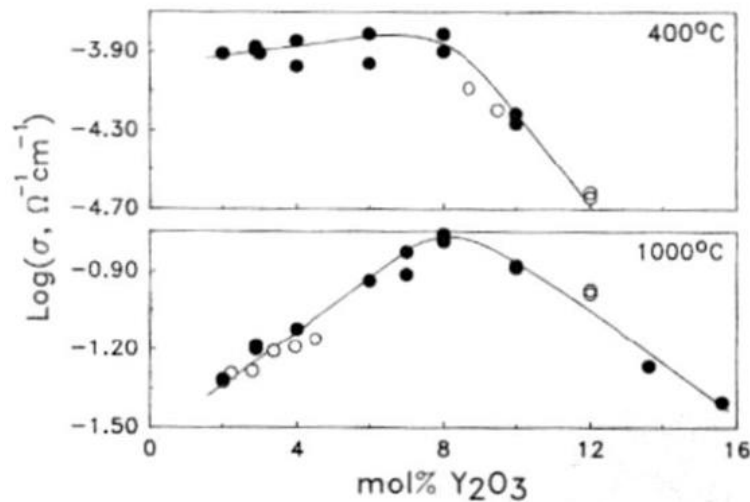


**Figure 4: Evolution of the ionic conductivity as a function of the substituting rate of Y<sub>2</sub>O<sub>3</sub> in YSZ; (○) single crystal (●) polycrystal [12].**

For a doping rate of about 3 mol% Y<sub>2</sub>O<sub>3</sub> doping in ZrO<sub>2</sub> (3YSZ), the thermo-mechanical properties are improved [18] with respect to 8YSZ, but the ionic conductivity is lower (**Figure 4**).

Nevertheless, the stabilized zirconia has the disadvantage of chemically reacting at high temperature with several cathode materials, including La<sub>1-x</sub>Sr<sub>x</sub>CoO<sub>3-δ</sub> (LSC), La<sub>1-x</sub>Sr<sub>x</sub>Co<sub>1-y</sub>Fe<sub>y</sub>O<sub>3-δ</sub> (LSCF), La<sub>1-x</sub>Sr<sub>x</sub>Cr<sub>1-y</sub>Mn<sub>y</sub>O<sub>3-δ</sub> (LSCM), LaNi<sub>1-x</sub>Fe<sub>x</sub>O<sub>3-δ</sub> (LNF), La<sub>1-x</sub>Sr<sub>x</sub>FeO<sub>3-δ</sub> (LSF), Ba<sub>1-x</sub>Sr<sub>x</sub>Co<sub>1-y</sub>Fe<sub>y</sub>O<sub>3-δ</sub> (BSCF), the most commonly used cathodes. This reactivity leads to the formation of two insulating phases at the electrode/electrolyte interface: SrZrO<sub>3</sub> and La<sub>2</sub>Zr<sub>2</sub>O<sub>7</sub>, which are of perovskite and pyrochlore-type, respectively [15, 19-22]. This chemical reactivity at the interface which appears during the synthesis and shaping of the cell components at high temperature becomes larger as a function of time at the operating

temperature. Then a degradation of the performance occurs during operation, because the conductivity of the formed two phases is substantially lower than that of electrolyte [23-27].

### 2.2.2. Doped ceria

Ceria is another well-known electrolyte material with fluorite-type structure [28, 29]. However, the un-doped ceria has a low ionic conductivity. To improve it,  $\text{CeO}_2$  can be substituted with trivalent cations, for ex.  $\text{Sm}^{3+}$ ,  $\text{Gd}^{3+}$ ,  $\text{Nd}^{3+}$ ,  $\text{Dy}^{3+}$ ,  $\text{Y}^{3+}$ ,  $\text{Yb}^{3+}$  and  $\text{Ho}^{3+}$ . Similarly to stabilized zirconia, the partial substitution of tetravalent cations with trivalent leads to the formation of oxygen vacancies, which result in the mobility of  $\text{O}^{2-}$  ions upon raising the temperature. Among the substituents cations, ionic conduction is maximal for samarium and gadolinium (**Figure 5**). However, substitution with gadolinium is the most promising, because of the high cost and low availability of samarium. In this case the substituted ceria can replace YSZ as electrolyte for IT-SOFC. A substituting level of 10 mol% ( $\text{Ce}_{0.9}\text{Gd}_{0.1}\text{O}_{1.95}$ : GDC10) offers a larger ionic conduction than 20 mol% doping ( $\text{Ce}_{0.8}\text{Gd}_{0.2}\text{O}_{1.9}$ : GDC20) [30, 31]. The ionic conductivity of ceria doped with 10GDC is higher than that of YSZ,  $\sigma_i = 2 \times 10^{-2} \text{ S.cm}^{-1}$  and  $\sigma_i = 8 \times 10^{-3} \text{ S.cm}^{-1}$  for 10GDC and YSZ at 650 °C, respectively [16, 31-33].

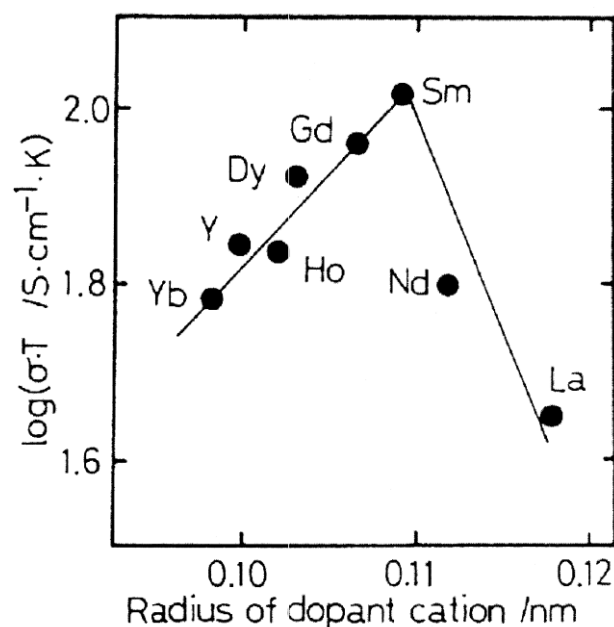


**Figure 5: Evolution of the ionic conductivity of ceria (20 mol. %) at 800 °C, based on the type of dopant [28].**

But a concern often expressed with regards to the use of GDC electrolytes in SOFCs is that, at elevated ( $> 600^\circ\text{C}$ ) temperatures,  $\text{Ce}^{4+}$  ions can be reduced to  $\text{Ce}^{3+}$  under fuel rich conditions, *i.e.* towards the anode compartment [14, 31, 34-35]. The mixed valence  $\text{Ce}^{4+}/\text{Ce}^{3+}$  creates electronic mobility and hence n-type electronic conductivity, which can detrimentally short circuit the SOFC cell. In addition, under reducing atmosphere ceria undergoes a strong volume expansion [36], leading to a sharp increase in thermo-mechanical stresses. However, at temperatures  $T < 600^\circ\text{C}$  the reduction of  $\text{Ce}^{4+}$  ions to  $\text{Ce}^{3+}$  at the GDC/anode interface is minimized [31, 37], and can be neglected under typical cell operating conditions.

The thermal expansion coefficient of ceria increases with the amount of dopant. For example, the TEC of GDC10 is in between  $11 \times 10^{-6} \text{ K}^{-1}$  and  $13 \times 10^{-6} \text{ K}^{-1}$  between 30 and  $1000^\circ\text{C}$  [38]. Unlike YSZ, GDC is more chemically stable with the typical electrode materials, LSM, LSC, LSF, LSCF, LNF [39-43], despite some possible lanthanum and strontium diffusion as evidenced by Izuki *et al.* [44].

Samarium doped Ceria (SDC) has also good electrolytic properties that however depends on the oxygen partial pressure. For example, Abrantes *et al.* studied the electronic conductivity of SDC as a function of  $p\text{O}_2$  [45] and reported an electronic conductivity of  $0.37 \text{ S.cm}^{-1}$  at  $p\text{O}_2 = 10^{-16} \text{ atm}$  and  $0.58 \text{ S.cm}^{-1}$  at  $p\text{O}_2 = 10^{-18} \text{ atm}$  at  $800^\circ\text{C}$ .

## 2.3. Cathode

### 2.3.1. General requirements – electronic conductors

The cathode, or oxygen electrode, is a porous layer where the reduction of the oxygen molecules to oxide ions  $\text{O}^{2-}$  (ORR) takes place:



Consequently, a high level of electronic conductivity of the cathode material is required. Moreover, the microstructure (especially the porosity) of the electrode is a key parameter to ensure the access of gaseous oxygen to the surface in between the cathode and the electrolyte, where  $\text{O}^{2-}$  species are available.

Let us summarize here the general requirements for SOFCs cathode:

- High electronic conductivity.
- High catalytic activity towards oxygen reduction.

- Thermal expansion coefficient (TEC) comparable to that of other SOFC-components.
- Low chemical reactivity towards other materials used in the SOFC.
- High thermal stability.
- Optimised microstructure, low cost materials and mechanical strength.
- Because the SOFC is operated at high temperatures for long periods of time, it should be able to withstand repeated thermal cycling.

In the case of electronic conductors, the ORR occurs at the interface between the electrode, the electrolyte and the gaseous phase, then on the triple contact lines (labelled TPB for Triple Phase Boundary). The number of TPBs has to be as high as possible. In order to increase the length of the triple contact lines, composites electrodes formed with electronic conductor (the cathode material) and an ionic conductor (possibly an electrolyte type conductor) are often prepared, as shown in **Figure 6**. It's mandatory that both phases formed two percolating networks.

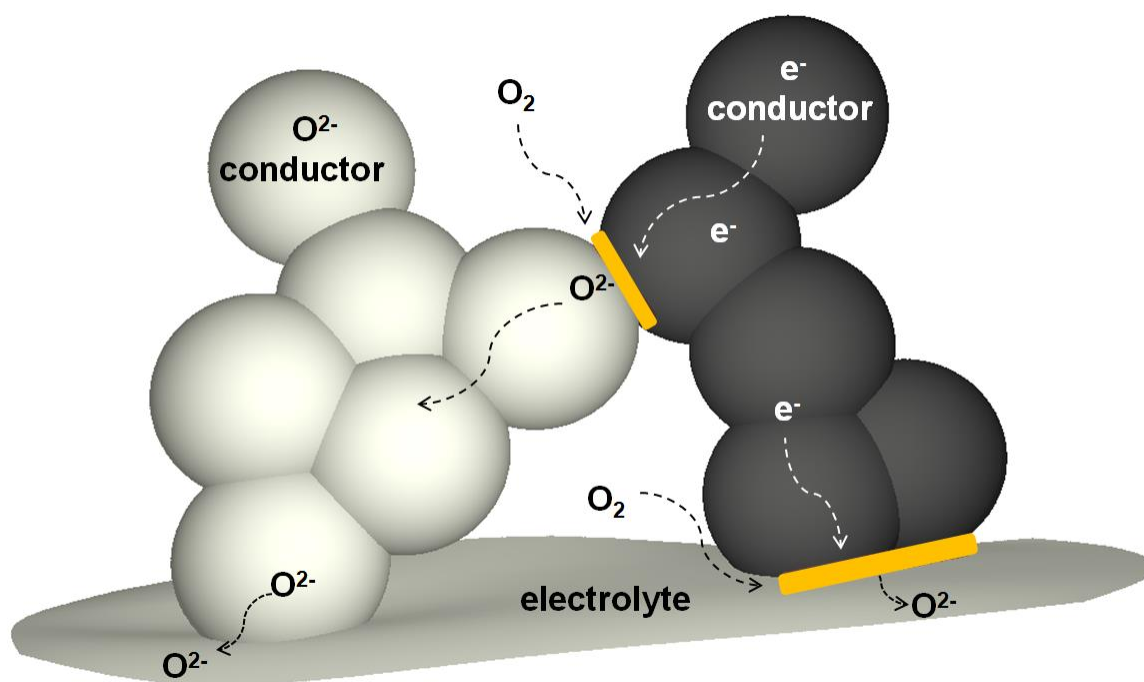


**Figure 6: Scheme of the oxygen reduction reaction occurring on the TPBs lines (in yellow) in a composite oxygen electrode including both an electronic conductor (black grains) and an ionic conductor (white grains).**

For instance the strontium substituted lanthanum manganite (LSM) [46], with very high electronic conductivity (thanks to the mixed valency of manganese,  $Mn^{3+}/Mn^{4+}$  with the formation of electronic holes), has been studied (including SOEC (Solid Oxide Electrolyzer

Cell) operations) in combination with YSZ [47-49]. LSM was during long time the classical SOFCs cathode material, in case of high operating temperature (900-1000 °C).

### 2.3.2. MIEC Materials

Materials with MIEC (Mixed Ionic and Electronic Conductivity) properties [50, 51] allow the incorporation of oxide ions directly in the network and their diffusion occurs through the material, as shown in **Figure 7**.

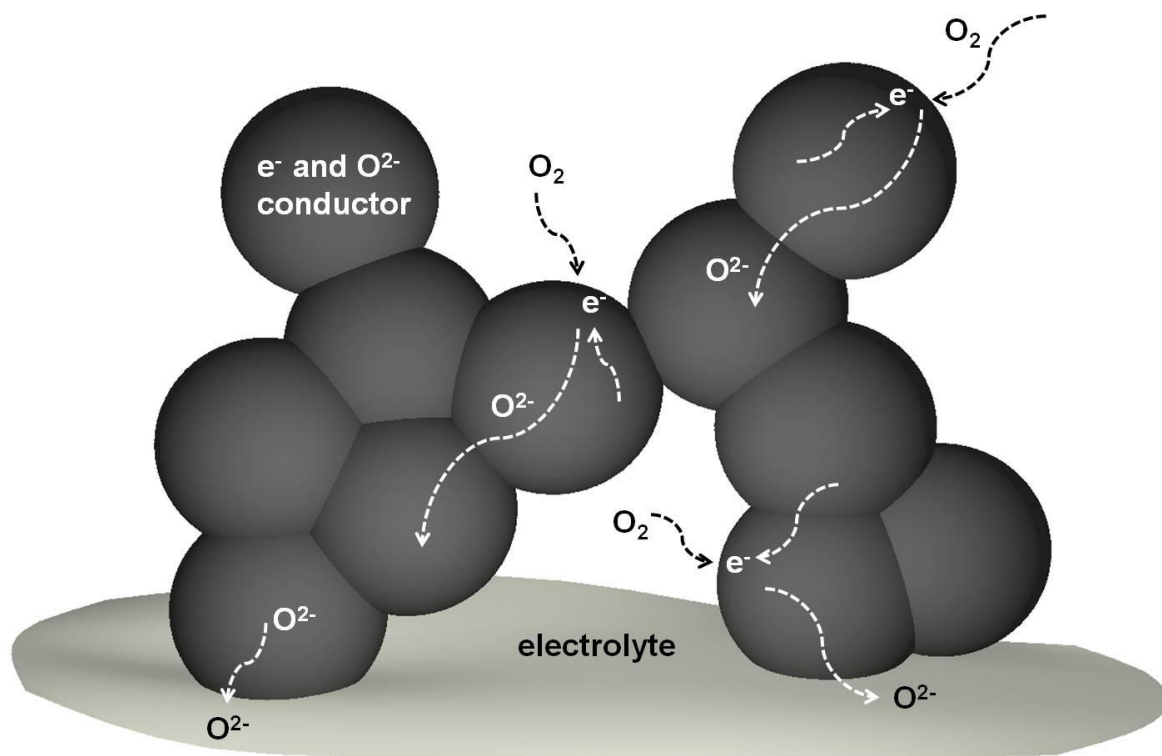


**Figure 7: Scheme of the oxygen reduction reaction occurring in an oxygen electrode with MIEC properties.**

In this case the effective area of the cathodic reaction is extended with respect to the first situation; hence the reaction is delocalized at the overall surface of the cathode, improving the cell performance. The use of cathode materials with MIEC properties has been largely developed over the last years. There are mainly three kinds of MIEC materials: i) oxygen deficient compounds with perovskite-type structure (ii) double perovskites, and iii) oxygen over-stoichiometric materials with Ruddlesden-Popper type structure.

### (a) Oxygen deficient MIEC Materials

Among the different materials with the perovskite structure (**Figure 8**) identified as MIEC conductors, the strontium-substituted cobaltites  $\text{La}_{1-x}\text{Sr}_x\text{CoO}_{3-\delta}$  (LSC) have a high ionic conductivity and good catalytic properties with respect to the oxygen reduction reaction (**Table 2**) [52-54]. However, their TEC coefficients are very high with respect to YSZ or GDC. Using the ferro-cobaltites  $\text{La}_{1-x}\text{Sr}_x\text{Fe}_{1-y}\text{Co}_y\text{O}_{3-\delta}$  (LSFC) a good compromise is obtained between the thermo-mechanical constraints and the ionic properties [55-58]. In LSFC materials, the electronic conductivity arises thanks to the strontium to lanthanum substitution leading to the mixed valencies  $\text{Fe}^{3+}/\text{Fe}^{4+}$  and  $\text{Co}^{3+}/\text{Co}^{4+}$ . Another consequence is the formation of oxygen vacancies in the 3D network, the under stoichiometry  $\delta$  being dependent on the  $x$  value as well as on the oxygen partial pressure. The higher  $\delta$  and best ionic conductivity (arising from migration of oxygen in the vacant network) values are obtained for Co-rich materials.

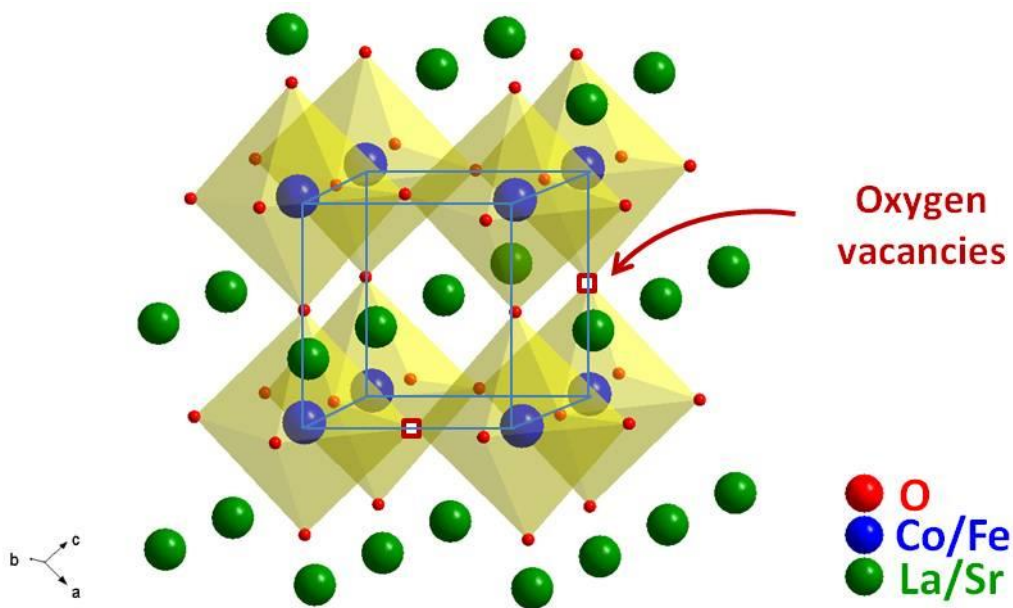


**Figure 8: Oxygen deficient perovskite structure (e.g. LSCF).**

Another studied composition as cathode material is  $\text{La}_{0.6}\text{Sr}_{0.4}\text{Fe}_{0.8}\text{Ni}_{0.2}\text{O}_{3-\delta}$  (LSFN). In **Table 2**, the electrical conductivity, TEC, oxygen diffusion ( $D^*$ , which is directly related to the ionic conductivity) and surface exchange ( $k^*$ , which characterize the ability of gaseous oxygen to be reduced at the surface of the material) coefficients of these perovskite materials are compared with traditional  $\text{La}_{1-x}\text{Sr}_x\text{MnO}_{3-\delta}$  (LSM).  $D^*$  and  $k^*$  values of these MIEC

perovskites are higher than those of LSM. The high TEC values [59-61] compared to those of LSM are evidenced. Another disadvantage of these materials is that they easily form insulating phases such as  $\text{La}_2\text{Zr}_2\text{O}_7$  and  $\text{SrCoO}_3$  at the interface with YSZ electrolyte, which further degrade the performance of the cell.

**Table 2: comparison of electrical conductivity, TEC, oxygen diffusion ( $D^*$ ) and surface exchange ( $k^*$ ) coefficients of some MIEC perovskite materials with LSM**

Composition	$\sigma_e$ at 900°C S.cm <sup>-1</sup>	TEC, $\alpha$ (10 <sup>-6</sup> K <sup>-1</sup> )	$D^*$ at 900°C (cm <sup>2</sup> .sec <sup>-1</sup> )	$k^*$ at 900°C (cm.sec <sup>-1</sup> )
LSC	500-1500 [62]	18-26 [63]	10 <sup>-9</sup> (x = 0.1) 3×10 <sup>-6</sup> (x=0.7) [64]	10 <sup>-6</sup> (x = 0.1) 2×10 <sup>-5</sup> (x=0.7) [64]
LSCF (6428)	200 [61]	16 [61]	5×10 <sup>-8</sup> [61]	7×10 <sup>-7</sup> [61]
LSFN (6428)	300 [61]	14 [61]	5×10 <sup>-8</sup> [61]	7×10 <sup>-7</sup> [61]
LSM	200 [65]	10-12 [66]	10 <sup>-13</sup> (x=2) [67]	5×10 <sup>-8</sup> (x=2) [67]

$\text{Ba}_{0.5}\text{Sr}_{0.5}\text{Co}_{0.8}\text{Fe}_{0.2}\text{O}_{3-\delta}$  (BSCF) can also be used as SOFC cathode materials [68]. Its electronic conductivity is high ( $\sim 30 \text{ S cm}^{-1}$  at 600°C) [69], the oxygen diffusion properties interesting ( $D^* \sim 5.10^{-7} \text{ cm}^2 \text{ s}^{-1}$  and  $k \sim 10^{-5} \text{ cm s}^{-1}$  at 600°C) [70], and the oxygen under stoichiometry high ( $\delta \sim 0.3$  at RT) [71]. However, BSCF is highly sensitive to the presence of  $\text{CO}_2$ . The formation of strontium and barium carbonates at the grains surfaces is observed, which is detrimental in particular for the oxygen diffusion properties [72, 73].

### (b) Double perovskites

Several materials belonging to a family directly derived from the perovskite have recently been studied as  $\text{O}^{2-}$  - SOFC cathodes: this family is labelled “double perovskites” with general formulation  $\text{AA}'\text{B}_2\text{O}_{5+\delta}$  (A = rare earth, A' = alkaline earth metal, B = transition metal). A characteristic of those phases is the ordering of the rare earth and alkaline earth metal layers along the (001) axis, leading to a doubling of the c parameter with respect to the perovskite with cubic symmetry [74]. As a result of this cationic ordering, the oxygen vacancies are mainly located in the rare-earth layer ( $\text{AO}_\delta$ ), and for an oxygen stoichiometry value  $\delta \sim 0.5$  they are as well ordered along the a-axis, leading to a doubling of the b parameter [75]. To our knowledge, only cobalt and manganese allow obtaining these compounds. Moreover, the ordering of the cationic layers is induced by a large difference

between the rare-earth and alkaline rare earth metal radii; therefore barium is mainly used, as well as rare-earths with small radii.

With respect to the applications, the main studies are focused on cobaltites. The first studies on the MIEC properties on these materials were performed by Taskin *et al.* [76-78]. The most studied compositions are  $\text{GdBaCo}_2\text{O}_{5+\delta}$  and  $\text{PrBaCo}_2\text{O}_{5+\delta}$  [77, 79-80]. However, substitutions (Co-Fe, Co-Ni and Ba-Sr) enable to slightly improve the electrode performance [81-83]. Currently, the oxygen diffusion values are still under debate; regarding the electronic conductivity, the higher value is obtained for  $\text{PrBaCo}_2\text{O}_{5+\delta}$  [84, 87].

### (c) The Ruddlesden-Popper (RP) series $\text{A}_{n+1}\text{M}_n\text{O}_{3n+1}$

The compounds belonging to the RP series adopt the general formulation  $\text{A}_{n+1}\text{M}_n\text{O}_{3n+1}$ . A is a lanthanide or alkaline-earth metal and M a transition metal. The structure can be described by the intergrowth of octahedra layers (perovskite type) with AO layers (NaCl -type). “ $n$ ” is related to the number of octahedra layers between the AO layers. **Figure 9** shows the first three terms of the RP series, which are the only ones known at least for the most used transition metals. For  $n = \infty$  the perovskite structure is described.

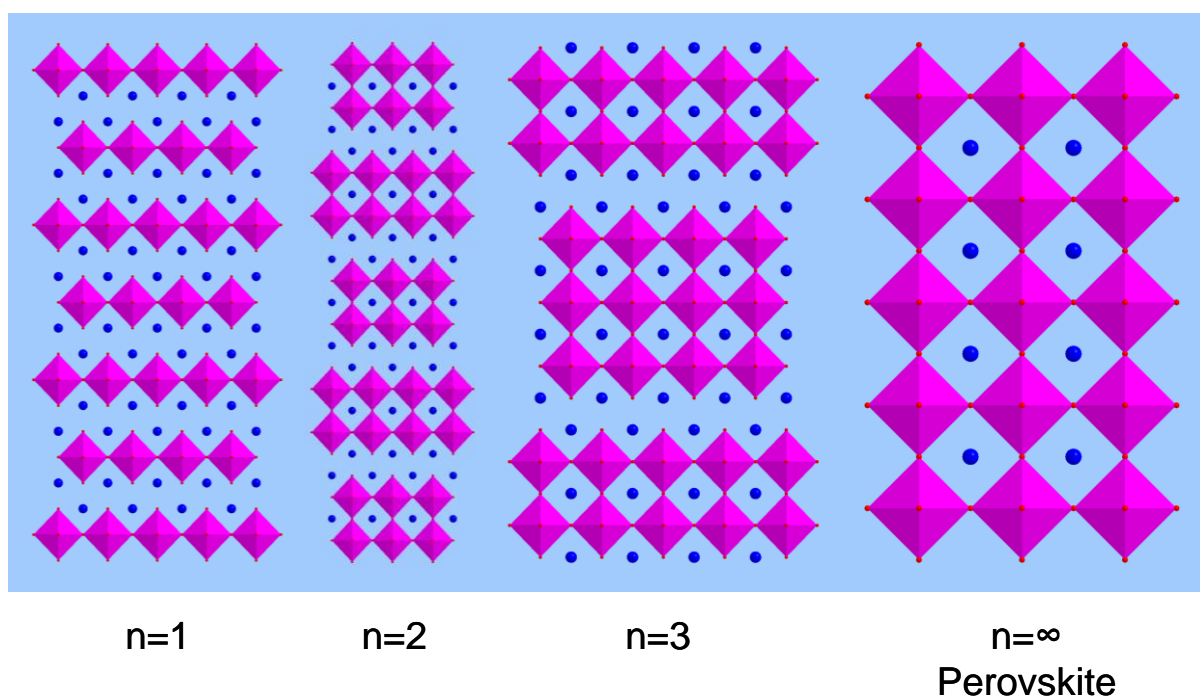


**Figure 9: Schematic representation of the different structures in the Ruddlesden-Popper series  $\text{A}_{n+1}\text{M}_n\text{O}_{3n+1}$ ,  $n=1, 2, 3, \infty$  ● : A cation, ◆ : M cation, • : oxygen.**

(d)  $\text{Ln}_2\text{NiO}_{4+\delta}$  ( $\text{Ln} = \text{La, Pr and Nd}$ )

With respect to the RP class of materials, the nickelate series  $\text{Ln}_{n+1}\text{Ni}_n\text{O}_{3n+1}$  where  $\text{Ln} = \text{La, Pr and Nd}$ , have gained significant attention in recent years, especially  $n = 1$  phases as alternative cathode materials [85-89]. It has been established that  $\text{Ln}_2\text{NiO}_{4+\delta}$  ( $\text{Ln} = \text{La, Pr and Nd}$ ) with  $\text{K}_2\text{NiF}_4$  structure exhibit a large range of oxygen over-stoichiometry. The reported mean oxygen over-stoichiometries values are 0.16 for  $\text{La}_2\text{NiO}_{4+\delta}$  [90, 91], 0.22 for  $\text{Pr}_2\text{NiO}_{4+\delta}$  [92, 93] and 0.25 for  $\text{Nd}_2\text{NiO}_{4+\delta}$  [94], then being dependent on the rare-earth size. The oxygen over-stoichiometry  $\delta$  value is also depending upon the condition of synthesis for a given composition [95, 96].

The additional (interstitial) oxygen is located in the  $\text{Ln}_2\text{O}_2$  rock-salt interlayer. Moreover, the  $\text{NiO}_6$  octahedra is elongated along the c-axis, hence three kinds of oxygen are finally distinguished:  $\text{O}_{\text{apical}}$ ,  $\text{O}_{\text{equatorial}}$  and  $\text{O}_{\text{interstitial}}$  (**Figure 10**).

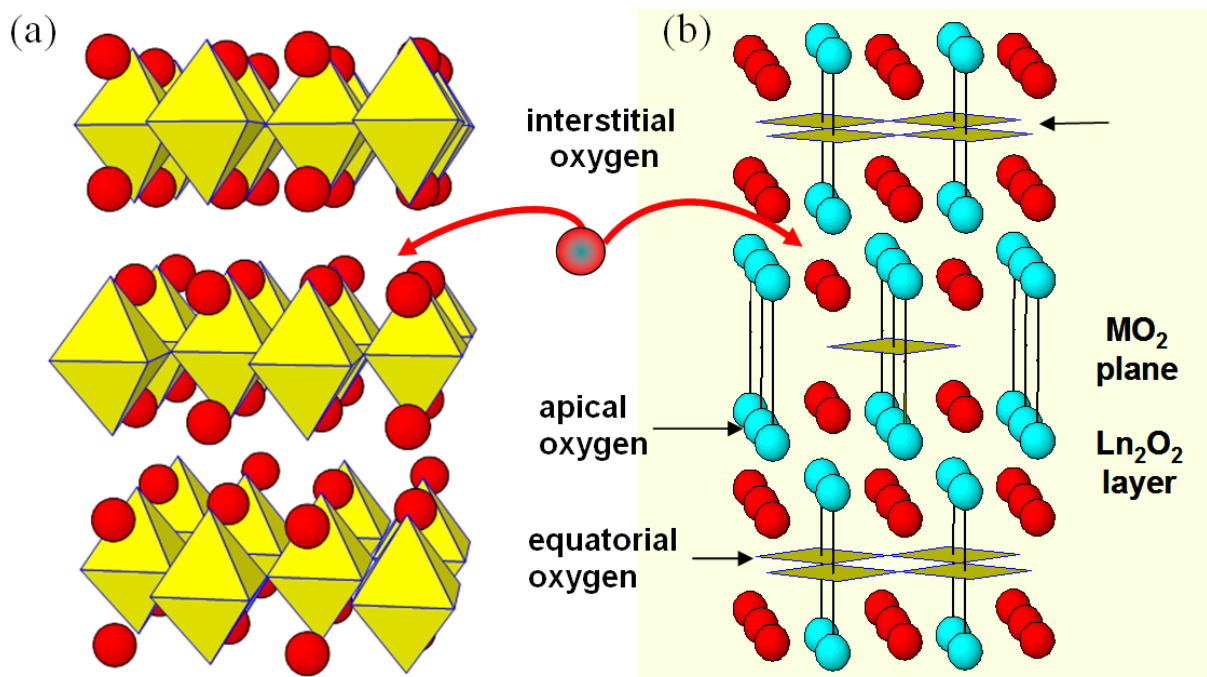


**Figure 10: Schematic representation of the  $\text{Ln}_2\text{MO}_{4+\delta}$  structure ( $\text{M} = \text{Ni, Co, Cu}$ ).**

Thanks to the oxygen over-stoichiometry, a mixed valence ( $\text{Ni}^{2+}/\text{Ni}^{3+}$ ) appears. The oxygen excess and charge compensating  $\text{Ni}^{3+}$  ions (electronic holes) stabilize the  $\text{K}_2\text{NiF}_4$  structure by reducing i) the intrinsic charge separation between the electropositive  $\text{Ln}_2\text{O}_2$  and electronegative  $\text{NiO}_2$  layers and ii) the structural strain due to the misfit between the  $\text{Ln}_2\text{O}_2$  and  $\text{NiO}_2$  layers. The Goldschmidt tolerance factor [97]:

$$t = \frac{(r_{Ln} + r_O)}{\sqrt{2} * (r_{Ni} + r_O)}$$

where  $r_{Ln}$ ,  $r_O$  and  $r_{Ni}$  are the effective ionic radii of  $Ln^{3+}$ ,  $O^{2-}$  and  $Ni^{2+/3+}$ , respectively enables to predict the stability domains of the various structural varieties (which are either tetragonal or orthorhombic) of the  $K_2NiF_4$  structure.

The oxygen diffusion ( $D^*$ ) and surface exchange ( $k^*$ ) coefficients of these nickelates are among the highest values available in the literature, especially at intermediate temperatures (about one order magnitude larger than that of conventional perovskites in an intermediate temperature range ( $600 < T^\circ C < 800$ )). For example, the reported  $D^*$  values at  $600^\circ C$  are  $1.5 \times 10^{-8}$ ,  $2.5 \times 10^{-8}$  and  $7 \times 10^{-9} \text{ cm}^2 \cdot \text{s}^{-1}$  for  $La_2NiO_{4+\delta}$ ,  $Pr_2NiO_{4+\delta}$  and  $Nd_2NiO_{4+\delta}$  respectively [86, 89, 98]. The ionic conductivity of these materials is directly related to the  $D^*$  value, hence the ionic conductivity is the highest for  $Pr_2NiO_{4+\delta}$  [99]. The favoured mechanism is probably of interstitialcy type, involving both apical and interstitial oxygens [100, 101]. Compared to the perovskite materials, the ionic conductivity of the here considered materials has a strong 2D character (being the values about 100 times higher in the (a,b) plane compared to the c-axis direction) [102-104]. The corresponding  $k^*$  values at  $600^\circ C$  are  $1 \times 10^{-6}$ ,  $5 \times 10^{-7}$  and  $10^{-7} \text{ cm} \cdot \text{s}^{-1}$  for  $La_2NiO_{4+\delta}$ ,  $Pr_2NiO_{4+\delta}$  and  $Nd_2NiO_{4+\delta}$  respectively [89], these characteristics are associated with good electro-catalytic activity and hence the oxygen reduction reaction (ORR).

Finally, thanks to the mixed valency of nickel and to the oxide ion conductivity,  $Ln_2NiO_{4+\delta}$  materials are mixed ionic and electronic ( $O^{2-}/e^-$ ) conductors, showing as well good electro-catalytic properties with respect to the oxygen reduction reaction.

Hence these materials are suitable for cathodes in SOFCs applications. Up to now, to our knowledge the best electrochemical result, *i.e.* the lowest polarization resistance ( $R_p = 0.1 \Omega \cdot \text{cm}^2$  at  $600^\circ C$ ), was obtained for  $Pr_2NiO_{4+\delta}$  (in symmetrical half-cell configuration  $Pr_2NiO_{4+\delta} // GDC // YSZ$  [105]). The power density is also maximum,  $400 \text{ mW} \cdot \text{cm}^{-2}$  for  $Pr_2NiO_{4+\delta}$  electrode with anode supported cells [105]. However, the chemical stability is an issue for  $Pr_2NiO_{4+\delta}$  material [106, 107] while  $La_2NiO_{4+\delta}$  and  $Nd_2NiO_{4+\delta}$  are stable [107] in the  $700-900^\circ C$  temperature range up to 72 hours.

As an additional point, it's interesting to note that the electronic conductivity of the upper- terms ( $n = 2, 3$ ) of the RP series involving nickel is generally increased with respect to the term  $n = 1$  [108, 109]. These materials can be either oxygen under or over stoichiometric,

also depending on the synthesis way [108, 110, 111]. To our knowledge, very few data are available regarding their ionic properties.

## 2.4. Interconnects

In order to generate enough power, fuel cells should be used in combination. This means that single cells need to be connected together, hence there is a need of interconnects. In a unit cell, interconnects are the current collectors, their main function is thus to collect electrons, but they are also used for the distribution of gases. These collectors must be carefully arranged and assembled to achieve a large contact surface with porous electrodes. In addition, they act as sealed barriers to prevent any reaction between the gases present at each electrode. Interconnects should have the following requirements. They should: i) have high electrical conductivity; ii) be chemically, mechanically and structurally stable in the overall  $pO_2$  range ( $10^{-22} < pO_2 < 0.2$  atm) ; iii) have no porosity (to avoid mixing of fuel and oxygen); iv) have a thermal expansion compatibility and be inert with respect to the other fuel cell components; v) be easy to manufacture. At high operating temperature (900-1100°C), nickel based alloys are generally used. At or below 800°C, ferritic steels can be used. At even lower temperature (below 700°C), stainless steels are used as interconnects. A variety of alloy systems have been investigated as interconnect materials, such as Fe-Cr, Fe-Ni, Ni-Cr and Fe-Ni-Cr alloys.

At low temperatures, it is possible to use metallic materials thanks to their high electronic and thermal conductivities, low cost and easy manufacturing. Many metal alloys which are resistant to heat and corrosion are studied [112-114].

## 2.5. IT-SOFCs

Fuel cells appear as good candidates for clean energy technology. However, their development at large scale is limited by problems related to the use of hydrogen, *durability* as well as economical reasons. The challenging issues facing the development of economically competitive SOFCs include lowering the operating temperature from above 1000 °C down to 600-700 °C (IT-SOFC) in order to reduce the overall cost and to increase the lifetime. Ageing problems due to the reactivity between the components of the cell at high temperature leading to insulating phases or solid solutions and characterized by lower ionic conductivity are one of the main limitations to their development. Long-term operation requires individual cell components that are thermally compatible, thus in particular stable interfaces have to be

established at 600-800 °C. Therefore, the need to improve the performance at intermediate temperatures is straight forward. However, it is generally recognized that the performance of SOFCs deteriorate at lower temperature, mainly due to the over-potentials generated at the cathodic interface and to the decrease in ionic conductivity of the electrolyte. Regarding the electrolyte, a way is to decrease the thickness of electrolyte to reduce the ohmic loss at intermediate temperature. When the operating temperature is decreased, the use of inexpensive metallic materials as interconnects is possible, improving the mechanical strength and seal efficiency of stack. Nowadays, researchers focused on metal supported cells (MSCs) which is also called the third generation of SOFCs. Since both the electrodes and electrolyte ceramic layers are thin in the new configuration, this is an additional step towards the cost limitation because the amount of the expensive ceramic materials is decreased to minimum.

## 2.6. Metal Supported Cells (MSCs)

### 2.6.1. Different SOFC designs

The majority of SOFC development to date focuses on Electrolyte-supported cells (ESCs) then more recently on Anode-supported cells (ASCs). The schematic is presented in **Figure 11**.

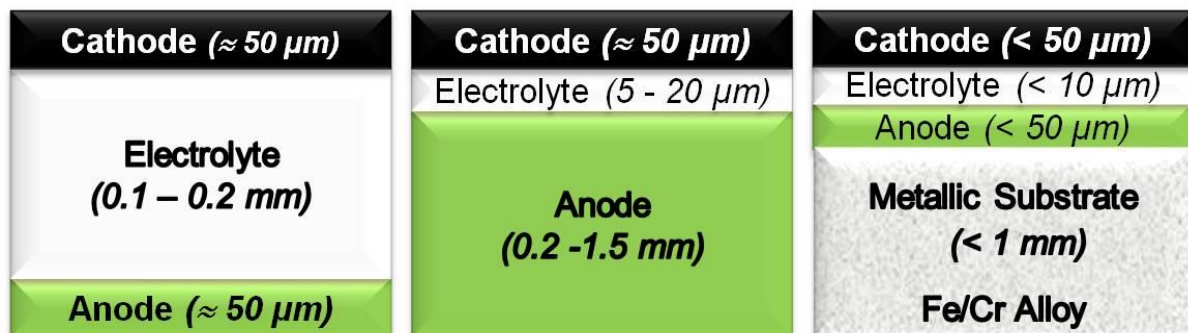


**Figure 11- Schematic representation of the ceramic cells architecture (left part: ESC, middle part: ASC and right part: MSC configurations).**

The very first ESC design utilizes a thick electrolyte layer to provide mechanical support for thin anode and cathode layers. Because an efficient cell operation is possible when the ohmic impedance of the electrolyte is minimized, a relatively high operating temperature is needed as the conductivity of typical SOFC electrolytes displays Arrhenius dependence on temperature [8, 115]. Thus, ESCs with 100 μm - 200 μm electrolyte, thick enough to provide mechanical support for the cell, are typically operating in the range 850 –

1000 °C. Such high temperatures cells require significant thermal insulation and expensive high-temperature materials to be used in the stack. Alternatively, the ohmic impedance of the electrolyte may be decreased simply by making it thinner. Then the thin-electrolyte-film ASC design was developed in order to reduce the operating temperature, enabling the use of more economical stack. Anode-supported electrolyte films are typically ~ 50 µm thick, allowing operation below 800 °C.

In the ESC and ASC cases, the mechanical support is a brittle ceramic or cermet, which contains expensive materials. In contrast, the metal supported cell (MSC) design utilizes three thin ceramic layers, only as thick as necessary for electrochemical function (within processing constraints); the mechanical support is made from inexpensive and robust porous metal, and the electrochemically active layers are directly applied to the metal support, as shown in **Figure 11**.

The MSC design provides significant lowering of the manufacturing cost, increased robustness, thus operational advantages that make it a promising candidate for commercialization. Many SOFC applications would benefit greatly from increased mechanical ruggedness, redox tolerance, and rapid thermal cycling promised by metal-supported cells. The benefits of mechanical ruggedness are especially obvious for portable applications where the cell or stack is likely to experience shock, vibration, or mechanical loading. The improved redox cycling tolerance is also important because it allows the cells to be cooled without damaging the components during a possible interruption in fuel supply. Rapid thermal cycling is of course advantageous for many SOFC applications, being till now one of the main drawbacks of the SOFC. Finally, a low oxidation rate of the MSC is preferred.

### **2.6.2. Early MSC development**

The advantages of the metal supported SOFC design were first recognized in the 1960s [115]. This early work used flame spray deposition of zirconia-based electrolyte onto pre-sintered stainless steel supports. Cells were operated in the range 700–800 °C, producing a power density of 115 mW.cm<sup>-2</sup> at 750 °C. Cell operation with hydrogen, methanol, and kerosene as fuels was demonstrated. At the end of 20<sup>th</sup> century, colloidal and wet-chemistry methods for applying and sintering thin films of electrolyte onto anode supports were recognized as suitable for metal-supported cell designs as well. These inexpensive deposition techniques resulted in thinner electrolytes that could be operated at lower temperatures

compatible with low-cost ferritic stainless steels. This approach was pioneered at Imperial College/Ceres Power for GDC electrolyte [116, 117], and at Lawrence Berkeley National Laboratory for YSZ electrolyte [118].

### **3.6.3. Choice of metal for support**

Metal-supported solid oxide fuel cells have recently been prepared on supports with a variety of metal compositions, mainly Fe-based and Ni-based materials. Although most metal-supported SOFC developers use planar supports, tubular supports are also gaining popularity [119-122]. Most developers favour ferritic stainless steel for the metal support. Ferritic stainless steels primarily contain iron and chromium with very low carbon content. Typical alloy designations include commercial labels such as 430, 409, 410 and 441. These alloys are widely used for automotive exhaust because of their low-cost and high-temperature oxidation resistance. The alloys often include Ni, Mo, Si, Ti, Al among others which help to improve the various physical properties. A number of advantageous properties of ferritic stainless steels recommend them for application as the mechanical support for SOFC devices: they are quite inexpensive [123], produce a thin, continuous and protective chromia scale, and can have very long lifetimes at the SOFC operating temperature. Furthermore, their TEC is around  $10 - 12 \times 10^{-6} \text{ }^\circ\text{C}^{-1}$  and therefore the metal is compatible with the ceramic cell components. Additional useful information, especially on shaping of the cells, can be found in refs [116-118, 120-139].

The Ni-based supports are mainly relative to NiCrAlY alloys. For instance, early work used thick plasma-sprayed yttria-stabilized zirconia (YSZ) electrolyte applied to porous NiCrAlY metal supports prepared by die pressing [140]. The excellent oxidation resistance of the NiCrAlY alloy ( $\text{TEC} = 15-16 \times 10^{-6} \text{ K}^{-1}$ ) allowed operation up to  $900 \text{ }^\circ\text{C}$ , so reasonable performance was obtained despite the thick electrolyte. In a less extend pure Ni and FeNi were also used. However nickel suffers for high cost and poor TEC matching with ceramic components. The addition of iron mitigates the cost and TEC mismatch of pure nickel, but it is sensitive towards sulphur and carbon poisoning, as well as redox tolerance. Additional information can be found in references [141-148].

### 3.6.4. Suitable operation temperature window

Normally the MSCs are operated under intermediate operating temperature range (500-800 °C) which is a relatively narrow but acceptable operation temperature window. This operating window can be determined by two ways. The first one is relative to the choice of the electrolyte materials and the other one to the oxidation of the metal support.

- 1) As usually and for each SOFC design, in order to select the operating temperature by considering the chosen electrolyte materials, it is assumed that the electrolyte component should not contribute more than  $0.15 \text{ } \Omega \cdot \text{cm}^{-2}$  to the total cell specific resistance (labelled ASR), then for an electrolyte film thickness (L) of  $15 \text{ } \mu\text{m}$  the associated specific ionic conductivity ( $\sigma$ ) value of the electrolyte should exceed  $10^{-2} \text{ S} \cdot \text{cm}^{-1}$ . The ionic conductivity of 8YSZ attains this target value above  $700^\circ\text{C}$ , while GDC attains this conductivity at temperatures above  $500^\circ\text{C}$  [149]. Therefore, the use of a GDC electrolyte allows the cell operating temperature to be lowered to around  $500^\circ\text{C}$ . However, with respect to the issue of the possible reduction of  $\text{Ce}^{4+}$  into  $\text{Ce}^{3+}$  already discussed (see 2.2.2.) the operating temperature window for SOFCs based on GDC is around  $500\text{-}600^\circ\text{C}$ .
- 2) The formation of a continuous and protective  $\text{Cr}_2\text{O}_3$  scale on ferritic stainless steel is critical for long term performance of a metal-supported SOFC (on both anode and cathode chamber), resulting in the spallation (cracking and delamination of the oxide scale). Also, the stainless steel acts as a current collector from the electrodes. The current passes between the electrode and the metal support through the chromia scale, and in that case spallation would lead to electrical disconnection of the electrochemically active area and therefore cannot be tolerated. The upper acceptable operating temperature is then also determined by the oxide growth kinetics and the desired SOFC device lifetime. Failure of the device will occur when the protective  $\text{Cr}_2\text{O}_3$  scale becomes thick enough that leads to spallation. Thus, expected lifetime is a strong function of temperature. The addition of reactive elements (Y, La, Ce, etc.) to the stainless steel is well-known to improve scale adhesion and reduce oxidation rate [124, 150]. For instance, the results reported by Belogolovsky *et al.* [151] suggest that using an yttria-treated steel the operating temperature can be decreased below  $800^\circ\text{C}$ . In the temperature range  $600\text{-}950^\circ\text{C}$ , ferritic stainless steels form the desired continuous and protective  $\text{Cr}_2\text{O}_3$  scale. To achieve the oxidation rates required for

5000 h lifetime the maximum temperature is about 800 °C, whereas for lifetimes greater than 50,000 h (as required for stationary power plants) the maximum acceptable temperature is in the 650-700 °C range. This lower temperature makes achieving high power. Most of the groups demonstrating metal-supported cells with YSZ electrolyte have reported performance and testing at 800 °C. Operating at such a high-temperature limits the expected lifetime to several thousand hours. The appropriate coatings, treatments, or alloy modifications can reduce the oxidation rate and improve the scale adhesion for dense interconnect materials, thereby improving expected lifetime before failure via scale spallation. Exploring the effects of similar treatments on oxidation of porous stainless steel supports leads as well to fruitful results.

## References

- [1] W. R. Grove, *Philosophical Magazine and Journal Science* S3, 15 (1839) 96.
- [2] F. T. Bacon, *Nature*, 186 (1960) 589–592.
- [3] J. Larminie, A. Dicks, *Fuel Cell Systems Explained*, Second Edition, *John Wiley & Sons Ltd.*, 2003.
- [4] S. Tao, J. T. S. Irvine, *Nature Materials*, 2 (2003) 320–323.
- [5] H. Kim, C. Lu, W. L. Worrell, J. M. Vohs, R. J. Gorte, *Journal of the Electrochemical Society*, 149 (3) (2002) A247–A250.
- [6] X. F. Ye, S. R. Wang, J. Zhou, F. R. Zeng, H. W. Nie, T. L. Wen, *Journal of Power Sources*, 195 (2010) 7264–7267.
- [7] B. Iwanschitz, J. Sfeir, A. Mai, M. Schutze, *Journal of the Electrochemical Society*, 157 (2010) B269–B278.
- [8] N. Q. Minh, T. Takahashi, *Science and Technology of Ceramic Fuel Cells*, *Elsevier Science Oxford*, UK, 1995.
- [9] O. Yamamoto, Y. Arachi, H. Sakai, Y. Takeda, N. Imanishi, Y. Mizutani, M. Kawai, Y. Nakamura, *Ionics*, 4 (1998) 403–408.
- [10] W. Tinglian, L. Xiaofei, K. Chukun, W. Weppner, *Solid State Ionics*, 18-19 (1986) 715–719.
- [11] R. D. Shannon, *Acta Crystallogr. Sect.*, A32 (1976) 751.
- [12] S. P. S. Badwal, *Solid State Ionics*, 52 (1992) 23–32.
- [13] R. J. Stafford, S. J. Rothman, J. L. Routbort, *Solid State Ionics*, 37 (1989) 67–72.
- [14] E. Ivers-Tiffe, A. Weber, D. Herbstritt, *Journal of the European Ceramic Society*, 21 (2001) 1805–1811.
- [15] S. P. S. Badwal, *Solid State Ionics*, 143 (2001) 39–46.
- [16] S. J. Skinner, J. A. Kilner, *Materials Today*, 6 (2003) 30–37.
- [17] T. Ishii, *Solid State Ionics*, 78 (1995) 333 – 338.
- [18] M. Morales, J. J. Roa, X. G. Capdevila, M. Segarra, S. Pinol, *Acta Materialia*, 58 (2010) 2504–2509.
- [19] Z. Duan, M. Yang, A. Yan, Z. Hou, Y. Dong, Y. Chong, M. Cheng, W. Yang, *Journal of Power Sources*, 160 (2006) 57–64.
- [20] G. C. Kostogloudis, G. Tsiniarakis, C. Ftikos, *Solid State Ionics*, 135 (2000) 529–535.

- [21] J. M. A. van Roosmalen, E. H. P. Cordfunke, *Solid State Ionics*, 52 (1992) 303–312.
- [22] A. M. Hernandez, L. Mogni, A. Caneiro, *International Journal of Hydrogen Energy*, 35 (2010) 6031–6036.
- [23] C. Brugnoli, U. Ducati, M. Scagliotti, *Solid State Ionics*, 76 (1995) 177–182.
- [24] G. Chiodelli, M. Scagliotti, *Solid State Ionics*, 73 (1994) 265–271.
- [25] H. Y. Lee, S. M. Oh, *Solid State Ionics*, 90 (1996) 133–140.
- [26] A. Mitterdorfer, L. J. Gauckler, *Solid State Ionics*, 111 (1998) 185–218.
- [27] S. A. Speakman, R. D. Carneim, E. A. Payzant, T. R. Armstrong, *Journal of Materials Engineering and Performance*, 13 (2004) 303–308.
- [28] M. Mogensen, N. M. Sammes, G. A. Tompsett, *Solid State Ionics*, 129 (2000) 63–94.
- [29] H. Yahiro, Y. Eguchi, K. Eguchi, H. Arai, *Journal of Applied Electrochemistry*, 18 (1988) 527–531.
- [30] M. Cassir, E. Gourba, *Annales de Chimie: Science des Materiaux*, 26 (2001) 49–58.
- [31] B. C. H. Steele, *Solid State Ionics*, 129 (2000) 95–110.
- [32] M. Han, X. Tang, H. Yin, S. Peng, *Journal of Power Sources*, 165 (2007) 757–763.
- [33] D. Perez-Coll, P. Nunez, J. R. Frade, J. C. C. Abrantes, *Electrochimica Acta*, 48 (2003) 1551–1557.
- [34] S. P. S. Badwal, F. T. Ciacchi, J. Drennan, *Solid State Ionics*, 121 (1999) 253–262.
- [35] H. Inaba, H. Tagawa, *Solid State Ionics*, 83 (1996) 1–16.
- [36] M. Mogensen, T. Lindegaard, U. R. Hansen, G. Mogensen, *Journal of the Electrochemical Society*, 141 (1994) 2122–2128.
- [37] R. T. Leah, N. P. Brandon, P. Aguiar, *Journal of Power Sources*, 145 (2005) 336–352.
- [38] H. Hayashi, M. Kanoh, C. J. Quan, H. Inaba, S. Wang, M. Dokiya, H. Tagawa, *Solid State Ionics*, 132 (2000) 227–233.
- [39] V. Dusastre, J. A. Kilner, *Solid State Ionics*, 126 (1999) 163–174.
- [40] L. Qiu, T. Ichikawa, A. Hirano, N. Imanishi, Y. Takeda, *Solid State Ionics*, 158 (2003) 55–65.
- [41] J. M. Ralph, C. Rossignol, R. Kumar, *Journal of the Electrochemical Society*, 150 (2003) A1518–A1522.
- [42] J. M. Ralph, A. C. Schoeler, M. Krumpelt, *Journal of Materials Science*, 36 (2001) 1161–1172.
- [43] D. Waller, J. A. Lane, J. A. Kilner, B. C. H. Steele, *Solid State Ionics*, 86–88 (1996) 767–772.
- [44] M. Izuki, M. E. Brito, K. Yamaji, H. Kishimoto, D. H. Cho, T. Shimonosono, T. Horita, H. Yokokawa, *Journal of Power Sources*, 196 (2011) 7232–7236.
- [45] J. C. C. Abrantes, D. Perez-Coll, P. Nunez, J. R. Frade, *Electrochimica Acta*, 48 (2003) 2761–2766.
- [46] P. Charpentier, P. Fragnaud, D. M. Schleich, C. Lunot, E. Gehain, *Ionics*, 3 (1997) 155–160.
- [47] C. Yang, A. Coffin, F. Chen, *International Journal of Hydrogen Energy*, 35 (2010) 3221–3226.
- [48] W. Wang, Y. Huang, S. Jung, J. M. Vohs, R. J. Gorte, *Journal of the Electrochemical Society*, 153 (2006) A2066–A2070.
- [49] P. Kim-Lohsoontorn, D. J. L. Brett, N. Laosiripojana, Y. -M. Kim, J. -M. Bae, *International Journal of Hydrogen Energy*, 35 (2010) 3958–3966.
- [50] M. Kleitz, F. Petitbon, *Solid State Ionics*, 92 (1996) 65–74.
- [51] E. Siebert, A. Hammouche, M. Kleitz, *Electrochimica Acta*, 40 (1995) 1741–1753.
- [52] S. R. Sehlin, H. U. Anderson, D. M. Sparlin, *Solid State Ionics*, 78 (1995) 235–243.
- [53] A. N. Petrov, O. F. Kononchuk, A. V. Andreev, V. A. Cherepanov, P. Kofstad, *Solid State Ionics*, 80 (1995) 189–199.

- [54] A. V. Berenov, A. Atkinson, J. A. Kilner, E. Bucher, W. Sitte, *Solid State Ionics*, 181 (2010) 819–826.
- [55] S. J. Skinner, J. A. Kilner, *Materials Today*, 6 (2003) 30–37.
- [56] A. Petric, P. Huang, F. Tietz, *Solid State Ionics*, 135 (2000) 719–725.
- [57] S. -I. Hashimoto, Y. Fukuda, M. Kuhn, K. Sato, K. Yashiro, J. Mizusaki, *Solid State Ionics*, 181 (2010) 1713–1719.
- [58] S. Carter, A. Selcuk, R. J. Chater, J. Kajda, J. A. Kilner, B. C. H Steele, *Solid State Ionics*, 53-56 (1992) 597–605.
- [59] G. C. Kostogloudis, C. Ftikos, *Solid State Ionics*, 126 (1999) 143–151.
- [60] V. V. Kharton, A. P. Viskup, D. M. Bochkov, E. N. Naumovich, O. P. Reut, *Solid State Ionics*, 110 (1998) 61–68.
- [61] J. N. Audinot, *Ph.D. thesis*, Thèse de Doctorat de l'Université de Bordeaux I (1999).
- [62] A. Mineshige, M. Kobune, S. Fujii, Z. Ogumi, M. Inaba, T. Yao, K. Kikuchi, *Journal of Solid State Chemistry*, 142 (1999) 374–381.
- [63] A. Petric, P. Huang, F. Tietz, *Solid State Ionics*, 135 (2000) 719–725.
- [64] R. H. E. Van Doorn, I. C. Fullarton, R. A. De Souza, J. A. Kilner, H. J. M Bouwmeester, A. J. Burggraaf, *Solid State Ionics*, 96 (1997) 1–7.
- [65] Q. Ming, M. D. Nersesyan, J. T. Richardson, D. Luss, A. A. Shiryaev, *Journal of Materials Science*, 35 (2000) 3599–3606.
- [66] Y. Sakaki, Y. Takeda, A. Kato, N. Imanishi, O. Yamamoto, M. Hattori, M. Iio, Y. Esaki, *Solid State Ionics*, 118 (1999) 187–194.
- [67] R. A. De Souza, J. A. Kilner, *Solid State Ionics*, 106 (1998) 175–187.
- [68] Z. Shao, S. M. Halle, *Nature*, 431 (2004) 170–173.
- [69] B. Wei, Z. Lu, S. Li, Y. Liu, K. Liu, W. Su, *Electrochemical and Solid-State Letters*, 8 (2005) A428–A431.
- [70] L. Wang, R. Merkle, J. Maier, T. Acarturk, U. Starke, *Applied Physics Letters*, 94 (2009).
- [71] E. Bucher, A. Egger, P. Ried, W. Sitte, P. Holtappels, *Solid State Ionics*, 179 (2008) 1032–1035.
- [72] A. Yan, V. Maragou, A. Arico, M. Cheng, P. Tsiakaras, *Applied Catalysis B: Environmental*, 76 (2007) 320–327.
- [73] E. Bucher, A. Egger, G. B. Caraman, W. Sitte, *Journal of the Electrochemical Society*, 155 (2008) B1218–B1224.
- [74] A. Maignan, C. Martin, D. Pelloquin, N. Nguyen, B. Raveau, *Journal of Solid State Chemistry*, 142 (1999) 247–260.
- [75] J. -H. Kim, A. Manthiram, *Solid State Ionics*, 180 (2009) 1478–1483.
- [76] A. Taskin, A. N. Lavrov, Y. Ando, *Applied Physics Letters*, 86 (2005) 1–3.
- [77] A. A. Taskin, A. N. Lavrov, Y. Ando, *Physical Review B - Condensed Matter and Materials Physics* 71 (2005) 132102.
- [78] A. Taskin, A. Lavrov, Y. Ando, *Progress in Solid State Chemistry*, 35 (2007) 481–490.
- [79] A. Tarançon, M. Burriel, J. Santiso, S. J. Skinner, J. A. Kilner, *Journal of Materials Chemistry*, 20 (2010) 3799–3813.
- [80] G. Kim, S. Wang, A. J. Jacobson, L. Reimus, P. Brodersen, C. A. Mims, *Journal of Materials Chemistry*, 17 (2007) 2500–2505.
- [81] J. H. Kim, F. Prado, A. Manthiram, *Journal of the Electrochemical Society*, 155 (2008) B1023–B1028.
- [82] J. H. Kim, A. Manthiram, *Electrochimica Acta*, 54 (2009) 7551–7557.
- [83] J. H. Kim, M. Cassidy, J. T. S. Irvine, J. Bae, *Journal of the Electrochemical Society*, 156 (2009) B682–B689.
- [84] Q. Zhou, F. Wang, Y. Shen, T. He, *Journal of Power Sources*, 195 (2010) 2174–2181.

- [85] V. V. Kharton, A. P. Viskup, E. N. Naumovkh, F. M. B. Marques, *Journal of Materials Chemistry*, 9 (1999) 2623–2629.
- [86] S. J. Skinner, J. A. Kilner, *Solid State Ionics*, 135 (2000) 709–712.
- [87] S. Yoo, S. Choi, J. Shin, M. Liu, Kim, *RSC Advances*, 2 (2012) 4648–4655.
- [88] A. Aguadero, L. Fawcett, S. Taub, R. Woolley, K. -T. Wu, N. Xu, J. A. Kilner, S. J. Skinner, *Journal of Materials Science*, 47 (2012) 3925–3948.
- [89] E. Boehm, J. -M. Bassat, P. Dordor, F. Mauvy, J. -C. Grenier, P. Stevens, *Solid State Ionics*, 176 (2005) 2717–2725.
- [90] J. -M. Bassat, P. Odier, J. P. Loup, *Journal of Solid State Chemistry*, 110 (1994) 124–135.
- [91] P. Odier, J. M. Bassat, J. C. Rifflet, J. P. Loup, *Solid State Communications*, 85 (1993) 561–564.
- [92] C. Allançon, J. Rodriguez-Carvajal, M. T. Fernandez-Diaz, P. Odier, J. M. Bassat, J. P. Loup, J. L. Martinez, *Zeitschrift fur Physik B-Condensed Matter*, 100 (1996) 85–90.
- [93] C. Allançon, P. Odier, J. M. Bassat, J. P. Loup, *Journal of Solid State Chemistry*, 131 (1997) 167–172.
- [94] M. T. Fernandez-Diaz, J. L. Martinez, J. Rodriguez-Carvajal, *Solid State Ionics*, 63-65 (1993) 902–906.
- [95] A. Aguadero, J. A. Alonso, M. J. Martinez-Lope, M. T. Fernandez-Diaz, M. J. Escudero, L. Daza, *Journal of Materials Chemistry*, 16 (2006) 3402–3408.
- [96] A. Demourgues, A. Wattiaux, J. C. Grenier, M. Pouchard, J. L. Soubeyroux, J. M. Dance, P. Hagenmuller, *Journal of Solid State Chemistry*, 105 (1993) 458–468.
- [97] F. S. Galasso, Structure, properties and preparation of perovskite-type compounds, *Pergamon Press*, (1990).
- [98] S. J. Skinner, J. A. Kilner, *Ionics*, 5 (1999) 171–174.
- [99] E. Boehm, *Ph.D. thesis*, ICMCB-CNRS, University of Bordeaux (2002).
- [100] M. Yashima, M. Enoki, T. Wakita, R. Ali, Y. Matsushita, F. Izumi, T. Ishihara, *Journal of the American Chemical Society*, 130 (2008) 2762–2763.
- [101] L. Minervini, R. W. Grimes, J. A. Kilner, K. E. Sickafus, *Journal of Materials Chemistry*, 10 (2000) 2349–2354.
- [102] M. Burriel, G. Garcia, J. Santiso, J. A. Kilner, R. J. Chater, S. J. Skinner, *Journal of Materials Chemistry*, 18 (2008) 416–422.
- [103] J. M. Bassat, M. Burriel, O. Wahyudi, R. Castaing, M. Ceretti, P. Veber, F. Weill, A. Villesuzanne, J. C. Grenier, W. Paulus, J. A. Kilner, *Journal of Physical Chemistry C*, 117 (2013) 26466–26472.
- [104] J. M. Bassat, P. Odier, A. Villesuzanne, C. Marin, M. Pouchard, *Solid State Ionics*, 167 (2004) 341–347.
- [105] C. Ferchaud, J. C. Grenier, Y. Zhang-Steenwinkel, M. M. A. Van Tuel, F. P. F Van Berkel, J. M. Bassat, *Journal of Power Sources*, 196 (2011) 1872–1879.
- [106] A. V. Kovalevsky, V. V. Kharton, A. A. Yaremchenko, Y. V. Pivak, E. V. Tsipis, S. O. Yakovlev, A. A. Markov, E. N. Naumovich, J. R. Frade, *Journal of Electroceramics*, 18 (2007) 205–218.
- [107] A. Montenegro-Hernandez, J. Vega-Castillo, L. Mogni, A. Caneiro, *International Journal of Hydrogen Energy*, 36 (2011) 15704–15714.
- [108] J. M. Bassat, C. Allançon, P. Odier, J. P. Loup, M. Deus Carvalho, A. Wattiaux, *European Journal of Solid State and Inorganic Chemistry*, 35 (1998) 173–188.
- [109] M. Greenblatt, *Current Opinion in Solid State and Materials Science*, 2 (1997) 174–183.
- [110] M. D. Carvalho, M. M. Cruz, A. Wattiaux, J. M. Bassat, F. M. A. Costa, M. Godinho, *Journal of Applied Physics*, 88 (2000) 544–549.
- [111] Z. Zhang, M. Greenblatt, *Journal of Solid State Chemistry*, 117 (1995) 236–246.

- [112] S. Shim, D. Mumm, *ECS Transaction*, 7 (2007) 795–804.
- [113] F. Tietz, P. Nikolopoulos, *Fuel Cells*, 9 (2009) 867–872.
- [114] B. D. White, O. Kesler, L. Rose, *ECS Transaction*, 7 (2007) 1107–1114.
- [115] S. C. Singhal, K. Kendall, *Elsevier Science Oxford*, UK, 2003.
- [116] P. Bance, N. P. Brandon, B. Girvan, P. Holbeche, S. O’Dea, B. C.H. Steele, *Journal of Power Sources*, 131 (2004) 86–90.
- [117] N. P. Brandon, A. Blake, D. Corcoran, D. Cumming, A. Duckett, K. El-Koury, D. Haigh, C. Kidd, R. Leah, G. Lewis, C. Matthews, N. Maynard, N. Oishi, T. McColm, R. Trezona, A. Selcuk, M. Schmidt, L. Verdugo, *Journal of Fuel Cell Science and Technology*, 1 (2004) 61–65.
- [118] I. Villarreal, C. Jacobson, A. Leming, Y. Matus, S. Visco, L. De Jonghe, *Electrochemical and Solid-State Letters*, 6 (2003) A178–A179.
- [119] Y. B. Matus, L. C. De Jonghe, C. P. Jacobson, S. J. Visco, *Solid State Ionics*, 176 (2005) 443–449.
- [120] M. C. Tucker, G. Y. Lau, C. P. Jacobson, L. C. DeJonghe, S. J. Visco, *Journal of Power Sources*, 171 (2007) 477–482.
- [121] M. C. Tucker, G. Y. Lau, C. P. Jacobson, L. C. DeJonghe, S. J. Visco, *Journal of Power Sources*, 175 (1) (2008) 447–451.
- [122] L. M. Rodriguez-Martinez, L. Otaegi, M. A. Alvarez, M. Rivas, N. Gomez, A. Zabala, N. Arizmendiarieta, I. Anteparra, M. Olave, A. Urriolabeitia, I. Villarreal, A. Laresgoiti, *ECS Transaction*, 25 (2009) 745–752.
- [123] M. C. Tucker, *Journal of Power Sources*, 195 (15) (2010) 4570–4582.
- [124] P. Y. Hou, J. Stringer, *Materials Science and Engineering A*, 202 (1995) 1–10.
- [125] N. Oishi, Y. Yoo, *ECS Transaction*, 25 (2009) 739–744.
- [126] P. Blennow, J. Hjelm, T. Klemens, A. Persson, K. Brodersen, A. K. Srivastava, H. L. Frandsen, M. Lundberg, S. Ramousse, M. Mogensen, *ECS Transaction*, 25 (2009) 701–710.
- [127] S. Sakuno, S. Takahashi, H. Sasatsu, *ECS Transaction*, 25 (2009) 731–737.
- [128] R. T. Leah, N. P. Brandon, P. Aguiar, *Journal of Power Sources*, 145 (2005) 336–352.
- [129] S. R. Hui, D. Yang, Z. Wang, S. Yick, C. Deces-Petit, W. Qu, A. Tuck, R. Maric, D. Ghosh, *Journal of Power Sources*, 167 (2007) 336–339.
- [130] Y. Xie, R. Neagu, C. -S. Hsu, X. Zhang, C. Deces-Petit, *Journal of the Electrochemical Society*, 155 (2008) B407–B410.
- [131] Q. A. Huang, J. Oberste-Berghaus, D. Yang, S. Yick, Z. Wang, B. Wang, R. Hui, *Journal of Power Sources*, 177 (2008) 339–347.
- [132] Z. Wang, J. O. Berghaus, S. Yick, C. Deces-Petit, W. Qu, R. Hui, R. Maric, D. Ghosh, *Journal of Power Sources*, 176 (2008) 90–95.
- [133] R. Hui, J. O. Berghaus, C. Deces-Petit, W. Qu, S. Yick, J. -G. Legoux, C. Moreau, *Journal of Power Sources*, 191 (2009) 371–376.
- [134] Q. A. Huang, B. Wang, W. Qu, R. Hui, *Journal of Power Sources*, 191 (2009) 297–303.
- [135] T. Franco, K. Schibinger, Z. Ilhan, G. Schiller, A. Venskutonis, *ECS Transaction*, 7 (2007) 771–780.
- [136] T. Franco, M. Brandner, M. Ruttinger, G. Kunschert, A. Venskutonis, L. S. Sigl, *ECS Transaction*, 25 (2009) 681–688.
- [137] P. Szabo, J. Arnold, T. Franco, M. Gindrat, A. Refke, A. Zagst, A. Ansar, *ECS Transaction*, 25 (2009) 175–185.
- [138] M. Brandner, M. Bram, J. Froitzheim, H. P. Buchkremer, D. Stover, *Solid State Ionics*, 179 (2008) 1501–1504.

- [139] H. Kurokawa, G. Y. Lau, C. P. Jacobson, L. C. De Jonghe, S. J. Visco, *Journal of Materials Processing Technology*, 182 (2007) 469–476.
- [140] A. Momma, Y. Kaga, T. Okuo, K. Fujii, K. Hohjyo, M. Kanazawa, *Bulletin of the Electrotechnical Laboratory*, 63 (1999) 1–11.
- [141] C. Hwang, C. -H. Tsai, C. H. Lo, C. H. Sun, *Journal of Power Sources*, 180 (2008) 132–142.
- [142] H. J. Cho, G. M. Choi, *Solid State Ionics*, 180 (2009) 792–795.
- [143] T. Ishihara, J. Yan, M. Enoki, S. Okada, H. Matsumoto, *Journal of Fuel Cell Science and Technology*, 5 (2008) 031205.
- [144] Y. W. Ju, H. Eto, T. Inagaki, T. Ishihara, *ECS Transaction*, 25 (2009) 719–726.
- [145] J. Yan, M. Enoki, H. Matsumoto, T. Ishihara, *Electrochemical and Solid-State Letters*, 10 (2007) 139–141.
- [146] T. Ishihara, J. Yan, M. Shinagawa, H. Matsumoto, *Electrochimica Acta*, 52 (2006) 1645–1650.
- [147] Y. Lee, G. M. Choi, *ECS Transaction*, 25 (2009) 727–730.
- [148] H. C. Park, A. V. Virkar, *Journal of Power Sources*, 186 (2009) 133–137.
- [149] B. C. H. Steele, *Solid State Ionics*, 134 (2000) 3–20.
- [150] N. Shaigan, W. Qu, D. G. Ivey, W. Chen, *Journal of Power Sources*, 195 (2010) 1529–1542.
- [151] I. Belogolovsky, P. Y. Hou, C. P. Jacobson, S. J. Visco, *Journal of Power Sources*, 182 (2008) 259–264.

## Chapter 2

---

*Vibhu et al., Solid State Ionics, 278 (2015) 32-37.*

# $\text{La}_{2-x}\text{Pr}_x\text{NiO}_{4+\delta}$ as suitable cathodes for Metal Supported SOFCs

Vaibhav Vibhu, Aline Rougier, Clément Nicollet, Aurélien Flura,  
Jean-Claude Grenier and Jean-Marc Bassat\*

CNRS, Université de Bordeaux, Institut de Chimie de la Matière Condensée de Bordeaux (ICMCB), 87 Av. Dr Schweitzer, F-33608 Pessac Cedex, France.

## Abstract

Aiming at a tradeoff between the chemical stability of  $\text{La}_2\text{NiO}_{4+\delta}$  (LNO) and the high electrochemical performance of  $\text{Pr}_2\text{NiO}_{4+\delta}$  (PNO),  $\text{La}_{2-x}\text{Pr}_x\text{NiO}_{4+\delta}$  mixed nickelates, further referred as LPNO, were studied as possible oxygen electrodes for Solid Oxide Fuel Cells (SOFCs). LPNO phases were synthesized using the modified citrate-nitrate route followed by a heat treatment at 1200 °C for 12 h under air. Structural characterizations of those  $\text{K}_2\text{NiF}_4$ -type compounds show the existence of two solid solutions with orthorhombic structure, namely a La rich one from  $x = 0$  to 0.5 with *Fmmm* space group, and a Pr rich one from  $x = 1.0$  to 2.0 with *Bmab* space group. The mixed ionic and electronic conducting (MIEC) properties of LPNO phases were investigated through the evolution of the oxygen over-stoichiometry,  $\delta$ , measured as a function of temperature and  $p\text{O}_2$ , the electrical conductivity, the diffusion and surface exchange coefficients versus  $x$ , showing that all compositions exhibit suitable characteristics as cathode materials for SOFCs. In particular, the electrochemical performance measured in symmetrical cells using LPNO materials sintered under low  $p\text{O}_2$ , as requested in Metal Supported Cell, (MSC-conditions) confirmed a decrease in polarization resistance values,  $R_p$ , from 0.93  $\Omega\cdot\text{cm}^2$  (LNO) down to 0.15  $\Omega\cdot\text{cm}^2$  (PNO) at 600 °C with increasing  $x$ .

**Keywords:** SOFCs, Metal Supported Cells, oxygen over-stoichiometry, lanthanum-praseodymium mixed nickelates, oxygen diffusivity

## 1. Introduction

Solid Oxide Fuel Cells (SOFCs) are good candidates for clean energy technology converting hydrogen into electricity through a clean electro-chemical process. Indeed, fuel cells provide many advantages over traditional energy conversion systems including high

efficiency, modularity and fuel adaptability [1, 2]. However, SOFCs are not used in large scale mainly because of issues related to the use of hydrogen, durability and also economic reasons. The challenging issues facing the development of economically competitive SOFCs include lowering the operating temperature from about 1000 °C down to 600–700 °C, in an intermediate temperature (IT) range so-called IT-SOFCs, in order to reduce their overall cost and increase their lifetime [3]. IT-SOFCs should reduce the thermal degradation and enable the use of low cost interconnect materials such as ferritic stainless steel.

Nowadays, metal supported cells (MSCs), also called 3<sup>rd</sup> generation of SOFC, are an attractive option for IT-SOFCs [4–11]. The main advantages of MSCs are summarized here, *i.e.* a) both electrode and electrolyte layers successively deposited on the metal support are thin, as a result the cost will be lower, b) an easier thermal cycling is anticipated, c) the metal support acts as a good current conductor due to its high electrical conductivity, d) the metal support is more ductile than the anode supported cells and e) MSCs can be used at intermediate operating temperatures. In most cases, a four-layer structure is commonly used for MSCs, consisting of thick porous alloy substrates and three thin functional layers - a dense electrolyte in between porous anode and cathode.

The main issue for MSCs deals with the chemical stability of the components at high temperature and under low  $pO_2$ , which are the sintering conditions required to avoid any detrimental oxidation of the metal support as for instance using  $N_2$  atmosphere ( $pO_2 \approx 10^{-4}$  atm). In this study, the work is focused on the cathodic part. In this respect, new cathode materials with mixed ionic and electronic conducting (MIEC) properties at intermediate temperature have to be developed, exhibiting good chemical stability as well as high activity towards the electrochemical oxygen reduction reaction in the 600–700 °C operating temperature range.

There are mainly two kinds of MIEC materials; the first one concerns oxygen deficient oxides, for example LSC ( $La_{0.8}Sr_{0.2}CoO_{3-\delta}$ ), LSCF ( $La_{0.4}Sr_{0.6}Co_{0.8}Fe_{0.2}O_{3-\delta}$ ) *etc.* The three main disadvantages of Sr-containing materials are a) their high values of thermal expansion coefficients (TECs) [12, 13], b) they react with zirconia to form  $SrZrO_3$  insulating phase [14] and c) they easily form  $SrSO_4$  insulating phase in presence of sulphur [15], leading to a degradation of the cell performance.

Another type of MIEC oxides deals with oxygen over-stoichiometry, for example nickelates  $Ln_2NiO_{4+\delta}$  ( $Ln = La, Pr, Nd$ ) [16, 17]. These compounds with the  $K_2NiF_4$ -type

layered structure have shown promising cathode performance for IT-SOFCs because of their large anionic bulk diffusion as well as surface exchange coefficients, combined with good electrical conductivity and thermal expansion properties matching with those of yttria-stabilized zirconia (YSZ) or  $\text{Ce}_{0.8}\text{Gd}_{0.2}\text{O}_{2-\delta}$  (GDC) used as electrolytes [18–21]. The structure of  $\text{Ln}_2\text{NiO}_{4+\delta}$  consists of alternate  $\text{NiO}_2$  square plane layers and  $\text{Ln}_2\text{O}_2$  rock salt type-layers, leading to the first member ( $n=1$ ) of the Ruddlesden-Popper series  $\text{Ln}_{n+1}\text{Ni}_n\text{O}_{3n+1}$ . This type of structure has a strong ability to accept interstitial oxygen located in the  $\text{Ln}_2\text{O}_2$  rock-salt interlayer leading to a mixed valence of Ni ( $\text{Ni}^{2+}/\text{Ni}^{3+}$ ), which further results in a mixed ionic and electronic conductivity ( $\text{O}^{2-}/\text{e}^-$ ) [18]. The  $\delta$ -value (the amount of interstitial oxygen) is closely dependent on the rare-earth cation size. For instance, the oxygen excess in  $\text{La}_2\text{NiO}_{4+\delta}$  (LNO) is  $\delta \sim 0.16$  at room temperature, as reported by Zhao *et al.* [22]. On the opposite,  $\text{Pr}_2\text{NiO}_{4+\delta}$  (PNO) shows a larger amount of interstitial oxygen ( $\delta \approx 0.22$ ), resulting from the smaller ionic radius of  $\text{Pr}^{3+}$  ( $r(\text{Pr}^{3+}) = 1.126 \text{ \AA}$  and  $r(\text{La}^{3+}) = 1.16 \text{ \AA}$ ) [23] that induces large structural stresses released by a larger oxygen insertion [24, 25].

The polarization resistance ( $R_p$ ) of the  $\text{Ln}_2\text{NiO}_{4+\delta}$  ( $\text{Ln} = \text{La}, \text{Pr}, \text{Nd}$ ) compounds deduced from electrochemical impedance spectroscopy measurements performed on symmetrical cells shows that the smallest values are obtained for the Pr phase [26], while LNO shows better chemical stability under low  $p\text{O}_2$  [27].

The present work is focused on praseodymium substituted lanthanum nickelates  $\text{La}_{2-x}\text{Pr}_x\text{NiO}_{4+\delta}$  ( $0.0 \leq x \leq 2.0$ ) (LPNO) and aims in particular at finding the optimized compositions to be used as cathodes in MSCs. At first, the chemical stability and the evolution of the oxygen over stoichiometry  $\delta$  with temperature (25–1000 °C) and under low  $p\text{O}_2$  conditions (down to  $10^{-4}$  atm) of LPNO phases synthesized in air, are studied. Then, further characterizations, including the electrical properties and electrochemical behavior, are investigated in SOFC operating conditions, namely in air over a temperature range 500–800 °C.

## 2. Experimental

### Chemical synthesis and characterization of the powders

LPNO phases ( $0.0 \leq x \leq 2.0$ ) were prepared using the citrate-nitrate route (modified Pechini method) [28] from  $\text{Pr}_6\text{O}_{11}$  (Aldrich chem, 99.9%),  $\text{La}_2\text{O}_3$  (Strem Chemical, 99.99%) and  $\text{Ni}(\text{NO}_3)_2 \cdot 6\text{H}_2\text{O}$  (Acros Organics, 99%) precursors.  $\text{Pr}_6\text{O}_{11}$  and  $\text{La}_2\text{O}_3$  were pre-fired in a

first step at  $T = 900\text{ }^{\circ}\text{C}$  overnight to remove the water content, due to their high hygroscopic character, then to weight the exact amount of precursors. The final annealing was performed at  $1200\text{ }^{\circ}\text{C}$  for 12 h in air, leading to well crystallized phases. The obtained powders were attrited with zirconia balls and ethanol for 4 h with the aim to obtain a mean particle size of about  $0.6$  to  $0.8\text{ }\mu\text{m}$  (as checked using laser granulometry measurements).

The powders were characterized by X-Ray diffraction (XRD) at room temperature using a PANalytical X'pert MPD diffractometer with  $\text{Cu-K}\alpha$  incident radiation.

Thermogravimetry analyses (TGA) were carried out using a TA Instrument TGA-Q50 device, with the aim i) to determine the  $\delta$  values (at room temperature) of the various nickelates under air and ii) to study the  $\delta$  variation *vs.*  $T$  under air as well as Ar atmospheres. In the first case the powders were previously heated under air up to  $1000\text{ }^{\circ}\text{C}$  then cooled down to room temperature with a slow rate ( $2\text{ }^{\circ}\text{C}\cdot\text{min}^{-1}$ ), this cycle being reproduced twice to ensure the reproducibility. Then a second cycle was performed under  $\text{Ar}-5\%\text{ H}_2$  flux with a very slow heating rate of ( $0.5\text{ }^{\circ}\text{C}\cdot\text{min}^{-1}$ ), the complete decomposition of the materials leading to determine the oxygen stoichiometry after cycling the sample down to room temperature [29]. Secondly, the variation of the oxygen stoichiometry of the materials was studied either under air ( $p_{\text{O}_2} = 0.21\text{ atm}$ ) or Ar atmosphere ( $p_{\text{O}_2} \approx 10^{-4}\text{ atm}$ ). For this purpose, the powders were first thermodynamically equilibrated under air in the TGA device as described above (*i.e.* two cycles were performed). Then the gas was changed from air to Ar at high temperature for faster solid/gas reactivity, and the same experiment was performed under Ar. Both experiments show a reversible oxygen exchange, at least along the second thermal cycle, the TGA curves being perfectly reversible. Thermal variations of the relative expansion of dense pellets ( $dL/L$ ) were carried out in the temperature range  $25-1000\text{ }^{\circ}\text{C}$ , under air using a differential dilatometer (Netzsch<sup>®</sup> 402 ED), with the aim to determine the TECs of the materials. The electrical conductivity of the materials was determined under air using the four-probe technique, in the temperature range  $25-1000\text{ }^{\circ}\text{C}$  with the heating and cooling rate of  $1\text{ }^{\circ}\text{C}\cdot\text{min}^{-1}$ . The nickelates were previously sintered at  $1350\text{ }^{\circ}\text{C}$  for 4 h in order to get dense pellets.

The oxygen diffusion coefficient  $D^*$  and surface exchange coefficient  $k^*$  were determined by the so-called isotopic exchange depth profile (IEDP) technique combining isotopic exchange of  $^{18}\text{O}$  (used as an oxygen tracer) for  $^{16}\text{O}$  then secondary ion mass spectrometry (SIMS) analyses [30, 31]. The ceramics were first abraded with silicon carbide papers of successive grades, and then polished with an alumina paste down to a roughness

close to 0.3  $\mu\text{m}$ . The samples were annealed at a pressure of 210 mbar in an  $^{18}\text{O}$  enriched atmosphere (97%, Eurisotop) for  $500 < T \text{ } ^\circ\text{C} < 700$ . The  $^{18}\text{O}$  penetration profiles, *i.e.* normalized  $^{18}\text{O}$  isotopic fraction ( $^{18}\text{O} / (^{16}\text{O} + ^{18}\text{O})$ ), were recorded as a function of the analyzed depth using a Cameca<sup>®</sup> IMS 6F SIMS apparatus with a  $\text{Cs}^+$  ions source [32]. The oxygen profiles were then fitted using an appropriate solution to the diffusion equation given by Crank, for a solution of the second Fick's law of gas diffusion in solids [33].

For the electrochemical studies, symmetrical half cells (electrode/GDC/8YSZ/GDC/electrode) were prepared. Dense pellets of 8YSZ (8 mol.% yttria stabilized zirconia) with diameter  $\approx 18$  mm and thickness  $\approx 1.2$  mm were used. Terpeneol-based slurries were prepared for each nickelate or GDC powder (from Rhodia). In order to increase the electrochemical performance of the half-cells [26], a 2  $\mu\text{m}$  GDC layer was initially screen printed on both sides of the 8YSZ electrolyte pellet and sintered at 1300  $^\circ\text{C}$  for 1 h under air. The nickelate layer (thickness  $\approx 20$   $\mu\text{m}$ ) was then screen printed on each side. The optimal sintering temperature of the cathode previously determined in air was 1150  $^\circ\text{C}$  for 1 h [26]. A similar study was performed for sintering conditions under low  $p\text{O}_2$  ( $\approx 10^{-4}$  atm.). Among three sintering temperatures  $T_s = 1100, 1150$  and  $1200$   $^\circ\text{C}$ , the best electrochemical performance (*i.e.* lowest  $R_p$  value) was found at  $T_s = 1150$   $^\circ\text{C}$ . Hence herein, sintering was performed at 1150  $^\circ\text{C}$  for 1 h under nitrogen ( $p\text{O}_2 \approx 10^{-4}$  atm) [27]. The half-cells were re-oxidized at 800 $^\circ\text{C}$  under air for 12 h before the measurements.

The electrochemical measurements were performed under air, using a two electrodes configuration with signal amplitude of 50 mV under zero current condition with the aim to determine the  $R_p$  values. The frequency range was scanned from  $10^6$  Hz to  $10^{-2}$  Hz with 91 points, using an Autolab PGSTAT 302N, equipped with a frequency response analyzer (FRA). All the impedance diagrams were fitted using the Zview<sup>®</sup> (Scribner Associates) software.

### 3. Results and Discussion

#### 3.1. XRD characterizations

The XRD study shows that all LPNO phases with  $0.0 \leq x \leq 0.5$  and  $1.0 \leq x \leq 2.0$  are single phases, their patterns being indexed with an orthorhombic cell described either by the  $Fm\bar{m}m$  space group for La rich solid solution [ $0.0 \leq x \leq 0.5$ ] or  $Bmab$  space group for Pr rich solid solution [ $1.0 \leq x \leq 2.0$ ]. Furthermore, full pattern matching was carried out using the

FULLPROF software. As examples, for  $\text{La}_{1.75}\text{Pr}_{0.25}\text{NiO}_{4+\delta}$  and  $\text{La}_{0.5}\text{Pr}_{1.5}\text{NiO}_{4+\delta}$ , a good agreement is obtained between the experimental and refined patterns (**Figure 1**).

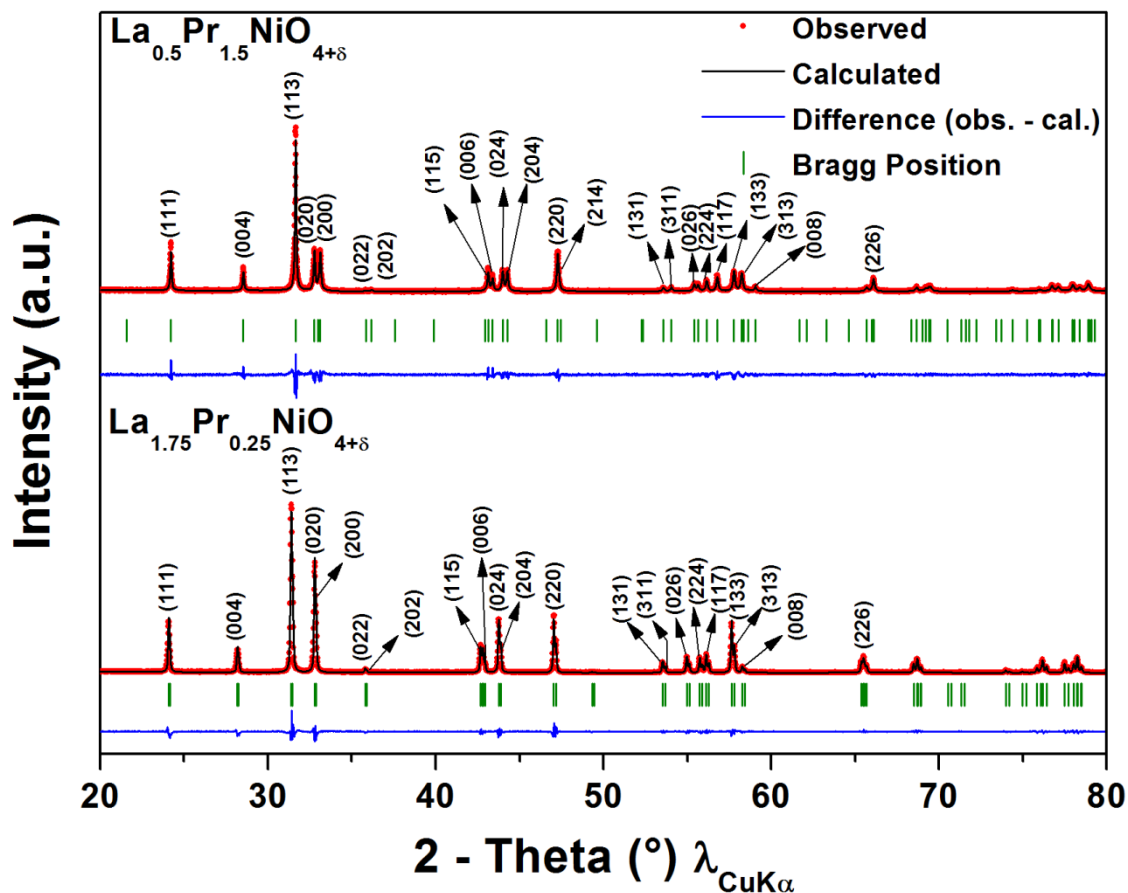


**Figure 1: Fullprof refinement of the X-ray patterns of  $\text{La}_{1.75}\text{Pr}_{0.25}\text{NiO}_{4+\delta}$  and  $\text{La}_{0.5}\text{Pr}_{1.5}\text{NiO}_{4+\delta}$  using  $Fm\bar{m}m$  and  $Bm\bar{a}b$  space group, respectively.**

For the XRD refinements,  $Bm\bar{a}b$  and  $Fm\bar{m}m$  space groups were used for Pr and La-rich phases, respectively. The variation of the lattice parameters as a function of  $x$  is reported in **Figure 2**. The substitution of lanthanum by praseodymium leads to a smooth decrease in each lattice parameters for both La-rich and Pr-rich solid solutions. This decrease in  $a$  and  $b$  cell parameters with the increasing Pr content is consistent with the variation of the ionic radius [23] leading to an overall decrease in the cell volume. For the  $x \approx 0.5-1.0$  region, the  $a$  parameter suddenly decreases while  $b$  suddenly increases suggesting a phase transition in agreement with the results reported by Allançon *et al.* [34] and Nishimoto *et al.* [35].

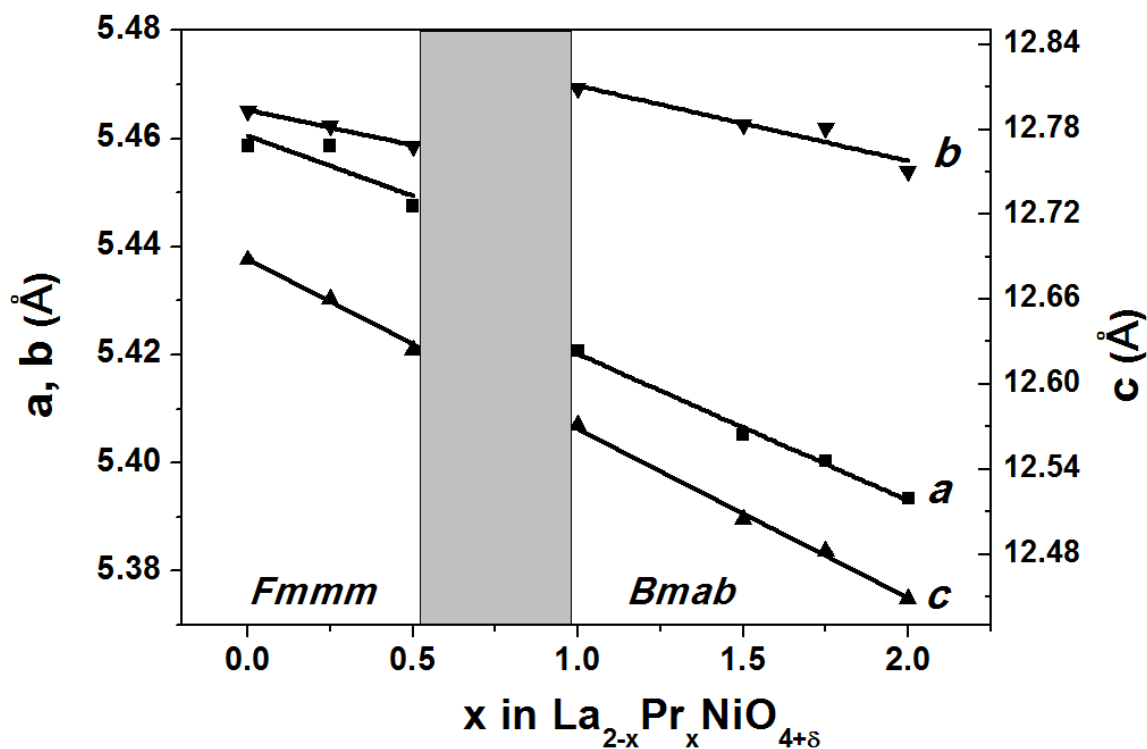


**Figure 2: Variation of the lattice parameters as a function of  $x$  for  $\text{La}_{2-x}\text{Pr}_x\text{NiO}_{4+\delta}$ . In grey, the biphasic domain.**

The exact chemical composition corresponding to this phase transition is still to be determined. For this purpose, additional compositions ( $x = 0.6, 0.7, 0.75, 0.8$  and  $0.85$ ) were synthesized and characterized. XRD patterns of those additional compositions could not be accurately fitted using a single space group, but it was possible using simultaneously both *Fmmm* and *Bmab* space groups, which suggests the existence of a biphasic domain in between  $x = 0.5$  and  $x = 1.0$ , represented by the grey region in **Figure 2**. Aiming at deeper understanding, synchrotron experiments are currently in progress<sup>2</sup>.

### 3.2. Thermo gravimetric analyses

The oxygen over-stoichiometry ( $\delta$ ) at room temperature for LPNO phases was calculated using the results of TGA experiments performed under reducing conditions (Ar-5%  $\text{H}_2$  atmosphere, heating rate  $0.5 \text{ }^\circ\text{C}\cdot\text{min}^{-1}$ ). As earlier reported [29], two weight losses occur. The first one, around  $400 \text{ }^\circ\text{C}$ , corresponds to the reduction of  $\text{Ni}^{3+}$  into  $\text{Ni}^{2+}$  (the oxygen over-stoichiometry being reduced down to  $\delta = 0$  when expecting only  $\text{La}^{3+}$  and  $\text{Pr}^{3+}$  cations). The second weight loss characterizes the complete reduction of LPNO in

<sup>2</sup> Chapter 3

appropriate ratio (*i.e.*  $x$  dependent) into  $\text{La}_2\text{O}_3$ ,  $\text{Pr}_2\text{O}_3$  and Ni, leading to the determination of  $1+\delta$ . The value of  $\delta$  was also calculated *via* iodometric titration of the  $\text{Ni}^{2+}/\text{Ni}^{3+}$  couple [18]. The  $\delta$  values calculated by iodometry and TGA are gathered in **Table 1**. As expected, an increase of  $\delta$ , from 0.16 (LNO) to 0.25 (PNO), is evidenced with praseodymium substituting lanthanum. In this study, the  $\delta$  value for PNO ( $\delta = 0.25$ ) is slightly higher than that earlier reported ( $\delta = 0.22$ ) [25]. This is probably due to small differences in the Pr over Ni ratio, which can easily decrease at least down to 1.95 leading to a simultaneous decrease in  $\delta$ , as evidenced in previous works for LNO [20, 36]. In the present work the Pr/Ni ratio is equal to 2 as determined by ICP measurements, probably explaining the higher  $\delta$  value.

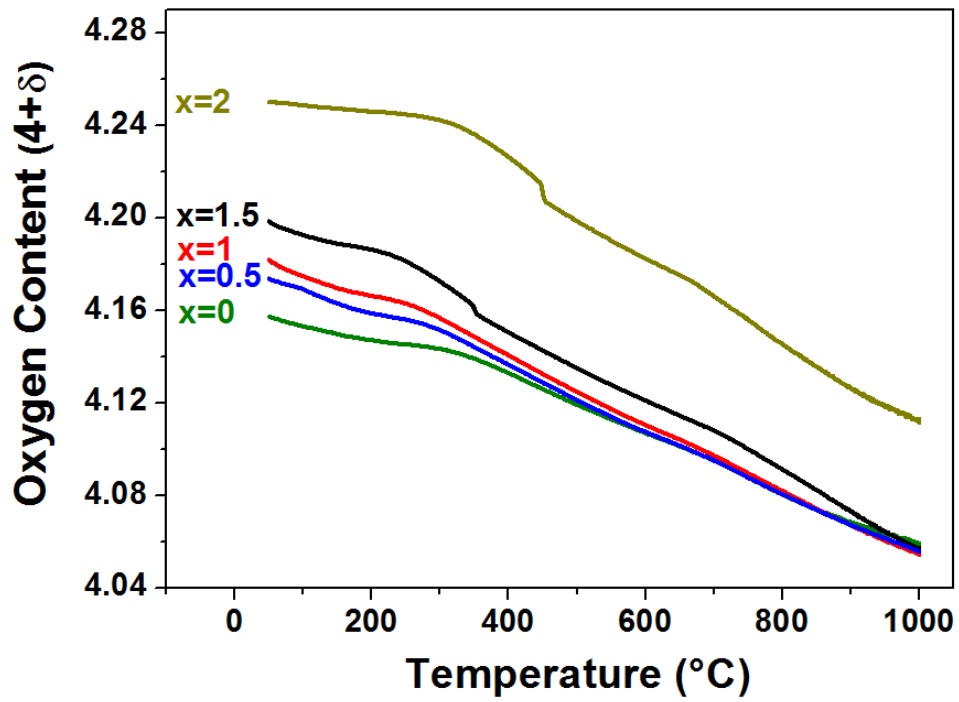
**Table 1 Oxygen over-stoichiometry  $\delta$  calculated from TGA and iodometry measurements, and the average  $\delta$  value.**

Nickelates	$\delta$ (by TGA)	$\delta$ (by Iodometry)	$\delta$ (average)
$\text{La}_2\text{NiO}_{4+\delta}$	0.16	0.16	0.16
$\text{La}_{1.5}\text{Pr}_{0.5}\text{NiO}_{4+\delta}$	0.16	0.17	0.17
$\text{LaPrNiO}_{4+\delta}$	0.19	0.19	0.19
$\text{La}_{0.5}\text{Pr}_{1.5}\text{NiO}_{4+\delta}$	0.22	0.20	0.21
$\text{Pr}_2\text{NiO}_{4+\delta}$	0.25	0.25	0.25

The thermal variations of the oxygen content,  $4+\delta$ , under air for the  $\text{La}_{2-x}\text{Pr}_x\text{NiO}_{4+\delta}$  phases and under air and Ar (*i.e.*,  $p\text{O}_2 \approx 10^{-4}$  atm) for  $\text{LaPrNiO}_{4+\delta}$  are plotted in **Figure 3a** and **Figure 3b**, respectively.

Under air and Ar atmosphere, LPNO nickelates remain always oxygen over-stoichiometric ( $\delta > 0$ ) over the whole temperature range confirming MIEC properties under air and under low  $p\text{O}_2$  conditions. A sudden release of oxygen around  $T \approx 400$  °C is evidenced under air upon heating for PNO ( $x = 2$ ) and for  $\text{La}_{0.5}\text{Pr}_{1.5}\text{NiO}_{4+\delta}$  ( $x = 1.5$ ) (**Figure 3a**). This discontinuity is ascribed to the structural phase transition from orthorhombic phase to the tetragonal one [37, 38]. For La rich domain ( $x = 0, 0.5$  and 1), a very smooth transition is observed. In addition for LNO, in good agreement with Nakamura *et al.*,  $\delta$  decreases from 0.11 to 0.08 at operating conditions from 600 °C to 800 °C [39]. The small drop in oxygen content ( $\Delta\delta = 0.02$ ) after changing the gas flow from air to Ar (**Figure 3b**) results from the oxygen loss under low  $p\text{O}_2$  condition.

(a)



(b)

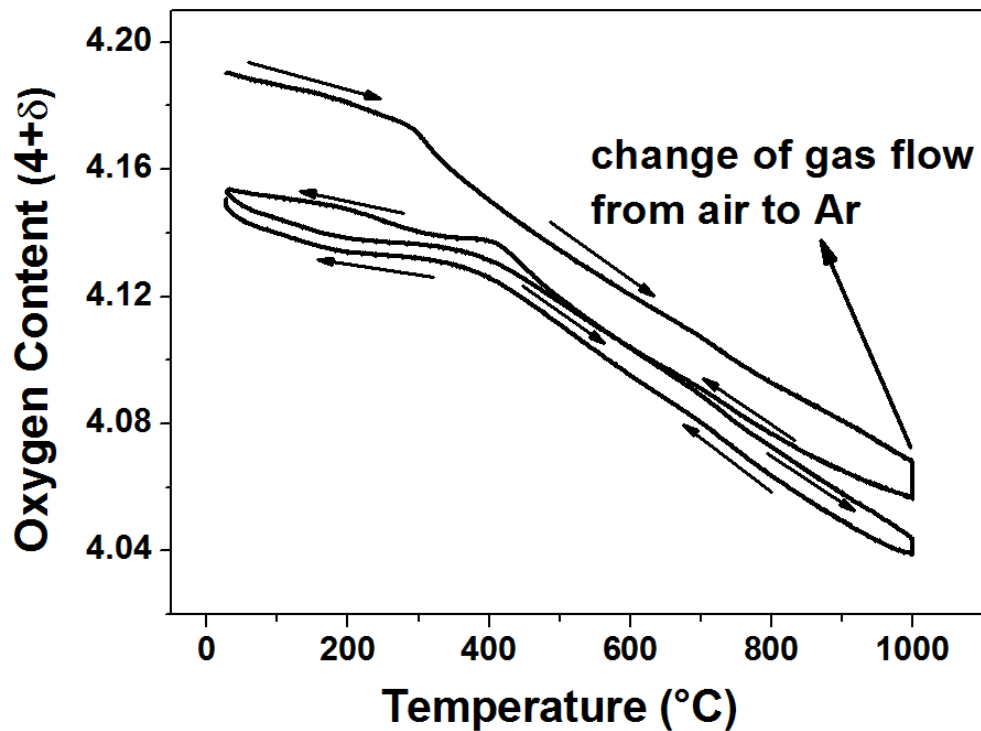
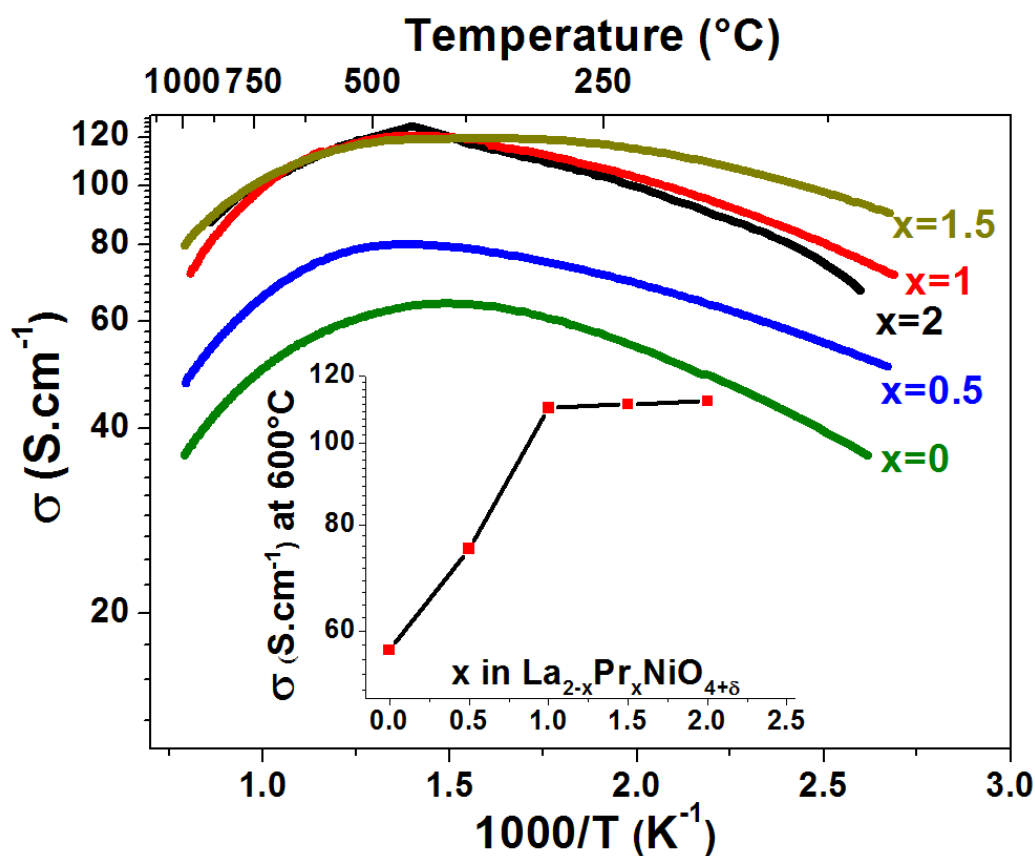


Figure 3: Thermal variation of the oxygen content ( $4+\delta$ ) ( $50^{\circ}\text{C} \leq T \leq 1000^{\circ}\text{C}$ ) (a) for  $\text{La}_{2-x}\text{Pr}_x\text{NiO}_{4+\delta}$ , under air; (b) for  $\text{LaPrNiO}_{4+\delta}$  under air and Ar.

### 3.3. Electrical Conductivity Measurements

The variation of the total electrical conductivity  $\sigma$  vs.  $1000/T$  under air for LPNO compounds is reported in **Figure 4**.



**Figure 4: Thermal variation of the electrical conductivity measured under air for  $\text{La}_{2-x}\text{Pr}_x\text{NiO}_{4+\delta}$ .**

The nickelates exhibit a semi-conducting behavior for  $T < 600$  °C, with a maximum of conductivity observed in the 400–600 °C range. Above this temperature range, their conductivity decreases; this pseudo-metallic behavior is directly correlated to the decrease of oxygen content as evidenced by TGA data (**Figure 3**) and correspondingly to the decrease of the hole carrier density even though the compounds remain semi-conducting [20]. Pr-containing phases exhibit higher conductivity than LNO in the considered temperature range. As an example, a small addition of Pr in LNO ( $x = 0.5$ ) leads to an increase of the conductivity from 50 to 70 S.cm<sup>-1</sup> at 600 °C. For  $x = 1, 1.5$  or 2, (*i.e.* high praseodymium contents), the conductivity largely increases, being about twice the one of LNO, reaching a value close to 110 S.cm<sup>-1</sup> at 600 °C for the three compositions (inset in **Figure 4**). Praseodymium-rich compositions are then of high interest to determine the best compromise, at least regarding the conductivity values at the operating temperature.

### 3.4. Dilatometry Measurements

The thermal variations of the relative expansion  $dL/L$  measured under air for LPNO phases are reported in **Figure 5**. The thermal expansion coefficients (TECs), calculated from the slope of the corresponding straight lines in the full range of temperature, are in between  $13$  to  $13.5 \times 10^{-6} \text{ }^\circ\text{C}^{-1}$  for all nickelates, indicating that from a thermo-mechanical point of view these nickelates can be used in SOFCs involving 8YSZ as well as GDC as electrolytes [38]. Besides the absence of a major deviation of the  $dL/L$  vs.  $T$ , the so-called chemical expansion contribution has not been considered as a significant feature. It agrees with previous works [37, 39–41] that report a near zero chemical expansion coefficient for  $\text{K}_2\text{NiF}_4$ -type phases.

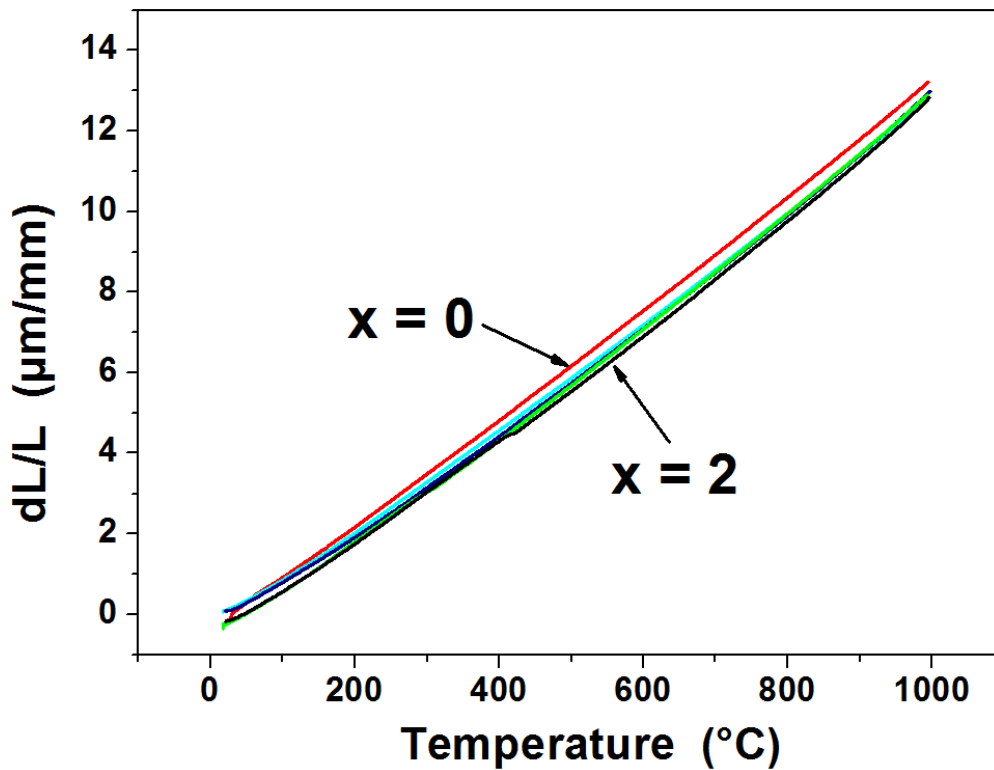


**Figure 5:** Thermal variation of the relative expansion ( $dL/L$ ) for  $\text{La}_{2-x}\text{Pr}_x\text{NiO}_{4+\delta}$ , under air ( $30 \text{ }^\circ\text{C} \leq T \leq 1000 \text{ }^\circ\text{C}$ ).

### 3.5. Oxygen diffusion and surface exchange coefficients ( $D^*$ , $k^*$ )

The thermal variation of the oxygen diffusion coefficients,  $D^*$ , and surface exchange coefficients,  $k^*$ , for LPNO ( $x = 0.5, 1$  and  $1.5$ ) are plotted in **Figure 6**, for  $T = 500, 600, 650$  and  $700 \text{ }^\circ\text{C}$  in comparison with PNO and LNO (data from reference [18]).

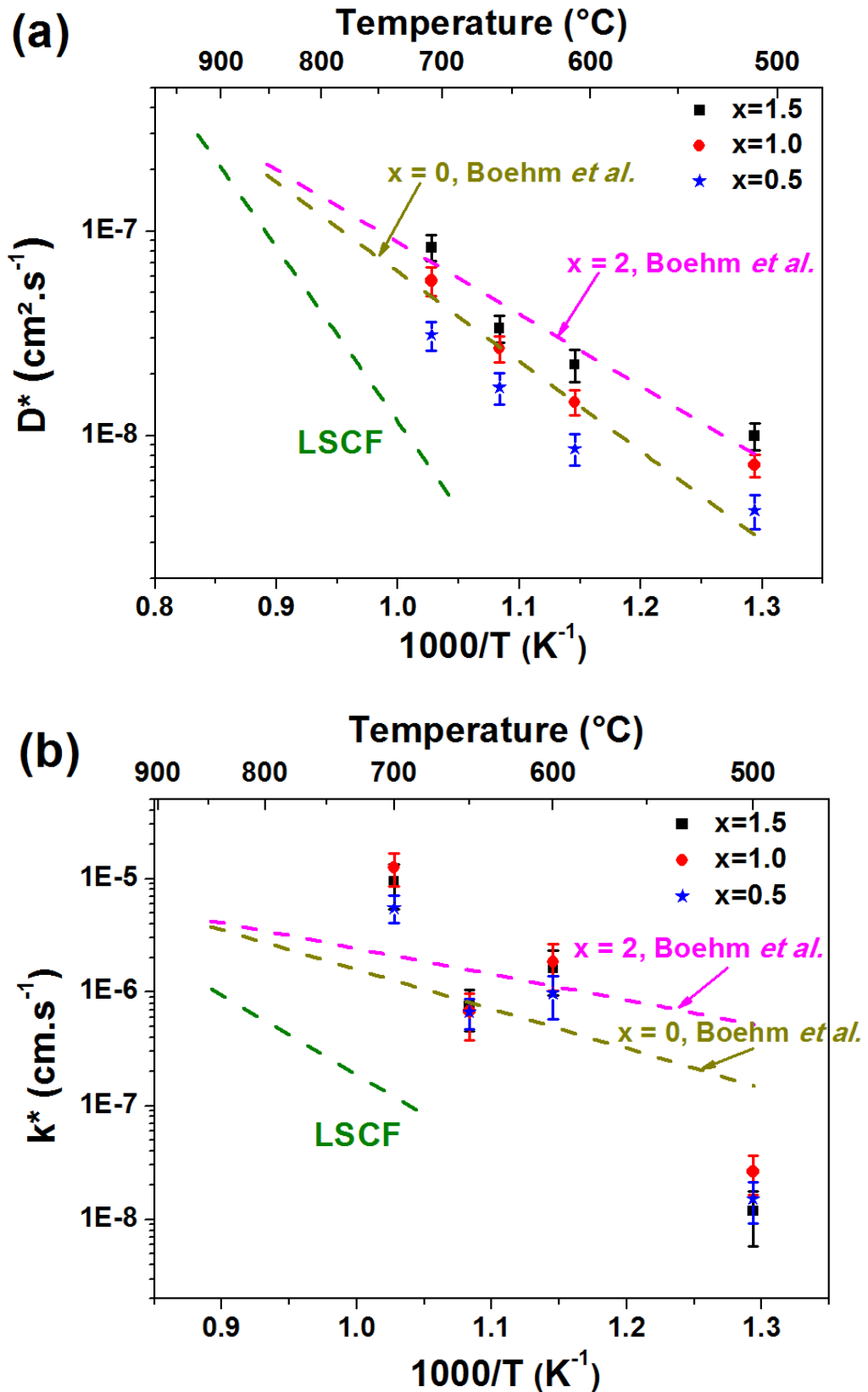


Figure 6: Thermal variation of (a) the diffusion coefficient  $D^*$  and (b) the surface exchange coefficient  $k^*$  for  $\text{La}_{2-x}\text{Pr}_x\text{NiO}_{4+\delta}$  ( $x = 0.5, 1$  and  $1.5$ ). The values of  $D^*$  for  $x = 0, 2$  and LSCF are from references [18]. The error bars represent the deviation from the average value of the coefficients determined using three different measurements.

The  $D^*$  values of mixed phases are in the range of those reported for PNO ( $2.5 \times 10^{-8} \text{ cm}^2 \cdot \text{s}^{-1}$ ) and LNO ( $1.5 \times 10^{-8} \text{ cm}^2 \cdot \text{s}^{-1}$ ) at 600 °C [18] with an increase of  $D^*$  with increasing Pr-content. It is worth mentioning that the  $D^*$  values of the nickelates are among the highest ones available in the literature, especially at low temperatures (around  $500 < T \text{ °C} < 600$ ) due to a low activation energy (0.6 to 0.7 eV, against 1.4 to 1.8 eV for the perovskite-type materials) [32]. Indeed, the  $D^*$  values for LSCF are much smaller than the ones of the nickelates (**Figure 6a**) [18].

Because the diffusion coefficients in the whole solid solution are found in between less than an order of magnitude at a given temperature, the ionic conductivity would normally not be a penalizing parameter, whatever the mixed nickelates composition, with respect to the SOFCs application.

Regarding the  $k^*$  values (**Figure 6b**), except at 500 °C, they are slightly higher at high temperature than those reported for PNO and LNO [18]. However, the  $k^*$  values highly depend on the surface state of the ceramics, itself being dependent on the grain size for similar polishing conditions. In addition, at a given temperature, the various  $k^*$  values are found in a range less than one order of magnitude.

### 3.6. Electrochemical Measurements

The impedance diagrams were recorded in the temperature range 500–800 °C under air following the sintering of the electrodes at high temperature under low  $p\text{O}_2$  as detailed in the experimental part, then allowing the determination of  $R_p$ . The  $R_p$  values were obtained by fitting the impedance diagrams recorded for all the LPNO half cells with two  $RCPE$  (constant phase element) in series, which is the simplest equivalent circuit model that yields a good fit to the data.

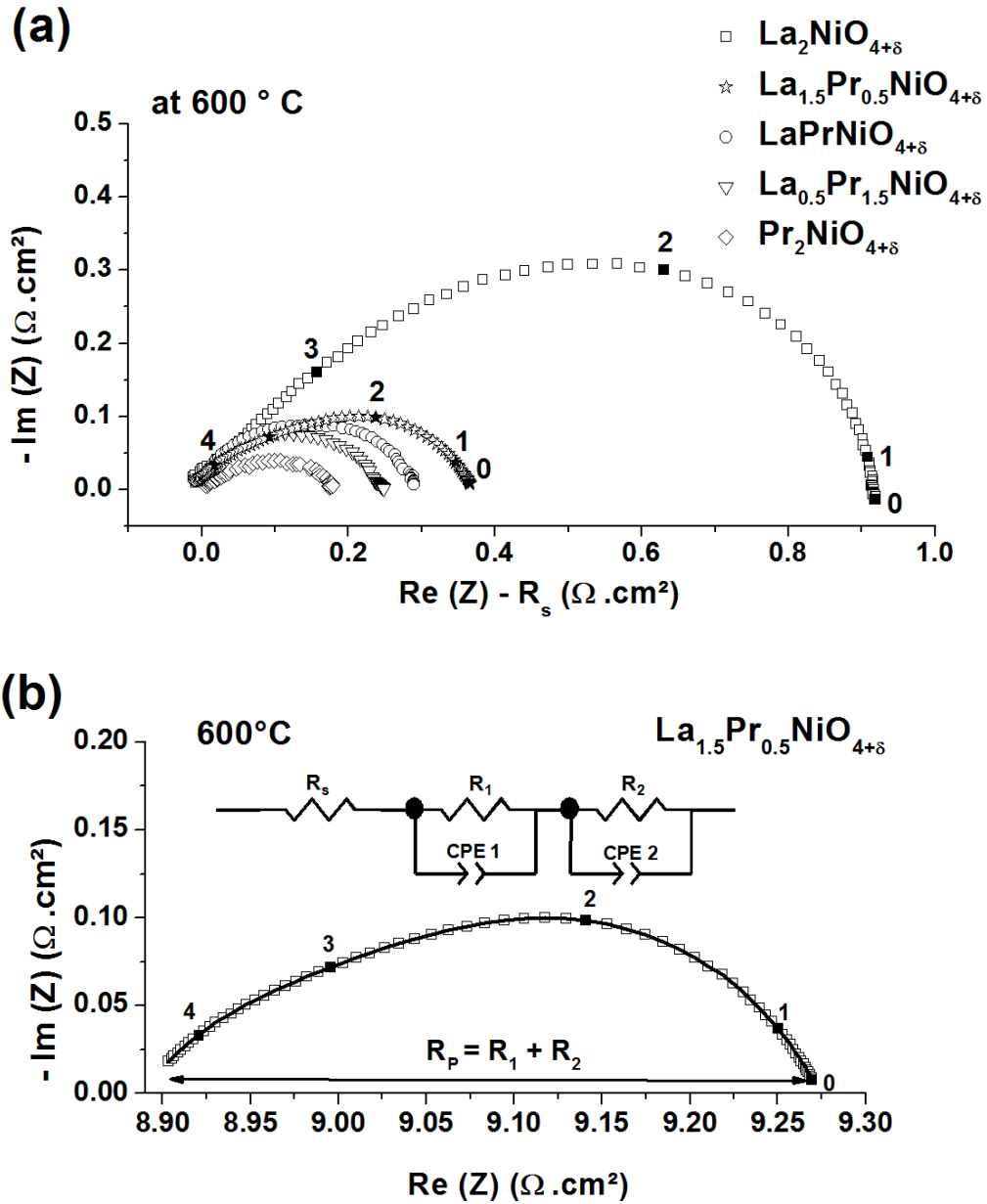


**Figure 7:** (a) Nyquist plots recorded for LPNO electrodes at 600 °C, (b) Impedance diagrams for  $\text{La}_{1.5}\text{Pr}_{0.5}\text{NiO}_{4+\delta}$  in symmetrical half cell, at 600 °C, fitted using  $R_s$  (series resistance),  $R_1||CPE_1$  and  $R_2||CPE_2$  elements.

However, the EIS diagram of the LNO electrode was fitted using Gerischer impedance as reported in earlier studies [42, 43]. In the current study the fit was limited to the extraction of the  $R_p$  value, therefore no attempt was made to interpret the two elements representing the total electrode processes. The Nyquist impedance diagrams for LPNO electrodes, at 600 °C, are shown in **Figure 7a**, whereas **Figure 7b** represents a typical fit of impedance data for the  $\text{La}_{1.5}\text{Pr}_{0.5}\text{NiO}_{4+\delta}$  electrode (600 °C) using two  $R||CPE$  elements.

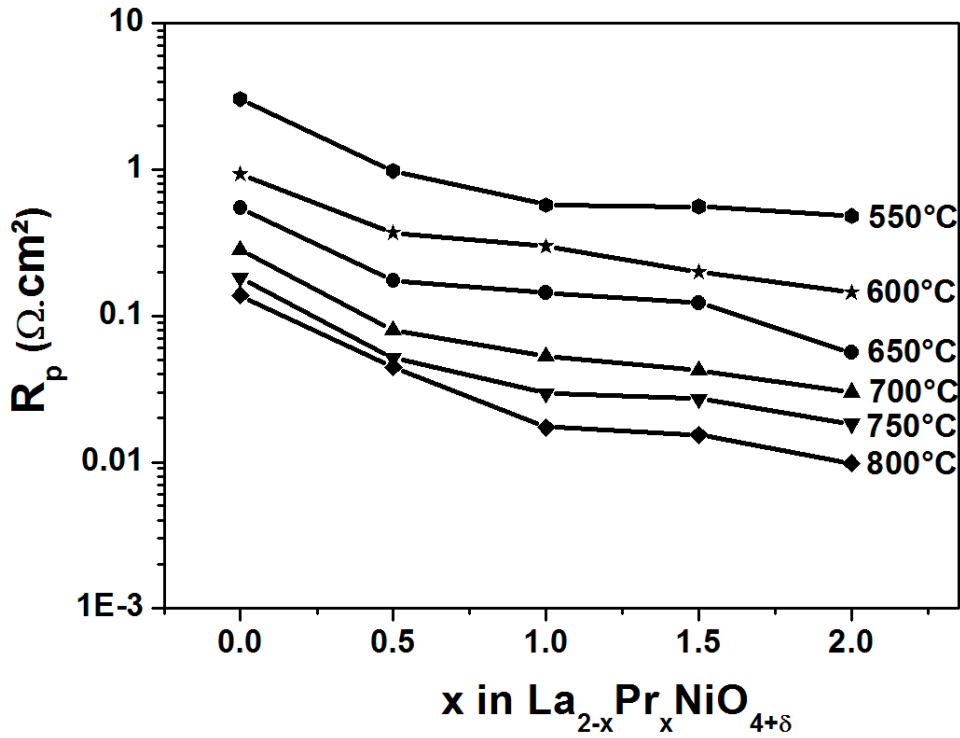


**Figure 8: Composition dependence of the polarization resistance,  $R_p$ , for  $\text{La}_{2-x}\text{Pr}_x\text{NiO}_{4+\delta}$  phases in the 550 °C to 800 °C temperature range.**

The variations of calculated  $R_p$  for LPNO electrodes, in the 550 °C to 800 °C temperature range, as a function of  $x$  are shown in **Figure 8**. The electrochemical performance is notably improved (*i.e.* decrease of  $R_p$ ) by the substitution of La by Pr, whatever the temperature. For instance, a  $R_p$  value of 0.93  $\Omega\cdot\text{cm}^2$  is achieved at 600 °C for LNO while after substitution of La by Pr, the  $R_p$  values decrease down to 0.37, 0.29, 0.23 and 0.15  $\Omega\cdot\text{cm}^2$  for  $\text{La}_{1.5}\text{Pr}_{0.5}\text{NiO}_{4+\delta}$ ,  $\text{LaPrNiO}_{4+\delta}$ ,  $\text{La}_{0.5}\text{Pr}_{1.5}\text{NiO}_{4+\delta}$  and PNO, respectively (**Figure 8**). Whatever the temperature,  $R_p$  notably decreases nonlinearly with increasing Pr content, for example, by 3 times (0.93 to 0.37  $\Omega\cdot\text{cm}^2$ ) from LNO to  $\text{La}_{1.5}\text{Pr}_{0.5}\text{NiO}_{4+\delta}$ . From those preliminary results, it can be concluded that the best electrochemical properties (*i.e.* lowest  $R_p$ ) are achieved with the PNO electrode. In addition it is worth mentioning that a lower  $R_p$  value of 0.08  $\Omega\cdot\text{cm}^2$  was earlier reported [26]. However, as pointed out in the introduction, a definitive conclusion on an optimized composition requires the study of long term ageing experiments. For this purpose, the chemical stability of the LPNO nickelates under air at operating temperatures as well as the variation of  $R_p$  during ageing (recorded under air at  $i_{dc} = 0$  and  $i_{dc} \neq 0$  conditions) are currently under investigation for duration up to one month. LNO is highly stable whereas PNO is completely dissociated after 1 month at 600, 700

and 800°C. Interestingly, the ageing of the mixed LPNO//GDC//8YSZ half cells during 1 month under air shows no change in the  $R_p$  value at  $i_{dc} = 0$  condition. The complete and detailed description of these experiments will be reported in a forthcoming paper<sup>3</sup>.

## 4. Conclusions

The present study is focused on alternative oxygen electrodes for IT-SOFCs prepared in MSC-type conditions, *i.e.* under low  $pO_2$ . Belonging to the  $K_2NiF_4$  structural type, the  $La_{2-x}Pr_xNiO_{4+\delta}$  mixed nickelates (LPNO) were synthesized and depending on the La/Pr ratio, two domains of solid solutions with orthorhombic structure were identified. One is related to La-rich phases, from  $x = 0$  to  $x = 0.5$ , with the  $Fmmm$  space group while Pr-rich phases, from  $x = 1.0$  to  $x = 2$ , crystallize with  $Bmab$  space group. All the Lanthanum-Praseodymium nickelates are oxygen over-stoichiometric in the whole temperature range either under air or argon. The  $\delta$  value increases with increasing  $x$ . All other physico-chemical properties including electrical conductivity, TECs, oxygen diffusion and surface exchange coefficients confirm the suitability of LPNO for MS-SOFCs application. Besides, the decrease in the polarization resistance as a function of  $x$  suggests that the Pr-rich compounds are more efficient for the oxygen electrode reaction than the La-rich ones. Studies of ageing behavior especially at the operating conditions are in progress.

## Acknowledgements

This work was performed under PEREN project (reference: ANR-2011-PREG-016-05). The authors wish to gratefully acknowledge the Agence Nationale de la Recherche (A.N.R., France) for supporting these scientific works and for the financial support. The authors also acknowledge Eric Lebraud for XRD, Nicolas Penin and Sébastien Fourcade for their valuable help in the experiments.

---

<sup>3</sup> Chapter 4

## References

- [1] E. Ivers-Tiffée, A. Weber, D. Herbristrit, *Journal of the European Ceramic Society*, 21 (2001) 1805–1811.
- [2] A. J. Jacobson, *Chemistry of Materials*, 22 (2010) 660–674.
- [3] D. J. L. Brett, A. Atkinson, N. P. Brandon, S. J. Skinner, *Chemical Society Reviews*, 37 (2008) 1568–1578.
- [4] I. Villarreal, C. Jacobson, A. Leming, Y. Matus, S. Visco, L. De Jonghe, *Electrochemical and Solid-State Letters*, 6 (2003) A178–A179.
- [5] Y. B. Matus, L. C. De Jonghe, C. P. Jacobson, S. J. Visco, *Solid State Ionics*, 176 (2005) 443–449.
- [6] S. Hui, D. Yang, Z. Wang, S. Yick, C. Decès-Petit, W. Qu, A. Tuck, R. Maric, D. Ghosh, *Journal of Power Sources*, 167 (2007) 336–339.
- [7] M. C. Tucker, G. Y. Lau, C. P. Jacobson, L. C. DeJonghe, S. J. Visco, *Journal of Power Sources*, 171 (2007) 477–482.
- [8] M. C. Tucker, G. Y. Lau, C. P. Jacobson, L. C. DeJonghe, S. J. Visco, *Journal of Power Sources*, 175 (2008) 447–451.
- [9] S. Sakuno, S. Takahashi, H. Sasatsu, *ECS Transaction*, 25 (2009) 731–737.
- [10] M. C. Tucker, *Journal of Power Sources*, 195 (2010) 4570–4582.
- [11] Y. Zhou, X. Xin, J. Li, X. Ye, C. Xia, S. Wang, Z. Zhan, *International Journal of Hydrogen Energy*, 39 (2014) 2279–2285.
- [12] G. Ch. Kostogloudis, Ch. Ftikos, *Solid State Ionics*, 126 (1999) 143–151.
- [13] V. V. Kharton, A. P. Viskup, D. M. Bochkov, E. N. Naumovich, O. P. Reut, *Solid State Ionics*, 110 (1998) 61–68.
- [14] G. Ch. Kostogloudis, G. Tsiniarakis, Ch. Ftikos, *Solid State Ionics*, 135 (2000) 529–535.
- [15] F. Wang, K. Yamaji, D.-H. Cho, T. Shimonosono, H. Kishimoto, M. E. Brito, T. Horita, H. Yokokawa, *Solid State Ionics*, 225 (2012) 157–160.
- [16] G. Amow, I. J. Davidson, S. J. Skinner, *Solid State Ionics*, 177 (2006) 1205–1210.
- [17] S. Takahashi, S. Nishimoto, M. Matsuda, M. Miyake, *Journal of the American Ceramic Society*, 93 (2010) 2329–2333.
- [18] E. Boehm, J.-M. Bassat, P. Dordor, F. Mauvy, J.-C. Grenier, P. Stevens, *Solid State Ionics*, 176 (2005) 2717–2725.
- [19] A. Aguadero, J. A. Alonso, M. J. Martinez-Lope, M. T. Fernandez-Diaz, M. J. Escudero, L. Daza, *Journal of Materials Chemistry*, 16 (2006) 3402–3408.
- [20] J.-M. Bassat, P. Odier, J. P. Loup, *Journal of Solid State Chemistry*, 110 (1994) 124–135.
- [21] C. N. Munnings, S. J. Skinner, G. Amow, P. S. Whitfield, I. J. Davidson, *Solid State Ionics*, 176 (2005) 1895–1901.
- [22] H. Zhao, F. Mauvy, C. Lalanne, J.-M. Bassat, S. Fourcade, J.-C. Grenier, *Solid State Ionics*, 179 (2008) 2000–2005.
- [23] R. D. Shannon, *Acta Crystallogr. Sect.*, A32 (1976) 751.
- [24] D. J. Buttrey, P. Ganguly, J. M. Honig, C. N. R. Rao, R. R. Schartman, G. N. Subbanna, *Journal of Solid State Chemistry*, 74 (1988) 233–238.
- [25] C. Allançon, A. Gonthier-Vassal, J.-M. Bassat, J. P. Loup, P. Odier, *Solid State Ionics*, 74 (1994) 239–248.
- [26] C. Ferchaud, J.-C. Grenier, Y. Zhang-Steenwinkel, M. M. A. Van Tuel, F. P. F. Van Berkel, J.-M. Bassat, *Journal of Power Sources*, 196 (2011) 1872–1879.
- [27] A. Flura, S. Dru, C. Nicollet, S. Fourcade, A. Rougier, J.-M. Bassat, J.-C. Grenier, A. Brevet, J. Mougin, *5th International Conference on Fundamentals and Development of Fuel Cells, FDFC 2013* (2013).
- [28] P. Courty, H. Ajot, C. Marcilly, B. Delmon, *Powder Technology*, 7 (1973) 21–38.

- [29] J. A. Kilner, C. K. M. Shaw, *Solid State Ionics*, 154-155 (2002) 523–527.
- [30] R. A. De Souza, J. Zehnpfenning, M. Martin, J. Maier, *Solid State Ionics*, 176 (2005) 1465–1471.
- [31] J.-M. Bassat, M. Petitjean, J. Fouletier, C. Lalanne, G. Caboche, F. Mauvy, J.-C. Grenier, *Applied Catalysis A: General*, 289 (2005) 84–89.
- [32] E. Boehm, J.-M. Bassat, M. C. Steil, P. Dordor, F. Mauvy, J.-C. Grenier, *Solid State Sciences*, 5 (2003) 973–981.
- [33] J. Crank, Oxford, 2nd Edition, 1975.
- [34] C. Allançon, P. Odier, J.-M. Bassat, J. P. Loup, *Journal of Solid State Chemistry*, 131 (1997) 167–172.
- [35] S. Nishimoto, S. Takahashi, Y. Kameshima, M. Matsuda, M. Miyake, *Journal of the Ceramic Society of Japan*, 119 (2011) 246–250.
- [36] P. Odier, J.-M. Bassat, J. C. Rifflet and J. P. Loup, *Solid State Communications*, 85 (1993) 561–564.
- [37] E. Niwa, K. Wakai, T. Hori, K. Yashiro, J. Mizusaki, T. Hashimoto, *Thermochimica Acta*, 575 (2014) 129–134.
- [38] A. Flura, C. Nicollet, V. Vibhu, S. Fourcade, E. Lebraud, A. Rougier, J.-M. Bassat, J.-C. Grenier, *Journal of Solid State Chemistry*, 228 (2015) 189-198.
- [39] T. Nakamura, Y. Takeyama, S. Watanabe, K. Yashiro, K. Sato, T. Hashida, J. Mizusaki, *ECS Transaction*, 25 (2009) 2573–2580.
- [40] J.-C. Grenier, F. Mauvy, C. Lalanne, J.-M. Bassat, F. Chauveau, J. Mougín, J. Dailly, M. Marrony, *ECS Transaction*, 25 (2009) 2537–2546.
- [41] S. Bishop, *Acta Mechanica Sinica*, 29 (2013) 312–317.
- [42] N. Hildenbrand, P. Nammensma, D. H. A. Blank, H. J. M. Bouwmeester, B. A. Boukamp, *Journal of Power Sources*, 238 (2013) 442–453.
- [43] G. T. Kim, A. J. Jacobson, *Mater. Res. Soc. Symp. Proc.*, 972 (2007) 175–180.

## Additional Information: Chapter 2

### Additional experiments under Argon

#### 1. Electrical conductivity measurements

The electrical conductivity of the nickelates was measured under argon using the four-probe technique, in the temperature range 25 - 1000 °C with the heating and cooling rate of 1 °C.min<sup>-1</sup>. The experiment was first performed under air (two cycles) then the gas flow was switched from air to argon at 1000 °C. The gas flow was kept for 6 h for the stabilization of the oxygen composition of the material and then the measurements were performed during two cycles under argon. The variation of the total electrical conductivity  $\sigma$  vs.  $1000/T$  under air and argon for LPNO ( $x = 0.5, 1.0, 1.5$ ) phases are compared in **Figure 1**.

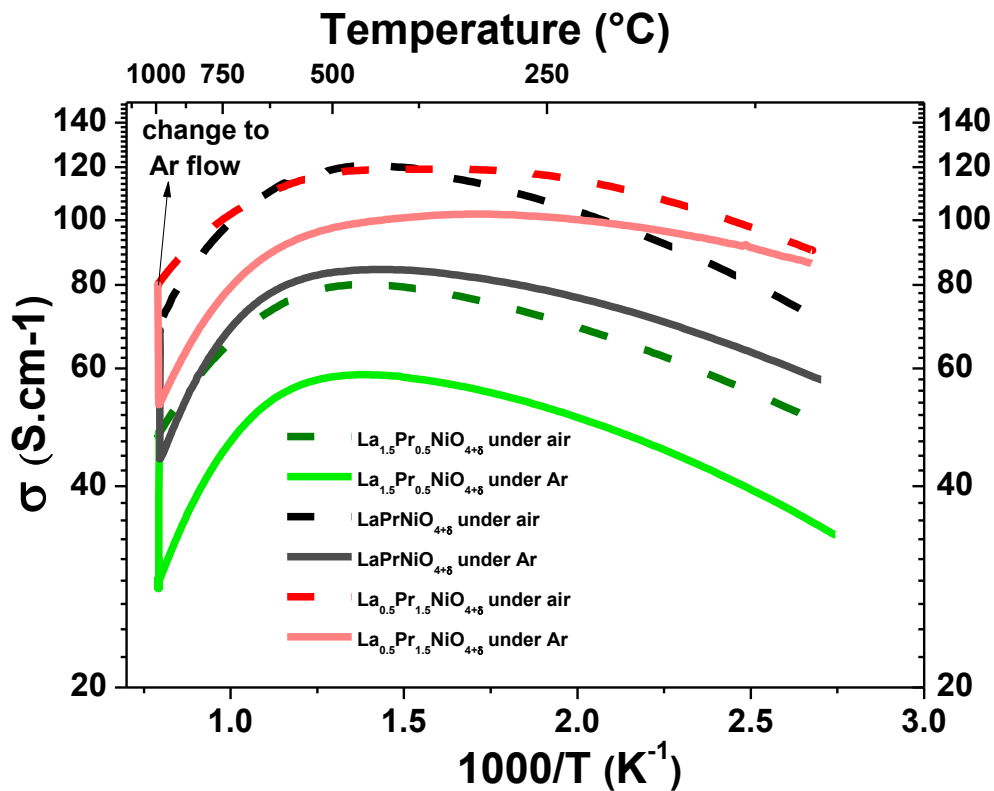


**Figure 1:** Thermal variation of the electrical conductivity for La<sub>2-x</sub>Pr<sub>x</sub>NiO<sub>4+ $\delta$</sub>  ( $x=0.5, 1.0, 1.5$ ). Dashed and bold lines represent the conductivity under air and argon respectively.

When the gas flow is switched from air to argon a sharp decrease in electrical conductivity is observed. The electrical conductivity is always higher under air than under argon throughout the whole temperature range (25-1000 °C). This sharp decrease under argon as well as the lower conductivity is directly correlated to the decrease of oxygen content. All the nickelates exhibit a semi-conducting behavior and the maximum conductivity is observed in the 400-600 °C range.

## 2. Dilatometry measurements

Thermal variations of the relative expansion of dense pellets ( $dL/L$ ) were carried out in the temperature range 25 – 1000 °C under argon for LPNO phases with the aim to determine the TECs of the materials. The corresponding results are reported in **Figure 2**.

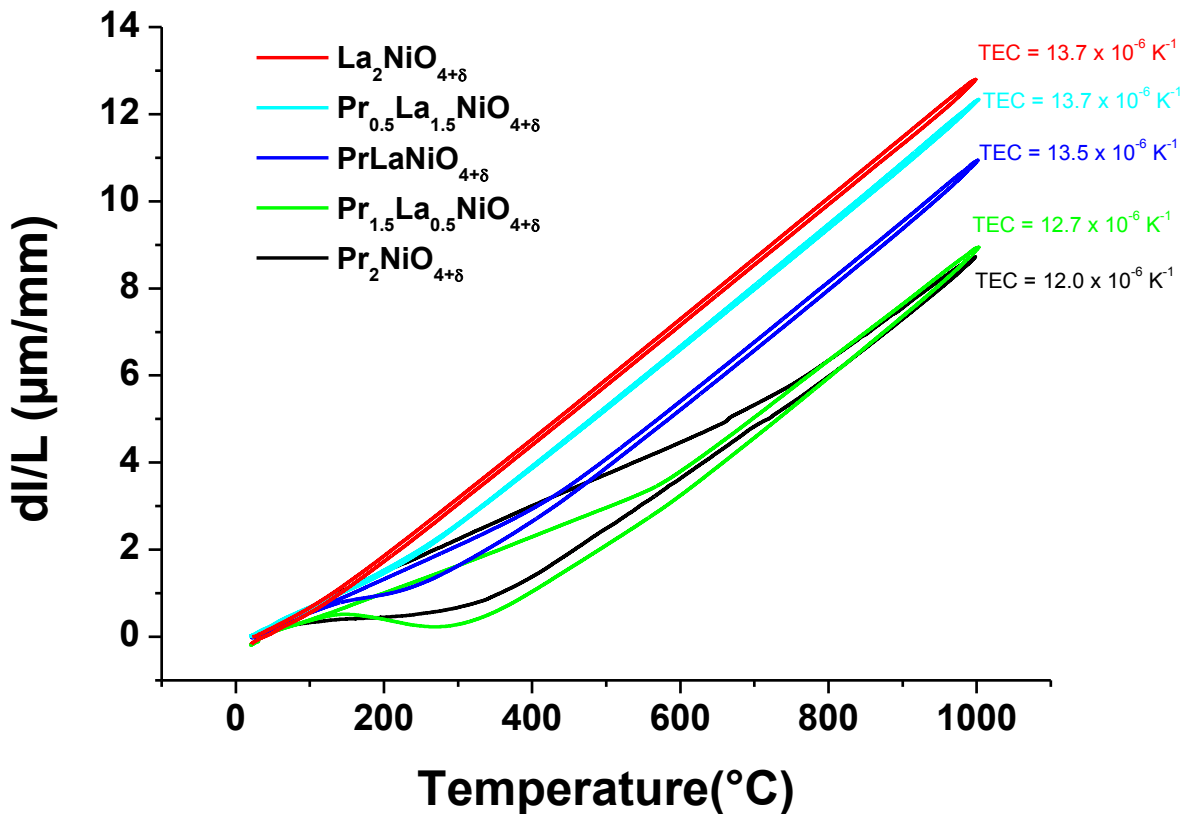


**Figure 2:** Thermal variation of the relative expansion ( $dL/L$ ) for  $\text{La}_{2-x}\text{Pr}_x\text{NiO}_{4+\delta}$  ( $x=0.0, 0.5, 1.0, 1.5$  and  $2.0$ ), under argon ( $30 \text{ °C} \leq T \leq 1000 \text{ °C}$ ).

For La rich phases ( $x = 0.0$  and  $0.5$ ), a single TEC value is measured for both heating and cooling. On the contrary, Pr rich phases ( $x = 1.0, 1.5$  and  $2.0$ ) show hysteresis during heating and cooling in the temperature range  $\sim 100$ - $600 \text{ °C}$ . A larger discrepancy in cooling

and heating is observed with increasing the Pr content. The reason for this hysteresis is still unclear.

The thermal expansion coefficients (TECs), calculated from the slope of the corresponding straight lines are in between  $12$  to  $13.7 \times 10^{-6} \text{ }^\circ\text{C}^{-1}$  for all nickelates. For La rich phases, the TEC values are the same under air (*cf.* chapter 2) and argon but for Pr- rich phases mainly  $x = 1.5$  and  $2.0$ , lower value are observed under argon.

# Chapter 3

---

*"To be submitted for publication"*

# Structural characterization of Pr-rich phases in $\text{La}_{2-x}\text{Pr}_x\text{NiO}_{4+\delta}$ series using Synchrotron and Neutron Powder Diffraction

Vaibhav Vibhu, Matthew Suchomel, Nicolas Penin, Clément Nicollet, Aurélien Flura, François Weill, Jean-Claude Grenier, Jean-Marc Bassat and Aline Rougier

*CNRS, Université de Bordeaux, Institut de Chimie de la Matière Condensée de Bordeaux (ICMCM), 87 Av. Dr Schweitzer, F-33608 Pessac Cedex, France.*

## Abstract

The present study is focused on the structural study of  $\text{La}_{2-x}\text{Pr}_x\text{NiO}_{4+\delta}$  (LPNO) mixed nickelates examined by analysis of powder samples using Synchrotron X-ray, Neutron and Electron diffraction probes. The properties of  $\text{La}_{2-x}\text{Pr}_x\text{NiO}_{4+\delta}$  (LPNO) mixed nickelates were recently investigated as cathode materials for Solid Oxide Fuel Cells (SOFCs). Based on structural analysis of LPNO nickelates, the existence of three domains depending on  $x$  value (*i.e.* Pr content) is evidenced. La-rich phases display an  $Fmmm$  orthorhombic structure ( $0 \leq x < 0.5$ ), Pr-rich phases ( $1.1 < x \leq 2.0$ ) display a  $C2/m$  monoclinic structure and in between, for  $0.5 \leq x \leq 1.1$ , a third mixed biphasic domain is observed. For Pr rich compositions, both the monoclinic unit cell distortion and additional weak unindexed reflections (observed both in X-ray and electron diffraction) are found to be dependent on both interstitial oxygen content and A-site cation substitution. These additional peaks for which the intensity decreases with reduced Pr content may be evidence of a complicated modulated structure that is not addressed in this work.

**Key words:** Nickelates, Oxygen over-stoichiometry, Neutron diffraction, Synchrotron diffraction, HR-TEM

## 1. Introduction

The importance of Mixed Ionic and Electronic conducting (MIEC) materials are increasing for future eco-friendly societies because for instance of their use as cathode materials for solid oxide fuel cells (SOFCs) and oxygen separation membranes [1-8]. It is well known that SOFCs directly and efficiently convert chemical energy to electrical energy. The operating temperature of SOFCs is high (e.g. about 800–1000 °C), which results in problems of costs and materials compatibility. Currently, a main objective is to decrease

SOFC operating temperatures down to around 600 – 700°C, in an effort to lower the device cost (for example, using stainless steel instead of ceramic materials as interconnects) and to improve the cell durability. However, since both electrode reactions and ion transport through the electrolyte are temperature-driven, the electrochemical performance drastically decreases at lower temperature. Hence, it is mandatory to improve the materials and architecture of the cell in order to reach reasonable performance at Intermediate Temperatures (IT-SOFCs). The MIEC cathode materials have received considerable attention because the cathode significantly contributes to the overall cell resistance.

Rare earth nickelates with the general formula  $\text{Ln}_2\text{NiO}_{4+\delta}$  ( $\text{Ln} = \text{La}, \text{Nd}$  or  $\text{Pr}$ ) have already shown good cathodic performance with various electrolytes (mainly YSZ, GDC and LSGM). In our previous research on  $\text{Ln}_2\text{NiO}_{4+\delta}$  ( $\text{Ln} = \text{La}, \text{Nd}$  or  $\text{Pr}$ ) compounds,  $\text{Pr}_2\text{NiO}_{4+\delta}$  (PNO) showed the lowest polarization resistance using GDC interface and YSZ electrolyte [9].

The MIEC properties of the nickelates are ultimately connected to their crystallographic structure, it is therefore interesting to examine carefully the structural trends in the  $\text{La}_{2-x}\text{Pr}_x\text{NiO}_{4+\delta}$  (LPNO) series. Generally, the structure of  $\text{Ln}_2\text{NiO}_{4+\delta}$  consists of alternate  $\text{NiO}_2$  square plane layers and  $\text{Ln}_2\text{O}_2$  rock salt type-layers, leading to the first member ( $n=1$ ) of the Ruddlesden-Popper series ( $\text{Ln}_{n+1}\text{Ni}_n\text{O}_{3n+1}$ ). This type of structure has a strong ability to accept interstitial oxygen (which is located in the  $\text{Ln}_2\text{O}_2$  rock-salt interlayer), leading to a mixed valence of Ni ( $\text{Ni}^{2+}/\text{Ni}^{3+}$ ), which further results in a mixed ionic and electronic conductivity ( $\text{O}^{2-}/\text{e}^-$ ) [10]. The amount of interstitial oxygen  $\delta$  is closely dependent on the rare-earth cation size and is also influenced by the cooling rate and annealing atmosphere. For instance, the oxygen excess in  $\text{La}_2\text{NiO}_{4+\delta}$  (LNO) is  $\delta \sim 0.16$  at room temperature, while it is larger in  $\text{Pr}_2\text{NiO}_{4+\delta}$  (PNO,  $\delta \approx 0.25$ ) [11], as a consequence of the smaller ionic radius of  $\text{Pr}^{3+}$  ( $r(\text{Pr}^{3+}) = 1.126 \text{ \AA}$  and  $r(\text{La}^{3+}) = 1.16 \text{ \AA}$ ) [12] that induces large structural stresses released by a greater interstitial oxygen insertion [13,14]. These materials show a reversible oxygen exchange during heating and cooling under air and low  $p\text{O}_2$  conditions [15]. In addition, a phase transition from orthorhombic to tetragonal was also reported during heating for  $\text{Ln}_2\text{NiO}_{4+\delta}$  ( $\text{Ln} = \text{La}, \text{Nd}$  or  $\text{Pr}$ ) compounds [15].

In the literature there are very few reports characterizing  $\text{La}_{2-x}\text{Pr}_x\text{NiO}_{4+\delta}$  mixed nickelates as SOFC with respect to their physico-chemical and electrochemical properties [11, 16-18], but except for the end members none discuss the structural properties of LPNO series in particular using high resolution synchrotron powder diffraction (HR-SPD) and

neutron powder diffraction (NPD). Herein, the structural properties of LPNO are discussed in detail based on an analysis of diffraction data collected on LPNO powder samples using synchrotron X-ray, neutron, and HR-TEM probes.

## 2. Experimental

LPNO phases ( $0.0 \leq x \leq 2.0$ ) were prepared using the citrate-nitrate route (modified Pechini method) from  $\text{Pr}_6\text{O}_{11}$  (Aldrich chem, 99.9%),  $\text{La}_2\text{O}_3$  (Strem Chemical, 99.99%) and  $\text{Ni}(\text{NO}_3)_2 \cdot 6\text{H}_2\text{O}$  (Acros Organics, 99%) precursors.  $\text{Pr}_6\text{O}_{11}$  and  $\text{La}_2\text{O}_3$  were pre-fired in a first step at  $T = 900$  °C overnight to remove the water content, due to their high hygroscopic character, then to weight the exact amount of precursors. The final annealing was performed at 1200 °C for 12 h in air, leading to well crystallized phases.

The powders were first characterized by laboratory X-ray diffraction (XRD) at room temperature using a PANalytical X'pert MPD diffractometer with  $\text{Cu-K}_\alpha$  incident radiation using a flat-plate reflection geometry.

Selected LPNO samples were also measured by high-resolution synchrotron powder diffraction (HR-SPD) at beamline 11-BM of the Advanced Photon Source (APS) at Argonne National Laboratory. The samples were measured at room temperature in a transmission capillary mode using an incident beam energy of 30 keV ( $\lambda \approx 0.41$  Å) over the range  $0.5$  to  $50^\circ$  in  $2\theta$ . For the PNO composition, *in situ* variable temperature synchrotron diffraction experiments at 11-BM were also performed in 100 to 450 K range.

In order to gain additional structural information on LPNO compositions, time of flight neutron powder diffraction (TOF-NPD) data were collected for selected compositions ( $x = 0.6, 1.2, 1.5$  and  $2$ ) at 298 K on the POWGEN beamline of the Spallation Neutron Source (SNS) at Oak Ridge National Laboratory. Data obtained via the POWGEN mail-in service were collected for  $\sim 2$  hours per sample on  $\sim 5$  grams of powder loaded into 8.0 mm diameter V cans using detector banks covering a range  $0.4 - 9.0$  Å. Rietveld refinement of both X-ray and Neutron powder diffraction (including combined joint refinements when HR-SPD and TOF-NPD were collected on exactly the same powder sample) were performed using both FullProf and GSAS/EXPGUI software packages [19, 20]. Refined crystal structures and difference Fourier maps were displayed using the VESTA software package [21].

High Resolution TEM (HR-TEM) electron diffraction analysis of PNO sample was performed at ICMCB using a JEOL 2100 electron microscope system. Experiments were achieved at 100 K in order to prevent a modification of the sample caused by the electron beam under high vacuum. The powder ground in ethanol was deposited on a carbon film supported copper grid. The electron diffraction patterns were obtained by selected area electron diffraction (SAED).

### 3. Results and Discussion

#### 3.1. Initial structural characterizations

Initial structural characterizations of the LPNO phases by laboratory powder XRD show that all nickelates crystallize in an orthorhombic  $K_2NiF_4$  type structure. Depending on  $x$  value (*i.e.* Pr content), different domains can be distinguished. One is related to La-rich phases, from  $x = 0$  to  $x = 0.5$ , fitted with the  $Fmmm$  space group, and the second one is related to Pr-rich phases, from  $x = 1$  to  $x = 2$ , that were initially fit with an orthorhombic  $Bmab$  space group as commonly done in the literature [11, 22-23]. A biphasic domain was evidenced in between  $\sim x = 0.5$  to  $x = 1.0$  but the exact region was unclear. A more detailed examination performed with a very long counting time laboratory XRD data analysis of PNO revealed that few reflection peaks ( $hhl$ ) split into two, as shown in **Figure 1**. Those were not fitted well using either  $Fmmm$  or  $Bmab$  symmetry, suggesting some distortion in the structure. It was determined later in this study that the distortion could be well fitted using a monoclinic unit cell. In **Table 1**, ambient temperature results of refinement performed on laboratory XRD data for PNO are compared in the orthorhombic  $Fmmm$  and monoclinic  $C2/m$  space groups. The fitting statistics parameters ( $\chi^2$ ,  $R_p$  and  $R_{wp}$ ) show lower values when refined using monoclinic  $C2/m$  structure, indicating that the monoclinic cell better describes the measured laboratory diffraction data.

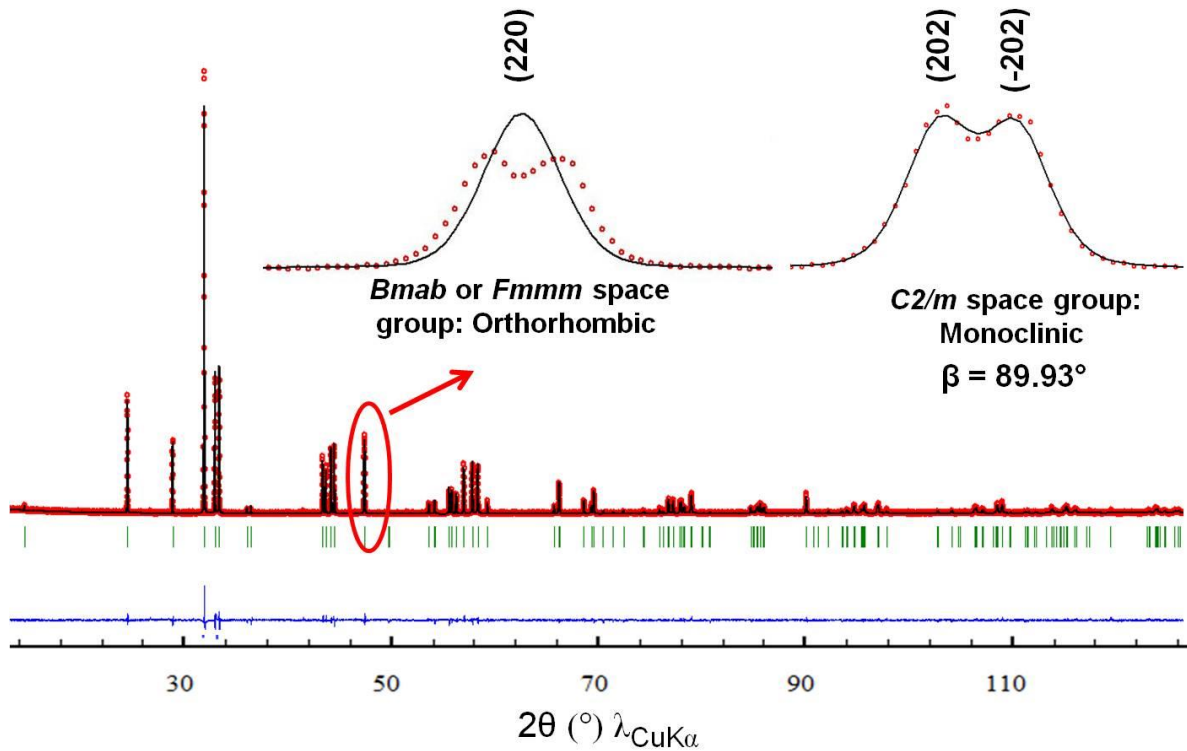


**Figure 1: Rietveld refinement of laboratory XRD data of  $\text{Pr}_2\text{NiO}_{4.25}$  at 25 °C, using  $C2/m$  space group. Example of peak splitting: (220) into (202) and (-202).**

**Table 1: Refined atomic position using  $Fmmm$  and  $C2/m$  space group for  $\text{Pr}_2\text{NiO}_{4+\delta}$  at RT**

	$\text{Pr}_2\text{NiO}_{4+\delta}$ $Fmmm$	$\text{Pr}_2\text{NiO}_{4+\delta}$ $C2/m$
<b>Lattice parameters and atomic positions</b>	$a = 5.3914(3) \text{ \AA}$ , $b = 12.4479(3) \text{ \AA}$ , $c = 5.4572(4) \text{ \AA}$ , $\beta = 90^\circ$ Pr1 ( $x, y, z$ ): 0, 0.359(3), 0 Ni1 ( $x, y, z$ ): 0, 0, 0 O1 ( $x, y, z$ ): 0.25, 0, 0.25 O2 ( $x, y, z$ ): 0, 0.175(2), 0	$a = 5.3913(3) \text{ \AA}$ , $b = 12.4476(4) \text{ \AA}$ , $c = 5.4573(1) \text{ \AA}$ , $\beta = 89.931(1)^\circ$
<b>Fit parameters</b>	$\chi^2 = 3.08$ , $R_p = 7.08 \%$ $R_{wp} = 9.93 \%$	$\chi^2 = 1.91$ , $R_p = 5.56 \%$ $R_{wp} = 7.40 \%$

For further investigation regarding the exact structure of these Pr-rich LPNO phases, high resolution synchrotron and neutron powder diffraction studies were performed. The high angular resolution of synchrotron powder diffraction collected at APS beamline 11-BM (using multiple single-crystal analyzer detectors) allows the detection of subtle pseudo-symmetry or weak intensity modulation peaks that could be missed by laboratory XRPD or

by Neutron Powder Diffraction (NPD). Additionally, TOF-NPD was also performed to provide complimentary diffraction data, exploiting the distinct elemental sensitivity of X-ray and neutron probes, to give extra details especially about oxygen atoms in the unit cell.

Before analyzing the data of mixed LPNO phases, we first considered the end members of the series *i.e.*  $\text{Pr}_2\text{NiO}_{4+\delta}$  (PNO) and  $\text{La}_2\text{NiO}_{4+\delta}$  (LNO). The structure of LNO is clearly orthorhombic type with  $Fmmm$  symmetry as reported in the literature [24, 25] while for PNO the structure is still not fully determined. Hence it was our first aim to investigate more carefully the structure of PNO then further move on the complete LPNO series.

The earlier studies regarding the structure of PNO at RT suggested its existence in orthorhombic structure with  $Fmmm$  or  $Bmab$  symmetry [23, 26-28]. The  $Bmab$  space group allows the systematic out of plane tilting of  $\text{NiO}_6$  octahedra on axes parallel to the square plane layers of  $\text{NiO}_6$ . On the other hand, Singh *et al.* [29] proposed for the first time the monoclinic symmetry in PNO on the basis of bond distances considerations but the authors did not discuss additional details about the structure.

Very narrow diffraction peaks in the high resolution synchrotron powder diffraction (HR-SPD) data of  $\text{Pr}_2\text{NiO}_{4.25}$  recorded at RT (**Figure 2a**) indicate notable crystalline quality. The indexing of major peaks suggests an average structure similar to previously reported  $Bmab$  models for PNO. However, splitting of selected (*hhl*) reflections are also clearly evidenced, *e.g.* the (220) peak is split into distinct (202) and (-202) reflections. As a result, a small monoclinic distortion of the unit cell is required to fully explain the observed splitting of the (*hhl*) reflections. Refinement and details of this model for PNO are discussed below.

## 3.2. Structure of $\text{Pr}_2\text{NiO}_{4+\delta}$

### 3.2.1. Joint synchrotron and neutron data refinement of $\text{Pr}_2\text{NiO}_{4+\delta}$

For further analysis a joint Rietveld refinement of synchrotron and neutron data was performed. X-rays interact with electrons, whereas neutrons are scattered by nuclei, which means that the two techniques probe the same structural parameters through different particles. The HR-SPD data are very sensitive to small distortions and weak intensity peaks. NPD data can provide more details about low Z ions like oxygen in the structure, which is important for studying MIEC materials. Also, NPD can provide greater contrast between similar Z cations (like Pr and La) than what is possible for synchrotron X-rays.

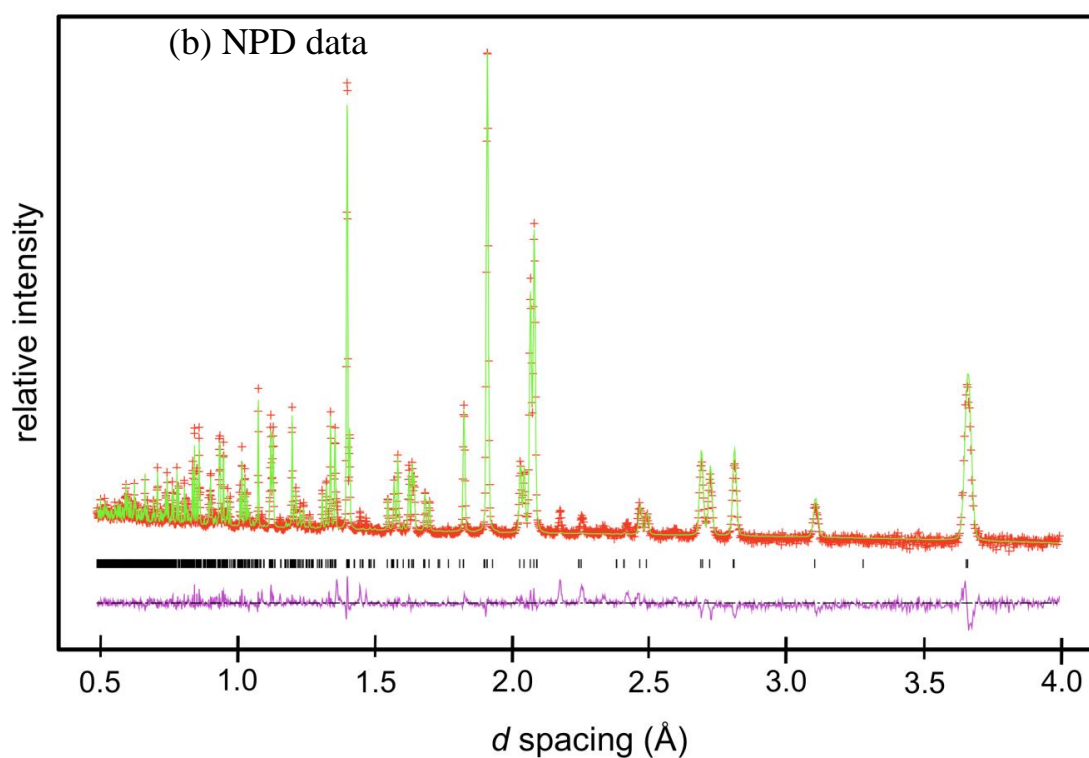
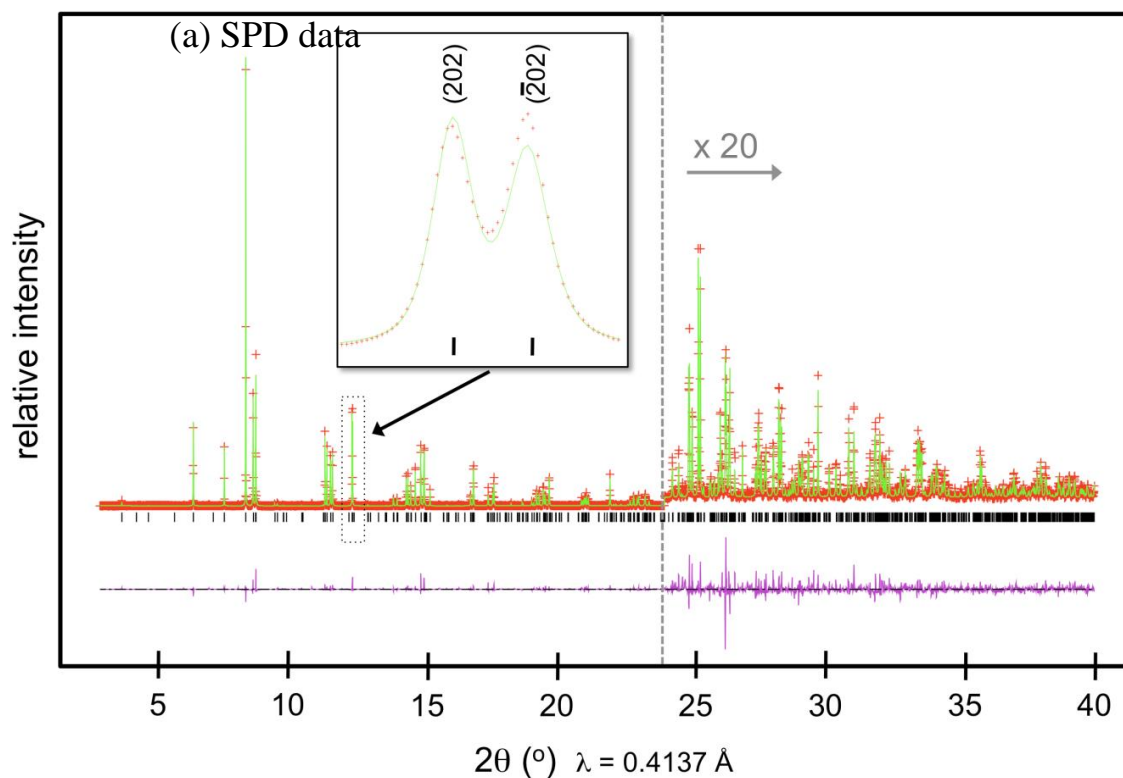


**Figure 2: Joint synchrotron (a) and neutron (b) powder diffraction data refinement of  $\text{Pr}_2\text{NiO}_{4+\delta}$  using  $C2/m$  space group, recorded at  $25^\circ\text{C}$ . (+) represent experimental data points, solid line refined data fit. The vertical sticks are  $\text{Pr}_2\text{NiO}_{4+\delta}$  monoclinic phase.**

Based on a best match with observed peak reflections in the data, a monoclinic space group  $C2/m$  ( $N^\circ 12$ ) was selected to describe the RT diffraction pattern of PNO and later on a new structural model is proposed. For the joint Rietveld refinements discussed here, structural models were refined simultaneously against both HR-SPD and TOF-NPD datasets. Refined values included: background functions, unit cell parameters, atom positions (except for  $O_i$  sites), occupancy of the interstitial oxygen sites, atom site thermal parameters (using anisotropic parameters for oxygen sites except  $O_i$ ), and instrument appropriate profile terms that included anisotropic strain terms for the HR-SPD dataset. Limited model constraints were included for cation sites with mixed Pr/La occupancies, and on oxygen anisotropic thermal parameters to improve the global refinement stability. Suitable sample absorption terms were included for both datasets. Phase scale factors were refined in cases of multiphase joint refinements (discussed later for the LPNO biphasic regions). The refined parameters obtained from the joint Rietveld refinement are listed in **Table 2**.

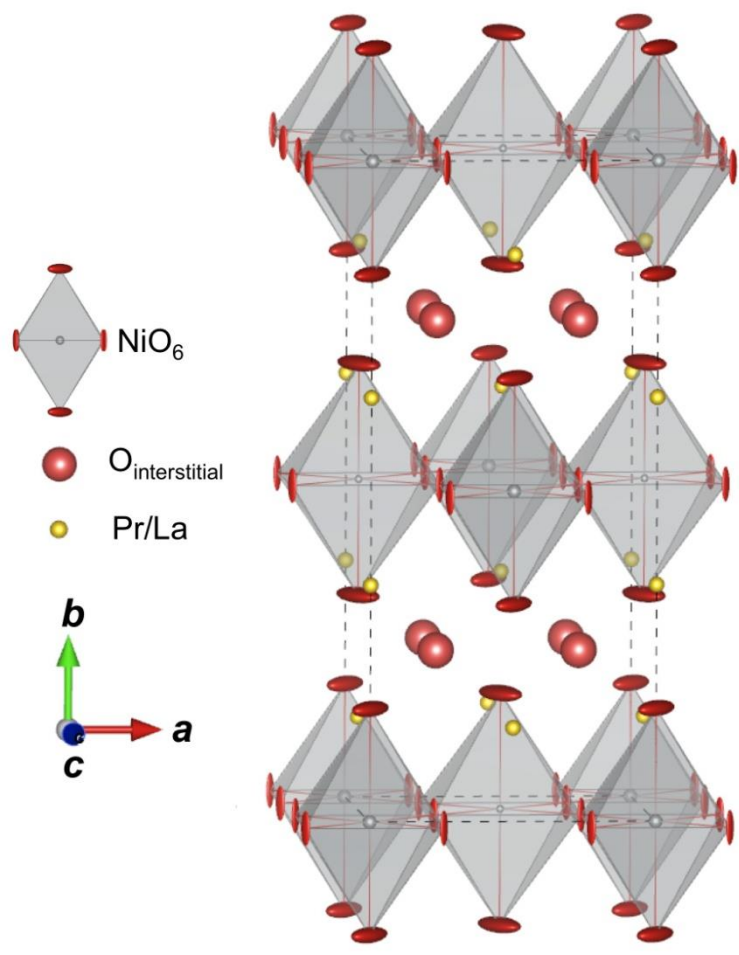
**Table 2: Refined lattice parameters and atomic positions from joint refinement of PNO using  $C2/m$  space group**

Lattice parameters	$a = 5.3917(2) \text{ \AA}$	$b = 12.4480(2) \text{ \AA}$	$c = 5.4572(3) \text{ \AA}$			
	$\beta = 89.931(3)^\circ$	$\chi^2 = 14.10, R_{wp} = 12.5 \%$				
Atom	x	y	z	occupancy	$U_{iso} \times 100$	
Pr1	0	0.358(2)	0	1	0.953(4)	
Pr2	0	0.140(1)	0.5	1	0.875(2)	
Ni1	0	0	0	1	0.732(3)	
Ni2	0	0.5	0.5	1	0.234(6)	
O1	0	0.171(1)	0	1	4.713(7)*	
O2	0.753(4)	0	0.253(1)	1	1.765(1)*	
O3	0	0.324(6)	0.5	1	8.988(8)*	
O4	0.237(2)	0	0.260(1)	1	1.764(8)*	
Oi	0.25	0.25	0.25	0.126(1)	5.00	
*	$U_{11}$	$U_{22}$	$U_{33}$	$U_{12}$	$U_{13}$	$U_{23}$
O1	5.97	0.97	7.22	0	-5.68	0
O2	0.26	4.66	0.37	0	0.21	0
O3	5.97	0.97	20.0	0	5.68	0
O4	0.26	4.66	0.37	0	-0.21	0

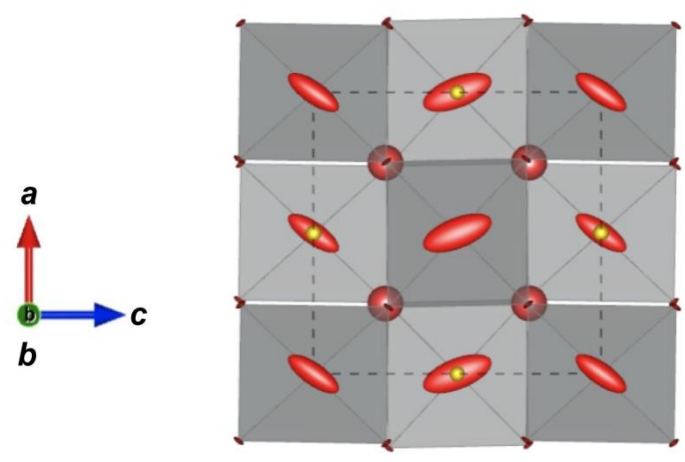
The joint refinement fits of HR-SPD and NPD data are shown in **Figure 2a** and **2b**, respectively. In the figure, red (+) points represent the experimental data, solid green line represent refined data fit, black sticks represents PNO monoclinic phase and the purple line represent the difference between experimental and calculated data. The lattice parameters are  $a = 5.3917(2)$ ,  $b = 12.4480(2)$ ,  $c = 5.4572(3)$  Å and  $\beta = 89.931(3)^\circ$  with  $\chi^2 = 14.1$  and  $R_{wp} = 12.5$  % for two histograms. The values obtained for the global  $\chi^2$  testify the quality of the refinements.

Schematics of the refined PNO monoclinic are shown in **Figure 3**. In **Figure 3a**, looking just off-axis along the  $c$  unit cell direction shows clearly the alternate layers of grey colour  $\text{NiO}_6$  octahedra between layers of yellow colour A site cations (occupied fully by Pr in the PNO structure). Red ellipsoids oxygen anions (reflecting the refined shape of anisotropic thermal parameters) are located at the vertices  $\text{NiO}_6$  octahedra, and a round partial occupied isotropic oxygen interstitial site is observed between the layers. **Figure 3b** shows the same PNO structure, but with a view looking along the long  $b$ -axis of the unit cell, where the distorted anisotropic shape of  $\text{NiO}_6$  apical oxygen ions is clearly visible. Two kinds of  $\text{NiO}_6$  octahedra (containing the Ni1 and Ni2 sites) are also noticed from a more detailed viewing along  $b$ -axis, (**Figure 3c**). The crystallographic structure of  $\text{Pr}_2\text{NiO}_{4.25}$  is basically same as that of the *Fmmm* or *Bmab* average model, but a monoclinic distortion leads to the loss of some symmetry elements. This symmetry loss generates two non-equivalent splitting of Pr, Ni, O1 and O2 positions [(0, 0.358, 0) and (0, 0.140, 0.5)], [(0, 0, 0) and (0, 0.5, 0.5)], [(0, 0.171, 0) and (0.753, 0, 0.253)] and [(0, 0.324, 0.5) and (0.237, 0, 0.260)] respectively, with respect to the *Fmmm* space group. The position of interstitial oxygen (*Oi*) in the *C2/m* model is fixed at (0.25, 0.25, 0.25) having been located by calculated difference Fourier maps of preliminary joint Rietveld refinement models that did not include an *Oi* site.

(a)



(b)



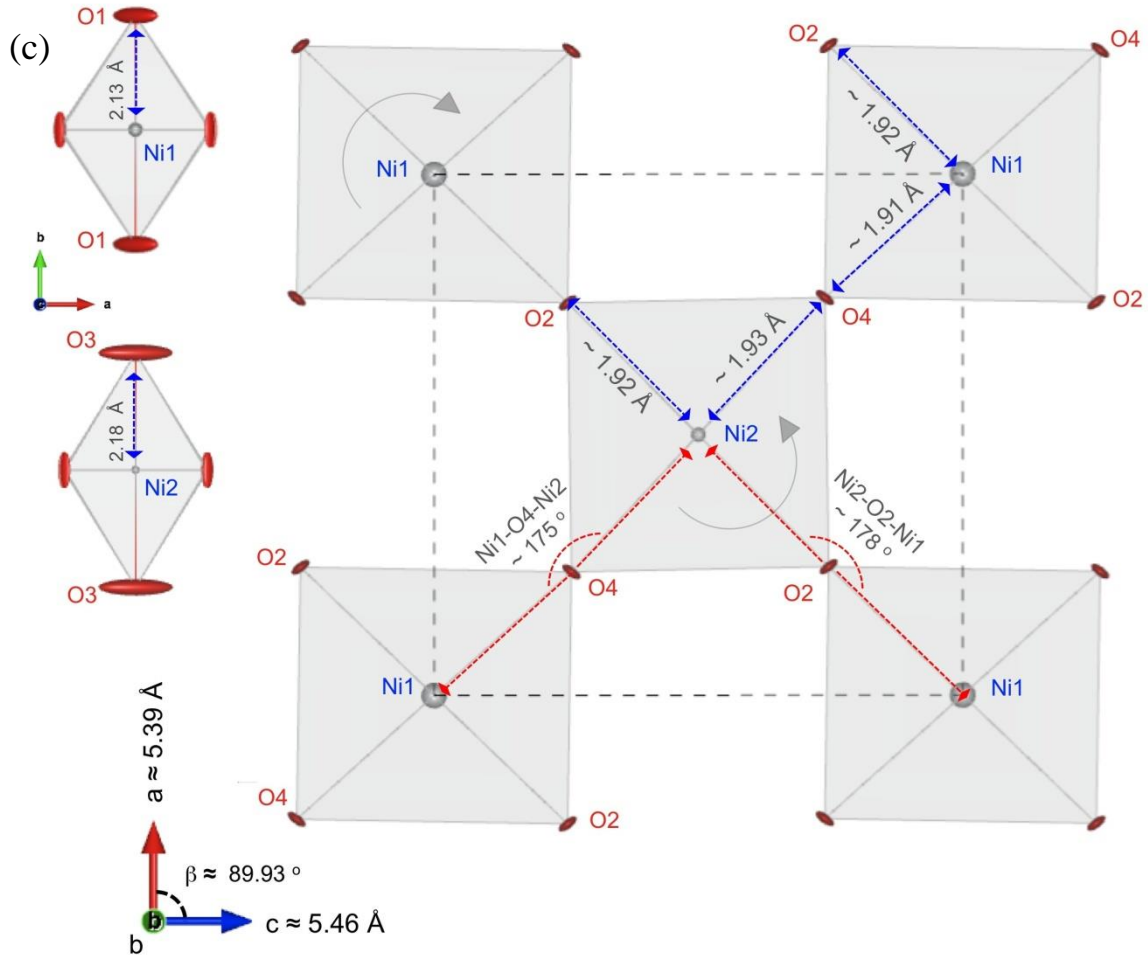


**Figure 3: a) Average structure of  $\text{Pr}_2\text{NiO}_{4.25}$  at RT along  $c$ -axis, b) view along the  $b$  axis evidencing the rotation along  $a, c$  plane, and c) again along  $b$ -axis showing schemes of octahedra tilts at the origin of monoclinic distortion.**

### 3.2.2. Discussion of distortion details in PNO structure

It is well known that  $\text{Ln}_2\text{NiO}_{4+\delta}$  type materials crystallize at high temperature under air in a tetragonal structure [15]. Indeed, at high temperature, the oxygen atoms mobility should be high leading possibly to the more symmetrical tetragonal structure. In the high temperature tetragonal phase of PNO, all Ni- $\text{O}_{\text{eq}}$  ( $\text{O}_{\text{eq}}$ : equatorial oxygen) bonds have the same length in the  $\text{NiO}_4$  square plane, whereas the longer Ni- $\text{O}_{\text{ap}}$  ( $\text{O}_{\text{ap}}$ : apical oxygen) bonds distort the  $\text{NiO}_6$  octahedra and thus the unit cell in a direction perpendicular to the  $\text{NiO}_4$  sheets (unit cell direction  $b$  for structures described here). In the tetragonal phase all  $\text{O}_{\text{eq}}\text{-Ni-O}_{\text{eq}}$  bond angles are equal to  $90^\circ$ . At RT, normally the movement of oxygen atoms is frozen and leads to rigid orthorhombic structure. Moving from high temperature tetragonal phase to a RT  $Fm\bar{3}m$  orthorhombic phase, all Ni- $\text{O}_{\text{eq}}$  bonds have the same length and the longer Ni-

$O_{ap}$  bonds from the tetragonal distortion are maintained. However, at RT the  $O_{eq}$ -Ni- $O_{eq}$  bond angles deviate from  $90^\circ$ , leading to additional orthorhombic distortion. Comparing the different possible orthorhombic  $Fmmm$  and  $Bmab$  models, a  $Bmab$  model would permit additional distortion caused by the tilting of octahedron due to oxygen displacements out of the  $NiO_4$  plane. However, in our diffraction data we find no experimental evidence for long range  $Bmab$  type tilting. But the refined ellipsoidal shaped oxygen anisotropic thermal parameters in the  $C2/m$  model are compatible with local range tilting and/or a long range modulated tilt distortion, which is not described in the refined monoclinic unit cell. We note that there is the possibility of a structural modulation in Pr-rich LPNO phases, where this monoclinic structure describes an average unit cell, as already reported for PNO single crystal [30]. This possibility is discussed later in the text, and may explain additional weak unindexed reflections observed in HR-SPD and HRTEM-ED.

Now approaching from an  $Fmmm$  orthorhombic to a  $C2/m$  monoclinic structure, an additional distortion appears caused by the deviation in the bond angles Ni1-O2-Ni2 and Ni1-O4-Ni2 from  $180^\circ$ , leading to a relative “twisting” of octahedron on axes parallel to the long unit cell direction, as indicated by grey arrows in **Figure 3c**. In the monoclinic cell two kinds of apical ( $O_{ap1}$ ,  $O_{ap3}$ ) and equatorial ( $O_{eq2}$ ,  $O_{eq4}$ ) oxygen can be evidenced **Figure 3c**. It can be noticed that Ni1-O2, Ni1-O4 and Ni1-O1 bonds are no longer exactly the distance as the Ni2-O2, Ni2-O4 and Ni2-O3 bonds, respectively. This results in different octahedra for the two Ni sites, which includes deformation along  $NiO_4$  plane and more significantly varying Ni1-O1 and Ni2-O3 bond length in the long axis unit cell direction. These distortions and changes in bond length are possibly due to two kinds of static distortion: *a*) the twist of octahedra releasing the strain between the perovskites and rock salt layers and/or *b*) the steric repulsion with interstitial oxygen ( $O_i$ ). The difference in the bond lengths leads to the distortion in the unit cell. From structural analysis (**Figure 3b, c**), the oxygen atoms show diffuse ellipsoid shape and indeed apical oxygen atoms seem more diffused than equatorial oxygen ones. At RT the origin of this diffuse apical oxygen  $O_{ap}$  is not thermal but possibly due to the static distortion effects and/or subtle structural modulations in Pr-rich LPNO phases as discussed above.

Despite the good statistical fit of our refined PNO  $C2/m$  monoclinic structure to the combined TOF-NDP and HR-SPD data, a number of minor intensity - but clearly visible - peaks remain unindexed in the synchrotron X-ray data refinement (see for instance **Figure 5c** later in the text). A very few number of unindexed peaks were observed as well in the neutron

data refinement. Such reflections are not associated with the monoclinic unit cell or any impurities. Demourgues *et al.* have proposed a monoclinic model for the homologous compound  $\text{La}_2\text{NiO}_{4.25}$  [31, 32], (space group  $C2$ ,  $a = 13.832$ ,  $b = 10.930$ ,  $c = 10.912$  Å and  $\beta = 113.31^\circ$ , four times larger than the orthorhombic unit cell). In this case also it was not possible to index all the above mentioned super-lattice peaks using smaller lattice. Hence, those unindexed reflections should be ascribed to another phenomenon such as an incommensurate structural modulation, probably associated with an ordered tilt scheme of the  $\text{NiO}_6$  octahedra and/or an occupational modulation of interstitial oxygen atoms ( $\text{O}_{int}$ ) as proposed previously by Allançon *et al.* [23].

### 3.2.3. Variation of extra peaks

To better understand the extra peaks observed in PNO diffraction data, we examined how they change as a function of interstitial oxygen amount and temperature, and used other probes like HRTEM.

#### *Variation of extra peaks with $\delta$ -value*

The variation of XRD patterns measured on different samples of PNO, namely: as prepared powder under air (cooling with  $2^\circ\text{C}$  from  $1200^\circ\text{C}$ ), slow cooled under air (cooling with  $1^\circ\text{C}$  from  $1200^\circ\text{C}$ ) and cooled under argon (cooling with  $2^\circ\text{C}$  from  $1000^\circ\text{C}$ ), are compared in **Figure 4**. Their  $\delta$ -values were determined by iodometry and TGA and found to be 0.25, 0.25 and 0.19, respectively.

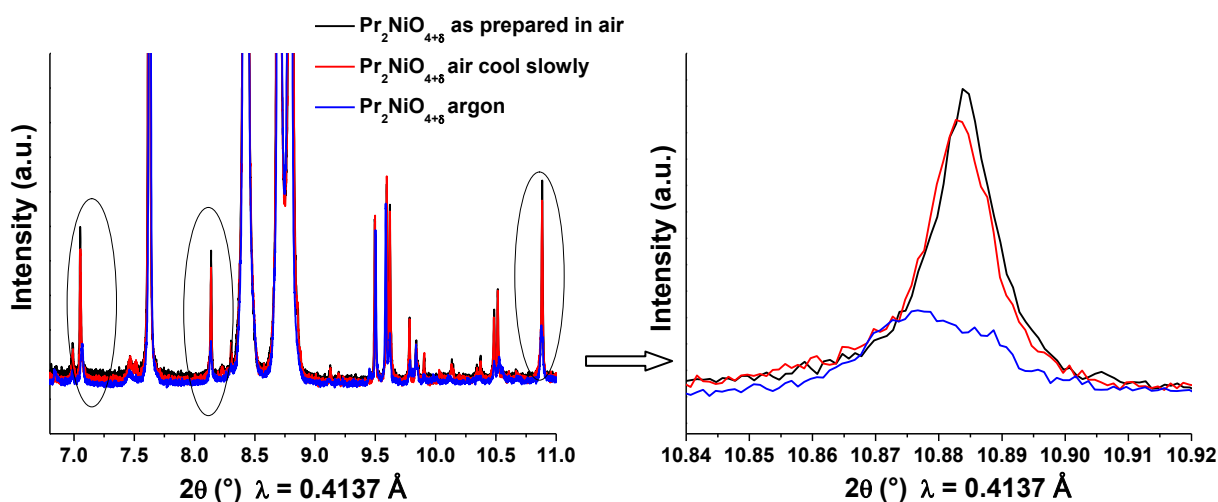


**Figure 4:** X-ray diffraction patterns for  $\text{Pr}_2\text{NiO}_{4+\delta}$  for as prepared powder in air (black), slowly cooled in air (red) and cooled in argon (blue). The magnification in  $10.84 - 10.92^\circ$  region is shown on the right side.

The slow cooled under air and as prepared samples do not show a significant change in the extra peaks intensity, shape and position. These samples have approximately the same oxygen  $\delta$  value. The extra peaks are also evidenced in the sample prepared under argon but the intensities are much smaller compared to air prepared samples.

In order to understand the origin of the extra peaks, a HRTEM analysis was performed on  $\text{Pr}_2\text{NiO}_{4.25}$  powders at room temperature as well as at low temperature (100 K) (**Figure 5**).

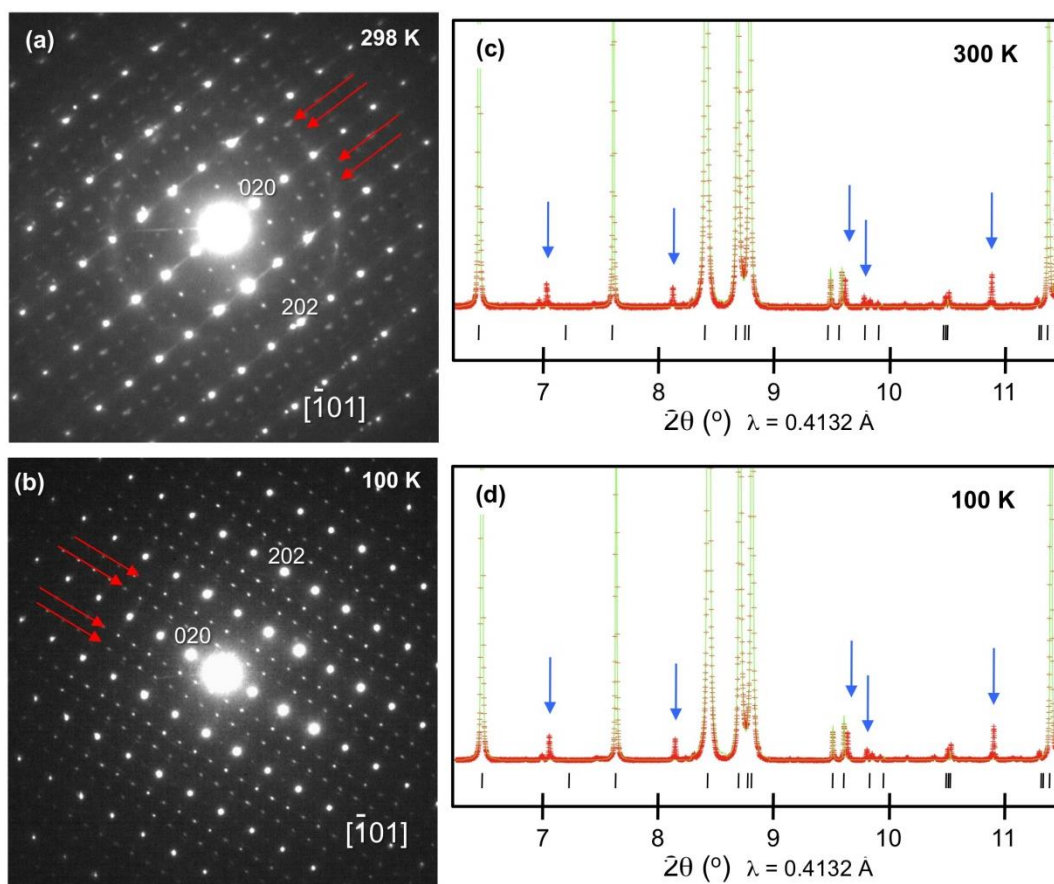


**Figure 5: HR-TEM electron diffraction (a, b) and HR-SPD (c, d) patterns of  $\text{Pr}_2\text{NiO}_{4.25}$  at 300 and 100 K. The red arrows in TEM-electron diffraction pattern and Blue arrow in HR-SPD show the unindexed reflections.**

A careful examination of these images shows the existence of several extra spots at RT as well as at 100 K, as shown in **Figure 5**. These extra spots in HRTEM-ED are not indexed by the main unit cell, and may be connected to the same modulation previously discussed, causing the extra reflections in the HR-SPD.

### 3.2.4. Synchrotron diffraction vs. Temperature for $\text{Pr}_2\text{NiO}_{4.25}$ from 450-100 K

High resolution synchrotron diffraction at “low” temperatures, *i.e.* XRD vs T (*in situ*), were performed with the aim to check the phase stability and most importantly the evolution of unindexed peaks in the low temperature range ( $100 < T \text{ (K)} < 450$ ). **Figure 6** shows the contour plot of  $\text{Pr}_2\text{NiO}_{4.25}$  synchrotron data, in which it is confirmed that the extra peaks appeared for all “low temperature” data. From 100 K to 450 K, a slight shift in the peaks is observed which is associated to the lattice expansion with increasing temperature.

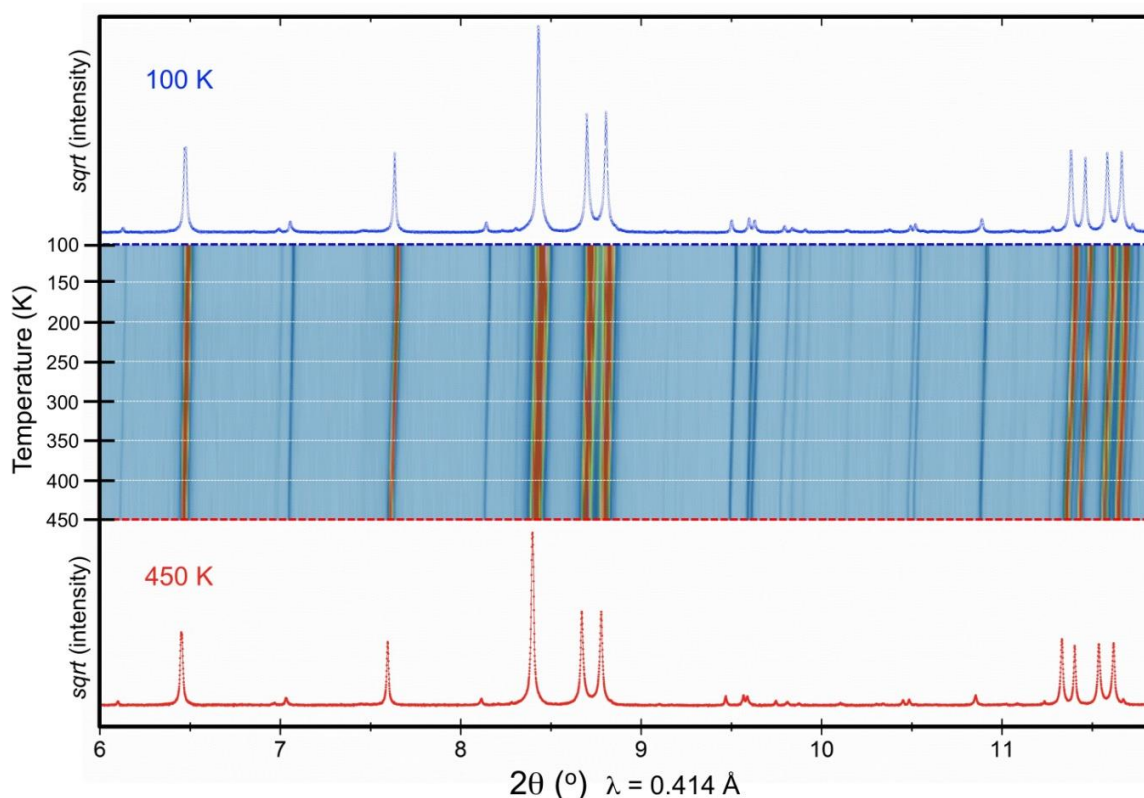


**Figure 6: Contour plot of  $\text{Pr}_2\text{NiO}_{4.25}$  HR-SPD data in the temperature range ( $100 \leq T \text{ (K)} \leq 450$ ).**

The  $\text{Pr}_2\text{NiO}_{4.25}$  phase is highly stable throughout the low temperature range. The structure always keeps monoclinic symmetry and is indexed with  $C2/m$  space group. The thermal variation of refined lattice parameters is shown in **Figure 7**. All the lattice parameters increase with increasing temperature from 100 K to 450 K, showing almost linear variation.

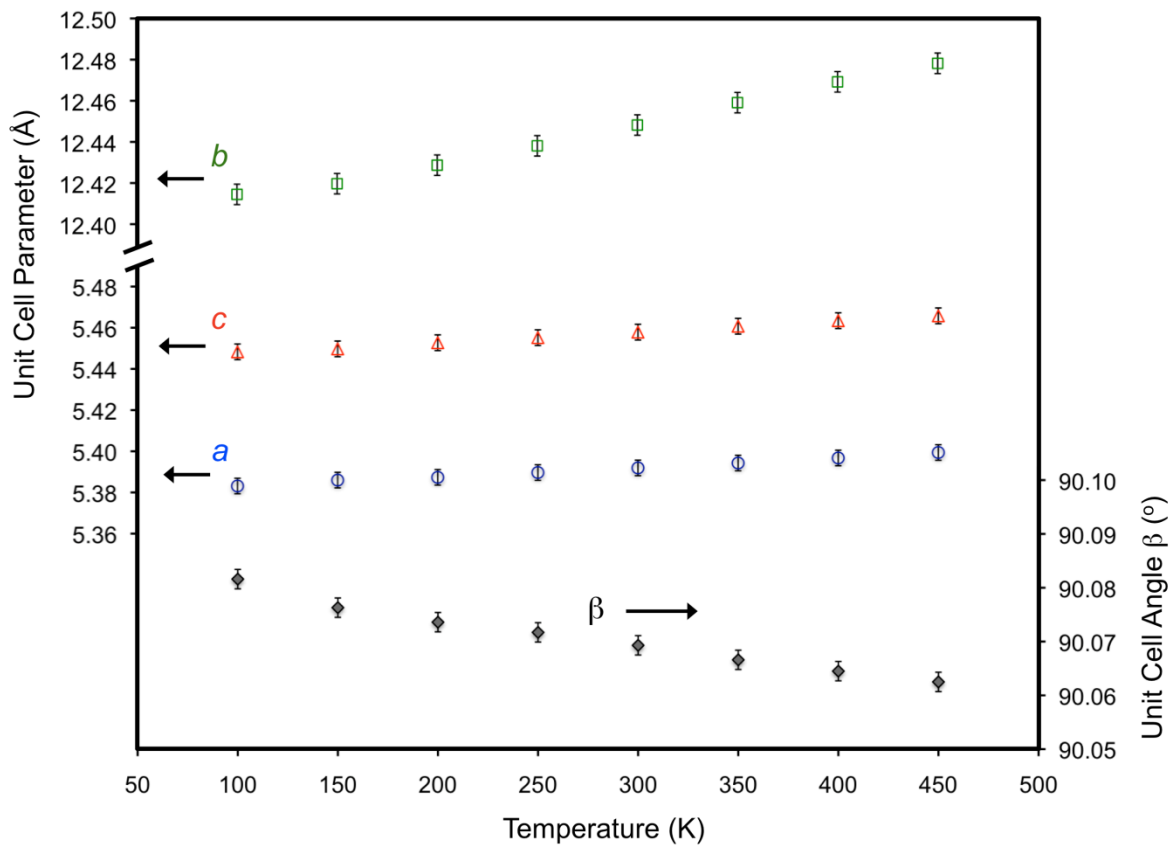


**Figure 7: Variation of lattice parameters  $a$ ,  $b$ ,  $c$  and  $\beta$  as a function of  $T$  ( $100 < T$  (K) < 450) for  $\text{Pr}_2\text{NiO}_{4.25}$ .**

Consequently, the volume of unit cell increases throughout the temperature range from 100 to 450 K and is connected with the lattice expansion with temperature. The monoclinic distortion associated with the lattice is also dependent on temperature: a smooth decrease in distortion angle is observed from 100 to 450 K temperature range. It means that the structure is more distorted at lower temperature than at RT.

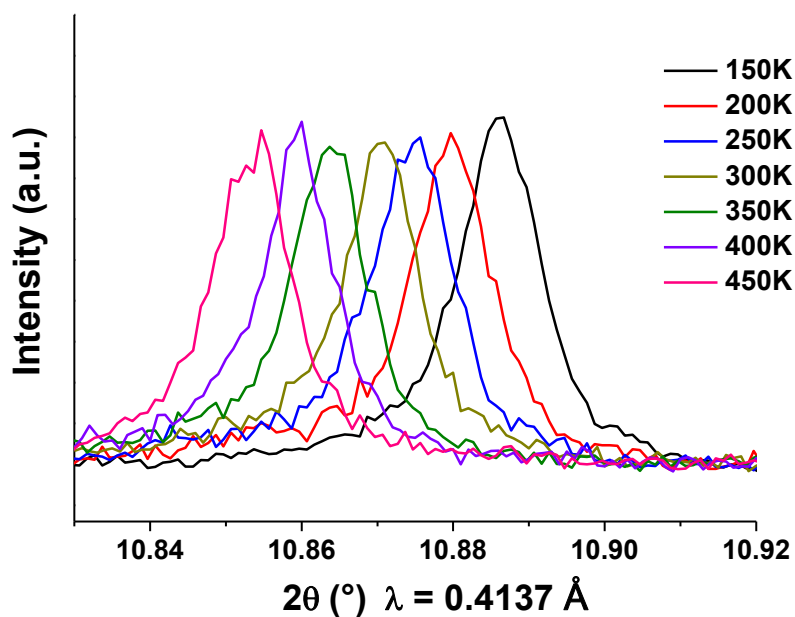


**Figure 8: Variation of one extra non monoclinic indexed peak in  $\text{Pr}_2\text{NiO}_{4.25}$  as a function of temperature.**

The variation of one extra non monoclinic indexed peak with temperature is shown in **Figure 8**. All the extra peaks are shifted towards lower angle by increasing temperature from 100 K to 450 K, while keeping the same intensity with temperature. It means that any possible incommensurate structural modulation existing in PNO is maintained throughout the temperature range studied here.

As an intermediate conclusion, the above study confirms that  $\text{Pr}_2\text{NiO}_{4.25}$  crystallizes with monoclinic structure with  $C2/m$  symmetry, with a possibility of a more complicated tilting or distorted modulation, of which the study is beyond the scope of our work. With this new insight about the structure of the PNO end member, we can now consider to study the all LPNO series.

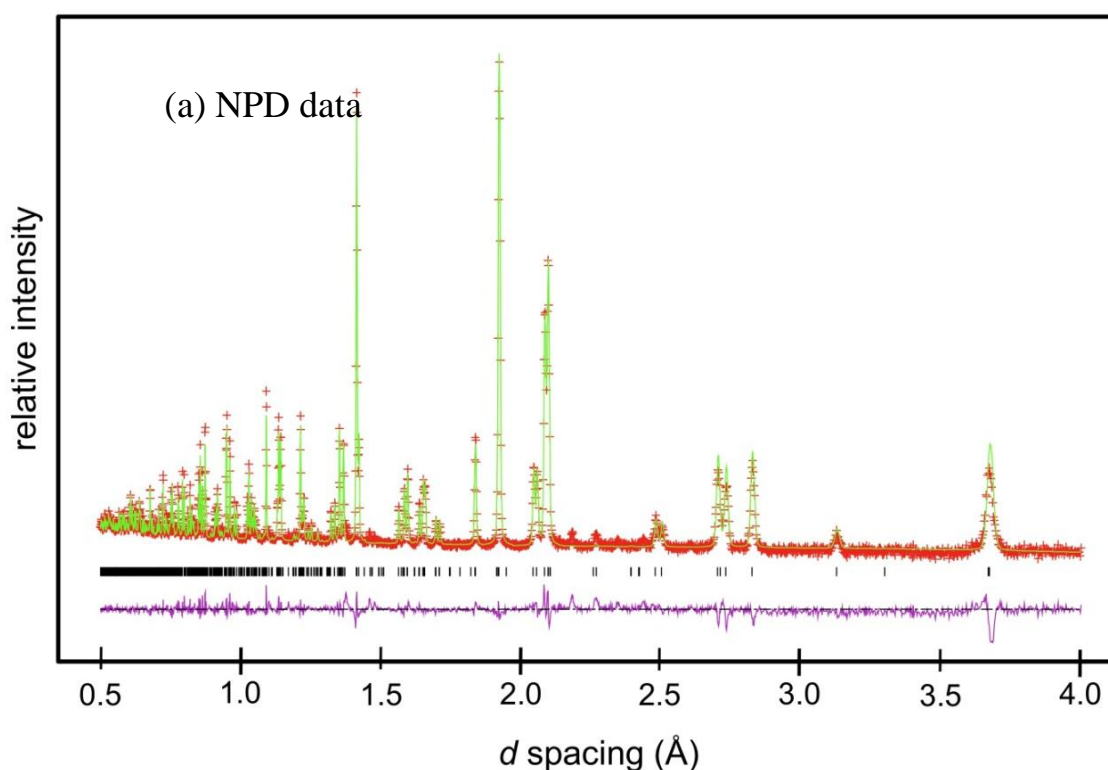
### 3.3. Pr-rich LPNO mixed nickelates

A careful investigation of high resolution synchrotron data revealed that all examined Pr-rich compositions ( $x = 2, 1.5$  and  $1.2$ ) exhibit a monoclinic structure and their distortion angle varies with the A-site cation substitution. Rietveld refinements of all Pr-rich phases described below were performed using an equivalent joint refinement approach and considering a similar structural model as discussed above for PNO.

### 3.3.1. Joint synchrotron and neutron data refinement of $\text{La}_{0.5}\text{Pr}_{1.5}\text{NiO}_{4+\delta}$

The crystal structure of  $\text{La}_{0.5}\text{Pr}_{1.5}\text{NiO}_{4+\delta}$  was refined using  $C2/m$  space group with a monoclinic structure using the same approach described above for PNO. The refined parameters obtained from the joint refinement are listed in **Table 3**. In the refined structure both Pr and La cations homogeneously occupy equivalent sites and are appropriately constrained when refined (*e.g.* same  $x$ ,  $y$ ,  $z$ ,  $U$ ). Test refinements found no statistical evidence in these data for preferred Pr/La site occupancy or a meaningful deviation from the target Pr/La stoichiometry, and thus La/Pr occupancies were fixed at 0.75/0.25 for the final refinement. The observed, calculated and difference plots for the jointly refined TOF-NPD and HR-SPD data are shown in **Figures 9a** and **9b**, respectively. The final refined lattice parameters are  $a = 5.4064(2) \text{ \AA}$ ,  $b = 12.5113(3) \text{ \AA}$ ,  $c = 5.4649(3) \text{ \AA}$  and  $\beta = 89.953(3)^\circ$  with a combined  $\chi^2 = 13.66$  and  $R_{\text{wp}} = 10.92 \%$ .

As observed for PNO, in the HR-SPD data refinement of  $\text{La}_{0.5}\text{Pr}_{1.5}\text{NiO}_{4+\delta}$ , several non-indexed peaks are also detected, and they may possibly be explained by the same conclusion discussed for PNO, for example by an incommensurate structural modulation.



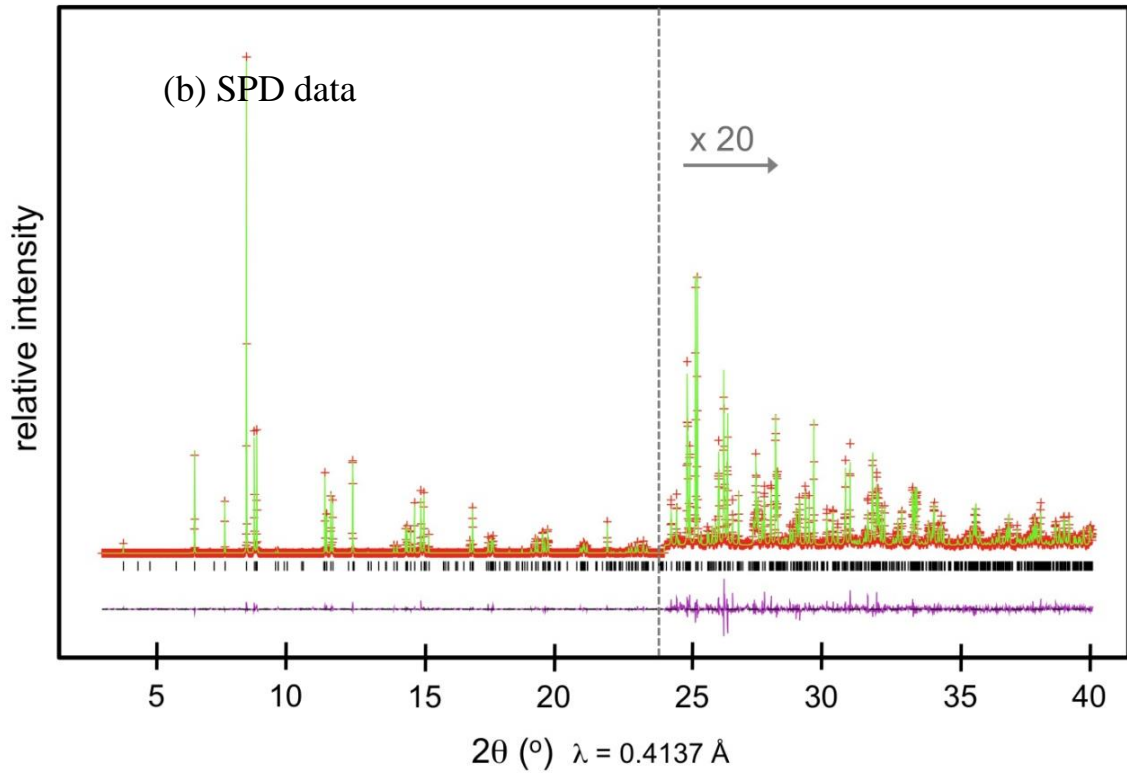


**Figure 9: Joint neutron (a) and synchrotron (b) powder diffraction data refinement of  $\text{La}_{0.5}\text{Pr}_{1.5}\text{NiO}_{4+\delta}$  using  $C2/m$  space group, recorded at 25 °C. (+) represent experimental data points, solid line refined data fit. The vertical sticks are  $\text{La}_{0.5}\text{Pr}_{1.5}\text{NiO}_{4+\delta}$  monoclinic phase.**

**Table 3: Refined parameters from joint refinement of  $\text{La}_{0.5}\text{Pr}_{1.5}\text{NiO}_{4+\delta}$ ,  $\text{La}_{0.8}\text{Pr}_{1.2}\text{NiO}_{4+\delta}$  and  $\text{La}_{1.4}\text{Pr}_{0.6}\text{NiO}_{4+\delta}$**

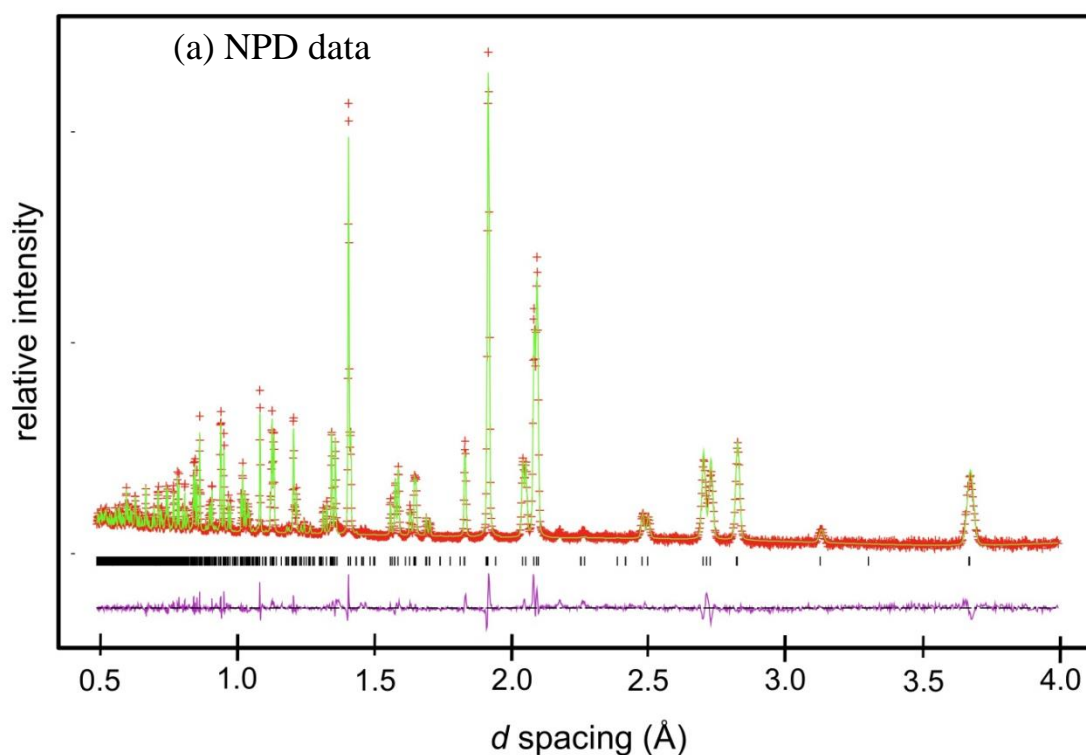
<i>Parameters</i>	$\text{La}_{0.5}\text{Pr}_{1.5}\text{NiO}_{4+\delta}$	$\text{La}_{0.8}\text{Pr}_{1.2}\text{NiO}_{4+\delta}$	$\text{La}_{1.4}\text{Pr}_{0.6}\text{NiO}_{4+\delta}$ (biphasic)	
<i>Space group</i>	$C2/m$	$C2/m$	<i>Pr-rich: Fmmm</i>	<i>La-rich: Fmmm</i>
<i>a</i> (Å)	5.4064(2)	5.4148(4)	5.4376(2)	5.4537(2)
<i>b</i> (Å)	12.5113(3)	12.5461(3)	12.6220(2)	12.6210(3)
<i>c</i> (Å)	5.4649(3)	5.4691(3)	5.4699(2)	5.4559(3)
$\beta$ (°)	89.953(3)	89.974(2)	90	90
<i>Site (Pr/La)1</i>				
<i>x, y, z</i>	0, 0.359(1), 0	0, 0.359(8), 0	0, 0.360(3), 0	0, 0.359(8), 0
<i>U-iso</i> × 100	0.648(4)	0.547(6)	0.789(5)	0.789(5)
<i>Occupancy</i>	0.25/0.75 (La/Pr)	0.4/0.6 (La/Pr)	0.7/0.3 (La/Pr)	0.7/0.3 (La/Pr)
<i>Site (Pr/La)2</i>				
<i>x, y, z</i>	0, 0.139(9), 0.5	0, 0.140(1), 0.5	--	--

<i>U-iso</i> × 100	0.648(4)	0.617(3)	--	--
<i>Occupancy</i>	0.75/0.25 (La/Pr)	0.4/0.6 (La/Pr)	--	--
<b>Site Ni1</b>				
<i>x, y, z</i>	0, 0, 0	0, 0, 0	0, 0, 0	0, 0, 0
<i>U-iso</i> × 100	0.206(7)	0.443(8)	0.512(2)	1.614(7)
<i>Occupancy</i>	1	1	1	1
<b>Site Ni2</b>				
<i>x, y, z</i>	0, 0.5, 0.5	0, 0.5, 0.5	--	--
<i>U-iso</i> × 100	0.206(7)	0.443(8)	--	--
<i>Occupancy</i>	1	1	--	--
<b>Site O1</b>				
<i>x, y, z</i>	0, 0.167(7), 0	0, 0.178(1), 0	0, 0.174(7), 0	0, 0.168(2), 0
<i>U-iso</i> × 100	4.221(7)	9.633(2)	1.933(7)	4.903(4)
<i>Occupancy</i>	1	1	1	1
<b>Site O2</b>				
<i>x, y, z</i>	0.745(4), 0, 0.248(6)	0.742(9), 0, 0.248(6)	0.25, 0, 0.25	0.25, 0, 0.25
<i>U-iso</i> × 100	0.494(5)	0.832(2)	1.093(8)	2.594(2)
<i>Occupancy</i>	1	1	1	1
<b>Site O3</b>				
<i>x, y, z</i>	0, 0.321(8), 0.5	0, 0.330(1), 0.5	--	--
<i>U-iso</i> × 100	4.221(7)	1.971(2)	--	--
<i>Occupancy</i>	1	1	--	--
<b>Site O4</b>				
<i>x, y, z</i>	0.258(1), 0, 0.255(7)	0.252(3), 0, 0.246(4)	--	--
<i>U-iso</i> × 100	0.494(5)	0.312(8)	--	--
<i>Occupancy</i>	1	1	--	--
<b>Site Oi</b>				
<i>x, y, z</i>	0.25, 0.25, 0.25	0.25, 0.25, 0.25	--	--
<i>U-iso</i> × 100	1.133(2)	--	--	--
<i>Occupancy</i>	0.09019	--	--	--
$\chi^2$	13.66	15.27	15.86	15.86
$R_{wp}$	10.92 %	11.29 %	11.68 %	11.68 %

### 3.3.2. $\text{La}_{0.8}\text{Pr}_{1.2}\text{NiO}_{4+\delta}$ joint refinement

The crystal structure of  $\text{La}_{0.8}\text{Pr}_{1.2}\text{NiO}_{4+\delta}$  is also well refined using a similar monoclinic  $C2/m$  model. The refined parameters obtained from the joint refinement are listed in **Table 3**. The model for Rietveld refinement was built on the basis of above reported atomic arrangement for PNO and  $\text{La}_{0.5}\text{Pr}_{1.5}\text{NiO}_{4+\delta}$ . The observed, calculated and difference for two patterns are shown in **Figures 10a** and **10b**. The lattice parameters are  $a = 5.4148(4) \text{ \AA}$ ,  $b = 12.5461(3) \text{ \AA}$ ,  $c = 5.4691(3) \text{ \AA}$  and  $\beta = 89.974(2)^\circ$  with  $\chi^2 = 15.27$  with  $R_{\text{wp}} = 11.29 \%$  for two histograms.

Once again, in the synchrotron data refinement, several extra weak unindexed peaks (not shown) are also detected and most probably are due to incommensurate structural modulation.



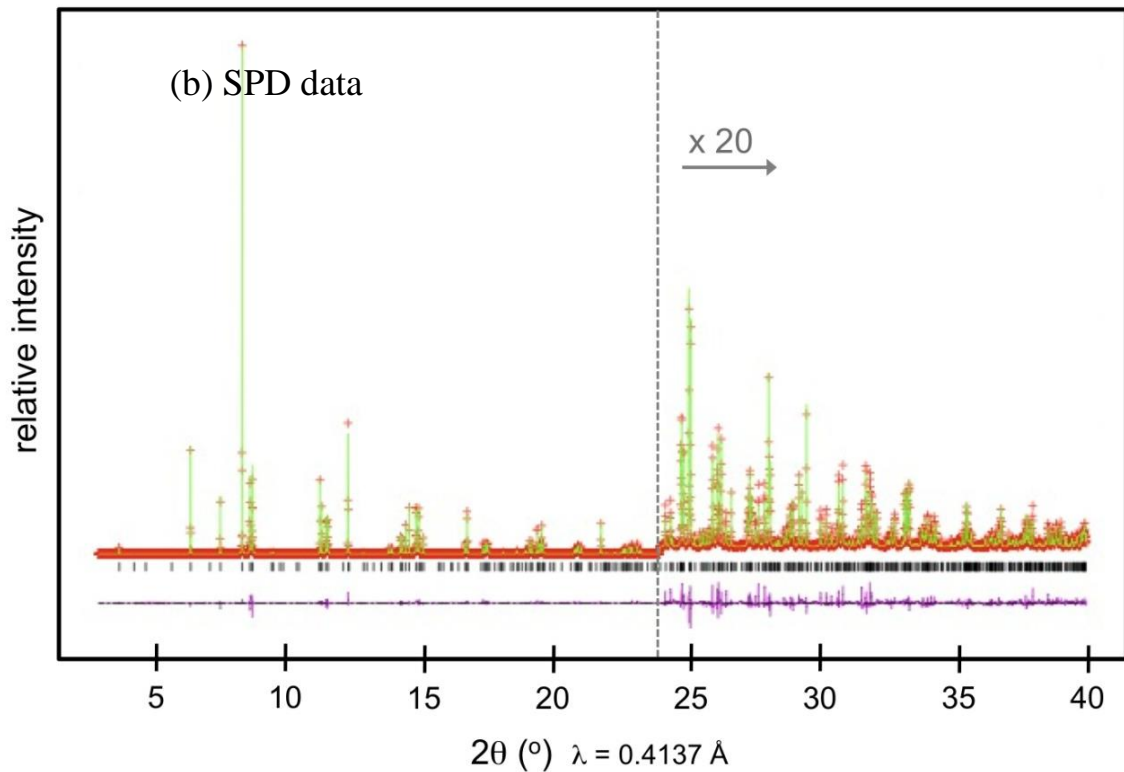


**Figure 10: Joint neutron (a) and synchrotron (b) powder diffraction data refinement of  $\text{La}_{0.8}\text{Pr}_{1.2}\text{NiO}_{4+\delta}$  using  $C2/m$  space group, recorded at  $25^\circ\text{C}$ . (+) represent experimental data points, solid line refined data fit. The vertical sticks are  $\text{La}_{0.8}\text{Pr}_{1.2}\text{NiO}_{4+\delta}$  monoclinic phase.**

Comparing  $\text{La}_{0.8}\text{Pr}_{1.2}\text{NiO}_{4+\delta}$  and  $\text{La}_{0.5}\text{Pr}_{1.5}\text{NiO}_{4+\delta}$  with PNO, the main difference appears in the distortion angle and in the intensity of extra peaks. The substitution on A-site cation (*i.e.* replacing Pr with La) affects the structure. Indeed, the  $\text{Pr}^{3+}$  cation size is smaller than that of  $\text{La}^{3+}$  cation ( $r(\text{Pr}^{3+}) = 1.126 \text{ \AA}$  and  $r(\text{La}^{3+}) = 1.16 \text{ \AA}$ ) [12], leading to a reduced distortion in the structure for compositions with lower Pr content. The intensity of extra peaks is also decreasing with reduced Pr-content.

### 3.3.3. Variation of $\beta$ –angle for Pr-rich phases

The variations of diffraction reflections split by the monoclinic distortion as well as the refined monoclinic distortion angle  $\beta$  are illustrated in **Figure 11** for samples with various Pr-rich compositions. The distortion angle decreases from PNO *i.e.*  $90.07^\circ$  down to  $90.03^\circ$  for  $\text{La}_{0.8}\text{Pr}_{1.2}\text{NiO}_{4+\delta}$  with decreasing the Pr-content. It means that this distortion is highly dependent on A-site cation substitution.

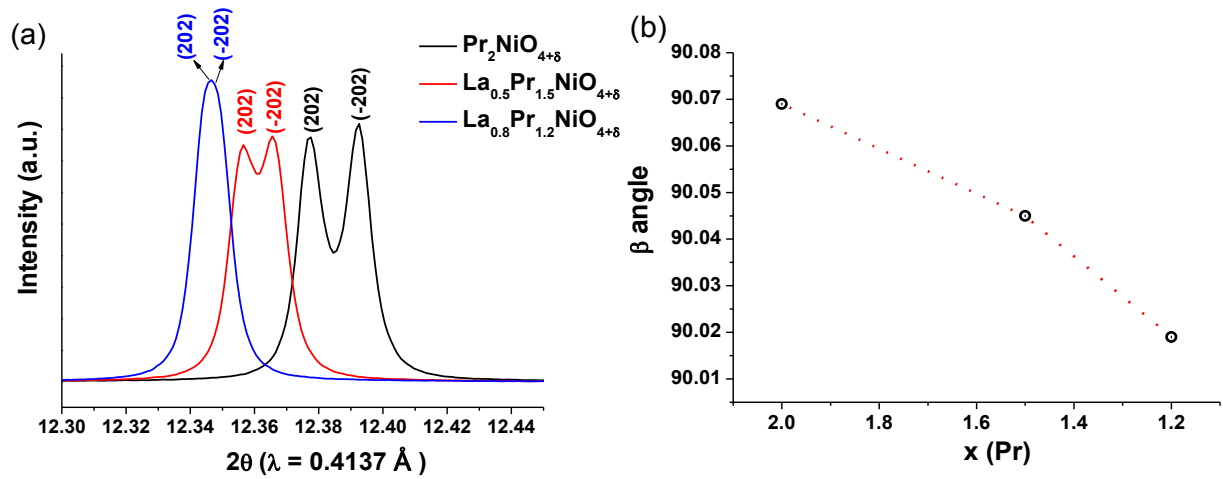


**Figure 11: Variation of (a) monoclinic distortion HR-SPD peaks and (b) the distortion angle, with  $x$  in Pr-rich LPNO phases.**

After the analysis of Pr-rich phases, the biphasic region was investigated using synchrotron diffraction data analysis.

### 3.3.4. Determination of biphasic zone

From the HR-SPD data analysis now it is clear that the examined Pr-rich phases for  $x = 2, 1.5$  and  $1.2$  exist with monoclinic structure with  $C2/m$  symmetry and the examined La-rich phases for  $x = 0$  and  $0.25$ , exist with an  $Fmmm$  orthorhombic structure. In between these single phase Pr rich monoclinic and La rich orthorhombic structure regions, a biphasic region exists from  $0.5 \leq x \leq 1.1$ , as shown in **Figure 12**.

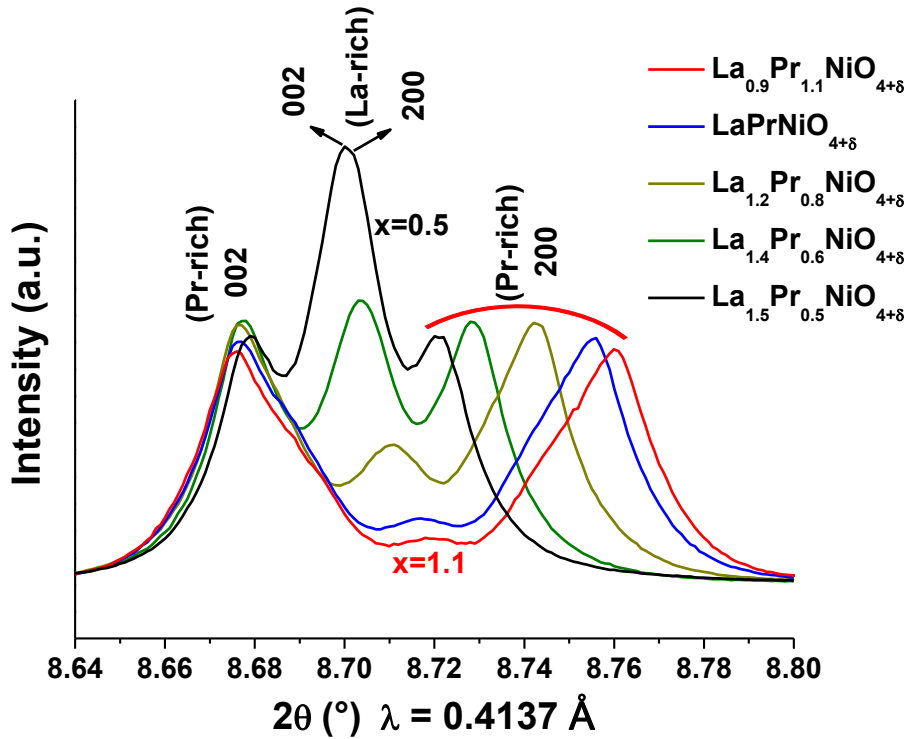


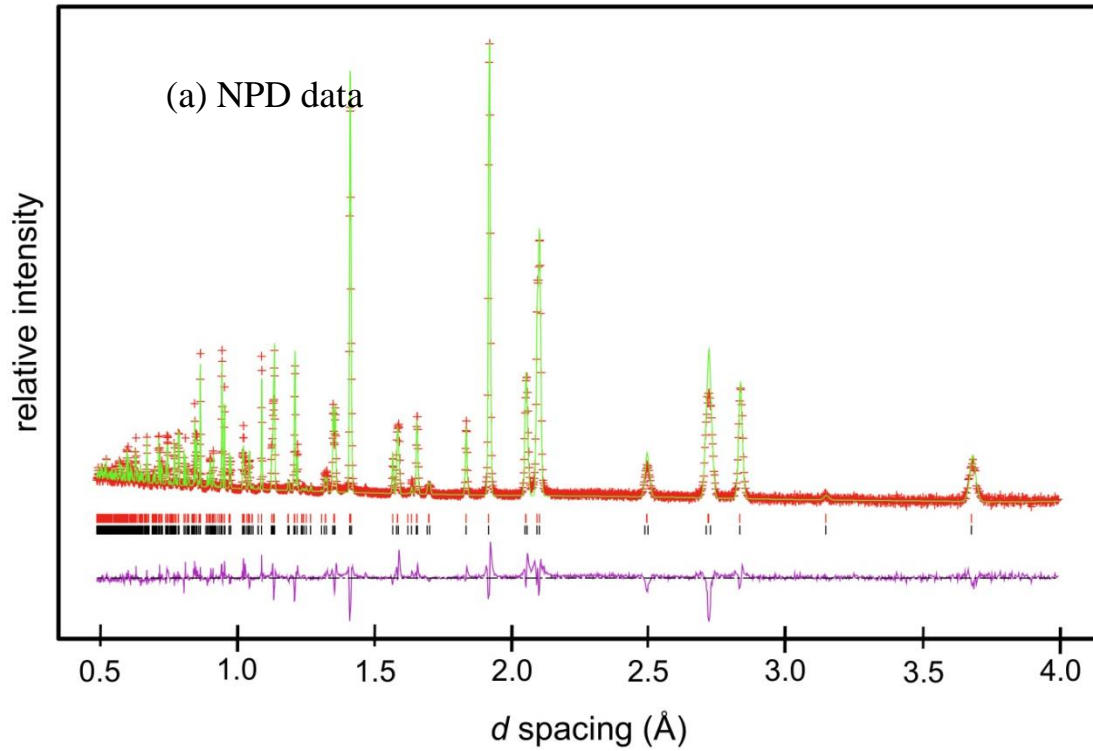
**Figure 12: HR-SPD data plots illustrating the co-existence of [(002) and (200)] family reflections from both Pr and La rich structures.**

In this region it was not possible to perform good refinement of the HR-SPD pattern using a single phase model (such as  $C2/m$ ,  $Fmmm$  or  $Bmab$ ). A satisfactory fit could only be achieved using a two-phase model. In this biphasic domain, no significant monoclinic distortion can be observed ( $\beta < 90.02^\circ$ ) and/or because of overlapping reflections with the mixed phases. Nor was any evidence found for extra reflections associated with long range  $Bmab$  tilting. Therefore, for the sake of simplicity and Rietveld refinement stability the biphasic refinements were performed considering two orthorhombic phases with  $Fmmm$  space group and in this way a satisfactory fit to the data is obtained for all the samples of biphasic region.

### 3.3.5. $\text{La}_{1.4}\text{Pr}_{0.6}\text{NiO}_{4+\delta}$ joint refinement

The  $\text{La}_{1.4}\text{Pr}_{0.6}\text{NiO}_{4+\delta}$  ( $x = 0.6$ ) composition belongs to the biphasic domain in between pure La- and pure Pr-rich phases ( $0.5 \leq x \leq 1.1$ ). It was impossible to refine the biphasic composition using single space group. The crystal structure of  $\text{La}_{1.4}\text{Pr}_{0.6}\text{NiO}_{4+\delta}$  was then refined using two  $Fmmm$  space groups with different orthorhombic structure. The refined parameters obtained from the joint refinement are listed in **Table 3**. In the two existing phases, one is for La-rich and the other one is Pr-rich phase. The observed, calculated and

difference for NPD and SPD patterns are shown in **Figure 13**. The lattice parameters are  $a = 5.4376(2) \text{ \AA}$ ,  $b = 12.6220(2) \text{ \AA}$ ,  $c = 5.4699(2) \text{ \AA}$ ,  $V = 375.5 \text{ \AA}^3$  and  $a = 5.4537(2) \text{ \AA}$ ,  $b = 12.6210(3) \text{ \AA}$ ,  $c = 5.4559(3) \text{ \AA}$ ,  $V = 375.9 \text{ \AA}^3$  for Pr-rich and La-rich phases respectively, with  $\chi^2 = 15.86$  with  $R_{\text{wp}} = 11.68 \%$  for two histograms. In addition, extra peaks are not detected for  $\text{La}_{1.4}\text{Pr}_{0.6}\text{NiO}_{4+\delta}$ .



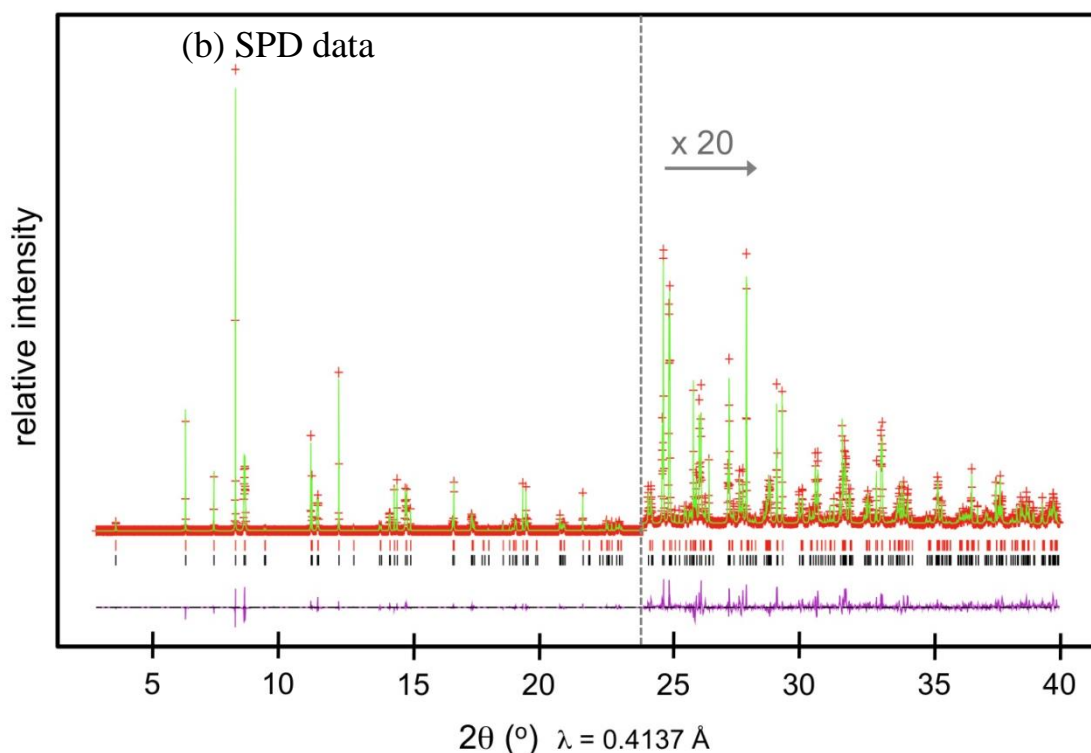


**Figure 13: Joint neutron (a) and synchrotron (b) powder diffraction data refinement of  $\text{La}_{1.4}\text{Pr}_{0.6}\text{NiO}_{4+\delta}$  using  $Fmmm$  space group, recorded at 25 °C. (+) represent experimental data points, solid line refined data fit. The upper markers (red sticks) are Pr-rich phase, lower markers (black sticks) are La-rich phase.**

Further it was tried to quantify Pr- and La-rich phases using the Rietveld refinements of HR-SPD data. The percentage of each phase is given in **Table 4**.

**Table 4: Percentage of Pr- and La-rich phases in biphasic domain**

Samples	Pr-rich phase (%)	La-rich phase (%)
$\text{La}_{1.5}\text{Pr}_{0.5}\text{NiO}_{4+\delta}$	58	42
$\text{La}_{1.4}\text{Pr}_{0.6}\text{NiO}_{4+\delta}$	70	30
$\text{LaPrNiO}_{4+\delta}$	80	20
$\text{La}_{0.9}\text{Pr}_{1.1}\text{NiO}_{4+\delta}$	93	7

Interestingly, in all compositions the percentage of Pr-rich phase is more than La-rich one. The percentage of Pr-rich phase is decreased with decreasing Pr-content. For example,  $\text{La}_{1.5}\text{Pr}_{0.5}\text{NiO}_{4+\delta}$  (with 25 % of Pr) contains of 58 % Pr- rich and 42 % of La-rich phases.

Finally, the variation of  $\text{La}_{2-x}\text{Pr}_x\text{NiO}_{4+\delta}$  phases with  $x$  is summarized as follows: the La rich phases exist only for  $(0.0 \leq x < 0.5)$ , then a biphasic domain  $(0.5 \leq x \leq 1.1)$  and Pr rich phases  $(1.1 < x \leq 2.0)$  are observed, as shown in **Table 5**.

**Table 5: Variation of all  $\text{La}_{2-x}\text{Pr}_x\text{NiO}_{4+\delta}$  phases with  $x$**

<p><b>La-rich side</b>  <math>(0 \leq x &lt; 0.5)</math>  <i>(Fmmm)</i>  <b>Orthorhombic</b></p>	<p><b>Biphasic region</b>  <math>(0.5 \leq x \leq 1.1)</math>  <i>(Fmmm + Fmmm)</i>  <b>Orthorhombic</b></p>	<p><b>Pr-rich side</b>  <math>(1.1 &lt; x \leq 2)</math>  <i>(C2/m)</i>  <b>Monoclinic</b></p>
--	--	--

### 3.3.6. Variation of lattice parameters

The lattice parameters of all the phases were determined by refinement of high resolution synchrotron data as well as joint refinement. Their variation as a function of  $x$  is reported in **Figures 14a** and **14b**. The substitution of La by Pr leads to a smooth decrease in each lattice parameters for all La- and Pr-rich phases. The lattice parameters  $a$  and  $c$  for La-rich phases smoothly decrease whereas for Pr-rich phases a separate increase in lattice parameter  $c$  and decrease in parameter  $a$  is evidenced. In the biphasic domain the lattice parameter  $c$  seems almost constant. The  $b$  parameter decreases throughout from  $x = 0$  to  $x = 2$ .

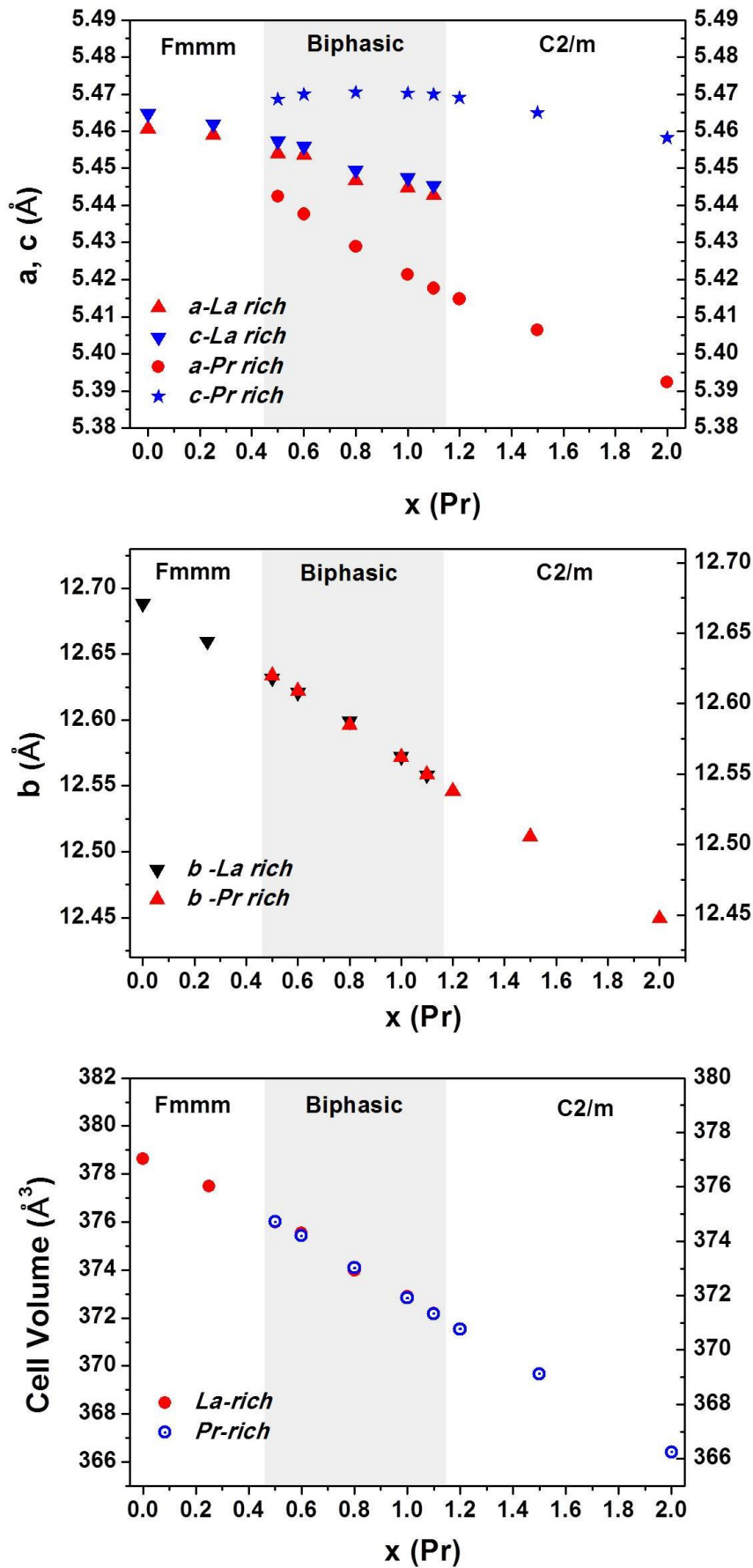
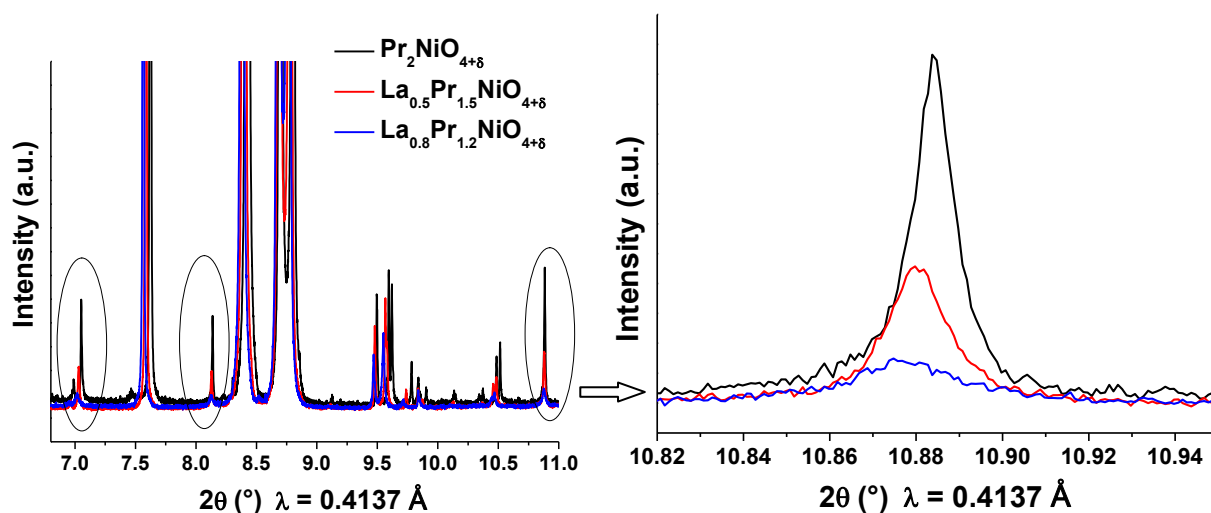


Figure 14: Variation of (a, b) lattice parameters and (c) volume, as a function of  $x$  for  $\text{La}_{2-x}\text{Pr}_x\text{NiO}_{4+\delta}$ .

The decrease of the cell parameters with increasing Pr-content is consistent with the variation of ionic radius ( $r(\text{Pr}^{3+}) = 1.126 \text{ \AA}$  and  $r(\text{La}^{3+}) = 1.16 \text{ \AA}$ ) [12], leading to the overall decrease in volume. An interesting point can be noted, *i.e.* the volume of both La- and Pr-rich phases is very similar in the biphasic domain, as shown in **Figure 14c**. This suggests both phases (La and Pr rich) have similar average A-site cation compositions for equivalent  $x$  values.

### 3.3.7. Variation of extra peaks with A-site cation substitution

The variation of weak extra unindexed peaks is also highly dependent on A-site cation substitution. First of all, these extra peaks are observed only for Pr-rich phases, while for La-rich and biphasic domain no extra peaks are evidenced. The evolution of unindexed peaks for Pr-rich phases ( $x = 2, 1.5$  and  $1.2$ ) is shown in **Figure 15**.



**Figure 15: HR-SPD pattern of Pr rich phases. (a) Circles highlight extra peaks that are not indexed in the  $C2/m$  unit cell and (b) Magnification of the  $10.82$  to  $10.94^\circ$  region.**

The intensity of extra peaks is the highest for PNO, it is decreased for  $\text{La}_{0.5}\text{Pr}_{1.5}\text{NiO}_{4+\delta}$  with decreasing Pr-content. In the case of  $\text{La}_{0.8}\text{Pr}_{1.2}\text{NiO}_{4+\delta}$  the intensities are almost negligible. Moreover, a shift in the unindexed peaks (towards the low  $2\theta$  values with La-substitution) is also noticed.

### 3.3.8. Effect of $\delta$ -value and A-site cation substitution

LPNO structural changes like cell volume and monoclinic distortion can be affected by two factors, a) the oxygen stoichiometry  $\delta$ -value and b) the A-site cation substitution. In order to better understand how these parameters modify the structure, the variation of the volume and distortion angle as a function of  $\delta$  is shown in **Figure 16**.

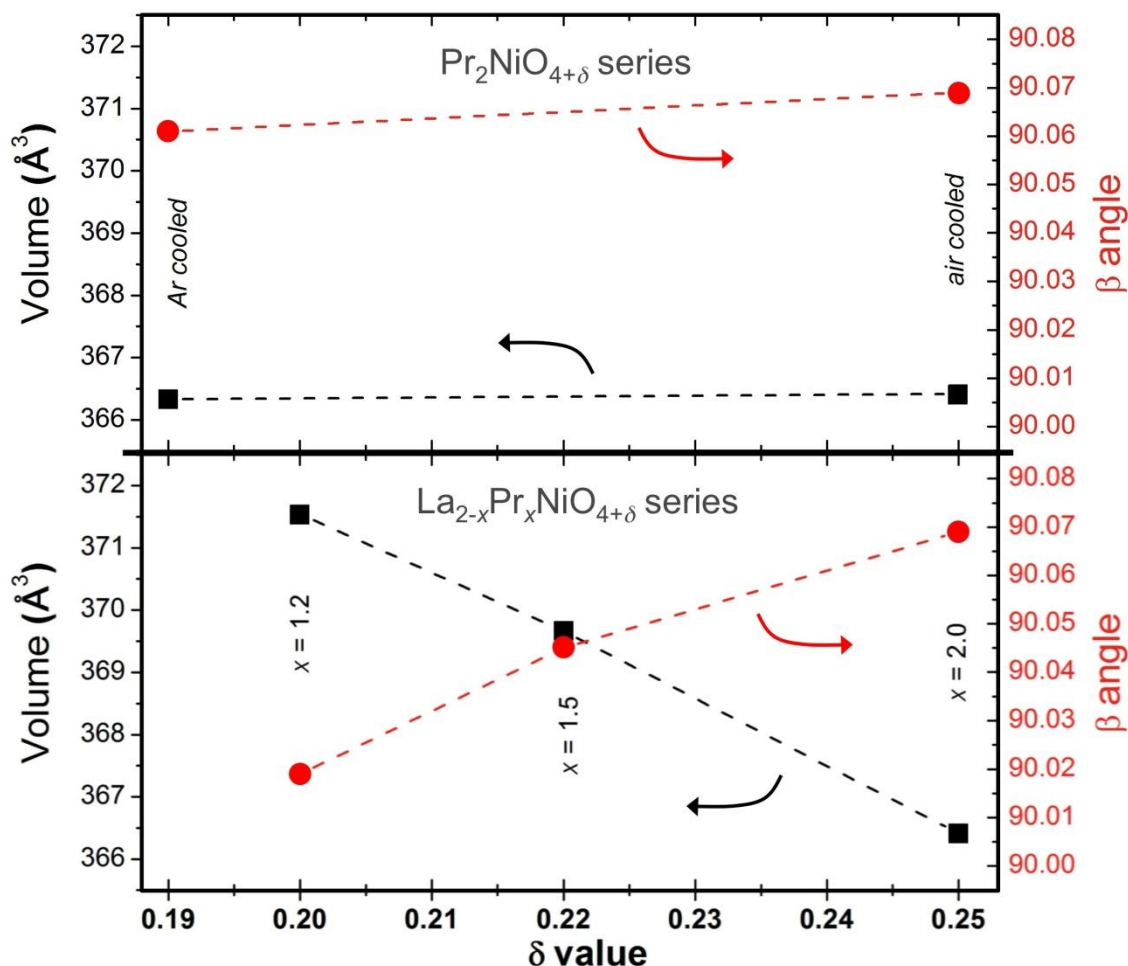


**Figure 16: Variation of volume and distortion angle as a function of  $\delta$  for Pr-rich phases.**

When the  $\delta$ -value is decreased in a fixed A-site cation composition (for example in  $\text{Pr}_2\text{NiO}_{4.25}$  (air) to  $\text{Pr}_2\text{NiO}_{4.19}$  (argon)), a very small decrease in the  $\beta$  angle (from 90.07 to 90.06) as well as in volume (from 366.41 to 366.30  $\text{\AA}^3$ ) is observed. On the contrary, in the case of a decrease of  $\delta$  by A-site cation substitution, *i.e.* by decreasing the Pr-content, a large increase in the cell volume and a large decrease in  $\beta$ - angle is observed. The volume of  $\text{Pr}_2\text{NiO}_{4.25}$  is 366.41  $\text{\AA}^3$ , and it increases to 369.66 and 371.54  $\text{\AA}^3$  for  $\text{La}_{0.5}\text{Pr}_{1.5}\text{NiO}_{4.22}$  and

$\text{La}_{0.8}\text{Pr}_{1.2}\text{NiO}_{4.20}$ , respectively. At the same time the distortion angle is decreased from  $90.07^\circ$  for  $\text{Pr}_2\text{NiO}_{4.25}$  to  $90.05^\circ$  and  $90.03^\circ$  for  $\text{La}_{0.5}\text{Pr}_{1.5}\text{NiO}_{4.22}$  and  $\text{La}_{0.8}\text{Pr}_{1.2}\text{NiO}_{4.20}$  respectively.

Finally it can be concluded that structural changes in the PLNO series such as volume and the distortion angle are more strongly affected by the overall A-site cation substitution than by the interstitial delta value.

## 4. Conclusions

$\text{La}_{2-x}\text{Pr}_x\text{NiO}_{4+\delta}$  ( $0.0 \leq x \leq 2.0$ ) phases were structurally characterized by synchrotron and neutron diffraction. Through this study it has been established that  $\text{Pr}_2\text{NiO}_{4+\delta}$  exists with a monoclinic structure and the model that provides the best fit to the diffraction data at room temperature is based on a  $C2/m$  unit cell. This structure is maintained from low temperature 100 K to 450 K.

The structural analysis of LPNO nickelates shows the existence of three different domains depending on  $x$  value (*i.e.* Pr content). One is related to the La-rich phases with  $Fmmm$  orthorhombic structure ( $0.0 \leq x < 0.5$ ), the second one is related to Pr-rich phases ( $1.1 < x \leq 2.0$ ) with  $C2/m$  monoclinic structure. In between ( $0.5 \leq x \leq 1.1$ ), a third one *i.e.* a biphasic domain is observed.

Few unindexed extra peaks with low intensity are observed on  $\text{Pr}_2\text{NiO}_{4+\delta}$  HR-SPD data, which could be related to incommensurate structure or modulation. The intensity of these unindexed peaks decreases with decreasing the Pr-content and the  $\delta$  value. Moreover, the additional unindexed extra peaks are not observed for La rich phases and in the biphasic domain.

The monoclinic distortion angle ( $\beta$ ) is observed only for Pr-rich phases, and it decreases with decreasing Pr-content. It is more highly dependent on A-site cation substitution than on the  $\delta$  value. In addition, the volume of unit cell does not show significant change by decreasing delta value but show larger changes with varying A-site cation substitution.

## References

- [1] H. Zhao, Q. Li, L. Sun, *Science China Chemistry*, 54 (2011) 898–910.
- [2] M. C. Tucker, L. Cheng, L. C. Dejonghe, *Journal of Power Sources*, 196 (2011) 8313–8322.
- [3] A. Tarançon, M. Burriel, J. Santiso, S. J. Skinner, J. A. Kilner, *Journal of Materials Chemistry*, 20 (2010) 3799–3813.
- [4] C. Sun, R. Hui, J. Roller, *Journal of Solid State Electrochemistry*, 14 (2010) 1125–1144.
- [5] S. Peng, Y. Wei, J. Xue, Y. Chen, H. Wang, *International Journal of Hydrogen Energy*, 38 (2013) 10552–10558.
- [6] A. J. Jacobson, *Chemistry of Materials*, 22 (2010) 660–674.
- [7] D. J. L. Brett, A. Atkinson, N. P. Brandon, S. J. Skinner, *Chemical Society Reviews*, 37 (2008) 1568–1578.
- [8] M. Yashima, N. Sirikanda, T. Ishihara, *Journal of the American Chemical Society*, 132 (2010) 2385–2392.
- [9] C. Ferchaud, J. C. Grenier, Y. Zhang-Steenwinkel, M. M. A. Van Tuel, F. P. F. Van Berkel, J. M. Bassat, *Journal of Power Sources*, 196 (2011) 1872–1879.
- [10] E. Boehm, J. M. Bassat, P. Dordor, F. Mauvy, J. C. Grenier, Ph. Stevens, *Solid State Ionics*, 176 (2005) 2717–2725.
- [11] V. Vibhu, A. Rougier, C. Nicollet, A. Flura, J. C. Grenier, J. M. Bassat, *Solid State Ionics*, 278 (2015) 32 – 37.
- [12] R. D. Shannon, *Acta Crystallogr. Sect.*, A32 (1976) 751.
- [13] D. J. Buttrey, P. Ganguly, J. M. Honig, C. N. R. Rao, R. R. Schartman, G. N. Subbanna, *Journal of Solid State Chemistry*, 74 (1988) 233–238.
- [14] C. Allançon, A. Gonthier-Vassal, J. M. Bassat, J. P. Loup, P. Odier, *Solid State Ionics*, 74 (1994) 239–248.
- [15] A. Flura, S. Dru, C. Nicollet, V. Vibhu, S. Fourcade, E. Lebraud, A. Rougier, J. M. Bassat, J. C. Grenier, *Journal of Solid State Chemistry*, 228 (2015) 189–198.
- [16] G. T. Kim, A. J. Jacobson, *Mater. Res. Symp. Proc.*, 972 (2007) 175–180.
- [17] S. Nishimoto, S. Takahashi, Y. Kameshima, M. Matsuda, M. Miyake, *Journal of the Ceramic Society of Japan*, 119 (3) (2011) 246–250.
- [18] V. Vibhu, J. M. Bassat, A. Flura, C. Nicollet, J. C. Grenier, A. Rougier, *ECS Transaction*, 68 (2015) 825–835.
- [19] J. Rodriguez-Carvajal, *Physica B: Physics of Condensed Matter*, 192 (1993) 55–69.
- [20] B. H. Toby, *Journal of Applied Crystallography*, 34 (2001) 210–213.
- [21] K. Momma, F. Izumi, *Journal of Applied Crystallography*, 44 (2011) 1272–1276.
- [22] R. Saez Puche, F. Fernandez, J. Rodriguez-Carvajal, J. L. Martinez, *Solid State Communications*, 72 (1989) 273–277.
- [23] C. Allançon, J. Rodriguez-Carvajal, M. T. Fernandez-Diaz, P. Odier, J. M. Bassat, J. P. Loup, J. L. Martinez, *Zeitschrift fur Physik B-Condensed Matter*, 100 (1996) 85–90.
- [24] S. J. Skinner, *Solid State Sciences*, 5 (2003) 419–426.
- [25] J. D. Jorgensen, B. Dabrowski, S. Pei, D. R. Richards, D. G. Hinks, *Physical Review B*, 40 (1989) 2187–2199.
- [26] P. Odier, C. Allançon, J. M. Bassat, *Journal of Solid State Chemistry*, 153 (2000) 381–385.
- [27] J. D. Sullivan, D. J. Buttrey, D. E. Cox, J. Hriljac, *Journal of Solid State Chemistry*, 94 (1991) 337–351.
- [28] M. T. Fernandez-Diaz, J. Rodriguez-Carvajal, J. L. Martinez, G. Fillion, F. Fernandez, R. Saez-Puche, *Zeitschrift fur Physik B-Condensed Matter*, 82 (1991) 275–282.
- [29] K. K. Singh, P. Ganguly, J. B. Goodenough, *Journal of Solid State Chemistry*, 52 (1984) 254–273.

- [30] M. Ceretti, O. Wahyudi, A. Cousson, A. Villesuzanne, M. Meven, B. Pedersen, J. M. Bassat, W. Paulus, *Journal of Materials Chemistry A*, 3 (2015) 21140–21148.
- [31] A. Demourgues, F. Weill, B. Darriet, A. Wattiaux, J. C. Grenier, P. Gravereau, M. Pouchard, *Journal of Solid State Chemistry*, 106 (1993) 330–338.
- [32] A. Demourgues, F. Weill, B. Darriet, A. Wattiaux, J. C. Grenier, P. Gravereau, M. Pouchard, *Journal of Solid State Chemistry*, 106 (1993) 317–329.

# Chapter 4

---

*"Submitted to Journal of Power Sources, 2016"*

# Ageing Study of Praseodymium-Lanthanum Nickelates $\text{La}_{2-x}\text{Pr}_x\text{NiO}_{4+\delta}$ as Cathodes for MS-SOFCs

Vaibhav Vibhu, Aline Rougier, Aurélien Flura, Clément Nicollet, Sébastien Fourcade,  
Teresa Hungria, Jean-Claude Grenier and Jean-Marc Bassat\*

<sup>a</sup>CNRS, Université de Bordeaux, Institut de Chimie de la Matière Condensée de Bordeaux  
(ICMCB), 87 Av. Dr Schweitzer, F-33608 Pessac Cedex, France.

<sup>b</sup>Centre de Micro-caractérisation Raymond Castaing (UMS3623), Espace Clément ADER,  
3, rue Caroline Aigle, 31400 TOULOUSE.

## Abstract

The present study is focused on the ageing study of  $\text{La}_{2-x}\text{Pr}_x\text{NiO}_{4+\delta}$  (LPNO) mixed nickelates, used as alternative oxygen electrodes for Solid Oxide Fuel Cells (SOFCs), thanks to their mixed ionic and electronic conductivity (*i.e.* MIEC properties). Herein, the chemical stability of the LPNO mixed nickelates under air at operating temperatures as well as the evolution of their polarization resistances during ageing (under air at  $i_{dc} = 0$  and  $i_{dc} \neq 0$  conditions, all impedance diagrams are recorded at OCV) were studied for duration up to one month. La-rich phases ( $x = 0$  and 0.5) are highly stable whereas Pr-rich phases ( $x = 1, 1.5$  and 2) show decomposition under air after 1 month at 600, 700 and 800°C. For instance  $\text{Pr}_2\text{NiO}_{4+\delta}$  (PNO) is completely decomposed into  $\text{PrNiO}_{3-\delta}$ ,  $\text{Pr}_4\text{Ni}_3\text{O}_{10+\delta}$  and  $\text{Pr}_6\text{O}_{11}$ . Interestingly, the ageing of the mixed LPNO//GDC//8YSZ half cells during 1 month under air shows no significant change in the polarization resistance ( $R_p$  value) at  $i_{dc} = 0$  condition, whatever the composition, despite their various degrees of chemical stability. For the three studied materials, a different behavior is observed under current ( $i_{dc} = \pm 300 \text{ mA}\cdot\text{cm}^{-2}$  conditions) with a faster degradation (*i.e.* large increase in  $R_p$ ) in SOFC (cathodic) mode compared to the SOEC mode, where the  $R_p$  values are stable.

Finally, we demonstrate that the electrochemical properties of  $\text{La}_{2-x}\text{Pr}_x\text{NiO}_{4+\delta}$  under ageing depend more on the interface and interphases formed between the cathode and the barrier layer GDC than on the chemical stability of the nickelates.

**Keywords:** SOFCs, Nickelates, Chemical stability, Ageing, Interface

## 1. Introduction

The reduction of the operating temperature of the SOFCs is a critical challenge for their commercialization. Currently, the main objective is to decrease it down to around 600 – 700°C, in an effort to decrease the device cost (for example, using stainless steel instead of ceramics as interconnects) and to improve the long term cells durability, which is a key issue to take into account when considering the commercialization of Solid Oxide Fuel Cells (SOFCs). In this scope the study of the long term stability of the SOFC components is very important, since the degradation rate of the fuel cell is determined by the degradation rates of its ceramic parts (*i.e.* cathode, electrolyte and anode) [1, 2]. The cell degradation generally occurs due to grain coarsening, particle smoothing/rounding, phase instability, interfacial segregation, evaporation, impurity accumulation at critical interfaces, inter-diffusion and reactions.

Our study focuses on the degradation phenomena related to the cathode materials. The degradation mechanisms directly affect the different steps involved in the oxygen reduction reaction (ORR) at the cathode, decreasing the electrochemical performance. In order to identify the different contributions to the ORR, electrochemical impedance spectroscopy (EIS) is normally recorded under varying conditions. Although the ORR at cathodes has been extensively investigated in the last decades, still today there is not yet a general agreement regarding which mechanisms are involved and which one is the rate limiting step. The overall rate-limiting mechanisms depend on the cathode composition and microstructure, temperature,  $pO_2$ , current density, polarization, and thermal and electrochemical conditions. On the other hand, since the electrode reactions as well as ion transport through the electrolyte are temperature-driven, the electrochemical performance drastically decreases with decreasing temperature.

It is as well important to develop the materials and architecture of the cell in order to reach reasonable performance. Recently, the third generation metal supported IT-SOFC ( $T \approx 700$  °C), namely Metal Supported Cell (MSC), has attracted many researchers because thinner electrodes and electrolyte layers are used in this architecture, which leads to lower the overall cost. In addition, good thermal cycling and easier current collection are expected from the metallic interconnect. However, the main issue with the MSC concerns the stability of the components (mainly the cathode) at high temperature under low  $pO_2$  (*i.e.* under  $N_2$ ,  $pO_2 \approx 10^{-4}$  atm). Indeed, the sintering of the complete cell has to be performed under such conditions to prevent the oxidation of the metallic support. As the cathode contributes to a

large extent to the cell polarization resistance, our work aims to design cathode materials with MIEC properties able to be used in MSC-type devices.

Today it is well known that the most promising materials for cathodes are Mixed Ionic and Electronic Conducting (MIEC) oxides [3-8]. Rare earth nickelates with general formula  $\text{Ln}_2\text{NiO}_{4+\delta}$  ( $\text{Ln} = \text{La}, \text{Nd}$  or  $\text{Pr}$ ) have already shown good cathodic performance in combination with various electrolytes (mainly YSZ and GDC) thanks to their MIEC properties [9-14]. Moreover,  $\text{Ln}_2\text{NiO}_{4+\delta}$  ( $\text{Ln} = \text{La}$  or  $\text{Pr}$ ) type materials are chemically stable under air as well as under low  $p\text{O}_2$  ( $10^{-4}$  atm) up to 1300 °C, which indicates the suitability of these two materials as MSCs [15]. The opposite conclusion was drawn for  $\text{Nd}_2\text{NiO}_{4+\delta}$  (NNO). Among  $\text{Ln}_2\text{NiO}_{4+\delta}$  ( $\text{Ln} = \text{La}, \text{Pr}$  or  $\text{Nd}$ ) compounds,  $\text{Pr}_2\text{NiO}_{4+\delta}$  (PNO) shows the lowest polarization resistance using GDC interface and YSZ electrolytes [12] while  $\text{La}_2\text{NiO}_{4+\delta}$  (LNO) exhibits high chemical stability. Aiming at high electrochemical performance, recently praseodymium substituted lanthanum nickelates  $\text{La}_{2-x}\text{Pr}_x\text{NiO}_{4+\delta}$  ( $0.0 \leq x \leq 2.0$ ) (hereafter labelled LPNO materials) were investigated [16]. However, in order to find the best compromise between high electrochemical performance and chemical stability, long term ageing experiments are mandatory. Some authors have previously reported the middle term chemical stability of these nickelates  $\text{Ln}_2\text{NiO}_{4+\delta}$  ( $\text{Ln} = \text{La}, \text{Pr}$  or  $\text{Nd}$ ). Montenegro-Hernandez *et al.* have reported that LNO and NNO are chemically stable whereas PNO is not, being partially decomposed into  $\text{Pr}_4\text{Ni}_3\text{O}_{10}$  and  $\text{Pr}_6\text{O}_{11}$ , at 700 and 900 °C up to 72 h [17]. Kovalevsky *et al.* have also reported such kind of decomposition of PNO below 950 °C [18, 19]. But the authors did not discuss the long term chemical stability of these materials.

To the best of our knowledge, the ageing of these nickelates used as electrodes for SOFCs and SOECs (Solid Oxide Electrolyzer Cells) has not yet been reported. An effort was then made in this work to characterize the LPNO electrodes during long term at operating conditions. We focus our attention on two points: 1) the study of the chemical stability of the LPNO powders under air at operating temperatures, 2) the measurements of  $R_p$  variation during ageing, either under  $i_{\text{dc}} = 0$  and  $i_{\text{dc}} \neq 0$  conditions, for duration up to one month, with the aim to find the best compromise between chemical stability and electrochemical performance.

## 2. Experimental

### Powder preparation

Five compositions belonging to the  $\text{La}_{2-x}\text{Pr}_x\text{NiO}_{4+\delta}$  ( $x = 0.0, 0.5, 1.0, 1.5$  and  $2.0$ ) solid solution were prepared using the citrate-nitrate route (modified Pechini method) [20]. The corresponding precursors were  $\text{Pr}_6\text{O}_{11}$  (Aldrich chem, 99.9%),  $\text{La}_2\text{O}_3$  (Strem Chemical, 99.99%) and  $\text{Ni}(\text{NO}_3)_2 \cdot 6\text{H}_2\text{O}$  (Acros Organics, 99%). The final annealing was performed at  $1200\text{ }^\circ\text{C}$  for 12 h under air, leading for all compositions to single and well crystallized phases. The resulting powders were attrited using zirconia balls and ethanol for 4 h with the aim to reach an average particle size of about  $0.6\text{ }\mu\text{m}$ . More details about the powders preparation are given in ref. [16].

### Thermal ageing of powders

Ageing of LPNO powders was performed under air. Green pellets (about 60 % density) were first prepared and then left into a furnace either for one week or for one month at  $600, 700$  and  $800\text{ }^\circ\text{C}$  (*i.e.* at the operating temperatures of IT-SOFCs). After one month, the pellets were crushed into powder and characterized by XRD by using a PANalytical X'pert MPD diffractometer with  $\text{Cu-K}_\alpha$  incident radiation.

### Cell manufacturing

Symmetrical half cells (electrode//GDC//8YSZ) were shaped for the electrochemical studies. Terpeneol-based slurries were prepared with each nickelate material as well as with gadolinium doped (20%) ceria GDC powder. First, GDC layers (thickness  $\approx 3\text{ }\mu\text{m}$ ) were symmetrically screen printed on both sides of dense 8YSZ pellets (diameter  $\approx 18\text{ mm}$  and thickness  $\approx 1.2\text{ mm}$ ), then sintered at  $1300\text{ }^\circ\text{C}$  for 1h under air. The nickelate layers (thickness  $\approx 10\text{-}15\text{ }\mu\text{m}$ ) were afterwards symmetrically screen printed and sintered at  $1150\text{ }^\circ\text{C}$  for 1 h under nitrogen atmosphere ( $p\text{O}_2 \approx 10^{-4}\text{ atm}$ , MSC conditions) [16]. These sintering temperatures were previously optimized to obtain a controlled homogeneous porous electrode microstructure. However let us recall that the electrodes show close behaviour when sintered either in air or nitrogen. More especially, the electrochemical performance of PNO electrode are the same after sintering under air or nitrogen, and it is even better for LNO when sintered under nitrogen [21].

## Electrochemical Characterization

In order to characterize the electrochemical properties of these electrodes on symmetrical half cells, two geometries were used: (i) two electrode system, both electrodes covering the GDC surface; in that case impedance spectroscopy measurements were performed under zero dc conditions, (ii) three electrodes system, a reference electrode being set all around the edge of the thick 8YSZ electrolyte ceramic in order to perform ageing under current.

The initial EIS measurements were carried out under air, in the temperature range 500 – 800 °C under zero dc conditions. Gold grids (1.024 cm<sup>-2</sup> meshes) were used as current collectors. When the negative current is applied from upper side of the symmetrical half cells, the working electrode (WE) behaves like cathode of the SOFC and the counter electrode (CE) behaves like anode of SOEC device. The current was removed and left 10 minutes for the stabilization before the EIS measurements at OCV, which were performed after each few hours of current flow. The impedance diagrams were recorded at steady state under potentiostatic control with 50 mV ac amplitude, from 10<sup>6</sup> Hz down to 10<sup>-1</sup> Hz, using a frequency response analyser module Autolab FRA2, coupled with a potentiostat/galvanostat PGSTAT 302N. The complex impedance diagrams were fitted using an equivalent circuit by means of the Zview<sup>®</sup> software. The polarization resistance  $R_p$  values were calculated from the difference between the low (LF) and the high frequencies (HF) diagram intercepts with the Z'-axis of the Nyquist representation.

## FIB-SEM analyses

The microstructures of the electrodes before and after ageing were observed by field emission Scanning Electron Microscopy (JEOL JSM 6330 A) equipped with an EDS detector. Cross sections preparations by focused ion beam milling, subsequent SEM images and elemental microanalysis were carried out using a Dual Beam SEM / FIB FEI Helios 600i equipped with an EDS X-MAN SDD detector.

## 3. Results and discussion

A detailed investigation of the  $\text{La}_{2-x}\text{Pr}_x\text{NiO}_{4+\delta}$  ( $0.0 \leq x \leq 2.0$ ) series was recently reported [16], a short summary being given there: XRD characterizations of the LPNO phases show that all nickelates crystallize in an orthorhombic  $\text{K}_2\text{NiF}_4$  type structure. Depending on  $x$

value (*i.e.* Pr content), two main domains can be distinguished. One is related to La-rich phases, from  $x = 0$  to  $x = 0.5$ , fitted with the *Fmmm* space group, and the second one is related to Pr-rich phases, from  $x = 1$  to  $x = 2$ , with *Bmab* space group [16]. All nickelates are always oxygen over-stoichiometric under air (the  $\delta$  value at room temperature increases from 0.16 (LNO) up to 0.25 (PNO) along with the increase of  $x$ ) as well as under low  $pO_2$  ( $\sim 10^{-4}$  atm) in the temperature range ( $25 < T$  ( $^{\circ}C$ )  $< 1000$ ), then keeping their MIEC properties in these temperatures and  $pO_2$  ranges. For all compositions, the TEC values are almost the same (around  $\sim 13 \times 10^{-6} \text{ }^{\circ}C^{-1}$ ) being nicely comparable with those of 8YSZ [16]. The electrical conductivity of LPNO increases with Pr-content up to  $x = 1.0$  while similar conductivity is observed for the Pr-rich phases, reaching a maximum value of  $\sim 100 \text{ S.cm}^{-1}$  at  $700 \text{ }^{\circ}C$  for  $\text{LaPrNiO}_{4+\delta}$ ,  $\text{La}_{0.5}\text{Pr}_{1.5}\text{NiO}_{4+\delta}$  and PNO. At this temperature, the oxygen diffusion ( $D^*$ ) and surface exchange ( $k^*$ ) coefficients of LPNO ( $x = 0.5, 1$  and  $1.5$ ) are in the order of  $10^{-8} \text{ cm}^2.\text{s}^{-1}$  and  $10^{-6} \text{ cm}.\text{s}^{-1}$ , respectively, which is also in the same range of the ones of PNO and LNO [16].

At the stage of our work, in order to propose the best composition suitable as an oxygen electrode, it became mandatory to study the ageing of these materials.

### 3.1. Thermal ageing of the mixed nickelates: powders

The XRD patterns of all LPNO phases ( $x = 0.0, 0.5, 1.0, 1.5$  and  $2.0$ ) after 1 month ageing under air at  $600, 700$  and  $800 \text{ }^{\circ}C$  are plotted in **Figure 1**. Depending on the composition, two different behaviors were observed: *i*) La-rich phases with  $x = 0$  and  $x = 0.5$  are highly stable, no additional XRD peaks being observed; this result is in agreement with the work of Solis *et al.* [22], who reported no decomposition of LNO and  $\text{La}_{1.5}\text{Pr}_{0.5}\text{NiO}_{4+\delta}$  after 2 weeks at  $750 \text{ }^{\circ}C$  *ii*) On the contrary, from  $x = 1$  to  $x = 2$  the XRD patterns of the aged LPNO samples show the appearance of new peaks attributed to the perovskite  $(\text{La,Pr})\text{NiO}_{3-\delta}$ , the Ruddlesden-Popper  $(\text{La,Pr})_4\text{Ni}_3\text{O}_{10+\delta}$  and  $\text{Pr}_6\text{O}_{11}$  phases, the amount of each of them depending on both the Pr content as well as the ageing temperature. At  $600 \text{ }^{\circ}C$  the perovskite  $(\text{La,Pr})\text{NiO}_{3-\delta}$  phase is the major phase. At  $700 \text{ }^{\circ}C$ , the strong decrease in the  $\text{La}_{2-x}\text{Pr}_x\text{NiO}_{4+\delta}$  proportion is associated with the coexistence of  $(\text{La,Pr})_4\text{Ni}_3\text{O}_{10+\delta}$ ,  $(\text{La,Pr})\text{NiO}_{3-\delta}$  and  $\text{Pr}_6\text{O}_{11}$  as illustrated in **Figure 1d** for  $\text{La}_{0.5}\text{Pr}_{1.5}\text{NiO}_{4+\delta}$ . At  $800 \text{ }^{\circ}C$  the  $(\text{Pr,L a})_4\text{Ni}_3\text{O}_{10+\delta}$  phase is predominant.

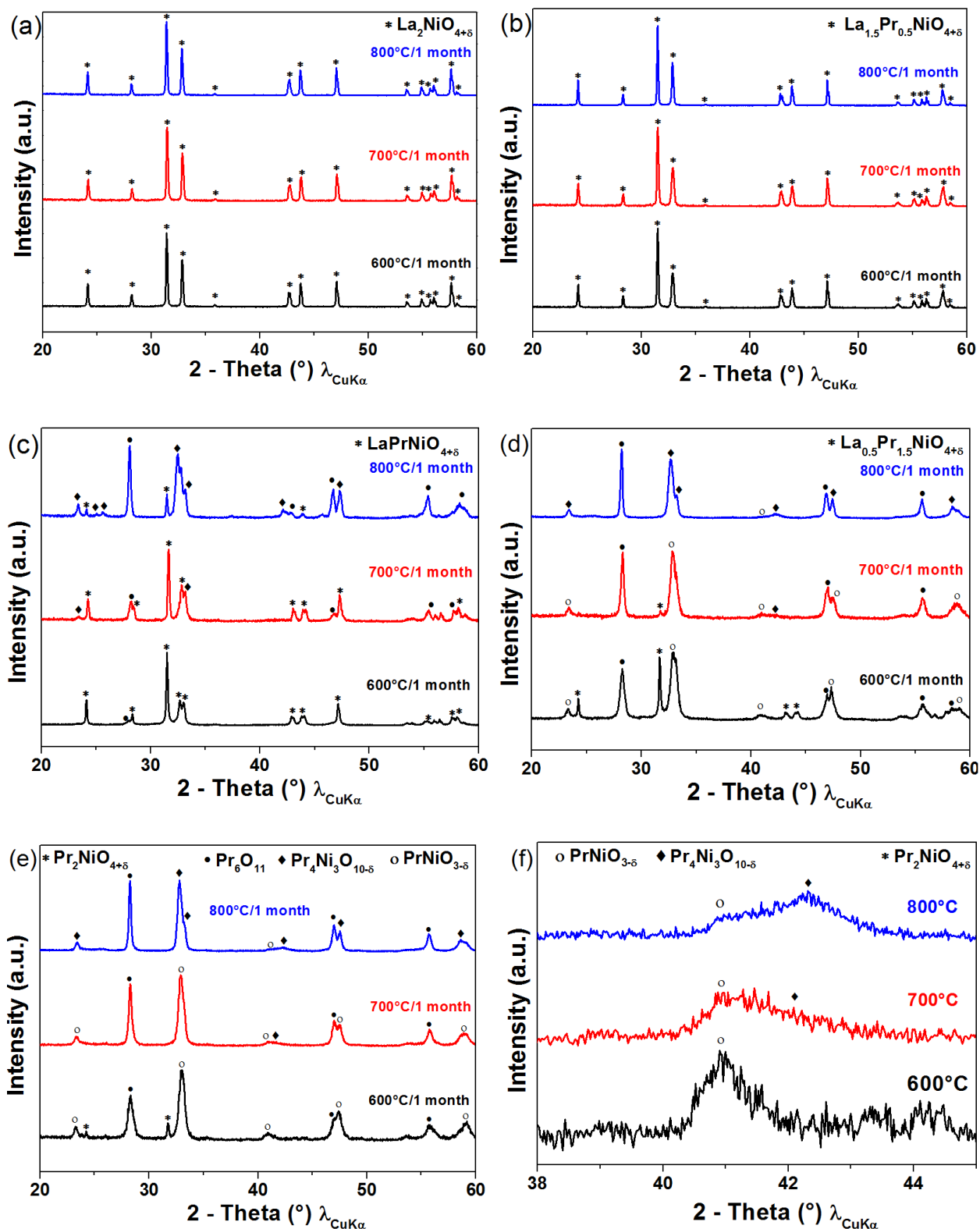


Figure 1: (a-e) XRD patterns of LPNO powders after 1 month ageing at 600, 700 and 800 °C under air, (f) zoom on the XRD pattern of PNO for  $38 < 2\theta < 45$ .

(\*)  $\text{La}_{2-x}\text{Pr}_x\text{NiO}_{4+\delta}$ , ( $\blacklozenge$ )  $(\text{La, Pr})_4\text{Ni}_3\text{O}_{10+\delta}$ , (o)  $(\text{La,Pr})\text{NiO}_{3-\delta}$ , ( $\bullet$ )  $\text{Pr}_6\text{O}_{11}$ .

Regarding the end-term (PNO), it is totally decomposed into  $\text{PrNiO}_{3-\delta}$  and  $\text{Pr}_6\text{O}_{11}$  at 600 °C, while at 700 °C and 800 °C, the Ruddlesden-Popper  $\text{Pr}_4\text{Ni}_3\text{O}_{10+\delta}$  phase also appears.

The amount of the various phases formed after ageing also depends on the duration at a given temperature. **Table 1** gathers the results obtained after 1 week and 1 month. However, due to some peak overlapping, we did not succeed to precisely quantify the amount of each phase. Depending on the intensity of the more intense peaks from X-ray diffractograms, major (M), minor (m) and very little (lit) phases were distinguished.

**Table 1: Phases appearing in LPNO powder after 1 week and 1month ageing at 600, 700 and 800 °C under air (M = major phase, m = minor phase, lit = small amount)**

Sample	600°C/ 1week	600°C/ 1month	700°C/ 1week	700°C/ 1month	800°C/ 1week	800°C/ 1month
$\text{La}_2\text{NiO}_{4+\delta}$	$\text{La}_2\text{NiO}_{4+\delta}$	$\text{La}_2\text{NiO}_{4+\delta}$	$\text{La}_2\text{NiO}_{4+\delta}$	$\text{La}_2\text{NiO}_{4+\delta}$	$\text{La}_2\text{NiO}_{4+\delta}$	$\text{La}_2\text{NiO}_{4+\delta}$
$\text{La}_{1.5}\text{Pr}_{0.5}\text{NiO}_{4+\delta}$	$(\text{La},\text{Pr})_2\text{NiO}_{4+\delta}$	$(\text{La},\text{Pr})_2\text{NiO}_{4+\delta}$	$(\text{La},\text{Pr})_2\text{NiO}_{4+\delta}$	$(\text{La},\text{Pr})_2\text{NiO}_{4+\delta}$	$(\text{La},\text{Pr})_2\text{NiO}_{4+\delta}$	$(\text{La},\text{Pr})_2\text{NiO}_{4+\delta}$
$\text{LaPrNiO}_{4+\delta}$	$(\text{La},\text{Pr})_2\text{NiO}_{4+\delta}$	$(\text{La},\text{Pr})_2\text{NiO}_{4+\delta}$ (M), $(\text{La},\text{Pr})\text{NiO}_{3-\delta}$ (m), $\text{Pr}_6\text{O}_{11}$ (m)	$(\text{La},\text{Pr})_2\text{NiO}_{4+\delta}$	$(\text{La},\text{Pr})_2\text{NiO}_{4+\delta}$ (M), $(\text{La},\text{Pr})\text{NiO}_{3-\delta}$ , $(\text{La},\text{Pr})_4\text{Ni}_3\text{O}_{10+\delta}$ , $\text{Pr}_6\text{O}_{11}$	$(\text{La},\text{Pr})_2\text{NiO}_{4+\delta}$ (M), $(\text{La},\text{Pr})\text{NiO}_{3-\delta}$ , $(\text{La},\text{Pr})_4\text{Ni}_3\text{O}_{10+\delta}$ , $\text{Pr}_6\text{O}_{11}$	$(\text{La},\text{Pr})_2\text{NiO}_{4+\delta}$ , $(\text{La},\text{Pr})\text{NiO}_{3-\delta}$ , $(\text{La},\text{Pr})_4\text{Ni}_3\text{O}_{10+\delta}$ (M), $\text{Pr}_6\text{O}_{11}$
$\text{La}_{0.5}\text{Pr}_{1.5}\text{NiO}_{4+\delta}$	$(\text{La},\text{Pr})_2\text{NiO}_{4+\delta}$	$(\text{La},\text{Pr})_2\text{NiO}_{4+\delta}$ (m), $(\text{La},\text{Pr})\text{NiO}_{3-\delta}$ (M), $\text{Pr}_6\text{O}_{11}$	$(\text{La},\text{Pr})_2\text{NiO}_{4+\delta}$ (M), $(\text{La},\text{Pr})\text{NiO}_{3-\delta}$ (m), $\text{Pr}_6\text{O}_{11}$ (lit)	$(\text{La},\text{Pr})_2\text{NiO}_{4+\delta}$ (lit), $(\text{La},\text{Pr})\text{NiO}_{3-\delta}$ , $(\text{La},\text{Pr})_4\text{Ni}_3\text{O}_{10+\delta}$ , $\text{Pr}_6\text{O}_{11}$	$(\text{La},\text{Pr})_2\text{NiO}_{4+\delta}$ (m), $(\text{La},\text{Pr})\text{NiO}_{3-\delta}$ , $(\text{La},\text{Pr})_4\text{Ni}_3\text{O}_{10+\delta}$ (M), $\text{Pr}_6\text{O}_{11}$ (M)	$(\text{La},\text{Pr})_2\text{NiO}_{4+\delta}$ (m), $(\text{La},\text{Pr})\text{NiO}_{3-\delta}$ , $(\text{La},\text{Pr})_4\text{Ni}_3\text{O}_{10+\delta}$ (M), $\text{Pr}_6\text{O}_{11}$ (M)
$\text{Pr}_2\text{NiO}_{4+\delta}$	$\text{Pr}_2\text{NiO}_{4+\delta}$ (M), $\text{PrNiO}_{3-\delta}$ , $\text{Pr}_6\text{O}_{11}$	$\text{Pr}_2\text{NiO}_{4+\delta}$ (traces), $\text{PrNiO}_{3-\delta}$ (M), $\text{Pr}_6\text{O}_{11}$	$\text{Pr}_2\text{NiO}_{4+\delta}$ (lit), $\text{PrNiO}_{3-\delta}$ (M), $\text{Pr}_4\text{Ni}_3\text{O}_{10+\delta}$ , $\text{Pr}_6\text{O}_{11}$	$\text{PrNiO}_{3-\delta}$ , $\text{Pr}_4\text{Ni}_3\text{O}_{10+\delta}$ , $\text{Pr}_6\text{O}_{11}$	$\text{PrNiO}_{3-\delta}$ , $\text{Pr}_4\text{Ni}_3\text{O}_{10+\delta}$ , $\text{Pr}_6\text{O}_{11}$	$\text{Pr}_4\text{Ni}_3\text{O}_{10+\delta}$ , $\text{PrNiO}_{3-\delta}$ , $\text{Pr}_6\text{O}_{11}$

### 3.2. Symmetrical half-cell characterization

In a first step, the measurements were performed on as prepared symmetrical half cells of LPNO//GDC//8YSZ//GDC//LPNO as a function of temperature under air [16]. Note that thin GDC layers, labelled as buffer layers, were deposited in order to increase the electrochemical performance of the cells [12]. The lowest polarization resistances were found for the PNO electrode, namely  $R_p = 0.01, 0.03$  and  $0.15 \text{ } \Omega\cdot\text{cm}^2$  at 800 °C, 700 °C and 600 °C respectively. The substitution of La for Pr leads to a significant increase in the polarization resistances up to values of 0.13, 0.28 and  $0.93 \text{ } \Omega\cdot\text{cm}^2$  at 800 °C, 700 °C and 600 °C respectively, for LNO.

### 3.3. Ageing of half cells under $i_{dc} = 0$

In a second step, half-cells were placed inside a furnace during one month at 600 and 700 °C, under air (Ageing at 800 °C was not performed due to lack of time). After one month ageing, EIS measurements were performed under  $i_{dc} = 0$  condition. The comparison of the polarization resistances for the five compositions ( $x = 0.0, 0.5, 1.0, 1.5$  and  $2.0$ ) is shown in **Figure 2** for as prepared and aged samples. As a very interesting result for all LPNO compositions, the polarization resistance remains almost the same before and after ageing, no significant evolution being observed. For example, at 700 °C  $R_p = 0.08 \Omega \cdot \text{cm}^2$  for  $\text{La}_{1.5}\text{Pr}_{0.5}\text{NiO}_{4+\delta}$  half-cell before and after ageing.

It's remarkable to note that this trend was observed despite the complete decomposition of PNO into  $\text{PrNiO}_{3-\delta}$ ,  $\text{Pr}_4\text{Ni}_3\text{O}_{10+\delta}$  and  $\text{Pr}_6\text{O}_{11}$ , firstly suggesting that those phases should be as well active in the oxygen electrode reaction (OER). Indeed, we have recently reported the electrochemical properties of these forming  $\text{PrNiO}_{3-\delta}$  and  $\text{Pr}_4\text{Ni}_3\text{O}_{10+\delta}$  materials [23, 24].  $\text{PrNiO}_{3-\delta}$  is not a very efficient material regarding its electrochemical performance ( $R_p = 0.91 \Omega \cdot \text{cm}^2$  at 600 °C) [23], the opposite conclusion being drawn for  $\text{Pr}_4\text{Ni}_3\text{O}_{10+\delta}$ , for which similar  $R_p$  values compared to PNO being recorded [24] ( $R_p = 0.16 \Omega \cdot \text{cm}^2$  and  $0.15 \Omega \cdot \text{cm}^2$  at 600 °C for  $\text{Pr}_4\text{Ni}_3\text{O}_{10+\delta}$  and PNO, respectively).

As examples, the evolution of the impedance diagrams for the two end-terms of the LPNO series *i.e.* LNO and PNO during electrochemical ageing at 700 °C, under air, is plotted in **Figure 3(a, b)** and **3(c, d)**, respectively. For LNO, the  $R_p$  value slightly increases from  $0.21^4$  (0 h) to  $0.24 \Omega \cdot \text{cm}^2$  (750 h) (**Figure 3a**) and the overall shape of impedance plot does not change with time, in good agreement with the chemical stability of the LNO electrode.

---

<sup>4</sup> The difference in  $R_p$  values in between chapter 2 and 3,  $R_p = 0.28 \Omega \cdot \text{cm}^2$  and  $R_p = 0.21 \Omega \cdot \text{cm}^2$  for LNO may be attributed to the use of different GDC inks.

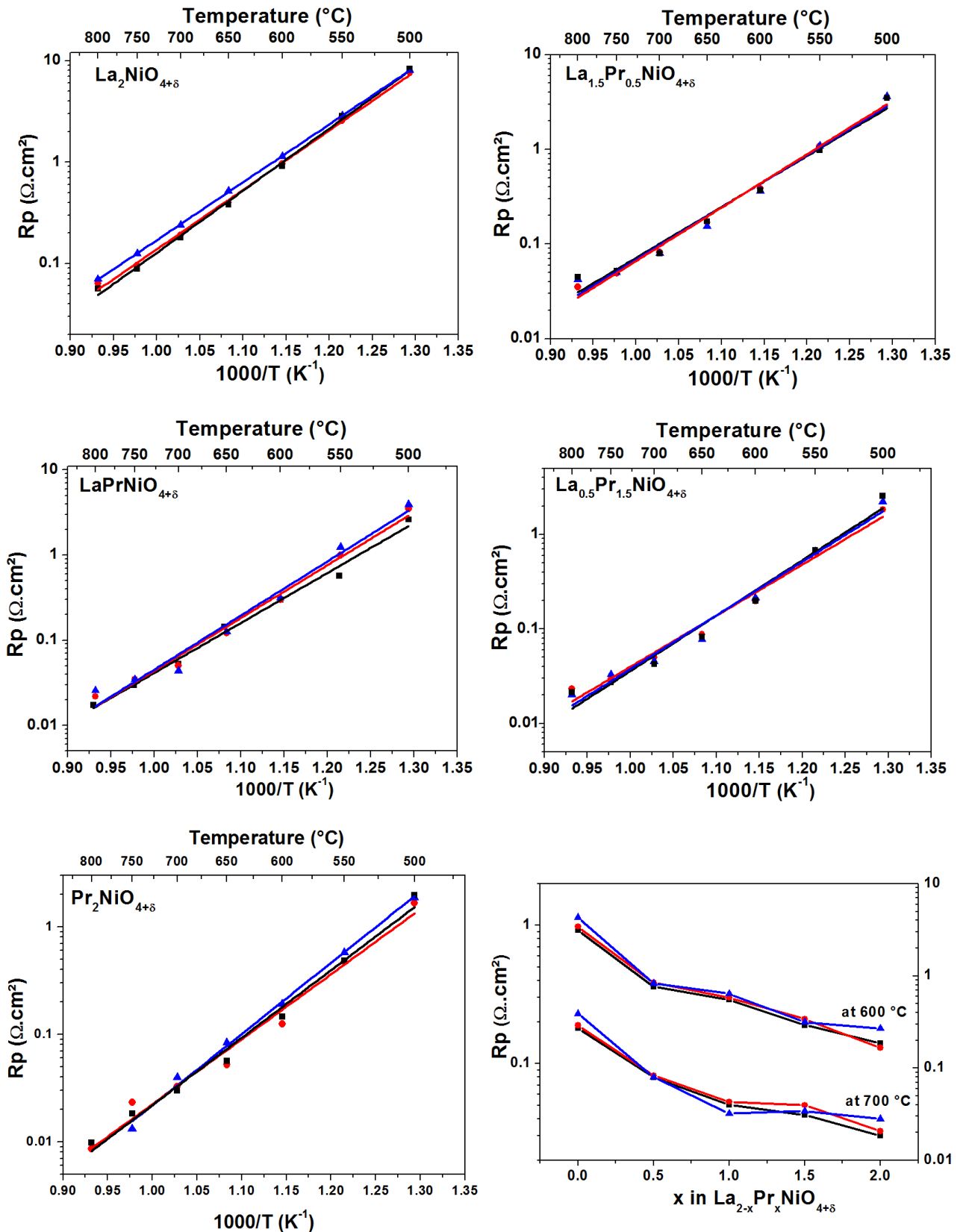
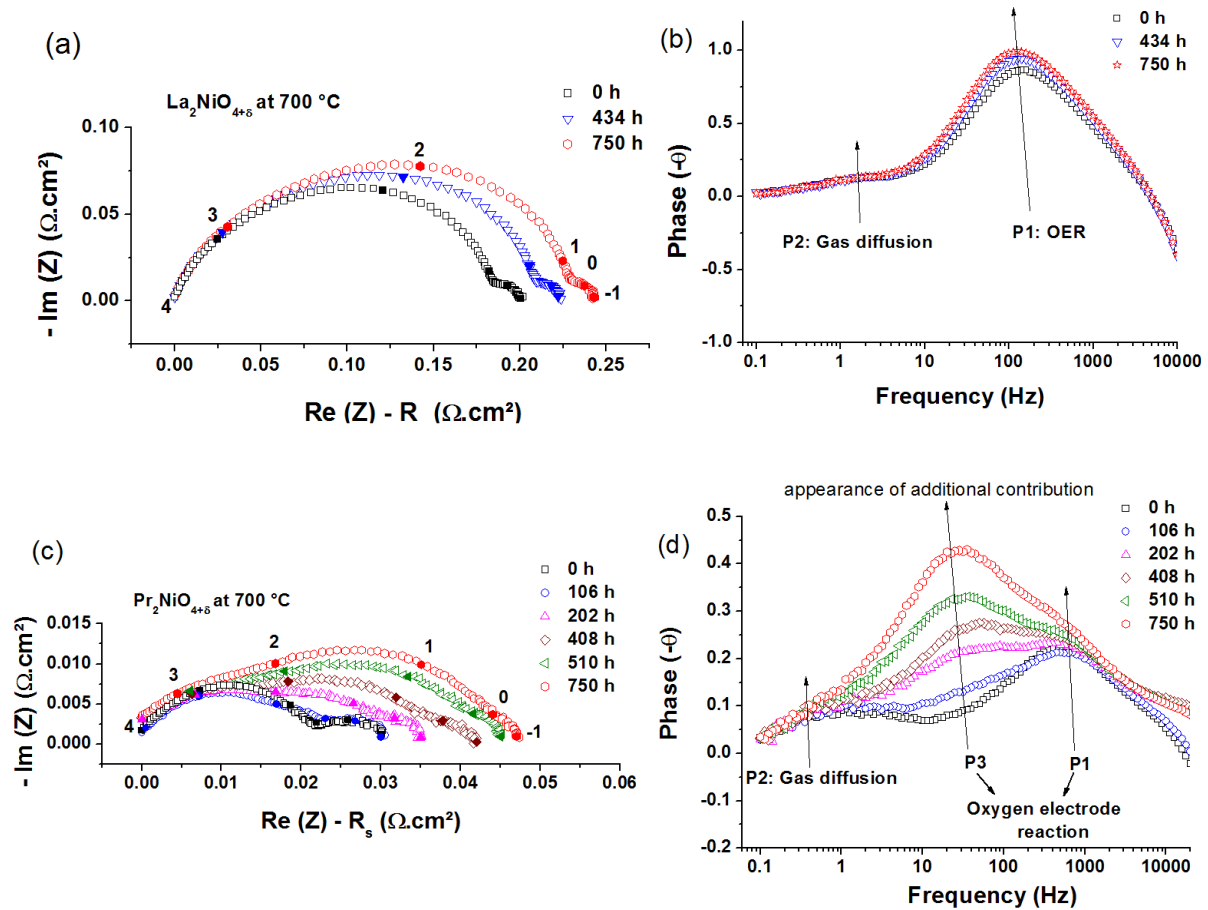


Figure 2:  $R_p$  measured on as prepared and aged ( $T = 600$  and  $700$  °C) symmetrical half cells (at  $i_{dc} = 0$  condition), under air, for LPNO electrodes. (■) as prepared, (●) aged at 600 °C/1 month, (▲) aged at 700 °C/1 month.



**Figure 3: Variation of the Nyquist and Bode diagrams for symmetrical cells (a, b) LNO and (c, d) PNO electrodes, at 700°C under air.**

For PNO the  $R_p$  value increases more significantly, *i.e.* about 50% from 0.03 to 0.045  $\Omega\cdot\text{cm}^2$  (**Figure 3c**). Moreover, contrarily to LNO the shape of the impedance plots changes with time. At an early stage ( $t < 106$  h), the Bode plots show only two contributions, namely P1 and P2, that correspond to the oxygen electrode reaction (OER) [25] and molecular  $\text{O}_2$  gas diffusion, respectively [26, 27]. Upon ageing, an extra contribution (P3 in between the frequency 1-100 Hz) more easily depicted in the bode plot (**Figure 3d**) appears and increases with time. This extra contribution could illustrate the dissociation of PNO.

### 3.4. Ageing of half cells under $i_{\text{dc}} \neq 0$ up to 1800 h

The ageing under current of three LPNO electrodes, *i.e.* namely LNO,  $\text{La}_{1.5}\text{Pr}_{0.5}\text{NiO}_{4+\delta}$  and PNO was studied using the electrochemical impedance spectroscopy measurements. In addition to the two end members,  $\text{La}_{1.5}\text{Pr}_{0.5}\text{NiO}_{4+\delta}$  was chosen due to its good chemical stability at operating temperature as LNO (contrarily to  $\text{PrLaNiO}_{4+\delta}$  and  $\text{La}_{0.5}\text{Pr}_{1.5}\text{NiO}_{4+\delta}$ ,

**Figures 1c, d**); moreover, the  $R_p$  at OCV is  $0.08 \Omega \cdot \text{cm}^2$  for  $\text{La}_{1.5}\text{Pr}_{0.5}\text{NiO}_{4+\delta}$ , which is around three times lower than LNO ( $R_p = 0.21 \Omega \cdot \text{cm}^2$ ).

*For the electrochemical measurement under current, a specific three electrode setup was used. The main interest of the three electrode EIS setup is to record the electrochemical performance of the working (WE) and counter electrodes (CE) separately, by using a reference electrode (RE). Usually the RE is placed on the electrolyte surface at some distance expected to be sufficiently far from the active electrodes in a region of un-uniform potential distribution [28-30]. However, several authors observed artifacts in the impedance diagrams related to the placement of the reference electrode [31-34].*

As an initial point, EIS measurements were performed before the ageing process. As an example, **Figure 4** shows the Nyquist plot of the data recorded on the half-cell including PNO as electrode, at  $700^\circ\text{C}$  and  $t = 0$  h. The  $R_p$  value and the shape of the diagram are the same when recorded on both sides of the half cell. This trend was observed with all LPNO samples.

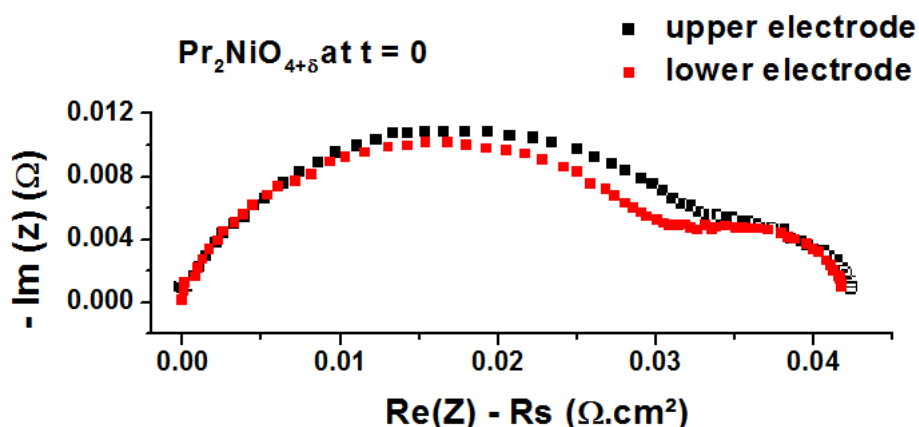


**Figure 4:** Nyquist plot measured by 3 electrodes system on both sides of the half cell including PNO as electrode, recorded at  $700^\circ\text{C}$  and  $t = 0$  h ( $i_{dc} = 0$ ).

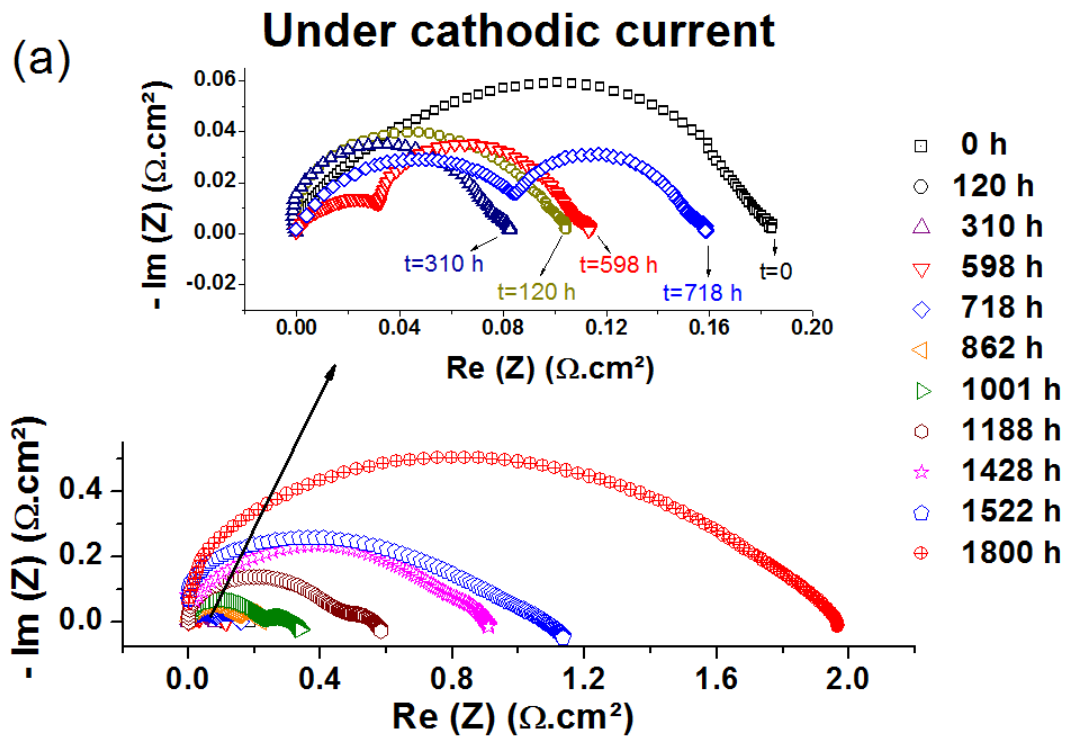
### 3.4.1. Behavior of the electrode in SOFC mode during ageing

The evolution of the impedance diagrams was recorded for LNO,  $\text{La}_{1.5}\text{Pr}_{0.5}\text{NiO}_{4+\delta}$  and PNO electrodes in SOFC and SOEC modes during ageing under current. An intermediate current value ( $i_{dc} \pm 300 \text{ mA} \cdot \text{cm}^{-2}$ ) was chosen for the ageing experiments. The results are plotted in **Figure 5**.

In SOFC mode (cathodic current), the polarization resistances of LNO,  $\text{La}_{1.5}\text{Pr}_{0.5}\text{NiO}_{4+\delta}$  and PNO samples significantly increase with time, while in SOEC mode the increase seems less significant. Let us discuss below the different situations regarding each considered composition.

### 3.4.2. Behaviour under cathodic current (SOFC mode)

For LNO the  $R_p$  value is  $\sim 0.19 \Omega \cdot \text{cm}^2$  for both upper and lower electrodes at  $i_{dc} = 0$  condition, but under current the impedance is affected on both short and long term. The performance of LNO electrode during ageing under cathodic current flow ( $-300 \text{ mA} \cdot \text{cm}^{-2}$ ) is compared in **Figure 5a**.



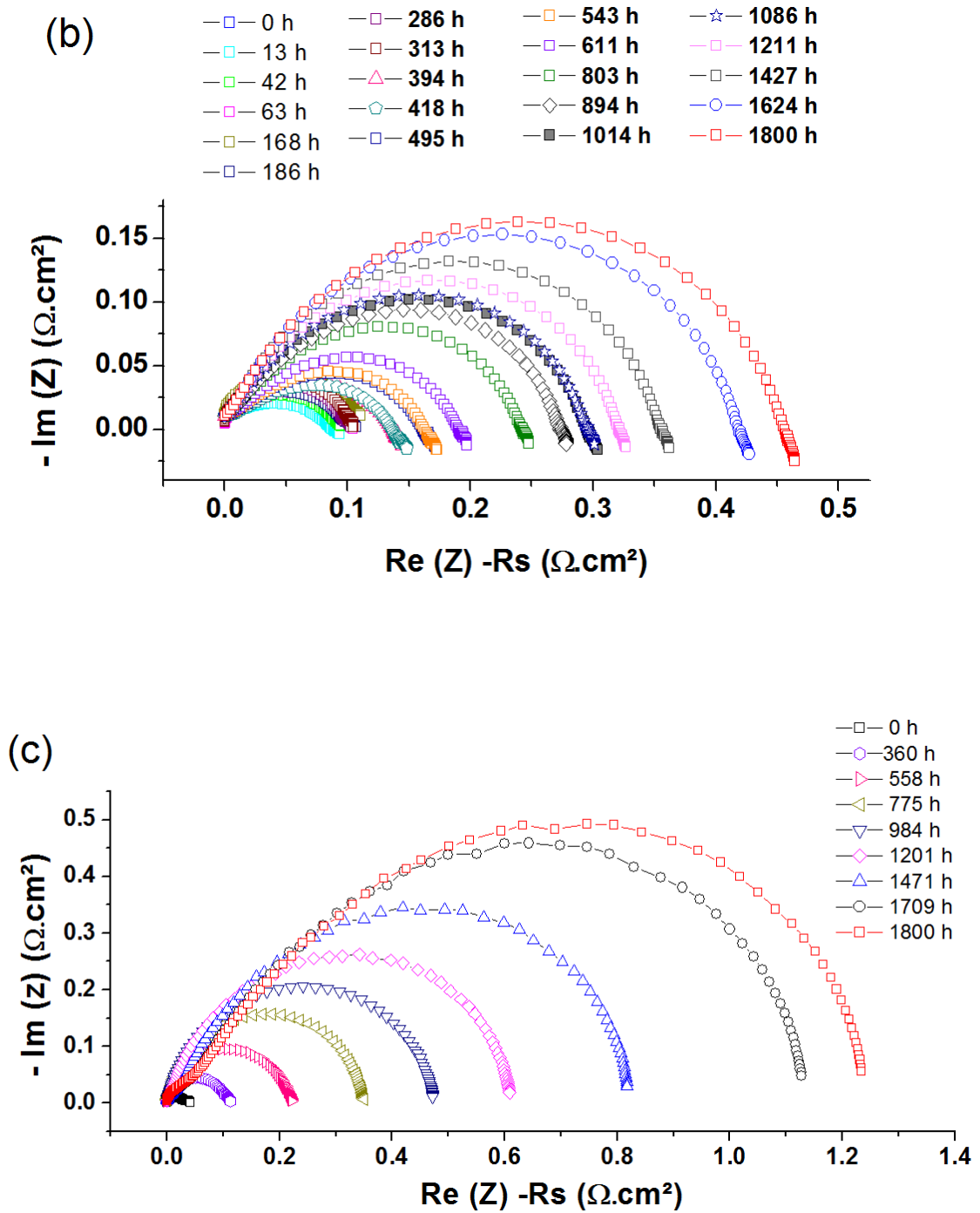


**Figure 5: Evolution of impedance diagrams (Nyquist plot) at 700 °C with time under cathodic current ( $i_{dc} = -300 \text{ mA}\cdot\text{cm}^{-2}$ ) for (a) LNO (b)  $\text{La}_{1.5}\text{Pr}_{0.5}\text{NiO}_{4+\delta}$  and (c) PNO electrode.**

As for some other electrodes, such as for example LSM [34], the LNO electrode is initially activated by the current load, *i.e.*  $R_p$  measured at OCV decreases upon increasing time. After 120 h under cathodic current (**Figure 5a**), the  $R_p$  of LNO electrode decreases down to  $0.10 \text{ }\Omega\cdot\text{cm}^2$ , then further decreases down to  $0.09 \text{ }\Omega\cdot\text{cm}^2$  after 310 h of ageing (see **Figure 5a** and inset inside). Further ageing leads to a short increase of the  $R_p$  values up to  $0.12 \text{ }\Omega\cdot\text{cm}^2$  after

589 h with addition of an extra contribution which kept on increasing up to 1800 h with higher rate. The capacitance of this additional contribution was calculated from the data obtained by fitting using R//CPE, it is equal to  $3.5 \times 10^{-4} \text{ F}\cdot\text{cm}^{-2}$ . This capacitance value reveals that this contribution is somewhat related to the interface. A long ageing (up to 1800 h) leads to a very large increase of the  $R_p$  values (up to about  $2 \text{ }\Omega\cdot\text{cm}^2$ ).

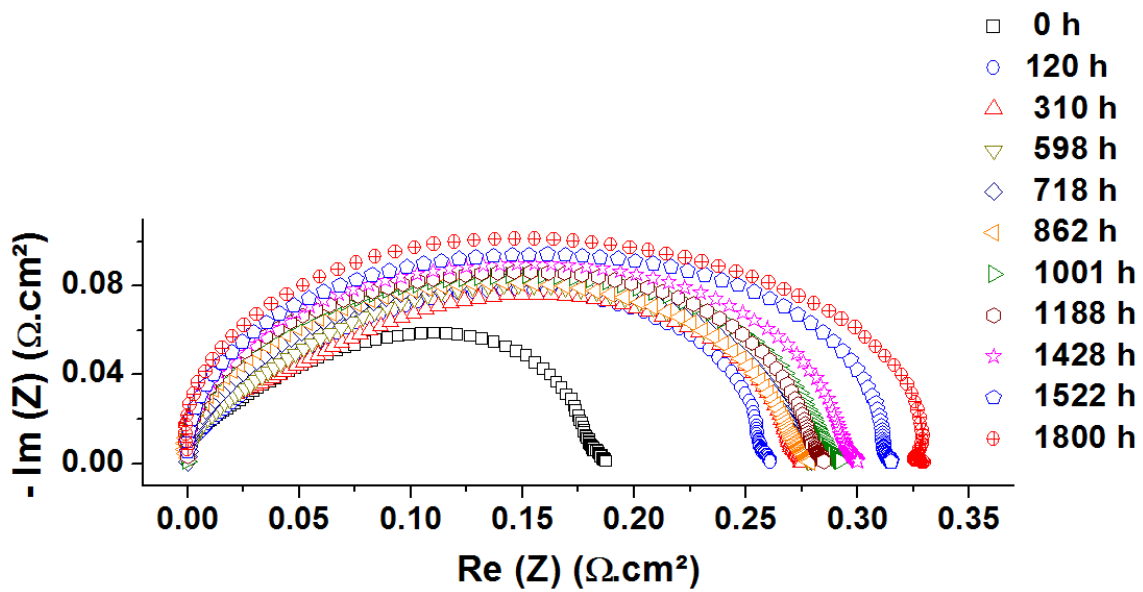
The activity of  $\text{La}_{1.5}\text{Pr}_{0.5}\text{NiO}_{4+\delta}$  electrode under cathodic current is different than the one of LNO. No decrease of  $R_p$  is noticed during the first few hours of ageing the polarization resistance remains stable at  $\sim 0.08 \text{ }\Omega\cdot\text{cm}^2$  up to 313 h of ageing under cathodic current. Upon further ageing, a quite large increase is observed up to  $R_p \sim 0.46 \text{ }\Omega\cdot\text{cm}^2$  after 1800 h ageing (**Figure 5b**).

PNO electrode shows a progressive very large increase in  $R_p$  as a function of time under cathodic current (**Figure 5c**). The  $R_p$  value is increased up to  $1.25 \text{ }\Omega\cdot\text{cm}^2$  after 1800 h (from the initial value  $0.03 \text{ }\Omega\cdot\text{cm}^2$ ). The gas diffusion process (smaller arc in **Figure 4**), which was clearly visible before starting the ageing process, is progressively overlapped by the OER process.

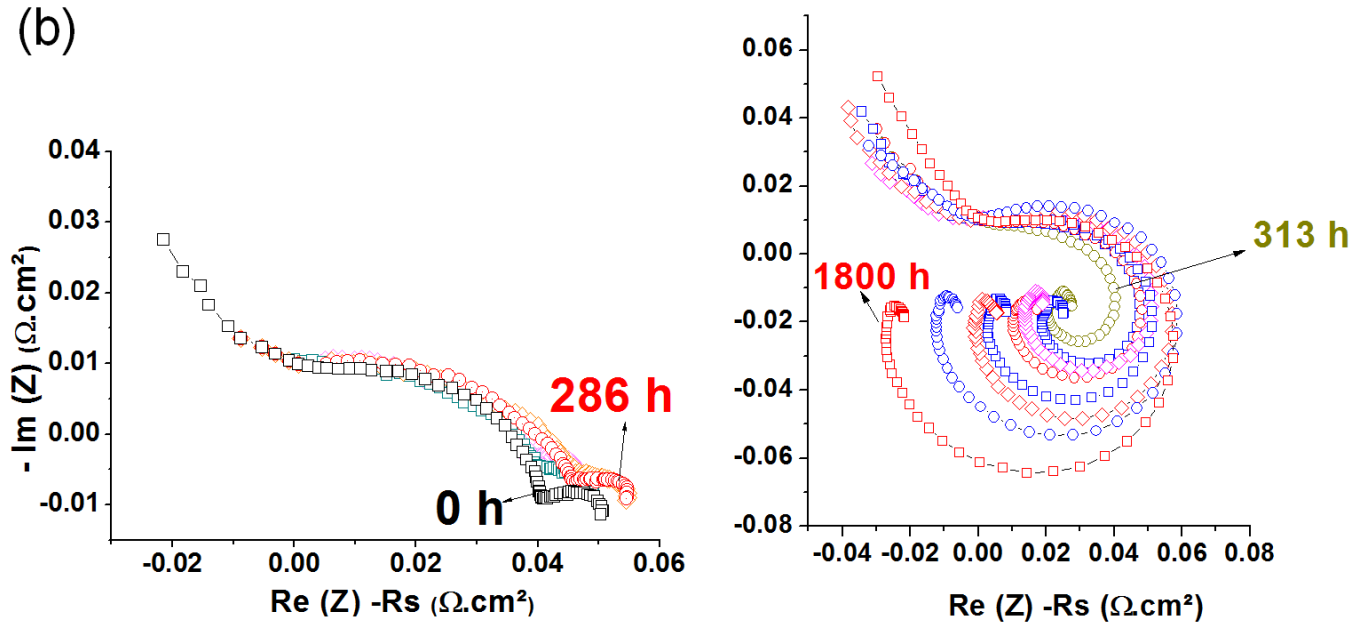
### 3.4.3. Behaviour under anodic current (SOEC mode)

The performance of LNO electrode during ageing performed under anodic current flow ( $+300 \text{ mA}\cdot\text{cm}^{-2}$ ) is plotted in **Figure 6a**. After 120 h of ageing, the polarization resistance  $R_p$  increases from 0.21 to  $0.26 \text{ }\Omega\cdot\text{cm}^2$ . Then a small similar increase is observed up to  $0.33 \text{ }\Omega\cdot\text{cm}^2$  in much longer time namely up to 1800 h. The behavior under anodic current then appears different and more “stable” than under cathodic current.

(a) Under anodic current



(b)



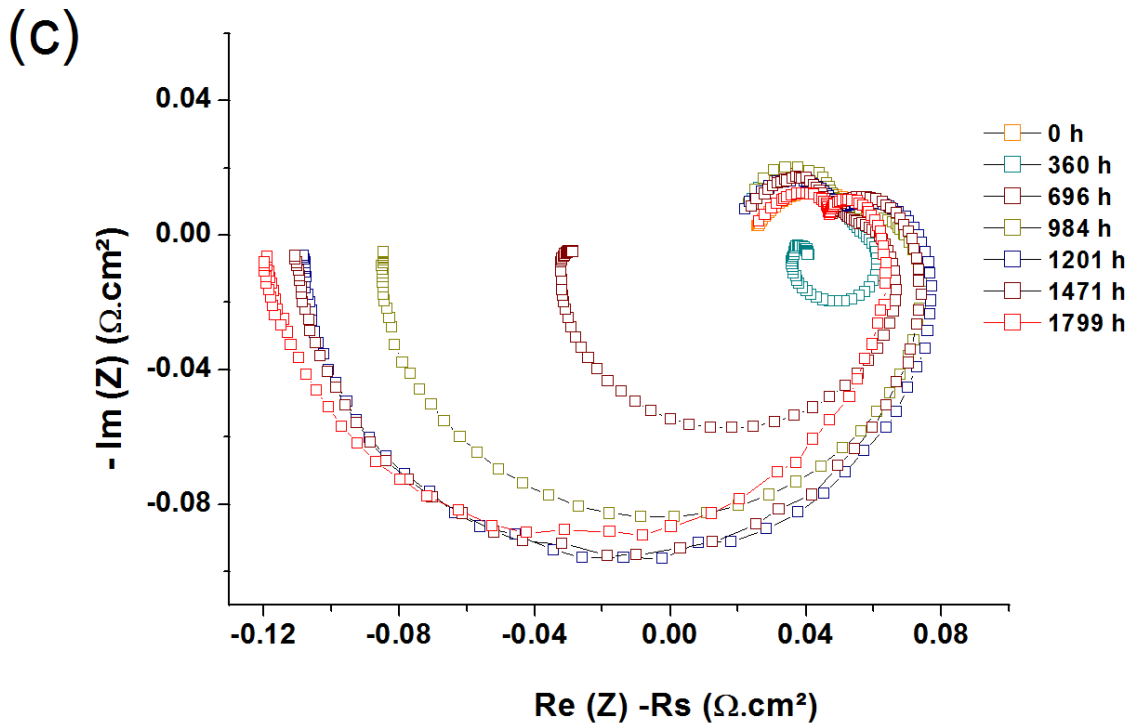


**Figure 6: Evolution of impedance diagrams (Nyquist plot) at 700 °C with time under anodic current ( $i_{dc} = + 300 \text{ mA}\cdot\text{cm}^{-2}$ ) for (a) LNO (b)  $\text{La}_{1.5}\text{Pr}_{0.5}\text{NiO}_{4+\delta}$  and (c) PNO electrode.**

The activity of  $\text{La}_{1.5}\text{Pr}_{0.5}\text{NiO}_{4+\delta}$  electrode under anodic current ( $+300 \text{ mA}\cdot\text{cm}^{-2}$ ) is somewhat complex: during the first few hours of ageing (up to 313 h)  $R_p$  values are almost stable ( $\sim 0.08 \text{ }\Omega\cdot\text{cm}^2$ ). Then the appearance of a small inductive loop is observed at lower frequency (**Figure 6b**). Further ageing leads to an increase in the inductive loop while the electrode contribution itself seems stable. The same behaviour is observed for PNO, the  $R_p$  value remains quite stable while again an inductive loop appears after 360 h of ageing, and increases up to 1800 h of ageing (**Figure 6c**).

#### 3.4.4. Discussion about the inductive loop

At  $t = 0$  *i.e.*  $i_{dc} = 0$  condition, the overall shape of the OER impedance diagrams at the cathodic and anodic side were the same, showing equivalent  $R_p$  values (as an example **Figure 4**). An inductive loop appears in the EIS diagram but only at the anodic side (SOEC mode) within the ageing process. Reinhardt *et al.* showed that change in the potential lines distribution in the solid electrolyte when the EIS measurements frequency varies, can induce distortions in the measured impedance using the three electrode system [35]. Adler suggested that misalignment of the electrodes, or differences in their time constant ( $\tau = R_p C_{dl}$ , where  $R_p$  is the polarization resistance and  $C_{dl}$  is the double layer capacitance of the

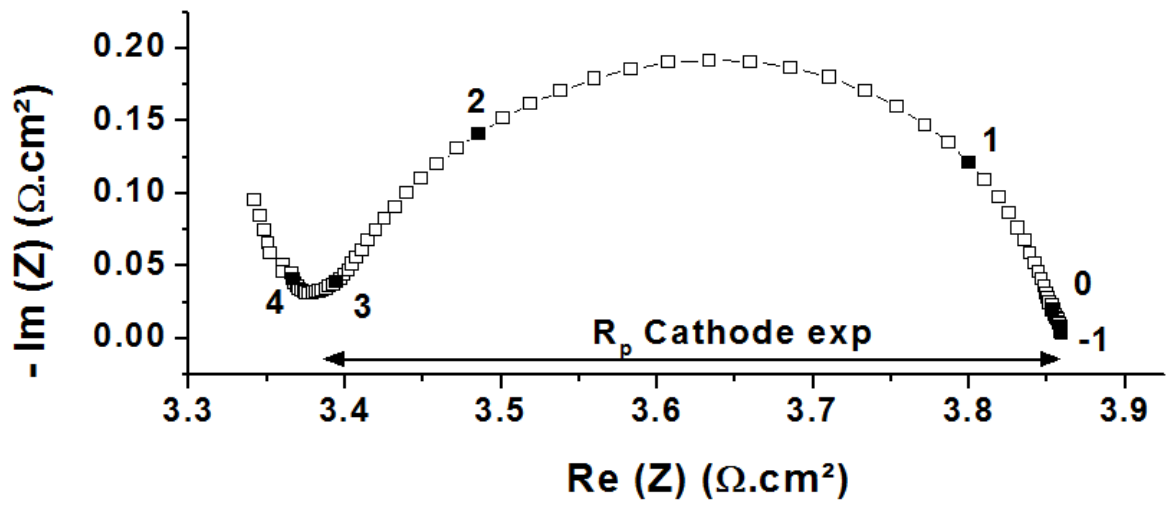
electrode/electrolyte double layer) can generate inductive loops in the impedance spectra, also known as inductive artifacts [29], leading to experimental misinterpretations. In summary, this artifact or distortion appears when the potential probed by the reference electrode is not stable toward the EIS frequency measurement.

In our case, the alignment of the electrode was satisfactory, since the  $R_p$  was the same for both electrodes before starting the ageing process, and no inductive loop was observed (**Figure 4**). During the ageing process, a differentiation in the relaxation time of the phenomena (anode and cathode) could occur, as the electrodes go through chemical changes, with respect to possible additional interface and/or change in composition of the electrode itself as discussed earlier) after few hours of ageing. These phenomena could be responsible for the progressive inductive loop appearance. This indicates that the ageing of the electrode material is different depending on the SOFC or SOEC mode. The calculation of  $R_p$  is complex in this situation. These kinds of impedance spectra (**Figure 6b, c**) lead to large errors in the determination of  $R_p$  and will not be accurate if only the intercept on  $Z'$  -axis of the Nyquist plot is taken into account.

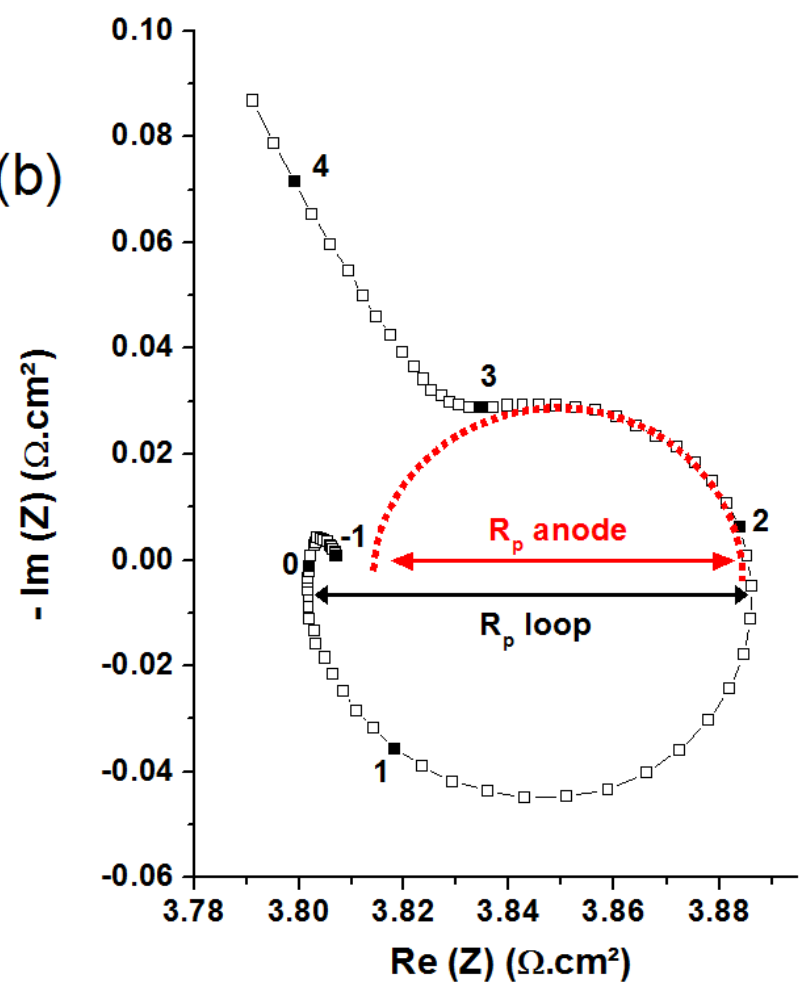
#### 3.4.5. Determination of the “true” $R_p$ in SOFC and SOEC modes

In case of LNO, no inductive loop was observed, and hence the  $R_p$  can be calculated simply fitting the experimental diagram using R//CPE elements. The situation is more complicated in the case of  $\text{La}_{1.5}\text{Pr}_{0.5}\text{NiO}_{4+\delta}$  and PNO because the appearance of the inductive loop. Typical impedance diagrams recorded for the cathodic and anodic side of electrodes (using the three electrode setup,  $i_{dc} \pm 300 \text{ mA}\cdot\text{cm}^{-2}$ ), as well as the global response of the cell (symmetrical measurements, using the two electrode setup,  $i_{dc} = 0$ ) are compared in **Figure 7** for  $\text{La}_{1.5}\text{Pr}_{0.5}\text{NiO}_{4+\delta}$  as an example. The inductive loop is only visible in the anodic side.

(a)



(b)



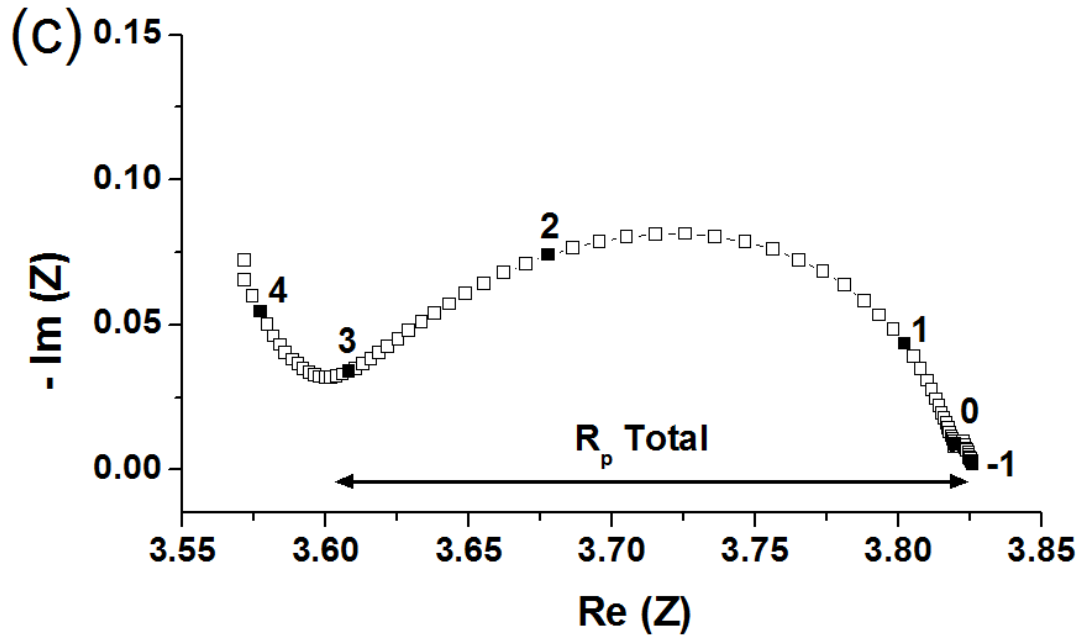


**Figure 7: Nyquist plot of the impedance diagrams, recorded at 700°C a) under current ( $i_{dc} = \pm 300 \text{ mA.cm}^{-2}$ ) after 1800 h for  $\text{La}_{1.5}\text{Pr}_{0.5}\text{NiO}_{4+\delta}$  a) cathodic side, b) anodic side and c) symmetrical half cell (measured by 2 electrode system) on the same sample.**

Usually, the  $R_p$  value is calculated from diagrams recorded on both cathodic and anodic sides, as well as in symmetrical configuration, considering the difference between low and high frequency intercepts on real  $Z$  axis as depicted in **Figure 7**. It is expected that [ $R_{p(\text{total, 2 electrodes})} = (R_{p(\text{anode})} + R_{p(\text{cathode})})/2 \text{ } \Omega.\text{cm}^2$ ], which is not verified in this study, as  $R_{p(\text{total, 2 electrodes})} = 0.23 \text{ } \Omega.\text{cm}^2 < (R_{p(\text{anode})} + R_{p(\text{cathode})})/2 \text{ } \Omega.\text{cm}^2 = 0.27 \text{ } \Omega.\text{cm}^2$ . Actually, the result includes some error because of the appearance of an inductive loop impedance at the anodic side. It is then particularly difficult to separate it from the “true” OER from the cathodic side. Boukamp [31] proposed to fit the loop appearing at one side using a *negative*  $R//C$  parallel circuit, and to use the same  $R//C$  circuit to fit the impedance diagram at the other side – together with the OER processes. The methodology is depicted in **Figure 8 and 9**.

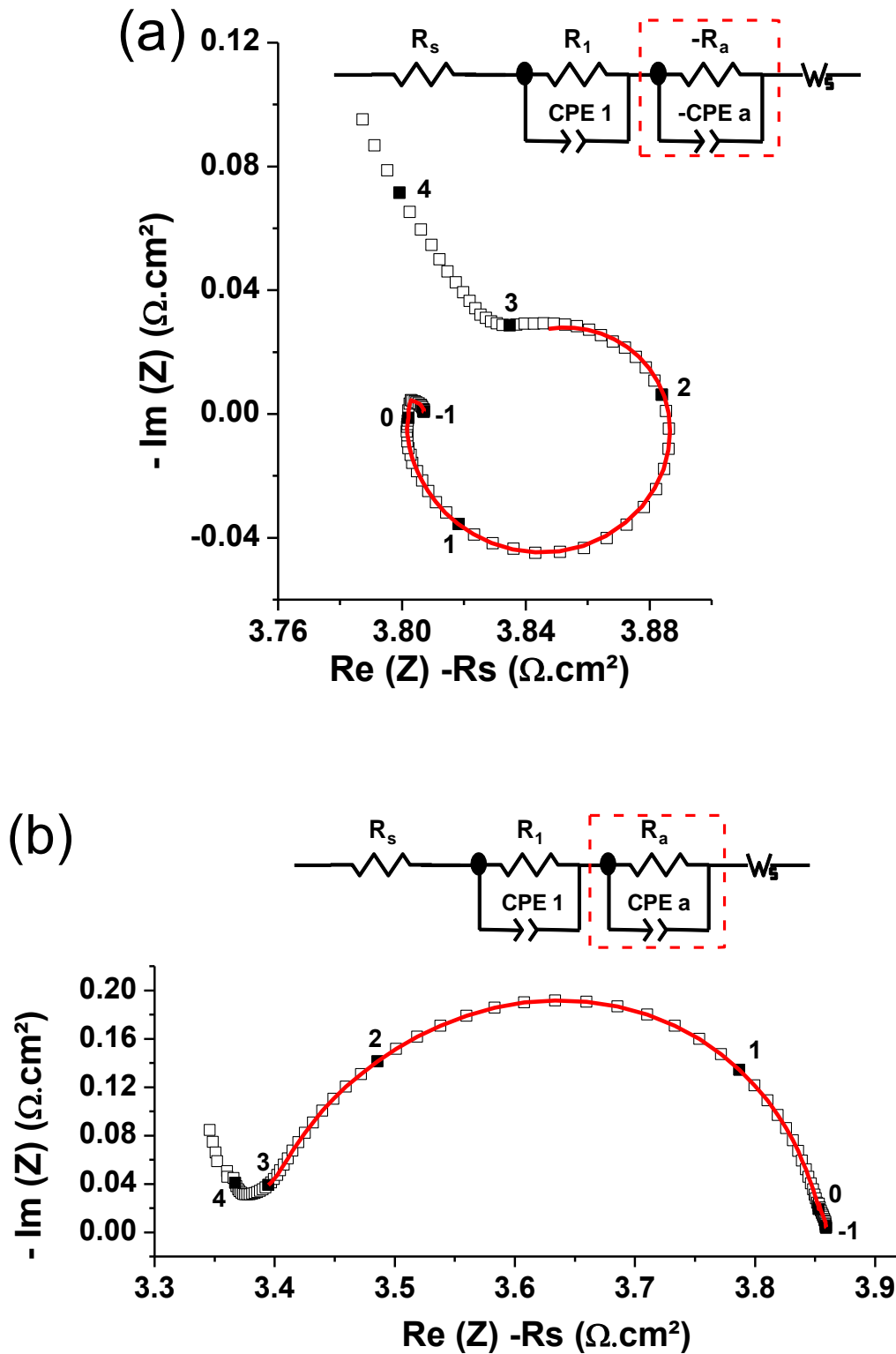


Figure 8: Nyquist plot of  $\text{La}_{1.5}\text{Pr}_{0.5}\text{NiO}_{4+\delta}$  impedance data fitted by Zview at  $700^\circ\text{C}$  under current ( $i_{\text{dc}} = \pm 300 \text{ mA}\cdot\text{cm}^{-2}$ ) after 1800 h a) anodic side and b) cathodic side.

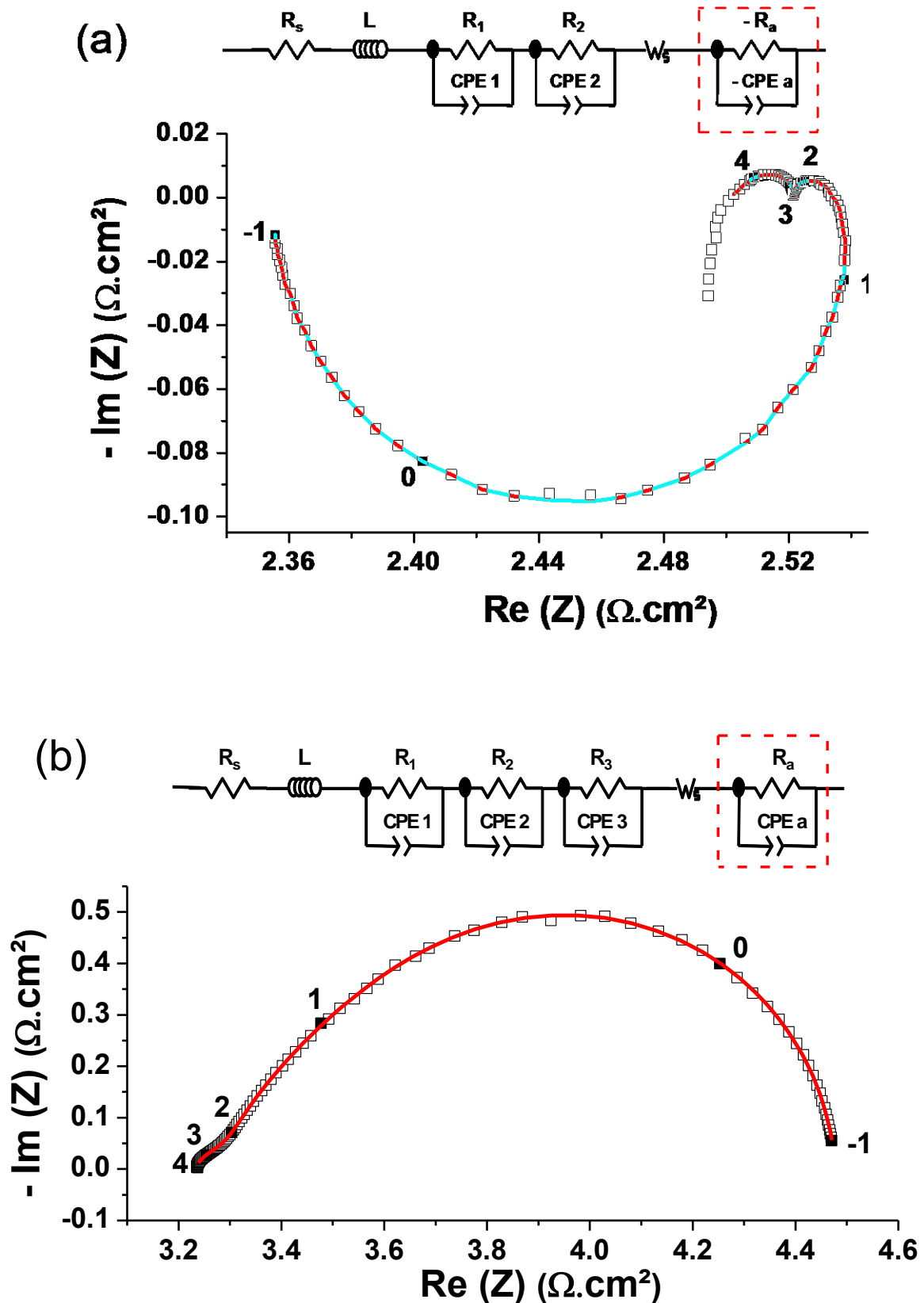


Figure 9: Nyquist plot of PNO with fitting by Zview at 700°C under current ( $i_{dc} = \pm 300 \text{ mA.cm}^{-2}$ ) after 1800 h a) anodic side and b) cathodic side. ( $R_s$  =series resistance and  $L$  = inductance)

For  $\text{La}_{1.5}\text{Pr}_{0.5}\text{NiO}_{4+\delta}$  electrodes, the impedance diagram at the anodic side was fitted considering two contributions: namely  $R1//CPE1$  and  $-Ra//CPEa$  (**Figure 8a**). The 1st and 2nd contributions are for the OER and the artifact, respectively. The impedance diagram at the cathodic side was fitted considering two contributions  $R1//CPE1$  and  $Ra//CPEa$  (**Figure 8b**). The first and second contributions correspond to the OER and the artifact, respectively.

For PNO electrode, the impedance diagram at the anodic side was fitted considering three contributions: namely  $R1//CPE1$ ,  $R2//CPE2$  and  $-Ra//CPEa$  (**Figure 9a**). The 1st and 2nd contributions are attributed to the OER while the 3<sup>rd</sup> contribution is attributed to the artifact. The impedance diagram at the cathodic side was fitted considering four contributions  $R1//CPE1$ ,  $R2//CPE2$ ,  $R3//CPE3$  and  $Ra//CPEa$  (**Figure 9b**). The first three contributions are for OER and/or oxygen diffusion at the interface, and the 4<sup>th</sup> one is for the artifact. Using this methodology, the relation  $[R_p(\text{total, 2 electrodes}) = (R_p(\text{anode}) + R_p(\text{cathode}))/2 \text{ } \Omega.\text{cm}^2]$  was verified, as listed in **Tables 2-3**. Regarding the origin of the additional contributions, it is expected that they could be related to different materials formed during ageing and/or formation of additional interphases at the GDC/electrode interface.

**Table 2:  $R_p$  determined by fitting the impedance data of  $\text{La}_{1.5}\text{Pr}_{0.5}\text{NiO}_{4+\delta}$  (after 1800 h ageing under current)**

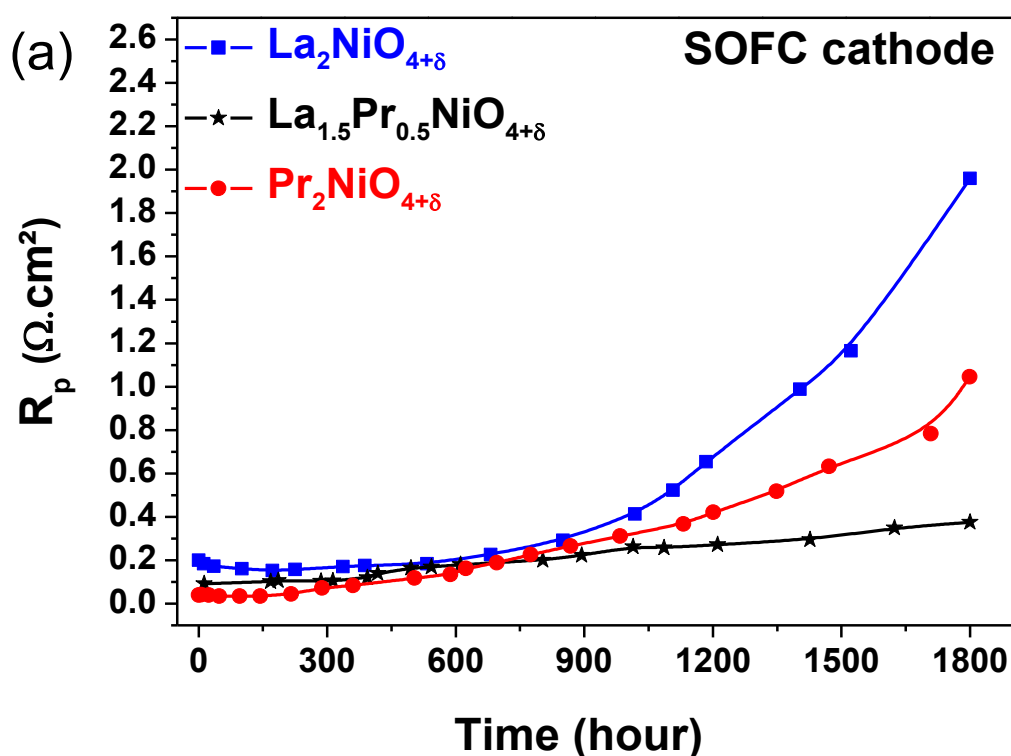
	<b>WE (cathode)</b>	<b>CE (anode)</b>
$R_1 (\Omega)$	<b>0.04</b>	<b>0.19</b>
$R_a (\Omega)$	<b>0.06</b>	<b>-0.06</b>
$R = R_1 (\Omega)$	<b>0.04</b>	<b>0.19</b>
$R_p (\Omega.\text{cm}^2)$	<b>0.08</b>	<b>0.38</b>
$R_{p \text{ total}} = (R_{p, \text{ WE}} + R_{p, \text{ CE}})/2 (\Omega.\text{cm}^2)$	<b>0.23</b>	
$R_{p \text{ total}}$ (by two electrode set up) ( $\Omega.\text{cm}^2$ )	<b>0.23</b>	

**Table 3:  $R_p$  determined by fitting of impedance data of  $\text{Pr}_2\text{NiO}_{4+\delta}$  (after 1800 h ageing under current)**

	WE (cathode)	CE (anode)
$R_1$ ( $\Omega$ )	0.03	0.01
$R_2$ ( $\Omega$ )	0.19	0.01
$R_3$ ( $\Omega$ )	0.40	--
$R_a$ ( $\Omega$ )	0.11	- 0.11
$R = R_1 + R_2 + R_3$ ( $\Omega$ )	0.62	0.02
$R_p$ ( $\Omega \cdot \text{cm}^2$ )	1.06	0.03
$R_{p \text{ total}} = (R_{p, \text{ WE}} + R_{p, \text{ CE}})/2$ ( $\Omega \cdot \text{cm}^2$ )	0.54	
$R_{p \text{ total}}$ (by two electrode set up) ( $\Omega \cdot \text{cm}^2$ )	0.54	

### 3.4.6. Variation of polarization resistance with time

The evolutions of  $R_p$  vs ageing time (up to 1800 h) for LNO,  $\text{La}_{1.5}\text{Pr}_{0.5}\text{NiO}_{4+\delta}$  and PNO are plotted in **Figures 10a and 10b** for cathodic (SOFC mode) and anodic (SOEC mode) sides, respectively. In SOFC mode, the  $R_p$  increases for all three electrodes.



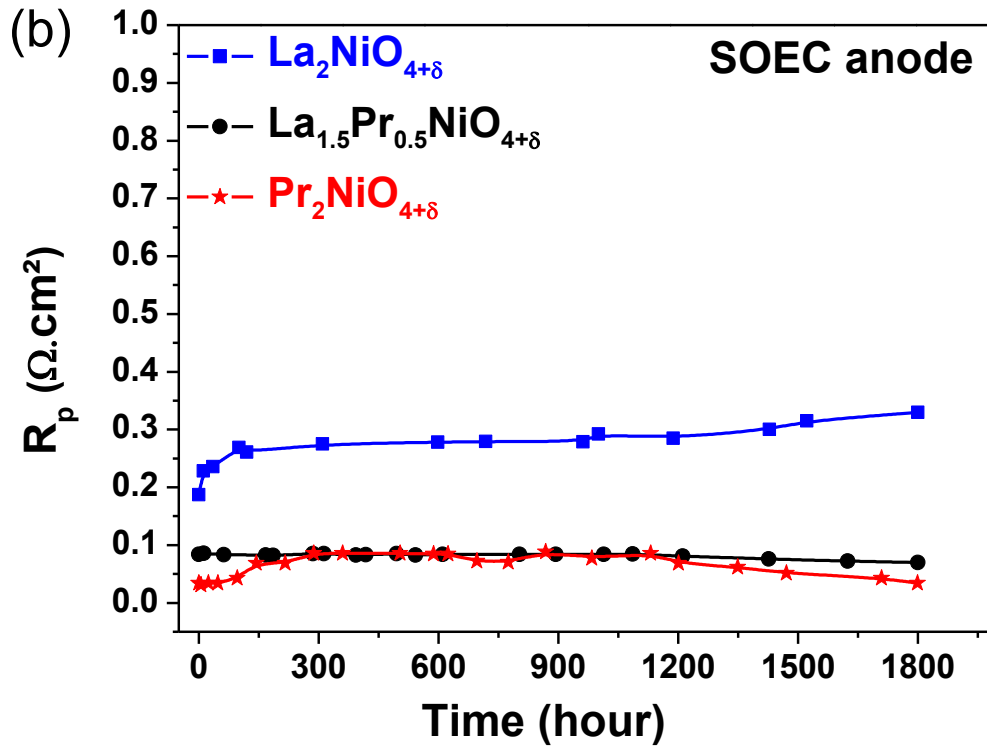


**Figure 10: Variation of  $R_p$  with time for LNO, PNO and  $\text{La}_{1.5}\text{Pr}_{0.5}\text{NiO}_{4+\delta}$  electrodes aged under current ( $i_{\text{dc}} = \pm 300 \text{ mA} \cdot \text{cm}^{-2}$ ) at  $700^\circ\text{C}$  up to 1800 h, (a) in SOFC and (b) in SOEC modes.**

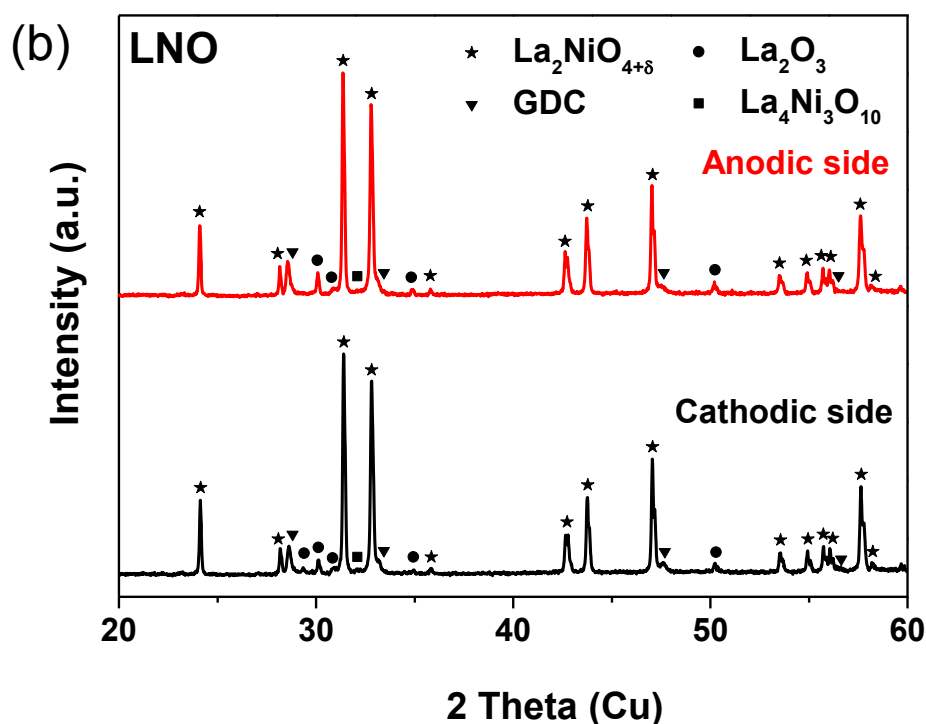
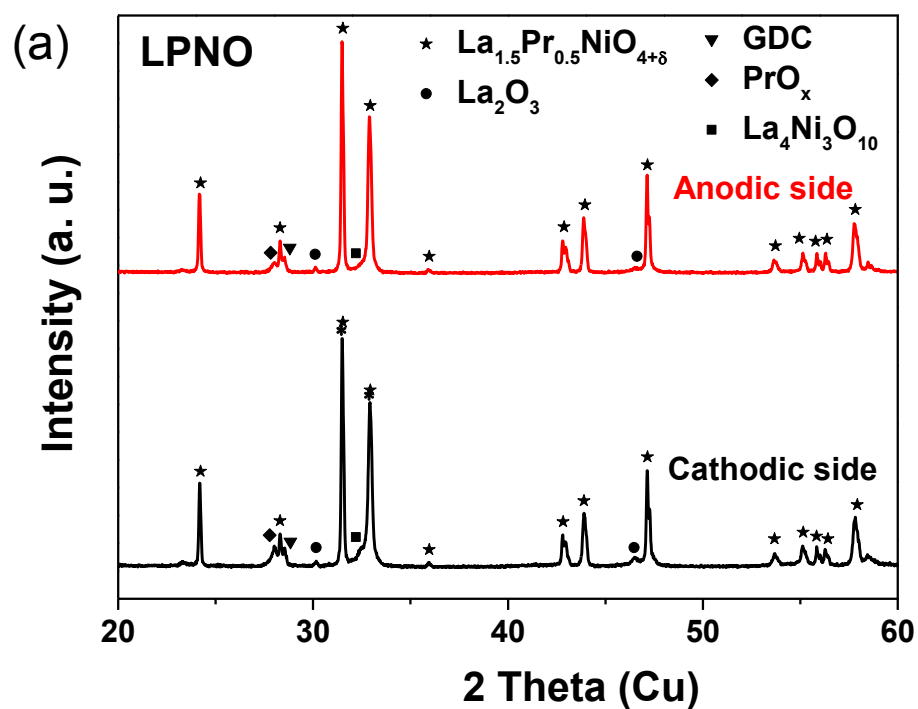
Interestingly, for  $\text{La}_{1.5}\text{Pr}_{0.5}\text{NiO}_{4+\delta}$ , the rate of increase in  $R_p$  is smaller than for PNO and LNO. The rate of increase is much faster for LNO and PNO after 1000 h:  $R_p$  increases  $\sim 35$  times from the initial value ( $0.03$  to  $1.06 \Omega \cdot \text{cm}^2$  at  $700^\circ\text{C}$ ) for PNO and  $\sim 9$  times from the initial value ( $0.21$  to  $1.96 \Omega \cdot \text{cm}^2$  at  $700^\circ\text{C}$ ) for LNO after 1800 h of ageing, while for  $\text{La}_{1.5}\text{Pr}_{0.5}\text{NiO}_{4+\delta}$ , it increases by  $\sim 4$  times ( $0.08$  to  $0.36 \Omega \cdot \text{cm}^2$  at  $700^\circ\text{C}$ ). On the contrary, in SOEC mode all the electrodes show rather stable and constant  $R_p$  values up to 1800 h ageing.

### 3.4.7. Postmortem analyses

In order to understand the evolution of  $R_p$ , post mortem analysis were performed on PNO,  $\text{La}_{1.5}\text{Pr}_{0.5}\text{NiO}_{4+\delta}$  and LNO electrodes just after the electrochemical ageing under current.

### (a) XRD analysis

XRD experiments were performed on the top surface of all the three electrodes after the ageing process under current. Similar XRD patterns are observed at the cathodic and anodic sides for  $\text{La}_{1.5}\text{Pr}_{0.5}\text{NiO}_{4+\delta}$  and LNO electrodes, as shown in **Figures 11 (a, b)**, a slight decomposition being observed whatever the side.



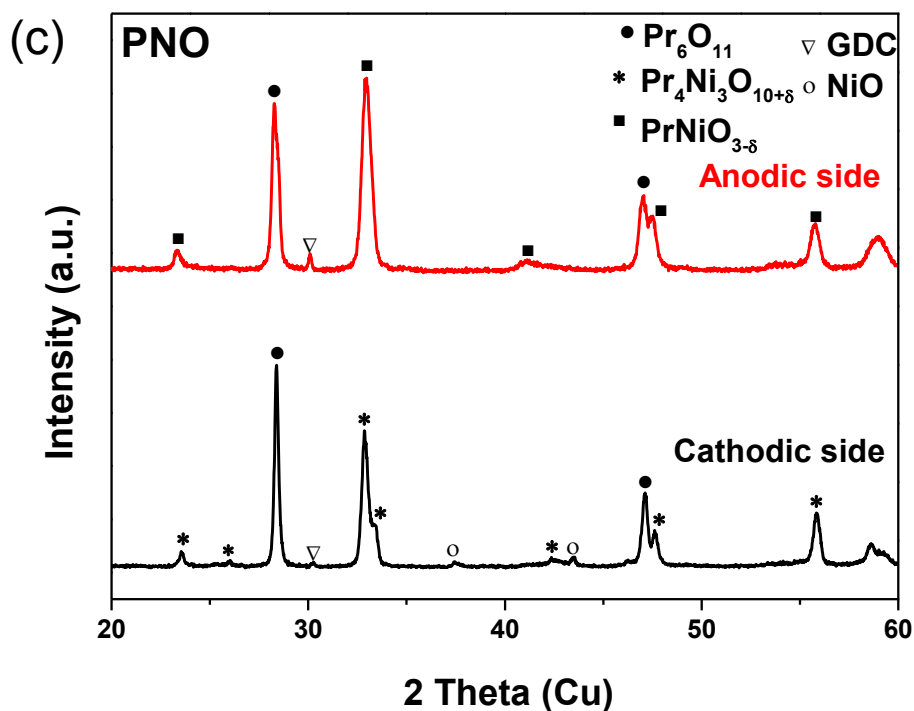


**Figure 11: X-ray patterns after 1800 h ageing under current ( $i_{dc} = \pm 300 \text{ mA.cm}^{-2}$ ) at  $700^\circ\text{C}$  for  $\text{La}_{1.5}\text{Pr}_{0.5}\text{NiO}_{4+\delta}$  (a), LNO (b) and PNO (c) electrodes.**

On the other hand, PNO electrode was completely dissociated on both sides, as shown in **Figure 11c**. On the cathodic side,  $\text{Pr}_4\text{Ni}_3\text{O}_{10+\delta}$ ,  $\text{Pr}_6\text{O}_{11}$  and NiO were observed, whereas on anodic side  $\text{PrNiO}_{3-\delta}$  and  $\text{Pr}_6\text{O}_{11}$  were detected. A small peak of GDC was also observed on both sides. As the local partial pressure of oxygen ( $p\text{O}_2$ ) is higher at anodic side (SOEC mode),  $\text{PrNiO}_{3-\delta}$  was preferentially formed (stable at high  $p\text{O}_2$ ) as expected, contrarily to the cathodic side (SOFC mode) where the  $p\text{O}_2$  is lower.

However, the phase decomposition does not explain the increase of  $R_p$  for the LNO and  $\text{La}_{1.5}\text{Pr}_{0.5}\text{NiO}_{4+\delta}$  electrodes in SOFC mode. It means that the chemical stability of material does not prevent an increase in  $R_p$  for these materials. Then the interface between the electrode and the electrolyte was further considered.

### **(b) Analysis of the interface between electrode and GDC/YSZ**

The interfaces at both sides of the symmetrical half cells were roughly analyzed by scratching the electrodes. As an example, for  $\text{La}_{1.5}\text{Pr}_{0.5}\text{NiO}_{4+\delta}$ , both sides were visually different, the side working in SOFC mode showing a light orange interface, while on the SOEC side the interface was grey (**Figure 12a, b**).

Light orange colour clearly indicates some chemical reactivity at the cathodic side between electrode and GDC, the main hypothesis being the partial diffusion of Pr in the GDC layer [36, 37]. The grey interface towards the anodic side reveals that there is almost no diffusion of Pr-cation into GDC layer.

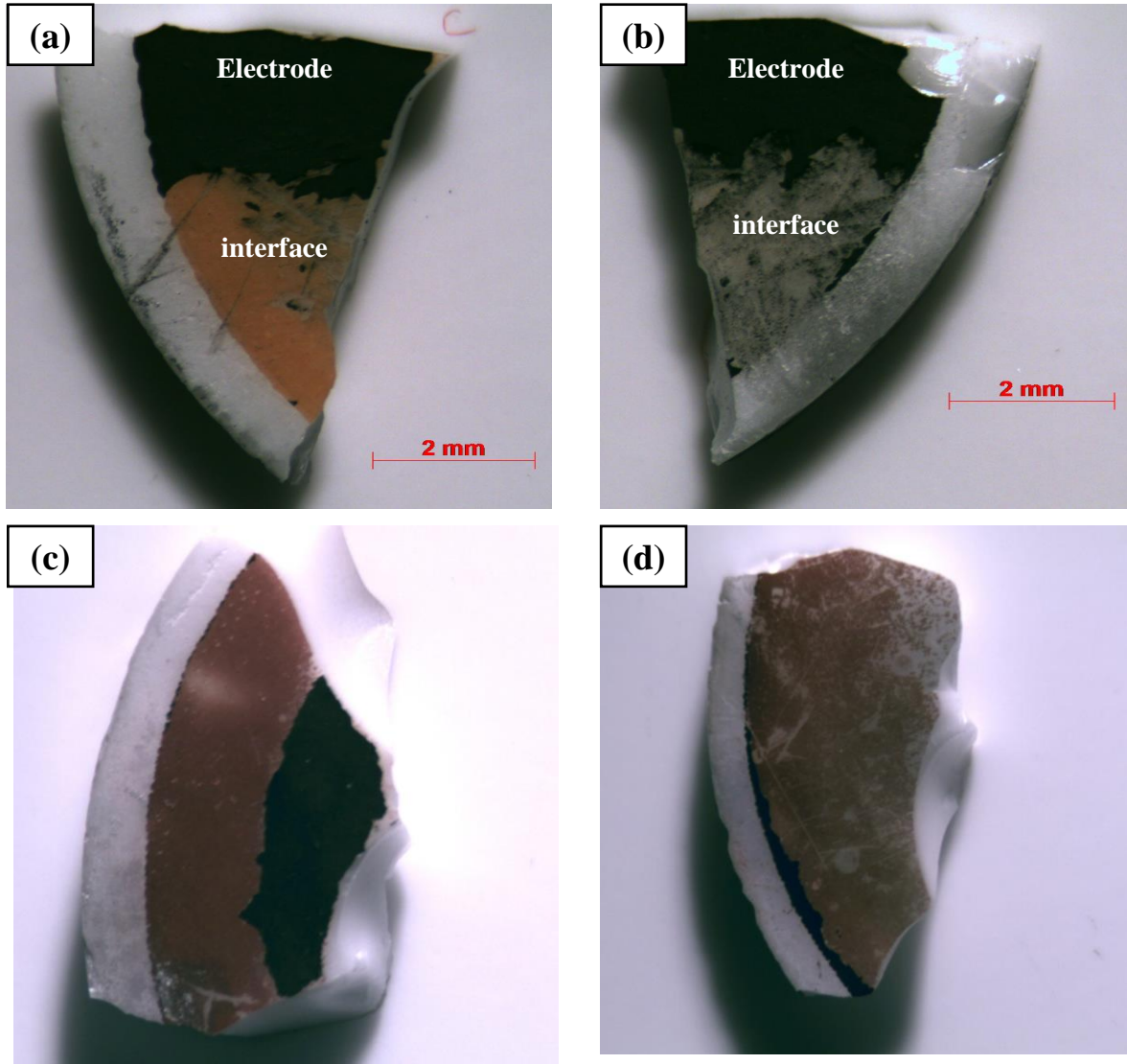


**Figure 12: Interfacial difference between cathodic (a, c) and anodic (b, d) sides after 1800 h ageing under current ( $i_{dc} = \pm 300 \text{ mA}\cdot\text{cm}^{-2}$ ) at  $700^\circ\text{C}$  for  $\text{La}_{1.5}\text{Pr}_{0.5}\text{NiO}_{4+\delta}$  (a, b) and PNO (c, d) electrode.**

In the case of PNO electrodes, both sides are brown, but on the SOFC mode the colour was darker and more intense than on the SOEC side (**Figure 12c, d**), which clearly indicate that on cathodic side the diffusion of Pr-cation is higher than on the anodic side. On the other hand, in case of LNO the interface is grey on both sides (not shown), which doesn't mean that there is no diffusion of La-cation into GDC layer. Indeed, the La-diffusion into GDC leads to

La-doped ceria which is whitish in colour and hence it is not further distinguishable by colour.

Then, as partial conclusions it can be expected that a Pr and/or La *diffusion at the electrode/GDC interface* takes place. The diffusion could occur *via* thermally activated chemical reactivity, but it should be as well driven by the current load, possibly explaining the differences between cathodic and anodic sides.

### (c) FIB-SEM analyses

In order to learn know more about the chemical diffusion at the electrode/GDC interface, FIB-SEM analyses were performed.

We first aim to compare the behavior of the two studied interfaces after ageing under cathodic current: i) for LNO an additional interphase is clearly observed between the electrode and GDC layer (see the white dashed circle on **Figure 13a**), clearly indicating that a chemical reactivity occurs between GDC and the electrode; a La-diffusion into GDC is expected, which was however not visible just looking at the color of the interface as previously explained, ii) on the contrary, only a minor change in the morphology of the GDC layer as well as in the interface between electrode and GDC layer is observed on the  $\text{La}_{1.5}\text{Pr}_{0.5}\text{NiO}_{4+\delta}$  cathodic half cell (**Figure 13b**). With respect to the FIB-SEM results, a slight chemical reactivity could be only suspected (see arrow on **Figure 13b**).

The additional interface layer is absent on the anodic sides whatever the studied half cells (see **Figure 13c** as an example).

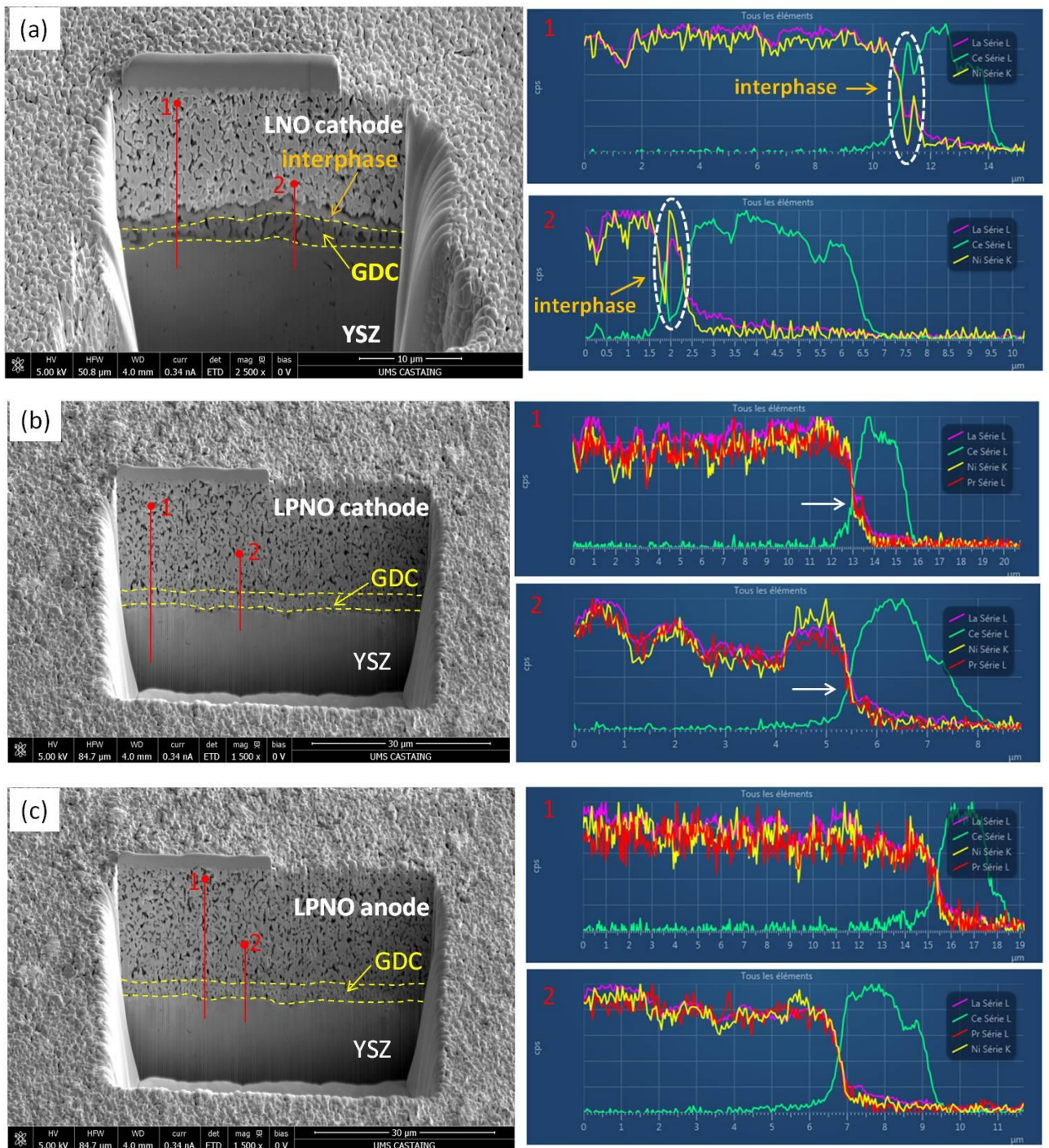


**Figure 13: SEM morphology and EDS of the electrode and interface at (a) LNO cathode side (b)  $\text{La}_{1.5}\text{Pr}_{0.5}\text{NiO}_{4+\delta}$  cathode side and (c)  $\text{La}_{1.5}\text{Pr}_{0.5}\text{NiO}_{4+\delta}$  anode side after 1800 h ageing under current ( $i_{dc} = \pm 300 \text{ mA}\cdot\text{cm}^{-2}$ ) at  $700 \text{ }^\circ\text{C}$ .**

#### (d) Discussion

During ageing either in SOFC or SOEC mode, a chemical reactivity occurs between the nickelates and the GDC layers. It is partly thermally driven then similar on both anodic

and cathodic sides of the cell. However, it is proposed that this chemical reactivity could be as well driven by the current load, being larger on the cathodic sides, especially for PNO and LNO. For instance, the cathodic interface of LPNO is orange (**Figure 12a**), which highlight the presence of Pr-doped ceria [36, 37]. On the contrary, on the anodic side, the interface is grey (**Figure 12b**), leading to conclude to a less pronounced chemical reactivity on this anodic side. Note that corresponding conclusions can't be drawn regarding the cathodic side of PNO (possibly giving orange interfaces as well), because it was not studied due to the delamination, while for LNO both interfaces are grey, but unfortunately it is also the colour of the La-doped ceria.

These differences regarding chemical reactivity lead to differences in electrochemical performance depending on the side, as shown on **Figure 10**. Moreover, the inductive loop in the EIS impedance diagram only appears on the anodic side. The behaviour of the new formed inter-phase (La or Pr-doped ceria) is very important to understand the degradation mechanism.

In case of LNO a large reactivity is observed on the cathodic side (**Figure 13b**). To our opinion, ageing under cathodic current leads to the diffusion of La cation in the GDC layer, forming a thin layer of La-doped ceria. This interphase is seen as the additional contribution in **Figure 5a**, which could be at least partly an oxygen ion blocking layer, leading to the huge increase in  $R_p$ . From the EIS measurements, an additional contribution was also appearing on the cathodic side of LNO half cell (*cf.* **Figure 5a**), which is in very good agreement with this expectation. On the contrary, under anodic current the reactivity is less and hence  $R_p$  seems stable.

In the case of PNO cathode, during ageing under current the diffusion of Pr into GDC layer leads to the formation of a layer of Pr-doped ceria between GDC and the electrode. Contrarily to the previous case, the Pr-doped ceria is known as a MIEC material [36, 37], then probably helping in the formation of an improved electrochemical interface. Then, the reason for the  $R_p$  increase should be different. Then we can suggest two main hypotheses for the increase of  $R_p$  for PNO cathode:

- a) Depending on the considered side (either cathodic or anodic), the local  $pO_2$  on the electrode is different. For ex. on cathodic side the  $O_2$  is reduced hence  $pO_2$  will be low. Contrarily, the  $O_2$  is produced towards anodic side resulting in higher  $pO_2$  at the local scale. We have already observed the effect of  $pO_2$  on each side, as the decomposition product is not the same on both side (*cf.* **Figure 11c**). Moreover, the

behavior of  $\text{Pr}_6\text{O}_{11}$  is different depending on  $p\text{O}_2$ . Under air or slightly low  $p\text{O}_2$  it shows a phase transition from  $\text{Pr}_6\text{O}_{11}$  to  $\text{Pr}_7\text{O}_{12}$  [38] ( $\text{Pr}_6\text{O}_{10.3}$ ) at  $\sim 700^\circ\text{C}$ , then corresponding to an oxygen amount decrease, which may lead to partial delamination of the electrode.

- b) As an additional point, it is also suggested that on the top surface of the cathode side, because of the  $\text{Pr}_6\text{O}_{11}$  segregation, the current collection is reduced, leading to an  $R_p$  increase.

On the anodic side  $R_p$  is not increased even after complete decomposition of PNO, which can be understood according to the following points:

- a) On anodic side the  $p\text{O}_2$  is high and in that condition the transition from  $\text{Pr}_6\text{O}_{11}$  to  $\text{Pr}_7\text{O}_{12}$  is only observed at  $\sim 800^\circ\text{C}$ . Correspondingly, because the ageing was performed at  $700^\circ\text{C}$ , no delamination is noticed.
- b) Moreover the decomposition products on anodic side may be active electrodes.

Finally  $\text{La}_{1.5}\text{Pr}_{0.5}\text{NiO}_{4+\delta}$  shows the most promising electrochemical behavior among all LPNO series. In the La/Pr nickelate, the diffusion of cation is also expected, but small amount of Pr makes the mixed nickelate different from LNO. Under current load, the diffusion of Pr into GDC forms a very thin layer of conducting Pr-doped ceria (orange color, **Figure 12a**), which is indeed helpful to form an improved electrochemical interphase between electrode and GDC layer due to its MIEC property. This Pr-doped ceria would act as a barrier layer for the La-cation diffusion and hence in this case only small increase in  $R_p$  is observed during ageing under cathodic current. On the anodic side again the diffusion of cation is negligible, hence showing stable  $R_p$  values throughout the ageing.

Finally it can be concluded that the formation of conducting interphase is a key point with respect to the long term electrochemical performance of the material.

## 4. Conclusion

This work reports the ageing study of mixed nickelates electrode,  $\text{La}_{2-x}\text{Pr}_x\text{NiO}_{4+\delta}$  (referred as LPNO), by both chemical and electrochemical ways. Initially, the ageing of powders was performed under air during one week then one month at  $600^\circ\text{C}$ ,  $700^\circ\text{C}$  and  $800^\circ\text{C}$ . La-rich nickelates (LNO and  $\text{La}_{1.5}\text{Pr}_{0.5}\text{NiO}_{4+\delta}$ ) are chemically stable, contrarily to the Pr-rich nickelates (PNO,  $\text{LaPrNiO}_{4+\delta}$  and  $\text{La}_{0.5}\text{Pr}_{1.5}\text{NiO}_{4+\delta}$ ). The extent of the decomposition

of LPNO decreases with La content. The end member PNO is completely dissociated into  $\text{PrNiO}_{3-\delta}$ ,  $\text{Pr}_4\text{Ni}_3\text{O}_{10+\delta}$  and  $\text{Pr}_6\text{O}_{11}$ , while the proportions of each phase changed as a function of the ageing temperature. In a second step, electrochemical measurements were performed on LPNO//GDC//YSZ half cells under  $i_{dc}=0$  conditions. As starting performance, the  $R_p$  progressively decreases from LNO ( $0.21 \text{ } \Omega\cdot\text{cm}^2$  at  $700 \text{ } ^\circ\text{C}$ ) to PNO ( $0.03 \text{ } \Omega\cdot\text{cm}^2$  at  $700 \text{ } ^\circ\text{C}$ ) by increasing Pr content. Despite various degrees of chemical stability, and even for a complete dissociation of the end member PNO,  $R_p$  values for all LPNO phases do not show significant change after ageing at  $i_{dc} = 0$  condition. A different behaviour is observed under current ( $i_{dc} = \pm 300 \text{ mA}\cdot\text{cm}^{-2}$  conditions) with a faster degradation (*i.e.* large increase in  $R_p$ ) in SOFC (cathodic) mode. For PNO and LNO, a large increase in  $R_p$  is observed after 1000 h of ageing up to 1800 h, while for  $\text{La}_{1.5}\text{Pr}_{0.5}\text{NiO}_{4+\delta}$ , the rate of increase of  $R_p$  is small. Contrarily, in SOEC (anodic) mode all the electrodes are stable with constant  $R_p$  values up to 1800 h. In this study it can be concluded that the chemical stability of  $\text{La}_{1.5}\text{Pr}_{0.5}\text{NiO}_{4+\delta}$  is the same as LNO even though there is small amount of Pr. The electrochemical performance of  $\text{La}_{1.5}\text{Pr}_{0.5}\text{NiO}_{4+\delta}$  under current is far better than the one of PNO and LNO in SOFC mode. So,  $\text{La}_{1.5}\text{Pr}_{0.5}\text{NiO}_{4+\delta}$  appears the best compromise as cathode in terms of chemical stability and electrochemical performance. Moreover, the chemical stability of the nickelate is not only an issue for the degradation, the major problem arising from the interface between electrode and GDC. The interface should be very efficient to achieve the long term electrochemical performance, either as a conductive interphase or a diffusion barrier layer.

## References

- [1] R. Knibbe, A. Hauch, J. Hjelm, S. D. Ebbesen, M. Mogensen, *Green*, 1 (2011) 141–169.
- [2] H. Yokokawa, H. Tu, B. Iwanschitz, A. Mai, *Journal of Power Sources*, 182 (2008) 400–412.
- [3] R. H. E. Van Doorn, I. C. Fullarton, R. A. De Souza, J. A. Kilner, H. J. M. Bouwmeester, A. J. Burggraaf, *Solid State Ionics*, 96 (1997) 1–7.
- [4] G. C. Kostogloudis, C. Ftikos, *Solid State Ionics*, 126 (1999) 143–151.
- [5] V. V. Kharton, A. P. Viskup, D. M. Bochkov, E. N. Naumovich, O. P. Reut, *Solid State Ionics*, 110 (1998) 61–68.
- [6] J. N. Audinot, *Ph.D. thesis*, Thèse de Doctorat de l'Université de Bordeaux I (1999).
- [7] A. J. Jacobson, *Chemistry of Materials*, 22 (3) (2010) 660–674.
- [8] H. Zhao, F. Mauvy, C. Lalanne, J. M. Bassat, S. Fourcade, J. C. Grenier, *Solid State Ionics*, 179 (2008) 2000–2005.
- [9] A. Aguadero, J. A. Alonso, M. J. Martinez-Lope, M.T. Fernandez-Diaz, M. J. Escudero, L. Daza, *Journal of Materials Chemistry*, 16 (2006) 3402–3408.
- [10] J. M. Bassat, P. Odier, J. P. Loup, *Journal of Solid State Chemistry*, 110 (1994) 124–135.

- [11] E. Boehm, J. M. Bassat, P. Dordor, F. Mauvy, J. C. Grenier, P. Stevens, *Solid State Ionics*, 176 (2005) 2717–2725.
- [12] C. Ferchaud, J. C. Grenier, Y. Zhang-Steenwinkel, M. M. A. Van Tuel, F. P. F. Van Berkel, J. M. Bassat, *Journal of Power Sources*, 196 (2011) 1872–1879.
- [13] C. N. Munnings, S. J. Skinner, G. Amow, P. S. Whitfield, I. J. Davidson, *Solid State Ionics*, 176 (2005) 1895–1901.
- [14] L. Minervini, R. W. Grimes, J. A. Kilner, K. E. Sickafus, *Journal of Materials Chemistry*, 10 (2000) 2349–2354.
- [15] A. Flura, S. Dru, C. Nicollet, V. Vibhu, S. Fourcade, E. Lebraud, A. Rougier, J. M. Bassat, J. C. Grenier, *Journal of Solid State Chemistry*, 228 (2015) 189–198.
- [16] V. Vibhu, A. Rougier, C. Nicollet, A. Flura, J. C. Grenier, J. M. Bassat, *Solid State Ionics*, 278 (2015) 32 – 37.
- [17] A. Montenegro-Hernandez, J. Vega-Castillo, L. Mogni, A. Caneiro, *International Journal of Hydrogen Energy*, 36 (2011) 15704–15714.
- [18] A. V. Kovalevsky, V. V. Kharton, A. A. Yaremchenko, Y. V. Pivak, E. N. Naumovich, J. R. Frade, *Journal of the European Ceramic Society*, 27 (2007) 4269–4272.
- [19] A. V. Kovalevsky, V. V. Kharton, A. A. Yaremchenko, Y. V. Pivak, E. V. Tsipis, S. O. Yakovlev, A. A. Markov, E. N. Naumovich, J. R. Frade, *Journal of Electroceramics*, 18 (2007) 205–218.
- [20] P. Courty, H. Ajot, C. Marcilly, B. Delmon, *Powder Technology*, 7 (1973) 21–38.
- [21] A. Rougier, A. Flura, C. Nicollet, V. Vibhu, S. Fourcade, E. Lebraud, J. M. Bassat, J. C. Grenier, *ECS Transaction*, 68 (2015) 817–823.
- [22] C. Solis, L. Navarrete, J. M. Serra, *Journal of Power Sources*, 240 (2013) 691–697.
- [23] V. Vibhu, J. M. Bassat, A. Flura, C. Nicollet, N. Penin, J. C. Grenier, A. Rougier, *Submitted in Journal of Material Chemistry A*, (2015).
- [24] V. Vibhu, A. Rougier, C. Nicollet, A. Flura, S. Fourcade, N. Penin, J. C. Grenier, J. M. Bassat, *Submitted in Journal of Power Sources*, (2015).
- [25] S. B. Adler, *Chemical Reviews*, 104 (2004) 4791–4843.
- [26] T. Jacobsen, P. V. Hendriksen, S. Koch, *Electrochimica Acta*, 53 (2008) 7500–7508.
- [27] S. Primdahl, M. Mogensen, *Journal of the Electrochemical Society*, 146 (1999) 2827–2833.
- [28] S. B. Adler, *Journal of the Electrochemical Society*, 149 (2002) E166–E172.
- [29] S. B. Adler, B. T. Henderson, M. A. Wilson, D. M. Taylor, R. E. Richards, *Solid State Ionics*, 134 (2000) 35–42.
- [30] J. Winkler, P. V. Hendriksen, N. Bonanos, M. Mogensen, *Journal of the Electrochemical Society*, 145 (1998) 1184–1192.
- [31] B. A. Boukamp, *Solid State Ionics*, 143 (2001) 47–55.
- [32] M. Cimenti, V. I. Birss, J. M. Hill, *Fuel Cells*, 7 (2007) 377–391.
- [33] M. Cimenti, A. C. Co, V. I. Birss, J. M. Hill, *Fuel Cells*, 7 (2007) 364–376.
- [34] M. J. Jorgensen, M. Mogensen, *Journal of the Electrochemical Society*, 148 (5) (2001) A433–A442.
- [35] G. Reinhardt, W. Gopel, *Ionic and mixed conducting ceramic III* (Eds. T. A. Ramanarayanan, W. L. Worrell, H. L. Tuller, M. Mogensen, A. A. Khandkar), (1997) 610–630.
- [36] P. Shuk, M. Greenblatt, *Solid State Ionics*, 116 (1999) 217–223.
- [37] R. Chockalingam, A. K. Ganguli, S. Basu, *Journal of Power Sources*, 250 (2014) 80–89.
- [38] B. G. Hyde, D. J. M. Bevan, L. Eyring, *Philosophical Transaction of the Royal Society of London, Series A, Mathematical and Physical Sciences*, (1966).

## Additional Information: Chapter 4

### 1. Three electrode set-up for EIS measurements

In order to perform the electrochemical ageing measurements under current, the three electrodes geometry was used, in which a reference electrode was set around the edge of the thick 8YSZ electrolyte. The corresponding setup is shown in **Figure 1**.

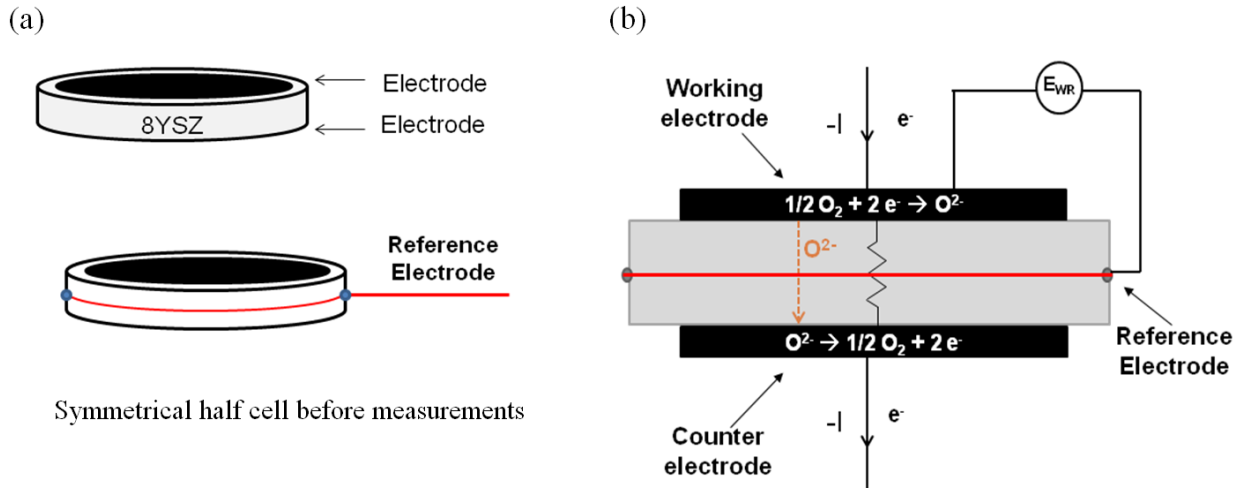


**Figure 1: a) Architecture of symmetrical half cell, b) Schematic of three electrode set-up.**

For the electrochemical ageing experiments, a negative current is supplied from the working electrode (WE). In this manner, the WE electrode behaves as cathode side for SOFC and the counter electrode (CE) behaves as anode side of SOEC (Solid Oxide Electrolyzer Cell). It is then possible to investigate the behavior of electrode on both SOFC and SOEC conditions.

### 2. Long term ageing of $La_{2-x}Pr_xO_{4+\delta}$ ( $x = 0.0, 0.5, 1.0, 1.5$ and $2.0$ ) phases under argon

Long term ageing of all LPNO powders was also investigated for 1 month at 700 °C under argon. Interestingly the mixed nickelates are stable under argon for one month. The X-ray diffraction pattern of  $Pr_2NiO_{4+\delta}$  after one month ageing at 700 °C is compared with as prepared powder in **Figure 2**, as an example.

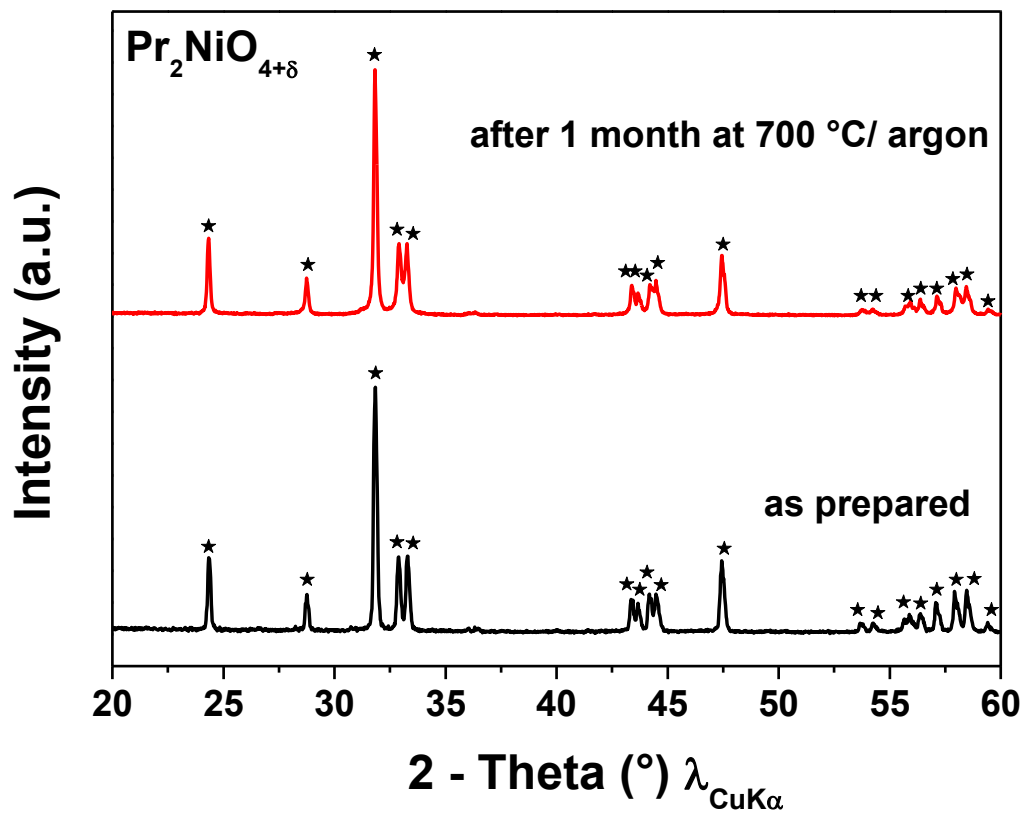


Figure 2: X-ray diffraction patterns of  $\text{Pr}_2\text{NiO}_{4+\delta}$  powders for as prepared and after ageing at 700 °C for 1 month under argon.



# Chapter 5

---

*“Submitted to Solid State Electrochemistry, 2016”*

# Structural and stability studies of PrNiO<sub>3-δ</sub> and characterization as air electrode in SOFCs

Vaibhav Vibhu, Jean-Marc Bassat, Aurélien Flura, Clément Nicollet, Nicolas Penin, Jean-Claude Grenier and Aline Rougier\*

CNRS, Université de Bordeaux, Institut de Chimie de la Matière Condensée de Bordeaux (ICMCB), 87 Av. Dr Schweitzer, F-33608 Pessac Cedex, France.

## Abstract

Careful investigation of the thermal stability and electrochemical properties of PrNiO<sub>3-δ</sub> phase, as cathode for Solid Oxide Fuel Cells (SOFCs) is reported. PrNiO<sub>3-δ</sub>, synthesized from citrate-nitrate route, crystallizes in an orthorhombic structure (S.G. : *Pbnm*). Under air, a transition to high temperature rhombohedral structure (S.G. : *R-3c*) occurs at around 600 °C. The variation of the oxygen content (3-δ) investigated as a function of temperature in various atmospheres (air, oxygen and argon) shows that PrNiO<sub>3-δ</sub> remains always sub-stoichiometric, starting from δ ≈ 0.05 at room temperature. Thermal gravimetry analysis (TGA) measurements coupled with X-ray diffraction (XRD) characterizations are used to compare the PrNiO<sub>3-δ</sub> phase stability in air, oxygen and argon. Above 800 °C (in Ar), 1000 °C (in air) and 1040 °C (in oxygen), PrNiO<sub>3-δ</sub> starts to decompose into Pr<sub>2</sub>NiO<sub>4+δ</sub> and NiO in a single step under Ar while intermediate transformation into Pr<sub>4</sub>Ni<sub>3</sub>O<sub>10+δ</sub> is observed under air and oxygen. The polarization resistance ( $R_p$ ) of co-sintered GDC-PrNiO<sub>3-δ</sub> electrode is of 0.91 Ω.cm<sup>2</sup> at 600 °C under air, while the value is about half ( $R_p \sim 0.46$  Ω.cm<sup>2</sup>) for a two-step sintered half-cell.

## 1. Introduction

Over the last few decades, there has been a growing interest towards fuel cell development. Due to high operating temperatures of Solid Oxide Fuel Cells (SOFCs), high quality heat is produced (at the same time as electricity) in the form of steam which can be used further for instance for the production of hydrogen by High Temperature Steam Electrolysis. The efficiency of SOFC is the highest among the other kind of fuel cells because of combined heat and power (CHP) technology. Nowadays many efforts are being carried out towards identifying an adequate cathode material for solid oxide fuel cells (SOFCs) working at intermediate temperatures ~700 °C because of too high over-potentials values at this side

of the cell. The promising materials for cathodes are Mixed Ionic and Electronic Conducting (MIEC) oxides [1-6]. If on one side,  $\text{La}_{0.6}\text{Sr}_{0.4}\text{Co}_{0.2}\text{Fe}_{0.8}\text{O}_{3-\delta}$  (LCSF) or  $\text{La}_{0.5}\text{Sr}_{0.5}\text{CoO}_{3-\delta}$  (LSC) remain largely investigated in respect of high performance ( $R_p = 0.13 \Omega\cdot\text{cm}^2$  at 600 °C for LCSF electrode [7]), on the other side rare earth nickelates,  $\text{Ln}_2\text{NiO}_{4+\delta}$  (Ln = La, Pr and Nd) compounds with the  $\text{K}_2\text{NiF}_4$ -type structure are promising candidates [8-10]. Among all the three nickelates,  $\text{Pr}_2\text{NiO}_{4+\delta}$  shows excellent electrochemical properties at intermediate temperature [11]. In a careful investigation, we recently reported that  $\text{Pr}_2\text{NiO}_{4+\delta}$  decomposes into  $\text{PrNiO}_{3-\delta}$ ,  $\text{Pr}_4\text{Ni}_3\text{O}_{10+\delta}$  and  $\text{Pr}_6\text{O}_{11}$  during long term operation at temperatures ranging between 600 to 800 °C [12]. However, it was evidenced that even after complete chemical dissociation of the material the electrochemical performance under  $i_{dc} = 0$  conditions do not show significant change (i.e.  $R_p$  remains the same). Aiming at a better understanding of the  $\text{Pr}_2\text{NiO}_{4+\delta}$  behaviour, the properties of  $\text{PrNiO}_{3-\delta}$ ,  $\text{Pr}_4\text{Ni}_3\text{O}_{10+\delta}$  were investigated. Herein, we focus our attention on the study of  $\text{PrNiO}_{3-\delta}$  while the one of  $\text{Pr}_4\text{Ni}_3\text{O}_{10+\delta}$  will be reported in a forthcoming paper [13].

The lanthanide perovskite oxides  $\text{LnNiO}_3$  (Ln= La, Pr and Nd) have been largely studied in the frame of high temperature superconductivity [14-20].  $\text{LnNiO}_3$  (Ln= La, Pr, Nd) compounds crystallize in a distorted orthorhombic perovskite structure belonging to  $Pbnm$  space group symmetry [14]. In these perovskites, the electrical conduction mechanism is directly dependent of the oxygen content. An increase in the amount of oxygen vacancies leads to a drastic change in the electrical conductivity from metal to insulator. For instance,  $\text{LaNiO}_3$ ,  $\text{LaNiO}_{2.75}$  and  $\text{LaNiO}_{2.5}$  exhibit metallic, metal-insulator transition and insulating behaviour, respectively, at temperature lower than 300 K.  $\text{PrNiO}_3$  and  $\text{NdNiO}_3$  also reveal a first order metal-insulator transition in 130-400 K temperature range [14], while  $\text{PrNiO}_3$  shows the highest electrical conductivity among  $\text{LnNiO}_3$  (Ln = Nd, Pr and Sm) in low temperature range (from 100–200 K) [14]. In addition, differential scanning calorimetric measurements on  $\text{PrNiO}_3$  reveal a first order phase transition at 780 K [20].

In the literature, the synthesis of stoichiometric  $\text{PrNiO}_3$  required high oxygen pressures as it is not easy to synthesize this phase at oxygen pressure  $p\text{O}_2 \leq 1$  atm,  $\text{Ni}^{3+}$  being difficult to stabilize. However as stated above, the oxygen stoichiometry (i.e. amount of oxygen vacancies) is a key feature in the perovskites properties. Synthesis of deficient perovskites  $\text{LnNiO}_{3-\delta}$  (Ln= La, Pr, Nd), have been reported on

LaNiO<sub>3-δ</sub> and NdNiO<sub>3-δ</sub> phases having small values of sub-stoichiometry [21-23], but to the best of our knowledge, no data is available yet for PrNiO<sub>3-δ</sub> in the literature. The combination of high electrical conductivity and sufficient concentration of disordered oxygen vacancies should lead to MIEC properties allowing sub-stoichiometry perovskites as oxygen electrode in the field of Solid Oxide Fuel Cells (SOFCs). In this work, we focus on the properties of PrNiO<sub>3-δ</sub>, mainly the structural and thermal stability, the electronic properties prior to the investigation of their electrochemical activity under air as oxygen electrode for SOFCs. In the field of SOFCs, recent evolutions towards the development of metal supported cells, MSCs also called 3<sup>rd</sup> generation of SOFC, required to sinter the electrode materials at high temperature under low *p*O<sub>2</sub> to avoid any detrimental oxidation of the metallic substrate. Aiming at fully investigating the suitability of PrNiO<sub>3-δ</sub> as oxygen electrode, herein, thermal stabilities in argon, air and oxygen atmospheres are compared allowing a further determination of the most appropriate sintering conditions.

## 2. Experimental

### Synthesis of powder

PrNiO<sub>3-δ</sub> was synthesised using the citrate-nitrate route (modified Pechini method) from Pr<sub>6</sub>O<sub>11</sub> (Aldrich Chem, 99.9%), and Ni(NO<sub>3</sub>)<sub>2</sub>.6H<sub>2</sub>O (Acros Organics, 99%) precursors [24]. The Pr<sub>6</sub>O<sub>11</sub> powder was pre-fired at T = 900 °C overnight to remove the remaining water content due to its highly hygroscopic character. After the auto combustion step, a final annealing was performed at 850 °C for 48 h under oxygen flow and repeated eight times leading to well crystallized phases.

### X-ray diffraction analysis

The as-prepared PrNiO<sub>3-δ</sub> powder was first characterized by X-ray diffraction (XRD) at room temperature using a PANanalytical X'pert MPD diffractometer with Cu-Kα incident radiation to check the phase purity. XRD *vs.* T, *i.e.* *in situ* XRD were afterwards, performed to check the stability of this phase with temperature under air. The XRD data were collected for both heating and cooling, after each 100 °C (for the 500-700 °C temperature range, the data were recorded after each 50 °C in order to carefully investigate the phase transition) up to 950 °C. The heating and cooling rate

was fixed to  $2\text{ }^{\circ}\text{C}\cdot\text{min}^{-1}$ . After reaching a given temperature, the powder was equilibrated for 1 h and then the XRD data was recorded. With respect to thermodynamic equilibrium reached more easily, the XRD diffractogram of powder during cooling is reported here. Ageing of the phase was performed under air. Pellets were first prepared and then left into a furnace for one month at 600, 700 and 800  $^{\circ}\text{C}$  before XRD characterization. The X-ray diffraction patterns were fitted by profile matching using the Fullprof software.

### **Thermo Gravimetric Analysis (TGA)**

TGA experiments were carried out using a TA Instrument TGA-Q50 device, with the aim *i)* to determine the oxygen deficiency, *i.e.* the delta value,  $\delta$ , at room temperature after heated the material in air up to 800  $^{\circ}\text{C}$  then cooled down to room temperature with a slow rate ( $2\text{ }^{\circ}\text{C}\cdot\text{min}^{-1}$ ), this cycle being reproduced twice to ensure the reproducibility. Then, the determination of the oxygen stoichiometry was achieved via the decomposition of the material into Ni metal and  $\text{Pr}_2\text{O}_3$  under Ar -5%  $\text{H}_2$  flux with a very slow heating rate of ( $0.5\text{ }^{\circ}\text{C}\cdot\text{min}^{-1}$ ), *ii)* to investigate its thermal stability under air, oxygen and argon atmospheres and *iii)* to study the  $\delta$  variation *vs.*  $T$  in the domain of stability, under air ( $p\text{O}_2 = 0.21\text{ atm}$ ), oxygen ( $p\text{O}_2 = 1\text{ atm}$ ) and argon atmosphere ( $p\text{O}_2 \approx 10^{-4}\text{ atm}$ ).

### **Conductivity measurements**

The electrical conductivity was determined under air using the four-probe technique, in the temperature range 25 - 800  $^{\circ}\text{C}$  with heating and cooling rates of  $1\text{ }^{\circ}\text{C}\cdot\text{min}^{-1}$ . The green pellet of  $\text{PrNiO}_{3-\delta}$  was previously sintered at 900  $^{\circ}\text{C}$  for 24 h (density  $\sim 65\%$ ). Two cycles were performed to confirm the reproducibility of measurement.

### **Preparation of symmetrical half cells and electrochemical measurements**

For the electrochemical studies, symmetrical half cells (electrode//GDC//8YSZ//GDC//electrode) were prepared. To increase the electrochemical performance [11], a GDC layer was added between the electrolyte and the cathode.

Dense pellets of 8YSZ (8 mol. % yttria stabilized zirconia) with diameter  $\approx$  18 mm and thickness  $\approx$  1.2 mm were used as electrolyte. Terpeneol-based inks were prepared from  $\text{PrNiO}_{3-\delta}$  and GDC powder (from Rhodia) for screen printing the cathode and the barrier layer, respectively.

The symmetrical half-cells were prepared using two ways, either a two-step sintering process or by co-sintering. At first, a 2  $\mu\text{m}$  GDC layer was screen printed on both sides of the 8YSZ electrolyte pellets and sintered at 1300  $^{\circ}\text{C}$  for 1 h in air. The electrode layer was then screen printed on each side. Several sintering temperatures were tried starting from 900  $^{\circ}\text{C}$  to 1150  $^{\circ}\text{C}$  in air with the aim to optimize the sintering conditions of the cathode.

In a second way, the symmetrical half-cells were prepared by co-sintering GDC and the electrode. For this purpose, single layer of GDC ink was first deposited on both sides of YSZ pellet and dried at  $T \sim 80$   $^{\circ}\text{C}$ ; then, the electrode layer was deposited on both sides. Finally, both layers were co-sintered at 950  $^{\circ}\text{C}$  for 2 h in air. The electrochemical properties of the symmetrical half cells were characterized by Electrochemical Impedance spectroscopy, EIS. The initial EIS measurements were carried out under air, in the temperature range 500 – 800  $^{\circ}\text{C}$  under zero dc conditions. Gold grids (1.024  $\text{cm}^{-2}$  mesh) were used as current collectors. The impedance diagrams were recorded at steady state under potentiostatic control with 50 mV ac amplitude, from  $10^6$  Hz down to  $10^{-1}$  Hz, using a frequency response analyser module Autolab FRA2, coupled with a potentiostat/galvanostat PGSTAT 302N.

The complex impedance diagrams were fitted using an equivalent circuit by means of the Zview<sup>®</sup> (Scribner Associates) software in order to extract the polarization resistance ( $R_p$ ) values. The  $R_p$  values were calculated from the difference between the low frequencies (LF) and the high frequencies (HF) diagram intercepts with the  $Z'$  axis of the Nyquist representation.

### 3. Results and discussion

#### 3.1. XRD Analysis

The XRD characterization of the powder shows that as-synthesized  $\text{PrNiO}_{3-\delta}$  phases are well crystallized in an orthorhombic structure described by  $Pbnm$  space

group. Two extra small peaks corresponding to non-reactive NiO as well as traces of PrO<sub>x</sub> are also detected.

In the literature, synthesis of pure phase is only reported under oxygen pressure. Aqino *et al.* have also synthesized PrNiO<sub>3</sub> using Pechini method but with very large amount of Pr<sub>6</sub>O<sub>11</sub> and NiO as impurities [25]. The full pattern profile matching is shown in **Figure 1**. The lattice parameters  $a = 5.4254(4) \text{ \AA}$ ,  $b = 5.3882(5) \text{ \AA}$  and  $c = 7.6414(4) \text{ \AA}$  are slightly higher than those reported by Lacorre *et al.* [20] and Huang *et al.* [26] for stoichiometric PrNiO<sub>3</sub>. This trend can be related to oxygen deficiency (*i.e* positive  $\delta$  values as determined below) associated with the presence of larger Ni<sup>2+</sup> than Ni<sup>3+</sup> ( $r(\text{Ni}^{3+}) \approx 0.60 < r(\text{Ni}^{2+}) \approx 0.69$ ) [27].

In addition, a close examination of the XRD pattern shows asymmetric tails located at the right side of some reflections, including (002) and (022). The anisotropic peak broadening mainly results from stacking faults, as earlier reported for SmNiO<sub>3</sub> and GdNiO<sub>3</sub> at room temperature by Alonso *et al.* [28].

### 3.1.1. Stability with Temperature (XRD vs. T)

The evolution of the X-ray patterns vs. T shows that the PrNiO<sub>3- $\delta$</sub>  phase remains stable up to 950 °C (**Figure 2**) while a structural transition from orthorhombic (S.G. Pbm<sub>n</sub>) to rhombohedral (S.G.  $R\text{-}3c$ ) occurs at about 600 °C, which is in good agreement with Huang *et al.* data [26]. The transition is completely reversible.

The full pattern profile matching of the XRD patterns was performed for all temperatures, which allows the determination of the lattice parameters and the calculation of the volume of the unit cell and TECs.

### 3.1.2. Variation of lattice parameters and TECs

The thermal variation of the lattice parameters is shown in **Figure 3a**. The lattice parameters of orthorhombic and rhombohedral unit cells were first normalized with respect to cubic unit cell [29].

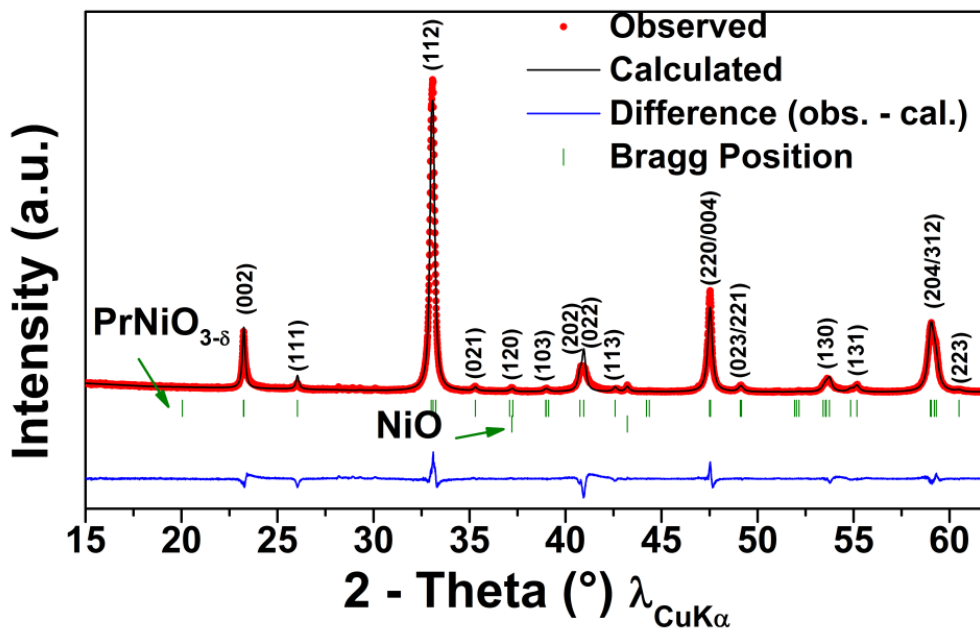


Figure 1: Fullprof refinement of the pattern of  $\text{PrNiO}_{3-\delta}$  using  $Pbnm$  space group.

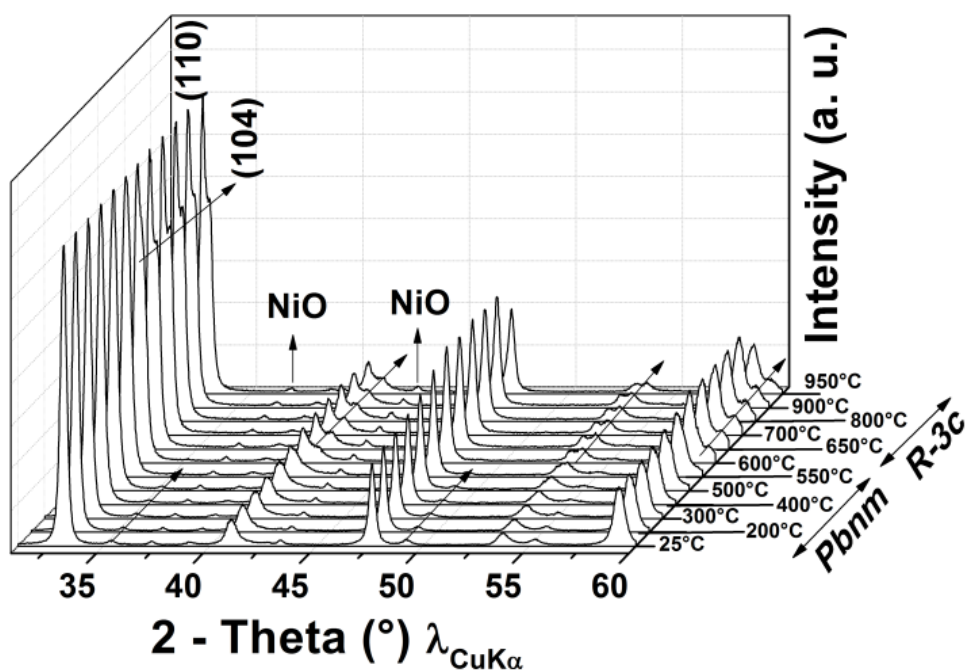


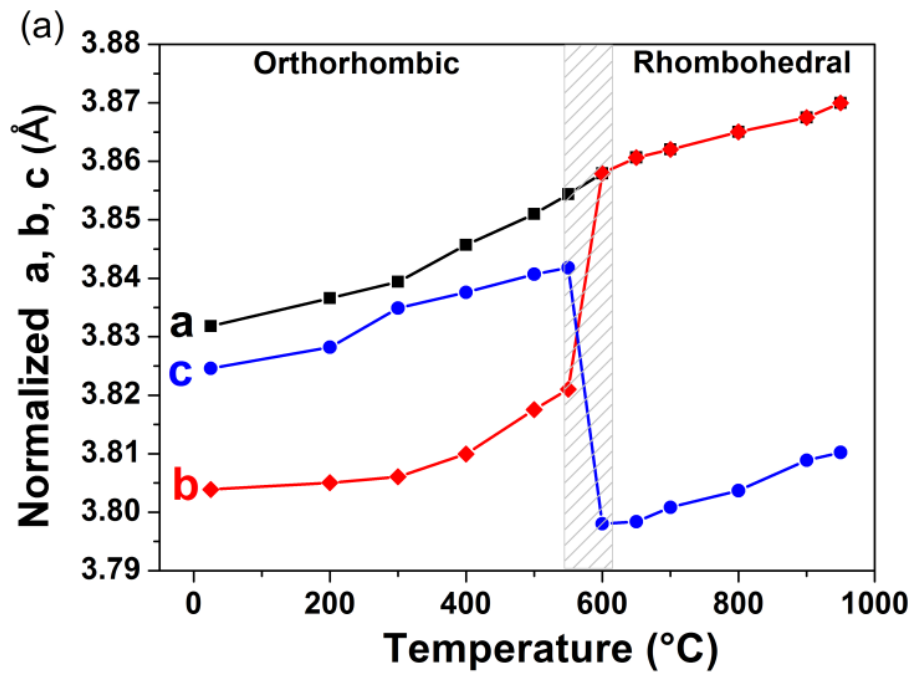
Figure 2: Evolution of the X-ray diffractograms vs.  $T$  of  $\text{PrNiO}_{3-\delta}$  powder under air up to  $950^\circ\text{C}$ .

$$(a, b)_{cubic} = \frac{(a, b)_{(Orthorhombic)}}{\sqrt{2}}$$

$$(a, b)_{cubic} = \frac{(a, b)_{(rhombohedral)}}{\sqrt{2}}$$

$$c_{cubic} = \frac{c_{(Orthorhombic)}}{2} \quad \text{and} \quad c_{cubic} = \frac{c_{(rhombohedral)}}{2\sqrt{3}}$$

The  $a$  and  $b$  lattice parameters increase non-linearly throughout the temperature range whereas the  $c$  parameter decreases after the structural transition. At around 600 °C, the change of symmetry from orthorhombic ( $Pbnm$ ) to rhombohedral ( $R-3c$ ) results in the concomitance of the  $a$  and  $b$  lattice parameters and sudden decrease in the  $c$  parameter. Overall, the volume of the unit cell increases throughout the temperature range while it exhibits a small plateau around 600 °C (**Figure 3b**).



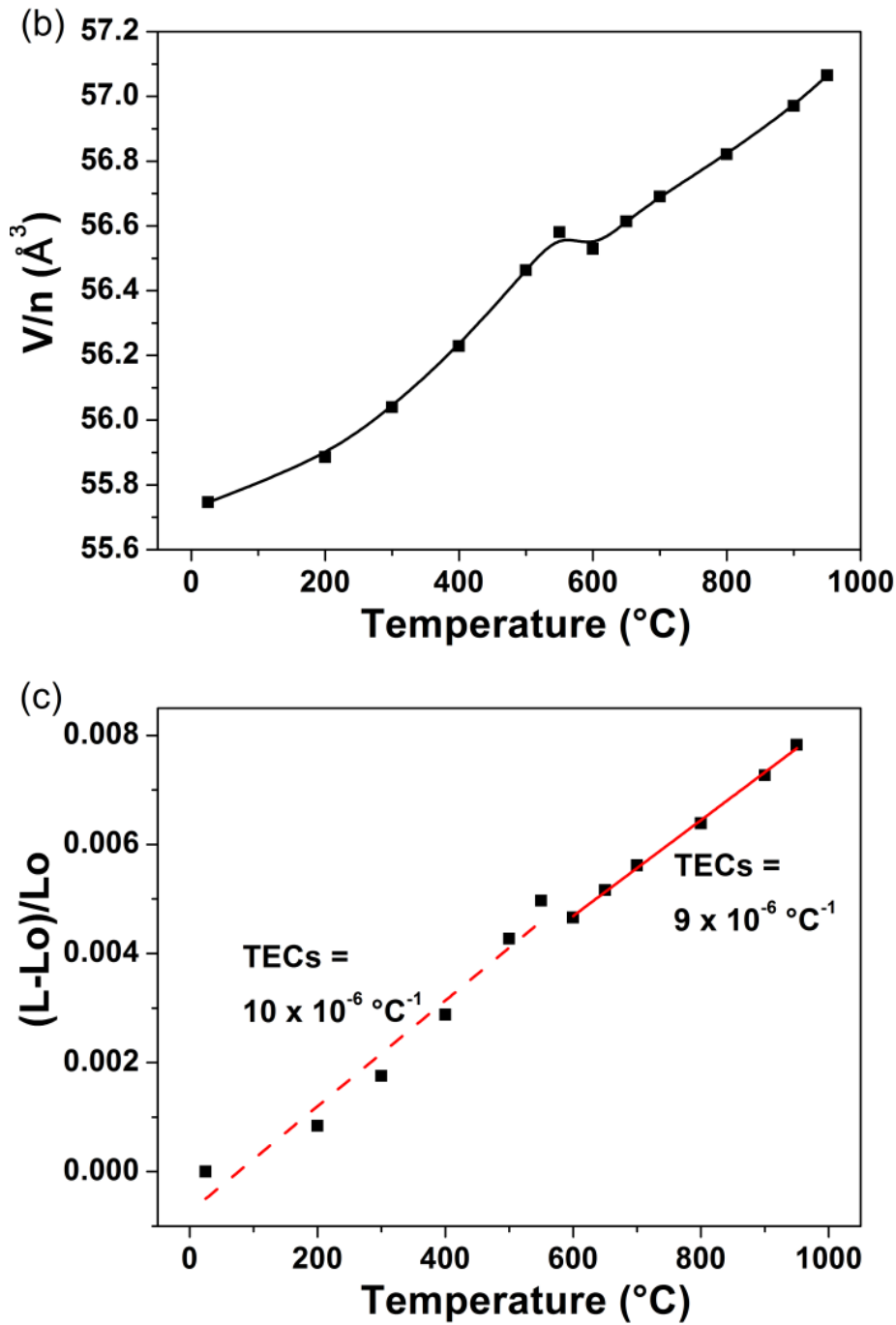


**Figure 3: Variation of (a) lattice parameters, (b) cell volume and (c) TECs of  $\text{PrNiO}_{3-\delta}$  as a function of temperature up to 950  $^{\circ}\text{C}$  under air.**

The non-linear evolution of the cell parameters and volume result in the distinction of two TECs values before and after the structural transition, namely of  $10 \times 10^{-6} \text{ }^{\circ}\text{C}^{-1}$  below 600  $^{\circ}\text{C}$  and of  $9 \times 10^{-6} \text{ }^{\circ}\text{C}^{-1}$  above 600  $^{\circ}\text{C}$  (**Figure 3c**). In comparison, a TEC value of  $13 \times 10^{-6} \text{ }^{\circ}\text{C}^{-1}$  was also calculated from dilatometry measurements; the discrepancy likely results from the fact that pellets with only 65 % density could be

prepared. Finally, the TEC values match rather well the one of GDC electrolyte  $\sim 12 \times 10^{-6} \text{ }^\circ\text{C}^{-1}$  [30].

## 3.2. TGA

### 3.2.1. Determination of $\delta$

The value of the oxygen sub-stoichiometry ( $\delta$ ) at room temperature for  $\text{PrNiO}_{3-\delta}$  phase was determined from the reduction of the material under 5%  $\text{H}_2$ -Ar atmosphere. The single weight loss occurring at around 400  $^\circ\text{C}$  (**Figure 4**) corresponds to a complete reduction of  $\text{PrNiO}_{3-\delta}$  into appropriate ratio of  $\text{Pr}_2\text{O}_3$  and Ni, as confirmed by XRD analysis. Indeed, the reduction of  $\text{Ni}^{3+}$  into  $\text{Ni}^0$  occurs without any intermediate stabilization of another composition containing either  $\text{Ni}^{2+}$  or even  $\text{Ni}^{1+}$  cation. This weight loss allows the determination a  $\delta$  value of 0.055, corresponding to the  $\text{PrNiO}_{2.945}$  formula at room temperature.

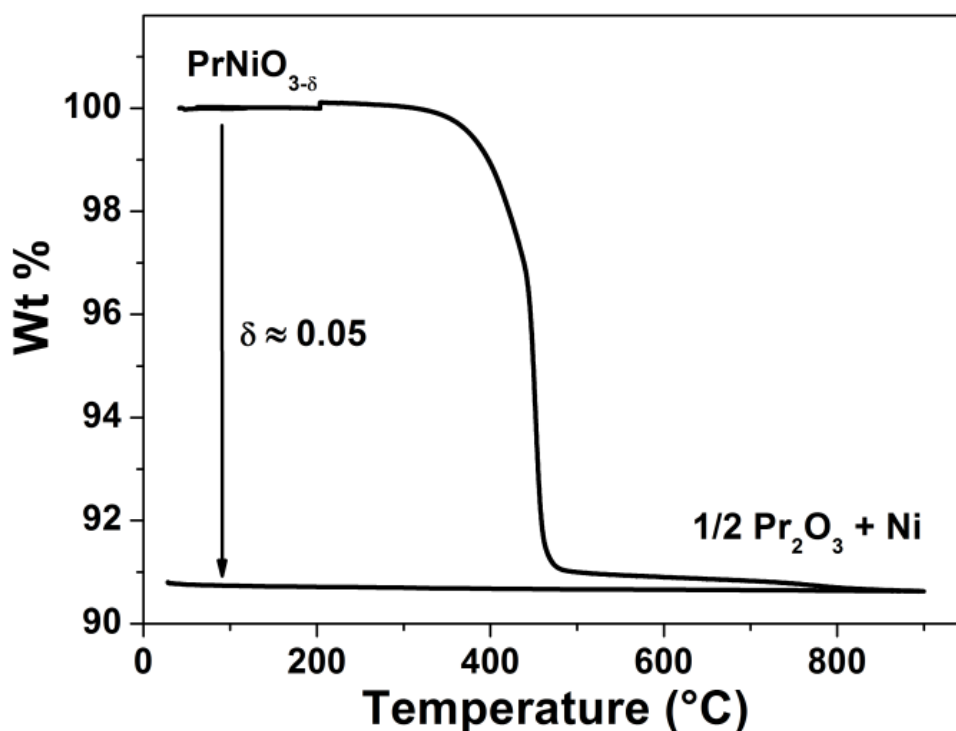
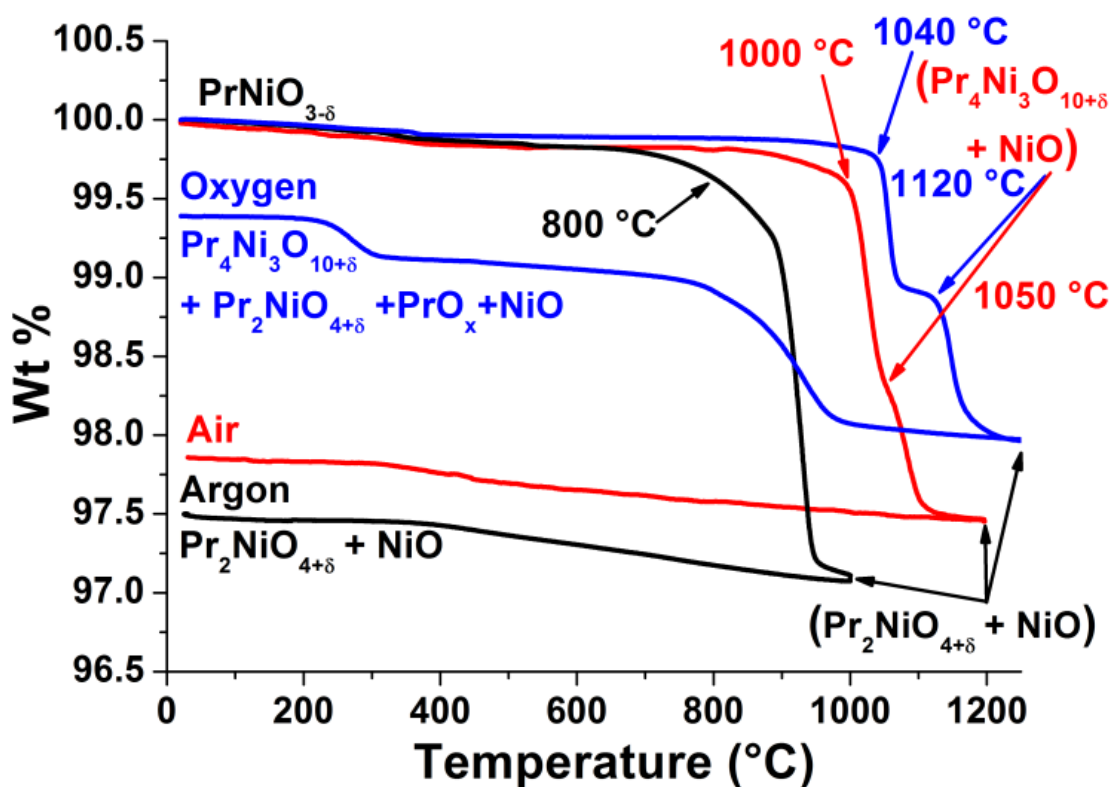


Figure 4: TGA plot under 5% Ar- $\text{H}_2$  for the determination of delta value.

### 3.2.2. Thermal stability under argon, air and oxygen

The thermal stability under argon, air and oxygen atmospheres was investigated in order to find the most appropriate sintering conditions for SOFC electrodes. The comparison of the weight loss variation with temperature for  $\text{PrNiO}_{3-\delta}$  under argon, air, and oxygen shows very different behaviours depending on the atmosphere (**Figure 5**). Under argon ( $p\text{O}_2 \sim 10^{-4}$  atm),  $\text{PrNiO}_{3-\delta}$  is stable up to  $\sim 800$  °C. Above this temperature, the material changes directly into  $\text{Pr}_2\text{NiO}_{4+\delta}$  and NiO, the decomposition being complete at 1000 °C as confirmed by XRD analysis at the end of cooling (**Figure 6a**). No significant evolution is observed during cooling.



**Figure 5:** Variation of the weight loss with temperature for  $\text{PrNiO}_{3-\delta}$  under argon, air and oxygen atmospheres with  $2^\circ\text{C}\cdot\text{min}^{-1}$  heating and cooling rates.

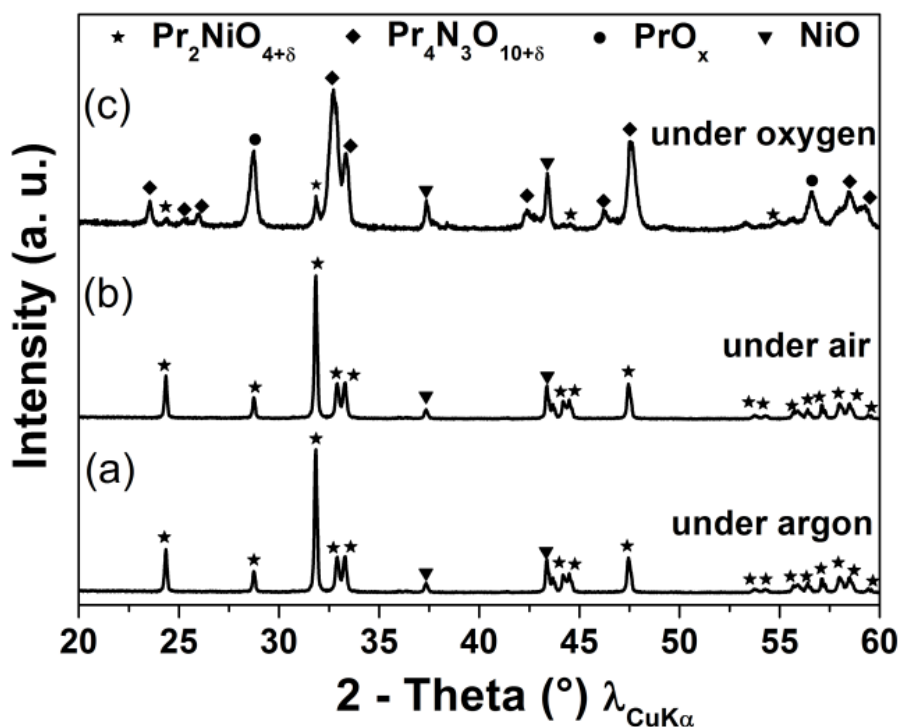


**Figure 6: X-ray diffractograms of the  $\text{PrNiO}_{3-\delta}$  powders after TGA under (a) argon, (b) air and (c) oxygen.**

Under air and oxygen,  $\text{PrNiO}_{3-\delta}$  exhibits a higher stability than under argon. The phase is stable up to 1000 °C under air, and then starts to decompose into  $\text{Pr}_4\text{Ni}_3\text{O}_{10+\delta}$  and NiO. The  $\text{Pr}_4\text{Ni}_3\text{O}_{10+\delta}$  phase remains stable over a very short temperature window (~ 1045–1055 °C) (**Figure 5**).

The XRD pattern of the  $\text{PrNiO}_{3-\delta}$  powder, quenched at 1050 °C under air confirms the presence of  $\text{Pr}_4\text{Ni}_3\text{O}_{10+\delta}$  and NiO phases (**Figure 7a**). Above this temperature,  $\text{Pr}_2\text{NiO}_{4+\delta}$  and NiO are again only present as under argon (**Figure 6b**) and remain upon cooling.

Among the three atmospheres,  $\text{PrNiO}_{3-\delta}$  shows maximum stability up to 1040 °C under oxygen (**Figure 5**). Above this temperature, it decomposes into  $\text{Pr}_4\text{Ni}_3\text{O}_{10+\delta}$  and NiO as confirmed by the X-ray diffractogram of the quenched powder at 1070 °C (**Figure 7b**). Again the  $\text{Pr}_4\text{Ni}_3\text{O}_{10+\delta}$  phase is only stable in a short temperature window (~ 1050–1120 °C). Above ~ 1120 °C  $\text{Pr}_2\text{NiO}_{4+\delta}$  and NiO are only present. Interestingly, the cooling behaviour under oxygen is completely different from that previously observed under air or argon (**Figure 5**). With a cooling rate of 2 °C.min<sup>-1</sup>,  $\text{Pr}_2\text{NiO}_{4+\delta}$  again starts changing into  $\text{Pr}_4\text{Ni}_3\text{O}_{10+\delta}$  and  $\text{PrO}_x$  (around 950°C). The XRD

analysis at the end of the cooling process shows the presence of a mixture of  $\text{Pr}_4\text{Ni}_3\text{O}_{10+\delta}$ ,  $\text{Pr}_2\text{NiO}_{4+\delta}$ ,  $\text{PrO}_x$  and  $\text{NiO}$  (**Figure 6c**), in relation with the instability of  $\text{Pr}_2\text{NiO}_{4+\delta}$  under oxygen.

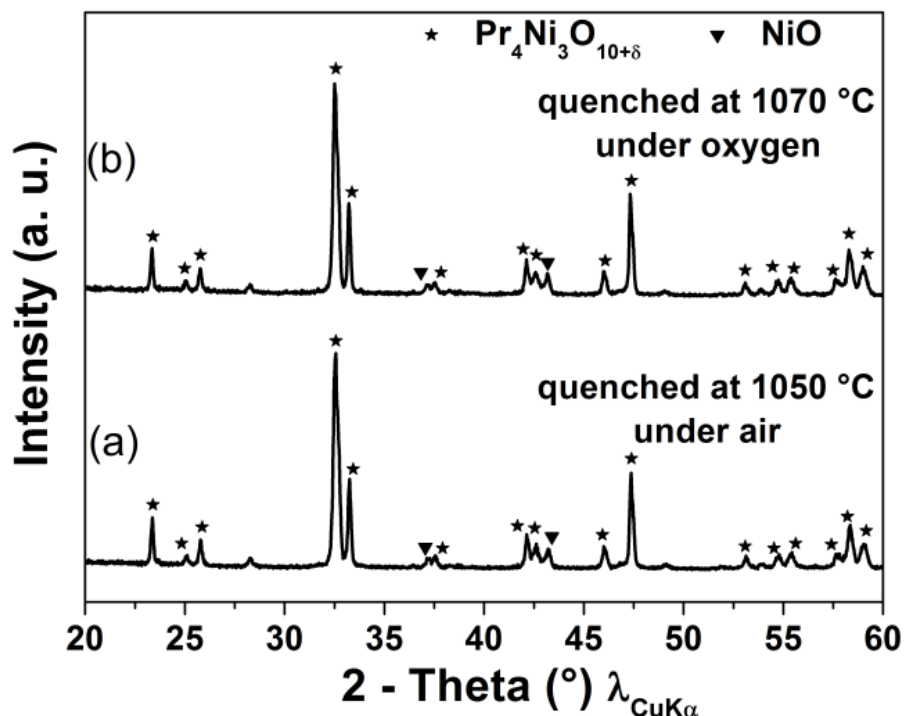


**Figure 7: X-ray diffractograms of quenched samples (a) from 1050 °C under air and (b) from 1070 °C under oxygen.**

In addition, aiming at better understanding of the thermal behaviour under oxygen, various heating and cooling rates, namely 1°, 2° and 5 °C.min<sup>-1</sup> up to 1300 °C were used (**Figure additional info. 1a, b, c**). Higher heating and cooling rates prevent the formation of  $\text{Pr}_4\text{Ni}_3\text{O}_{10+\delta}$  leading to a final mixture of  $\text{Pr}_2\text{NiO}_{4+\delta}$ ,  $\text{PrO}_x$  and  $\text{NiO}$  as end products.

The thermal evolution of  $\text{PrNiO}_{3-\delta}$  with the corresponding derivatives observed during heating and cooling, under argon, air and oxygen atmospheres is summarized in **Figure 8a** and **8b**, respectively.

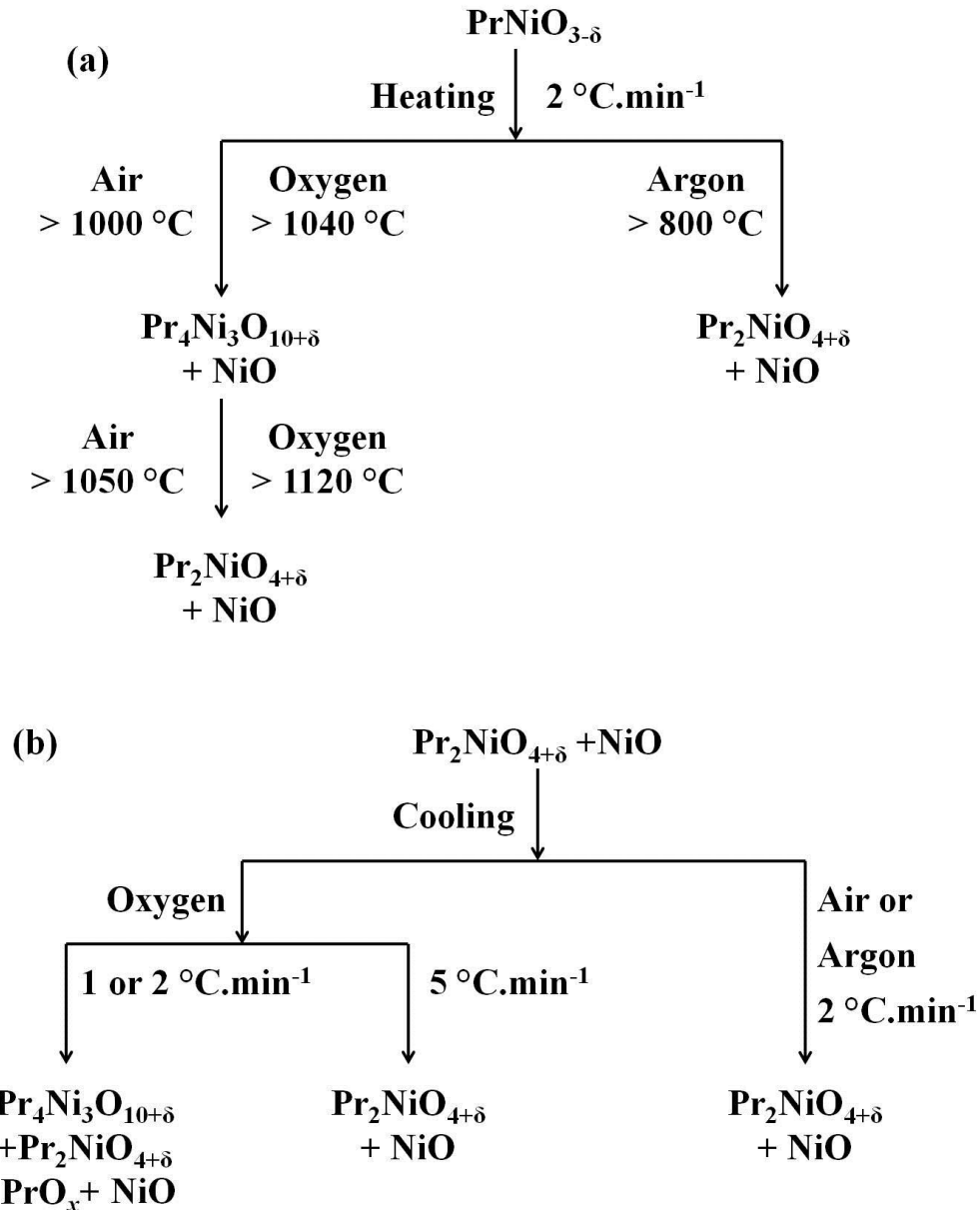


**Figure 8: Thermal stability of  $\text{PrNiO}_{3-\delta}$ , and its derivatives under air, oxygen and argon during (a) heating and (b) cooling.**

To summarize, one can conclude that the maximum temperature at which  $\text{PrNiO}_{3-\delta}$  is stable varies from  $800\text{ }^\circ\text{C}$ ,  $1000\text{ }^\circ\text{C}$ , and  $1040\text{ }^\circ\text{C}$  under argon, air and oxygen, respectively. When heated above these temperatures, the decomposition into  $\text{Pr}_2\text{NiO}_{4+\delta}$  and NiO seems to be irreversible. We are aware that those observations are governed by kinetics and that a complete study requires to take into account the thermodynamics of the system.

### 3.2.3. Variation of oxygen content under argon, air and oxygen

Remaining in the stability domain of  $\text{PrNiO}_{3-\delta}$  in the different considered atmospheres (see above), the variation of the oxygen content was studied by TGA. For any atmosphere, two cycles were performed to check the reversibility while the powder was kept for 1 hour at the maximum temperature before cooling.

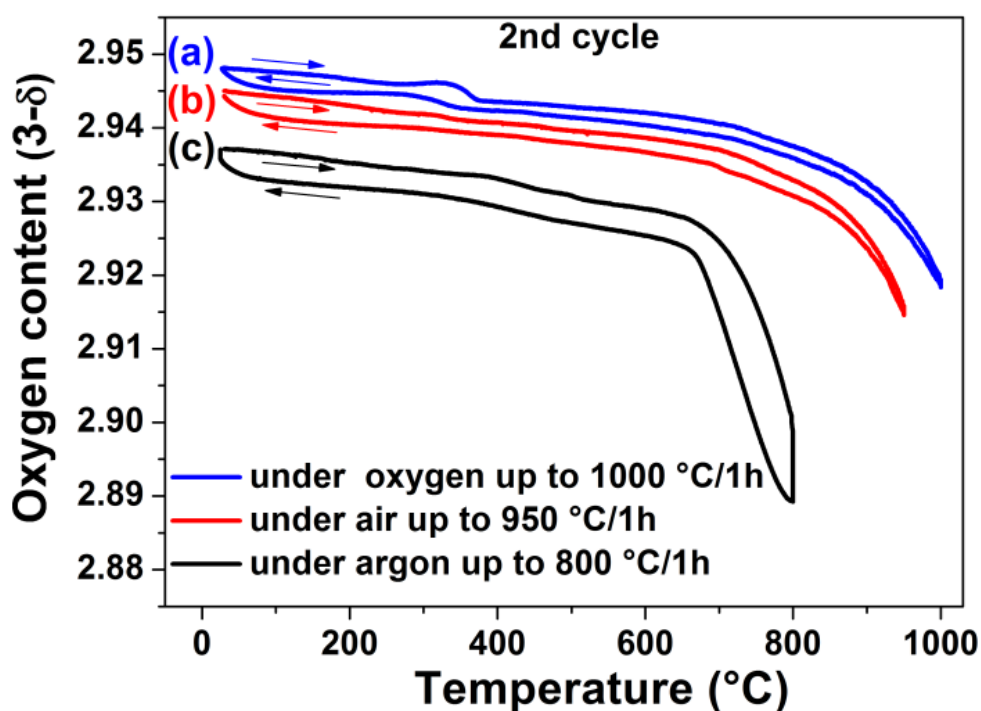


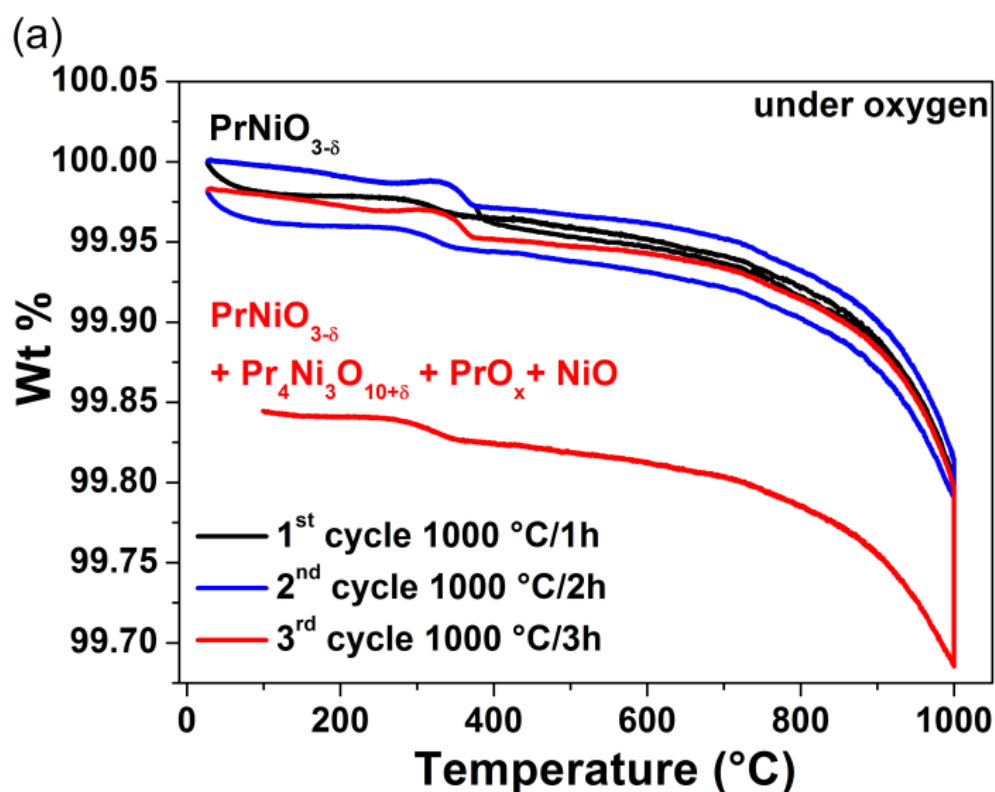
**Figure 9:** Thermal variation of the oxygen content ( $3-\delta$ ) of  $\text{PrNiO}_{3-\delta}$ , (a) under oxygen ( $30\text{ }^{\circ}\text{C} \leq T \leq 1000\text{ }^{\circ}\text{C}$ ), (b) under air ( $30\text{ }^{\circ}\text{C} \leq T \leq 950\text{ }^{\circ}\text{C}$ ) and (c) under argon ( $30\text{ }^{\circ}\text{C} \leq T \leq 800\text{ }^{\circ}\text{C}$ ).

In all atmospheres, a reversible behaviour is observed (**Figure 9**). The drop in  $3-\delta$  occurs at lower temperature under Ar ( $T \approx 680\text{ }^{\circ}\text{C}$ ) in relation with a slightly larger drop of about 0.04, while under air and oxygen, a smoother drop of about 0.025 is observed for  $T$  above  $700\text{ }^{\circ}\text{C}$ . However, those values have to be considered with care as for instance, the equilibrium time of 1 h appears not sufficient under Ar atmosphere (*i.e.* drop of 0.01 between cooling and further heating). The initial (room temperature) calculated  $\delta$  values decrease from 0.063, 0.055 and 0.052 under argon, air and oxygen, respectively. In other words, the content of oxygen is maximum (2.948) under oxygen and slightly decreases in air (2.945) and a bit more in argon (2.937). The corresponding  $\text{Ni}^{2+}$  percentage in the structure increases from 10 % under  $\text{O}_2$ , to 11 % under air and reaches 13 % under argon.

### 3.2.4. Stability above 950 °C and in operating SOFCs condition

To go further in the investigation of the stability duration at 1000 °C and 950 °C under oxygen and air respectively (as maximum stability under these atmospheres), additional TGA experiments were carried out. For this purpose cycles were performed in each case with the heating and cooling rate of 2 °C.min<sup>-1</sup> for a different dwell time (till 5 h with 1 h steps) at 1000 °C and 950°C, respectively. The variations of weight during heating and cooling are plotted in **Figure 10a, b**.

Under oxygen, the PrNiO<sub>3-δ</sub> phase is stable during the first two cycles and shows almost reversible behaviour. In the third cycle, for a dwelling time of 3 h, a large weight loss associated with a partial decomposition of PrNiO<sub>3-δ</sub> into Pr<sub>4</sub>Ni<sub>3</sub>O<sub>10+δ</sub> is observed, as confirmed by XRD (**Figure 11**).



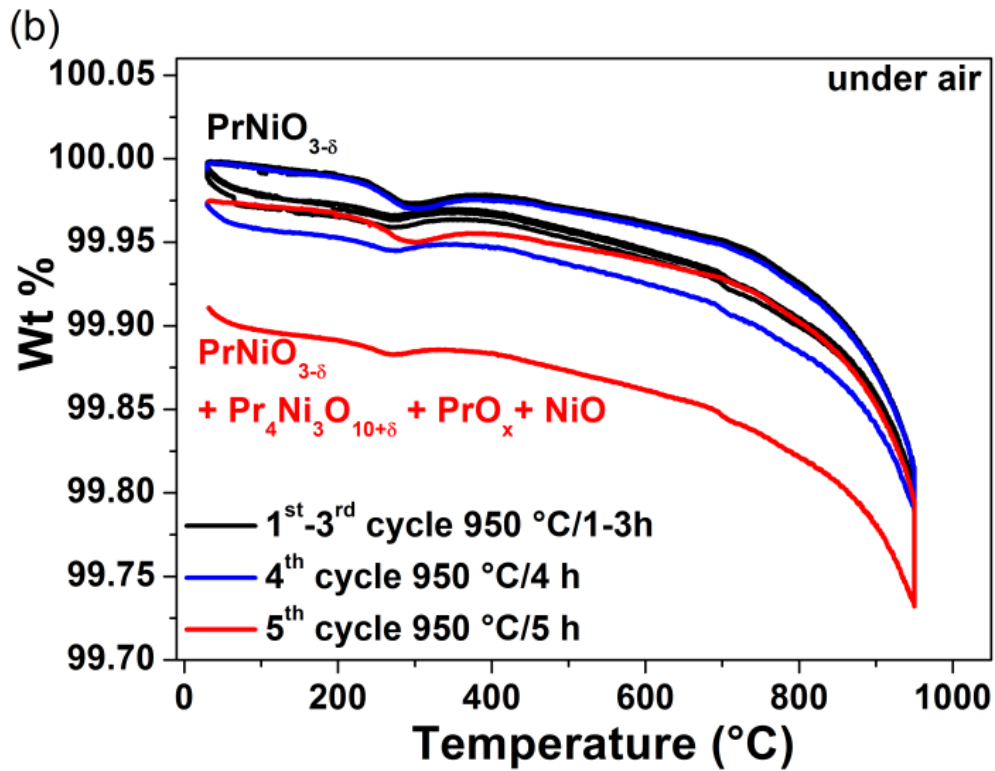


**Figure 10:** Thermal variation of the oxygen content ( $3-\delta$ ) of  $\text{PrNiO}_{3-\delta}$ , (a) under oxygen ( $30\text{ }^{\circ}\text{C} \leq T \leq 1000\text{ }^{\circ}\text{C}$ ) for various dwell times 1h, 2h and 3h at  $1000\text{ }^{\circ}\text{C}$  (b) under air ( $30\text{ }^{\circ}\text{C} \leq T \leq 950\text{ }^{\circ}\text{C}$ ) for different dwell times 1 h, 2 h, 3 h, 4h and 5 h at  $950\text{ }^{\circ}\text{C}$  ( with heating and cooling rate of  $2\text{ }^{\circ}\text{C}\cdot\text{min}^{-1}$ ).

Under air,  $\text{PrNiO}_{3-\delta}$  phase is only stable up to 4 h at  $950\text{ }^{\circ}\text{C}$ , for longer time it also starts to decompose into  $\text{Pr}_4\text{Ni}_3\text{O}_{10+\delta}$  and NiO (**Figure 10b**). Similarly, Martinez-Lope *et al.* reported the thermal stability of  $\text{PrNiO}_{3-\delta}$  under air up to  $900\text{ }^{\circ}\text{C}$  up to 4 hours [31].

Such observations were further used as guidelines for the sintering of the electrode. Basically for pure phase, only two options, either  $950\text{ }^{\circ}\text{C}/4\text{h}$  (maximum dwell time) under air or  $1000\text{ }^{\circ}\text{C}/2\text{h}$  (*idem*) under oxygen can be chosen. Sintering under Ar will be avoided due to a too low value of the stability temperature (i.e.  $T_{\text{max}} \approx 800\text{ }^{\circ}\text{C}$ ).

### 3.3. Long term chemical stability of $\text{PrNiO}_{3-\delta}$ powder under air at operating conditions

The XRD patterns of  $\text{PrNiO}_{3-\delta}$  powder after ageing at 600, 700 and 800 °C under air along with as prepared powder are compared in **Figure 12**. Overall, there is no modification of the XRD pattern after the ageing period. The  $\text{PrNiO}_{3-\delta}$  powder is chemically stable at the operating temperature of SOFCs *i.e.* 600, 700 and 800 °C under air up to 1 month. Although it is somewhat difficult to synthesize this material, once it is formed, then it shows high stability.

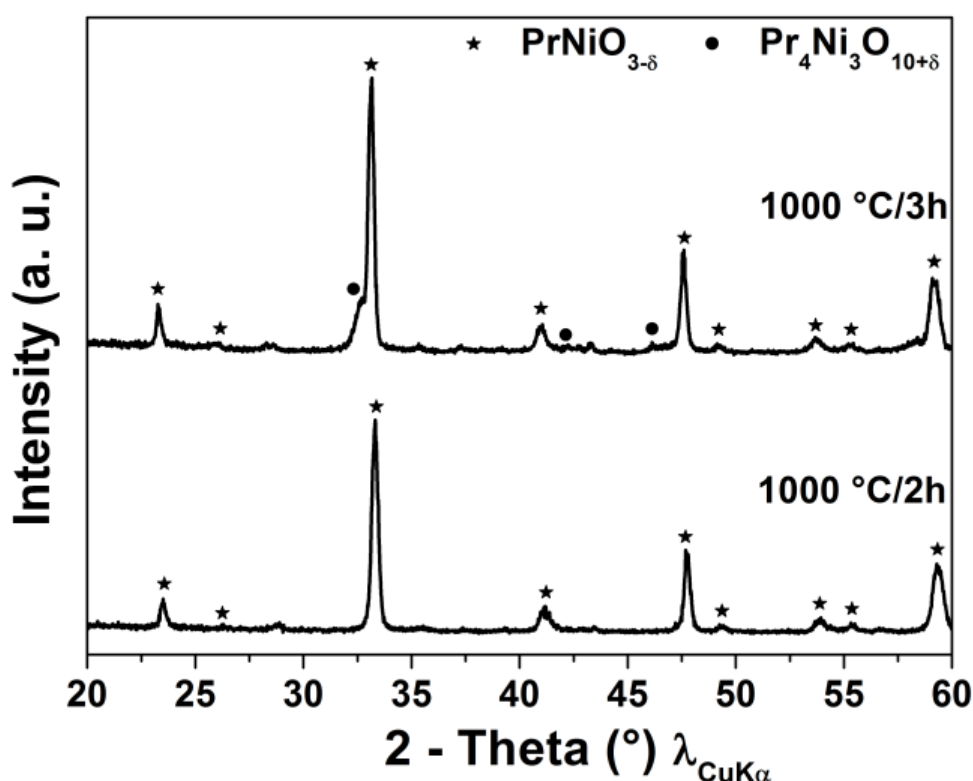


**Figure 11:** X-ray diffractograms of  $\text{PrNiO}_{3-\delta}$  powder, after TGA experiment under oxygen ( $30\text{ °C} \leq T \leq 1000\text{ °C}$ ) with the rate of  $2\text{ °C}\cdot\text{min}^{-1}$  for different dwell times of 2 h and 3 h at 1000 °C.

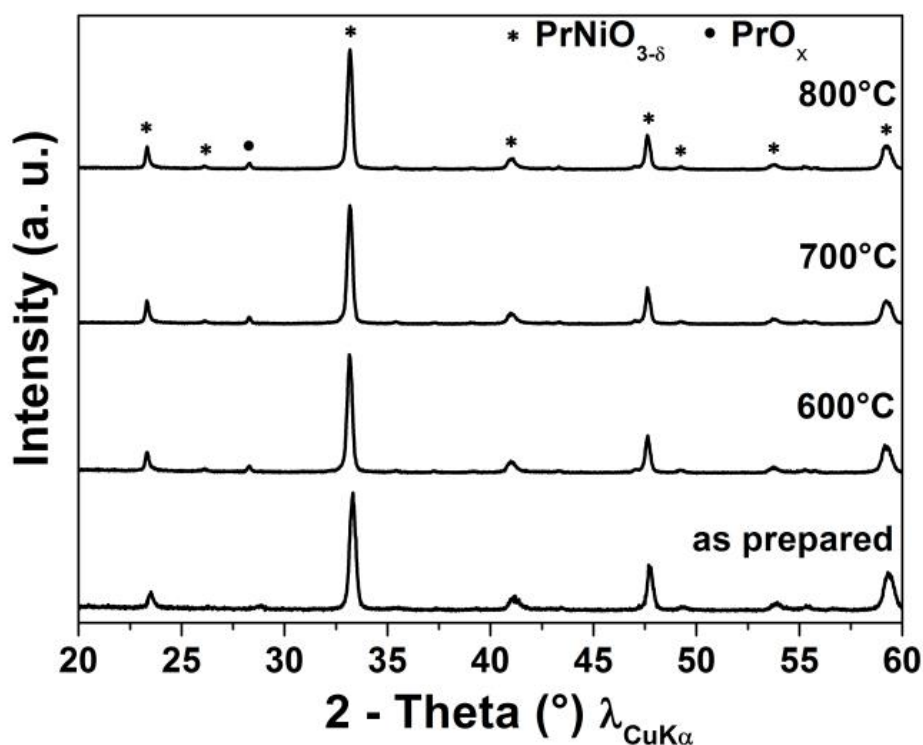


Figure 12: X-ray diffractograms of PrNiO<sub>3-δ</sub>, as prepared and after ageing for 1 month at 600, 700 and 800 °C, under air.

### 3.4. Electrical Conductivity

The electrical conductivity shows a metal-like behaviour over the temperature range up to 800 °C, under air. The maximum of the conductivity value, close to  $\sigma = 180 \text{ S.cm}^{-1}$ , recorded at room temperature, decreases to  $\sigma = 120 \text{ S.cm}^{-1}$  at 600 °C. Interestingly, the latter value is close to the one of Pr<sub>2</sub>NiO<sub>4+δ</sub> that exhibits however a semi-conductor behaviour as shown in **Figure 13**.

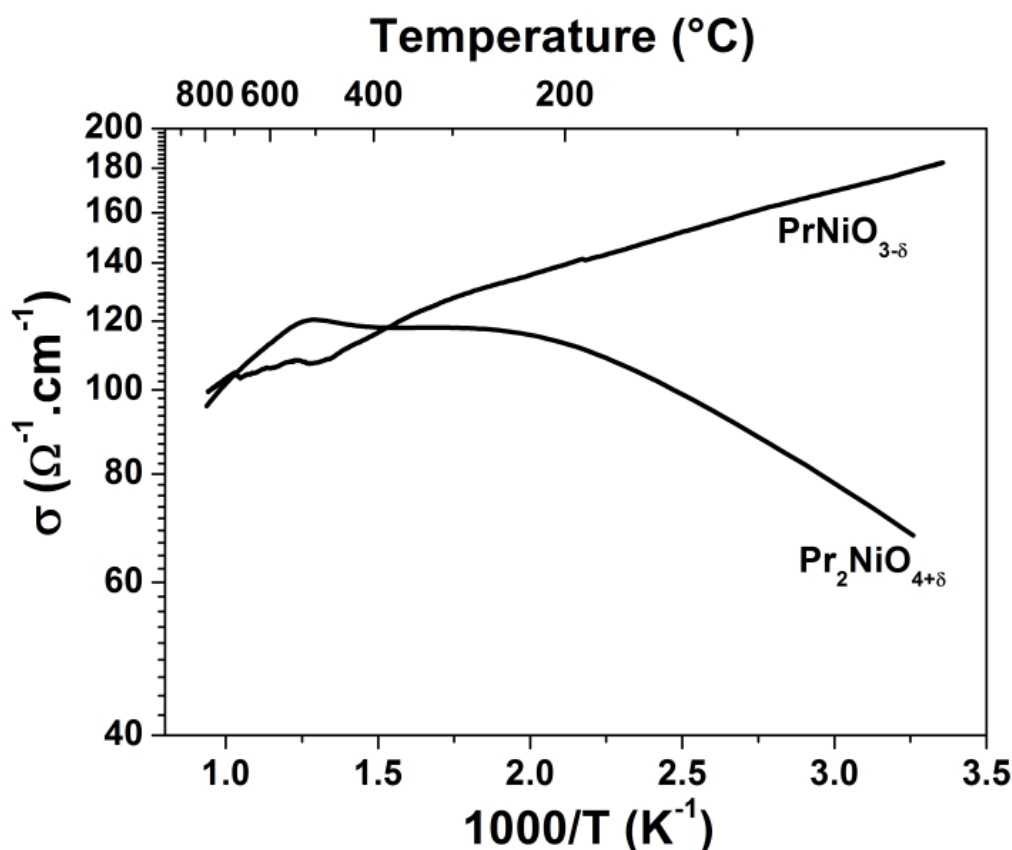


Figure 13: Thermal variation of the electrical conductivity of  $\text{PrNiO}_{3-\delta}$  and  $\text{Pr}_2\text{NiO}_{4+\delta}$  under air up to 800 °C.

### 3.5. Electrochemical measurements

EIS measurements were carried out on  $\text{PrNiO}_{3-\delta}$ //GDC//8YSZ symmetrical half cells prepared using two ways, namely a two-step process and co-sintering, as detailed in the experimental part.

#### 3.5.1. Optimization of the sintering two-step process

Initial sintering at 950 °C for 2 h, in agreement with phase stability discussed above, leads to very high  $R_p$  value of 4.5  $\Omega\cdot\text{cm}^2$  (Figure 14). Therefore, sintering at higher temperatures, namely 1050 °C and 1150 °C, followed by an additional step at 800 °C for 24 h under oxygen associated with a partial recovery of the  $\text{PrNiO}_{3-\delta}$  together with a small amount of  $\text{PrO}_x$  and NiO (Figure 15b) were carried out. The  $R_p$  values decrease down to 1.6 and 0.44  $\Omega\cdot\text{cm}^2$ , respectively.

These results first indicate that the temperatures of 950 °C and 1050 °C are not high enough, either to form a good quality GDC//electrode interface, and/or to form enough sufficient connections between the electrode grains themselves.

### 3.5.2. Co-sintering of GDC and PrNiO<sub>3-δ</sub> half cell

Pure PrNiO<sub>3-δ</sub> phase was successfully maintained for symmetrical half-cell, prepared by the co-sintering of GDC and the electrode, at 950 °C for 2h, as confirmed by X-ray diffraction (**Figure 16**). By both *in-situ* and *ex-situ* co-sintering at 950 °C/2h under air lead to similar  $R_p$  values of 0.91  $\Omega\cdot\text{cm}^2$  at 600 °C.

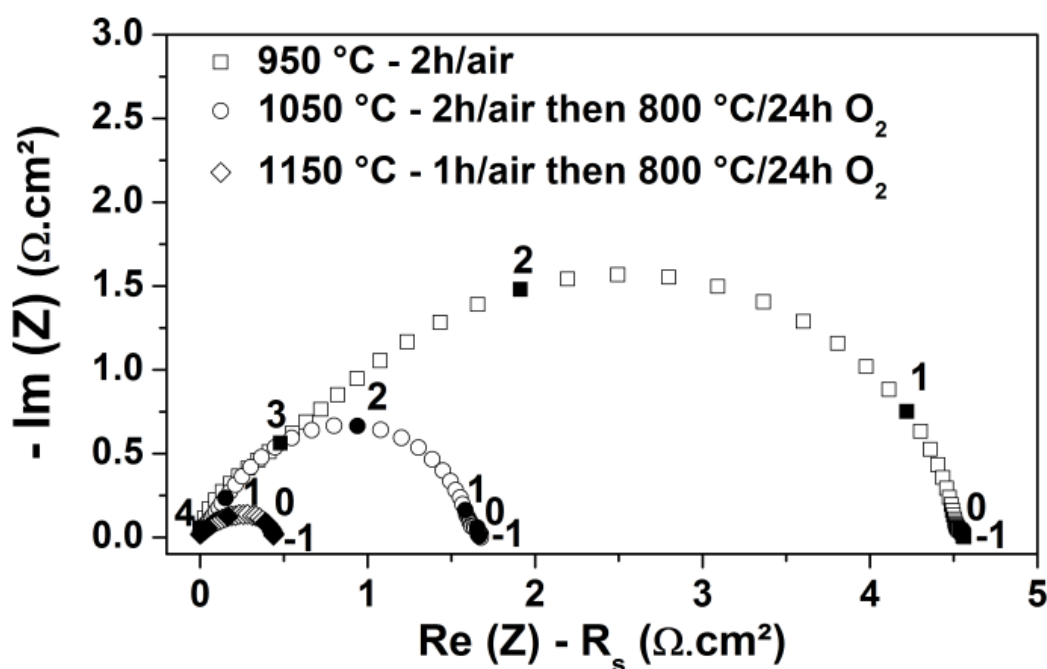


**Figure 14:** Polarization resistances,  $R_p$ , measured under air on the half cells prepared by two-step sintering process at 950/2h/air, 1050°C/2h/air (+ 800 °C/24h/O<sub>2</sub>) and 1150°C/1h/air (+ 800 °C/24h/O<sub>2</sub>).

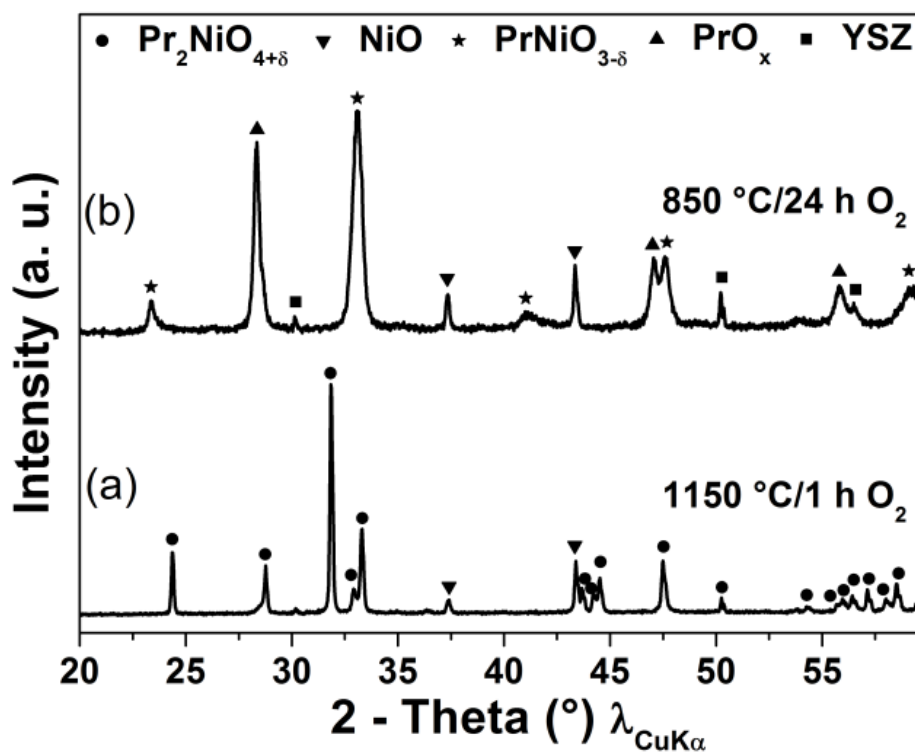


Figure 15: X-ray diffractograms of half cells (a) after sintering at 1150 °C for 1h under air, (b) after recovery of  $\text{PrNiO}_{3-\delta}$  phase respectively.

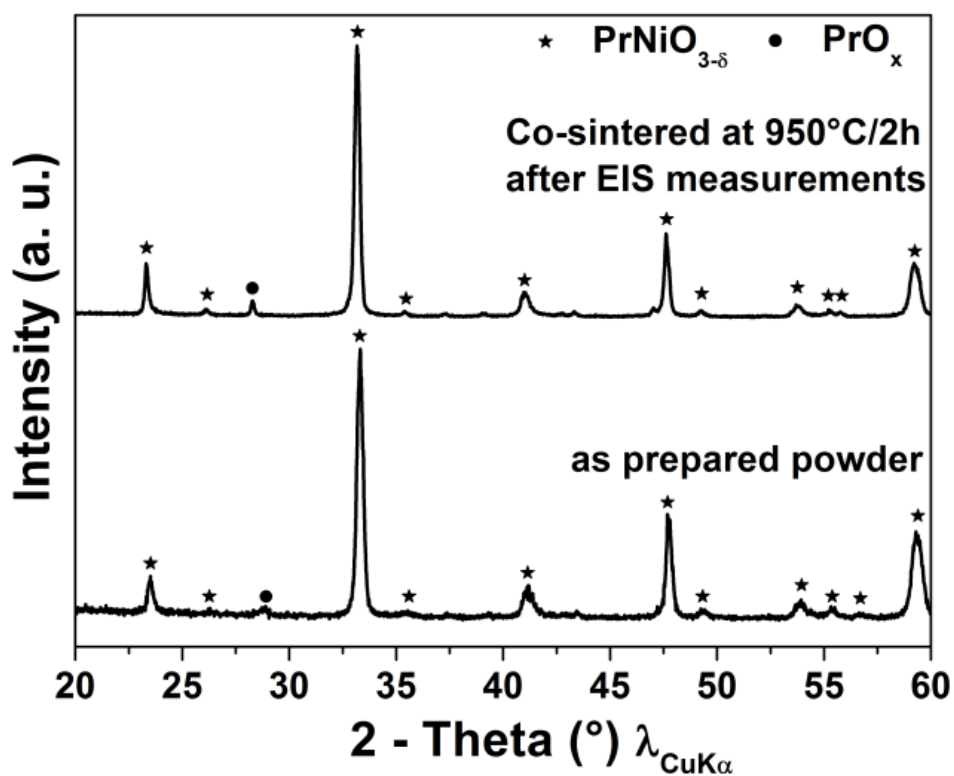
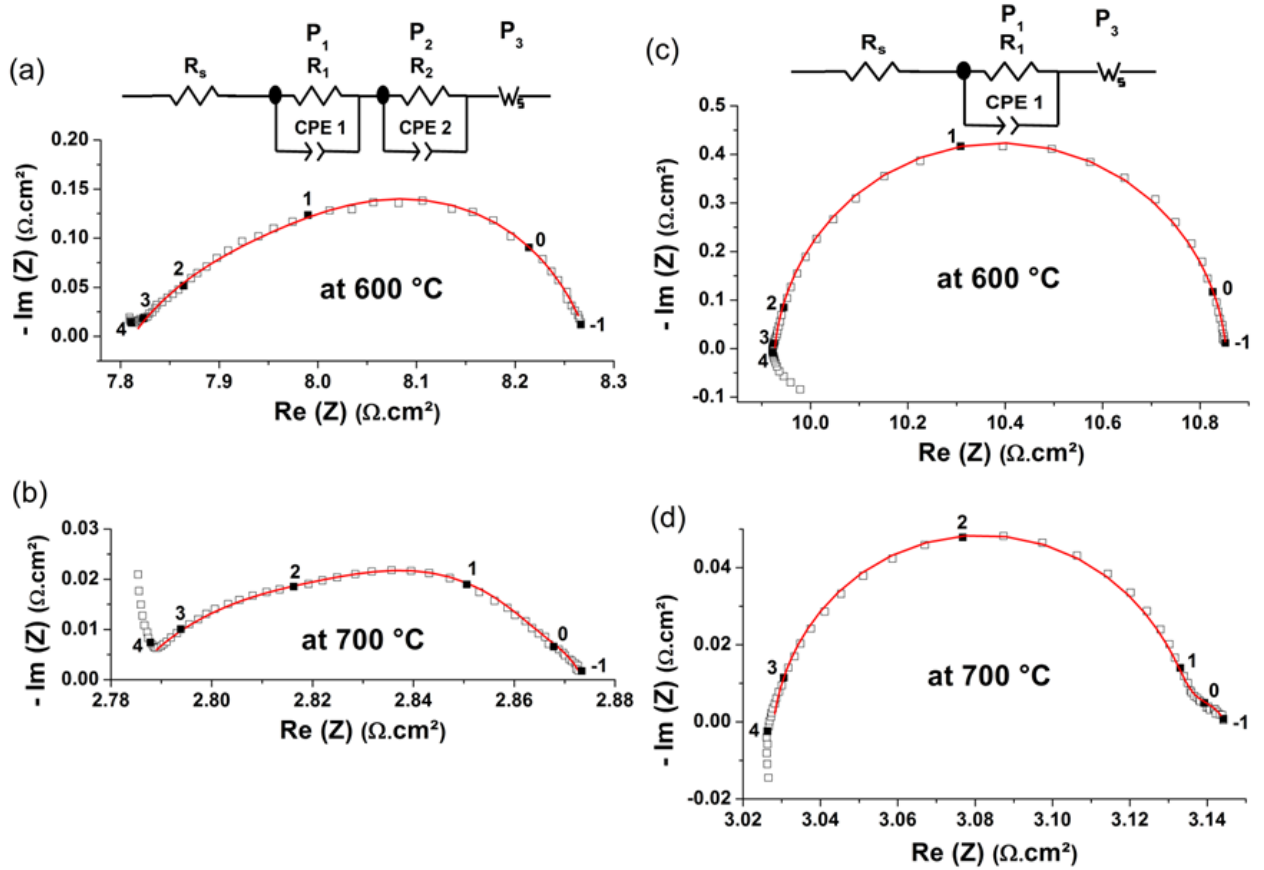


Figure 16: X-ray diffractograms after EIS measurement by co-sintering technique (comparison with as-prepared powder).

### 3.5.3. Discussion

**Figure 17 (a, b)** and **Figure 17 (c, d)** compare the Nyquist impedance diagrams, recorded for  $\text{PrNiO}_{3-\delta}$  electrode at 600 °C and 700 °C for two-step sintering and co-sintering half-cells, respectively.



**Figure 17:** Nyquist plots recorded for  $\text{PrNiO}_{3-\delta}$  electrode at 600 °C and 700 °C for: (a, b) two-step sintered and (c, d) co-sintered half cells. The diagrams are fitted using an equivalent circuit composed of  $R_s$  (series resistance),  $R//CPE$  and Warburg element ( $W_s$ ).

Depending on the sintering conditions, either three processes ( $P_1$ ,  $P_2$  and  $P_3$ ) for the two-step sintering or two processes ( $P_1$  and  $P_3$ ) for the co-sintering are distinguishable. The  $P_1$  and  $P_2$  (occurring at middle frequencies ( $10^3 - 1$  Hz)) processes are assigned to the oxygen electrode reaction (OER) and were fitted for the sake of simplicity using two parallel  $R//CPE$  elements. The process  $P_3$  is assigned to gas diffusion impedance as already reported [32, 33], and usually fitted using a Warburg element  $W_s$ . The origin of the co-existence of two contributions  $P_1$  and  $P_2$  is still unclear. Our assumption is that the two processes are related to the OER in two

different materials. Indeed, for the two-steps sintering process XRD experiments showed that  $\text{PrNiO}_{3-\delta}$ ,  $\text{PrO}_x$  and  $\text{NiO}$  are present (**Figure 15**), while for the co-sintering process  $\text{PrNiO}_{3-\delta}$  is almost pure (**Figure 16**). For co-sintered sample, as shown in **Figure 17(c, d)** from  $10^3$  Hz down to 1 Hz, the diffusion of  $\text{O}^{2-}$  is probed into the  $\text{PrNiO}_{3-\delta}$  electrode, which yields only one R//CPE contribution.

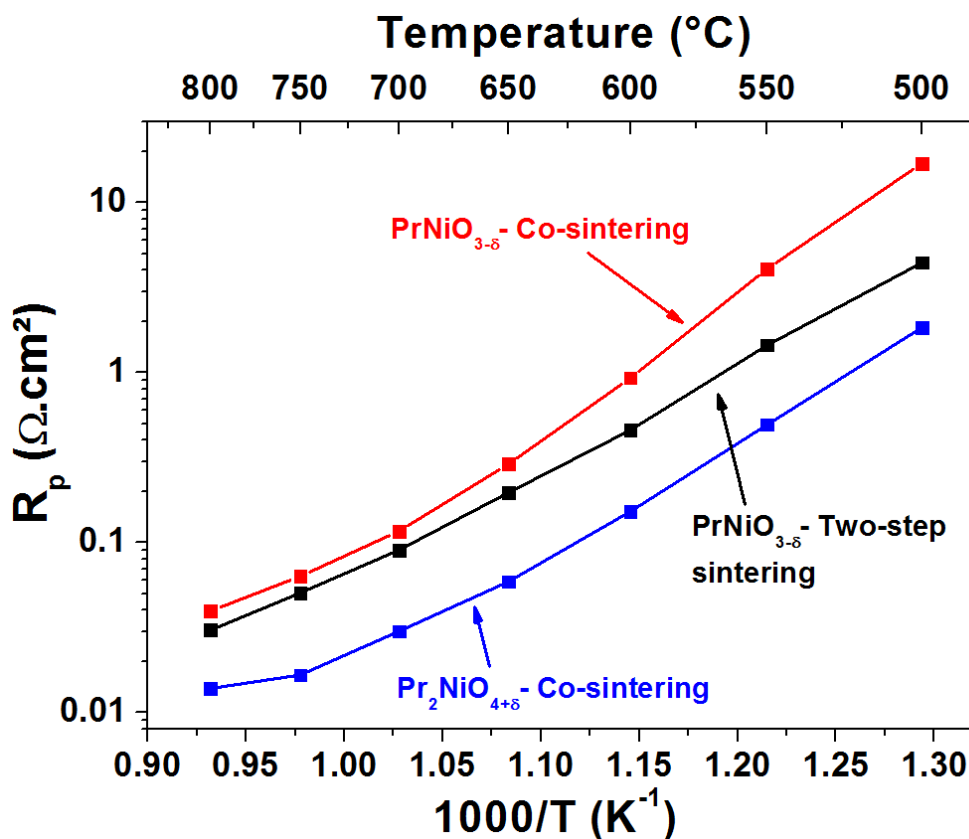


**Figure 18: Variation of the polarization resistance  $R_p$  as a function of temperature for both two-step,  $\text{PrNiO}_{3-\delta}$ , and co-sintered  $\text{PrNiO}_{3-\delta}$  and  $\text{Pr}_2\text{NiO}_{4+\delta}$  half cells .**

This shape is typical of electrode for which only the relaxation of the oxygen exchange at the gas//electrode interface is measured [34]. The comparison of the  $R_p$  values calculated in the temperature range 500–800 °C shows that the  $R_p$  values obtained by co-sintering are always higher and up to almost twice the ones of the two-step process (**Figure 18**). For instance, it is of 0.91  $\Omega\cdot\text{cm}^2$  at 600 °C for co-sintering, as compared to 0.46  $\Omega\cdot\text{cm}^2$  for two-step sintering. In addition, these values are higher than the ones of GDC and  $\text{Pr}_2\text{NiO}_{4+\delta}$  co-sintered half cell, showing for  $\text{Pr}_2\text{NiO}_{4+\delta}$  similar low  $R_p$  value of 0.15  $\Omega\cdot\text{cm}^2$  at 600 °C as for two-step sintering [35]<sup>5</sup>.

<sup>5</sup> The optimization of the co-sintering process in terms of temperature under air is not detailed in this dissertation but corresponds to a nice achievement in terms of half-cells fabrication at “low” temperature.

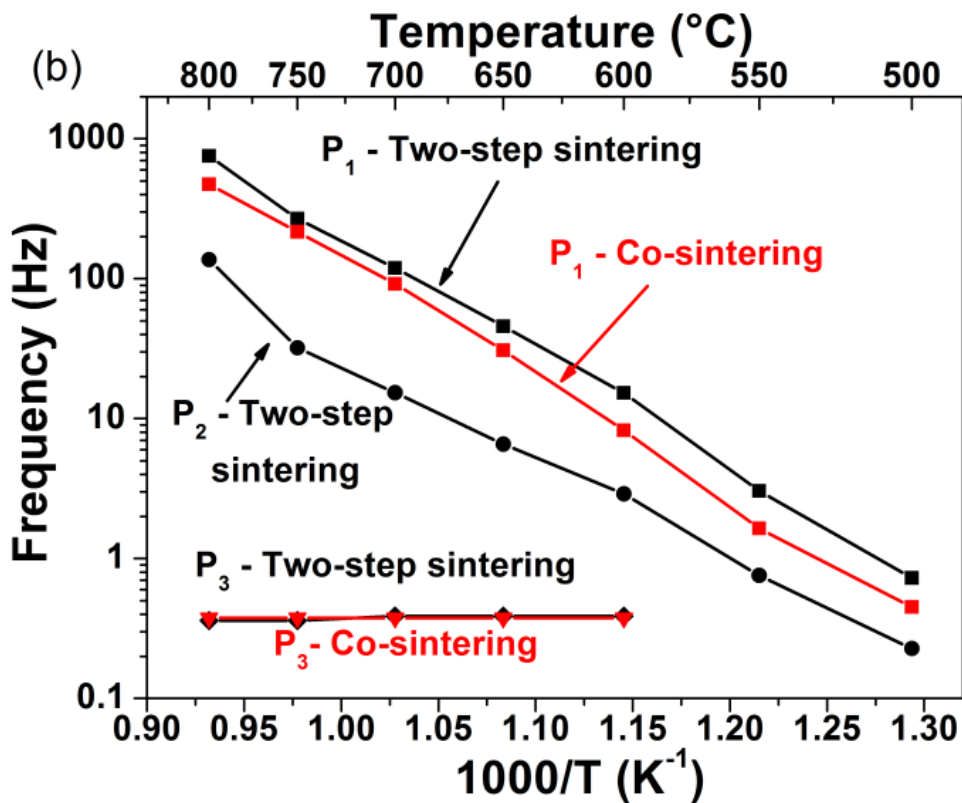
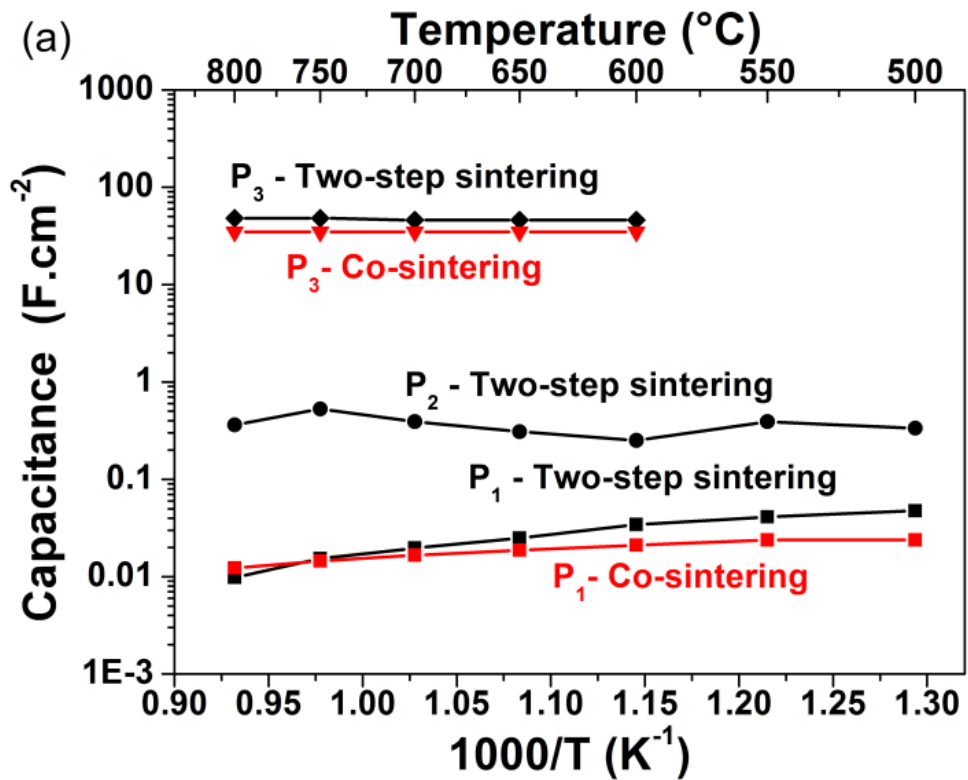


Figure 19: Thermal variation of (a) Capacitance and (b) Frequency of relaxation of the different processes occurring on  $\text{PrNiO}_{3-\delta}$  electrodes operating in air and prepared using two-step or co-sintering technique.

The capacitance and frequency of relaxation of the different processes involved for both two-step and co-sintered half cells are reported in **Figure 19a, b**. It is worth noting that the capacitance of process  $P_1$ , which corresponds to  $\text{PrNiO}_{3-\delta}$  electrode process for both two-step and co-sintered half cells are quite comparable and the value of capacitance is in between  $1-2 \times 10^{-2} \text{ F.cm}^{-2}$ . The process  $P_2$  evidenced for the two-steps sintered half-cell has a higher capacitance value ( $\sim 0.2-0.3 \text{ F.cm}^{-2}$ ), its origin being unclear at this moment.

The capacitances corresponding to gas diffusion process are higher ( $\sim 40-50 \text{ F.cm}^{-2}$ ), and in the same range for both two-steps and co-sintered half cells. The frequency plot in **Figure 19b** also confirms that the processes  $P_1$  of both half cells are equivalent.

## 4. Conclusion

This work reports the structural and thermal stability studies of  $\text{PrNiO}_{3-\delta}$  as a cathode material for IT-SOFCs.  $\text{PrNiO}_{3-\delta}$  was successfully synthesized via citrate-nitrate route under oxygen flow ( $p\text{O}_2 \sim 1 \text{ atm}$ ). The XRD *vs.* temperature study shows a phase transition from the room temperature ( $Pbnm$  space group) orthorhombic to rhombohedral structure at  $\sim 600 \text{ }^\circ\text{C}$ . Whatever the atmosphere  $\text{PrNiO}_{3-\delta}$  remains always sub-stoichiometric. For instance, a delta value  $\delta \approx 0.05$  is obtained in air. In all atmospheres and temperature,  $\text{PrNiO}_{3-\delta}$  decomposes into  $\text{Pr}_2\text{NiO}_{4+\delta}$  and NiO end products while intermediate  $\text{Pr}_4\text{Ni}_3\text{O}_{10+\delta}$  appears under air and oxygen. Electrochemical characterizations as oxygen electrode in SOFC, shows that the half cells prepared by two-steps sintering process exhibits lower  $R_p$  value ( $R_p = 0.46 \text{ } \Omega.\text{cm}^2$  at  $600^\circ\text{C}$ ) than the co-sintered half cell ( $R_p = 0.91 \text{ } \Omega.\text{cm}^2$  at the same temperature). However, the  $R_p$  values remain by far higher than the one of  $\text{Pr}_2\text{NiO}_{4+\delta}$  ( $R_p = 0.15 \text{ } \Omega.\text{cm}^2$  at  $600 \text{ }^\circ\text{C}$ ) [35], suggesting that the mechanism of degradation, at the origin of our investigation is more complicated and further investigation, on  $\text{Pr}_4\text{Ni}_3\text{O}_{10+\delta}$  for instance, are currently carried out.

## Acknowledgements

The authors wish to gratefully acknowledge the Agence Nationale de la Recherche (A.N.R., France) for financial support. The authors also acknowledge Eric

Lebraud for XRD, Dominique Denux for thermal measurements and Sébastien Fourcade for his valuable help.

## References

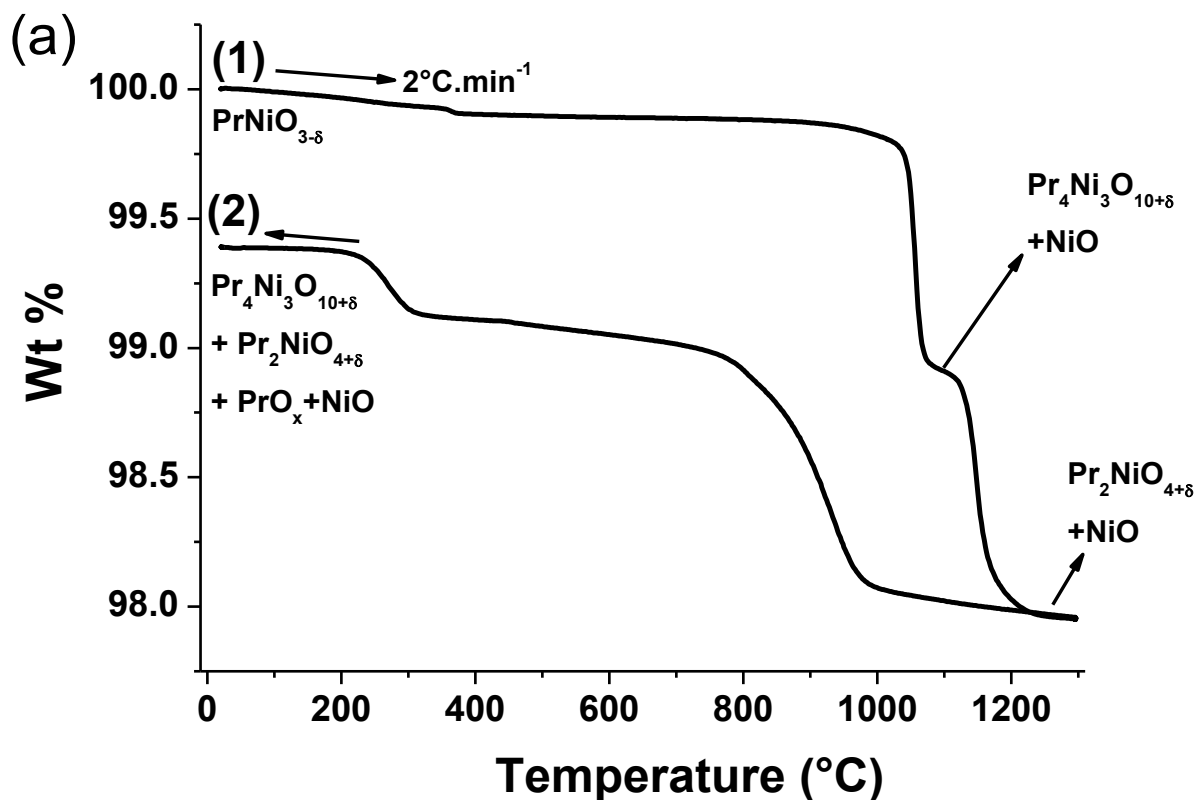
- [1] R. H. E. van Doorn, I. C. Fullarton, R. A. De Souza, J. A. Kilner, H. J. M. Bouwmeester, A. J. Burggraaf, *Solid State Ionics*, 96 (1997) 1-7.
- [2] G. Ch. Kostoglou, Ch. Ftikos, *Solid State Ionics*, 126 (1999) 143-151.
- [3] V. V. Kharton, A. P. Viskup, D. M. Bochkov, E. N. Naumovich, O. P. Reut, *Solid State Ionics*, 110 (1998) 61-68.
- [4] J. N. Audinot, Ph.D. thesis, Thèse de Doctorat de l'Université de Bordeaux I, 1999.
- [5] A. J. Jacobson, *Chemistry of Materials*, 22 (2010) 660-674.
- [6] H. Zhao, F. Mauvy, C. Lalanne, J.-M. Bassat, S. Fourcade, J.-C. Grenier, *Solid State Ionics*, 179 (2008) 2000-2005.
- [7] D. Marinha, J. Hayd, L. Dessemond, E. Ivers-Tiffée, E. Djurado, *Journal of Power Sources*, 196 (2011) 5084-5090.
- [8] A. Agüero, J. A. Alonso, M. J. Martínez-Lope, M. T. Fernández-Díaz, M. J. Escudero, L. Daza, *Journal of Materials Chemistry*, 16 (2006) 3402-3408.
- [9] E. Boehm, J.-M. Bassat, P. Dordor, F. Mauvy, J.-C. Grenier, Ph. Stevens, *Solid State Ionics*, 176 (2005) 2717-2725.
- [10] C. N. Munnings, S. J. Skinner, G. Amow, P. S. Whitfield, I. J. Davidson, *Solid State Ionics*, 176 (2005) 1895-1901.
- [11] C. Ferchaud, J.-C. Grenier, Y. Zhang-Steenwinkel, M. M. A. van Tuel, F. P. F. van Berkel, J.-M. Bassat, *Journal of Power Sources*, 196 (2011) 1872-1879.
- [12] V. Vibhu, J.-M. Bassat, A. Flura, C. Nicollet, J.-C. Grenier, A. Rougier, *ECS Transaction*, 68 (2015) 825-835.
- [13] V. Vibhu, A. Rougier, C. Nicollet, A. Flura, N. Penin, J.-C. Grenier, J.-M. Bassat, To be Submitted in *Journal of Power Sources*, 2015.
- [14] M. T. Escote, A. M. L. da Silva, J. R. Matos, R. F. Jardim, *Journal of Solid State Chemistry*, 151 (2000) 298-307.
- [15] A. K. Norman, M. A. Morris, *Journal of Materials Processing Technology*, 92-93 (1999) 91-96.
- [16] X. Obradors, L. M. Paulius, M. B. Maple, J. B. Torrance, A. I. Nazzal, J. Fontcuberta, X. Granados, *Physical Review B*, 47 (1993) 12353-12356.
- [17] P. C. Canfield, J. D. Thompson, S.-W. Cheong, L. W. Rupp, *Physical Review B*, 47 (1993) 12357-12360.
- [18] J. B. Torrance, P. Lacorre, A. I. Nazzal, E. J. Ansaldo, C. Niedermayer, *Physical Review B*, 45 (1992) 8209-8212.
- [19] J. L. Garcia-Munoz, J. Rodriguez-Carvajal, P. Lacorre, *Europhysics Letters*, 20, 1992, 241-247.
- [20] P. Lacorre, J. B. Torrance, J. Pannetier, A. I. Nazzal, P. W. Wang, T. C. Huang, *Journal of Solid State Chemistry*, 91 (1991) 225-237.
- [21] B. Berini, N. Keller, B. Pigeau, Y. Dumont, E. Popova, N. Franco, R. M. C. da Silva, *Journal of Applied Physics*, 104 (2008) 103539-1 – 103539-10.
- [22] L. Qiao, X. Bi, *Europhysics Letters*, 93 (2011) 57002 P1-P6.
- [23] A. Boileau, F. Capon, P. Laffez, S. Barrat, J. L. Endrino, R. E. Galindo, D. Horwat, J. F. Pierson, *Journal of Physical Chemistry C*, 118 (2014) 5908-5917.
- [24] P. Courty, H. Ajot, C. Marcilly, B. Delmon, *Powder Technology*, 7 (1973) 21-38.

- [25] F. M. Aquino, D. M. A. Melo, P. M. Pimentel, R. M. Braga, M. A. F. Melo, A. E. Martinelli, A. F. Costa. *Materials Research Bulletin*, 47 (2012) 2605-2609.
- [26] T. C. Huang, W. Parrish, H. Toraya, P. Lacorre, J. B. Torrance, *Materials Research Bulletin*, 25 (1990) 1091-1098.
- [27] R. D. Shannon. *Acta Crystallogr. Sect.*, A32 (1976) 751-767.
- [28] J. A. Alonso, M. J. Martinez-Lope, M. T. Casais, M. A. G. Aranda, M. T. Fernandez-Diaz, *Journal of the American Chemical Society*, 121 (1999) 4754-4762.
- [29] R. H. Mitchell, *Perovskites Modern and Ancient*, Almaz Press, 2002.
- [30] A. Flura, S. Dru, C. Nicollet, V. Vibhu, S. Fourcade, E. Lebraud, A. Rougier, J.-M. Bassat, J.-C. Grenier, *Journal of Solid State Chemistry*, 228 (2015) 189-198.
- [31] M. J. Martinez-Lope, J. A. Alonso, *European Journal of Solid State and Inorganic Chemistry*, 32 (1995) 361-371.
- [32] S. Primdahl, M. Mogensen, *Journal of the Electrochemical Society*, 146 (1999) 2827-2833.
- [33] T. Jacobsen, P. V. Hendriksen, S. Koch, *Electrochimica Acta*, 53 (2008) 7500-7508.
- [34] S. Adler, *Chemical Reviews*, 104 (2004) 4791-4843.
- [35] V. Vibhu, A. Rougier, C. Nicollet, A. Flura, J.-C. Grenier, J.-M. Bassat, *Solid State Ionics*, 278 (2015) 32-37.

## Additional Information: Chapter 5

### *Additional TGA experiments under oxygen*

While heating under oxygen  $\text{PrNiO}_{3-\delta}$  is completely dissociated into  $\text{Pr}_2\text{NiO}_{4+\delta}$  and NiO above 1120 °C, the cooling behavior in the same atmosphere is different. This experiment is important to understand the stability of the Pr-based nickelates ( $\text{PrNiO}_{3-\delta}$ ,  $\text{Pr}_4\text{Ni}_3\text{O}_{10+\delta}$  and  $\text{Pr}_2\text{NiO}_{4+\delta}$ ) and their inter conversion into one to another under oxygen, which is highly dependent on heating and cooling rates. The TGA plots of  $\text{PrNiO}_{3-\delta}$  recorded under oxygen with 2°, 5° and 1°  $\text{C}\cdot\text{min}^{-1}$  are reported in **Figure 1a, b** and **c** respectively. The description about these plots is discussed in chapter 5 (**Figure 8**).



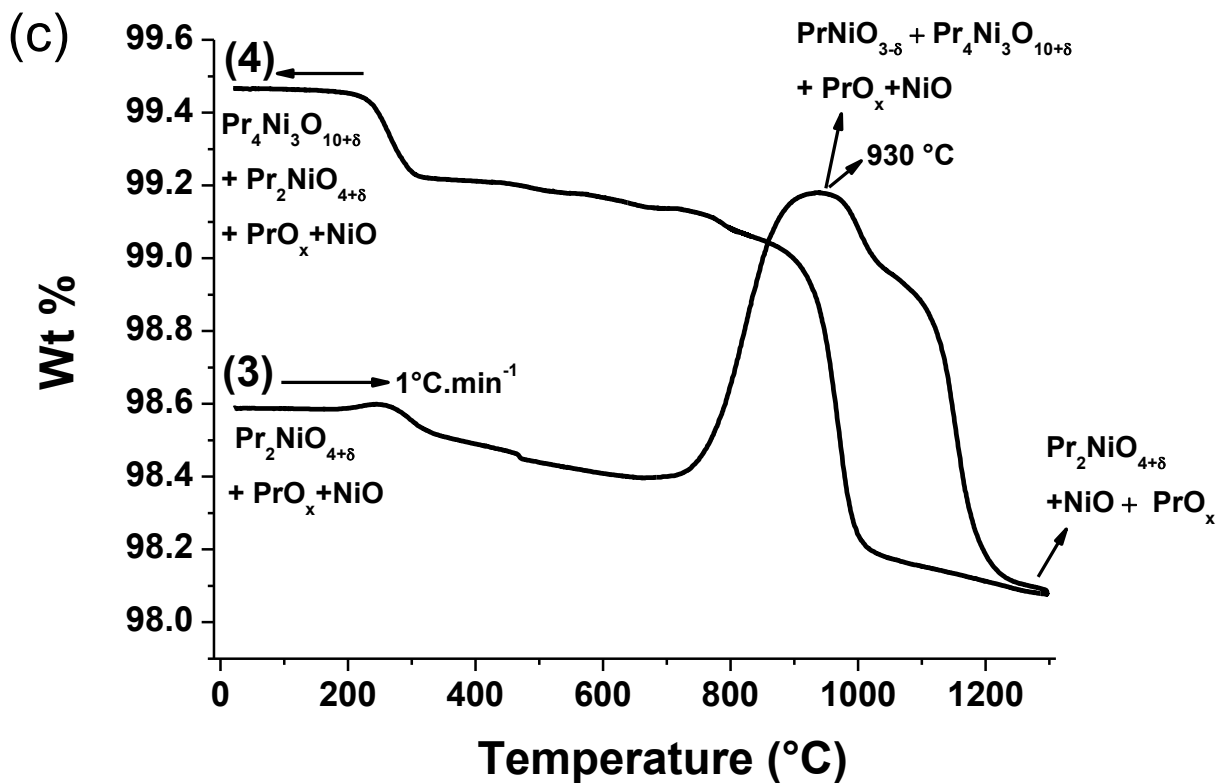
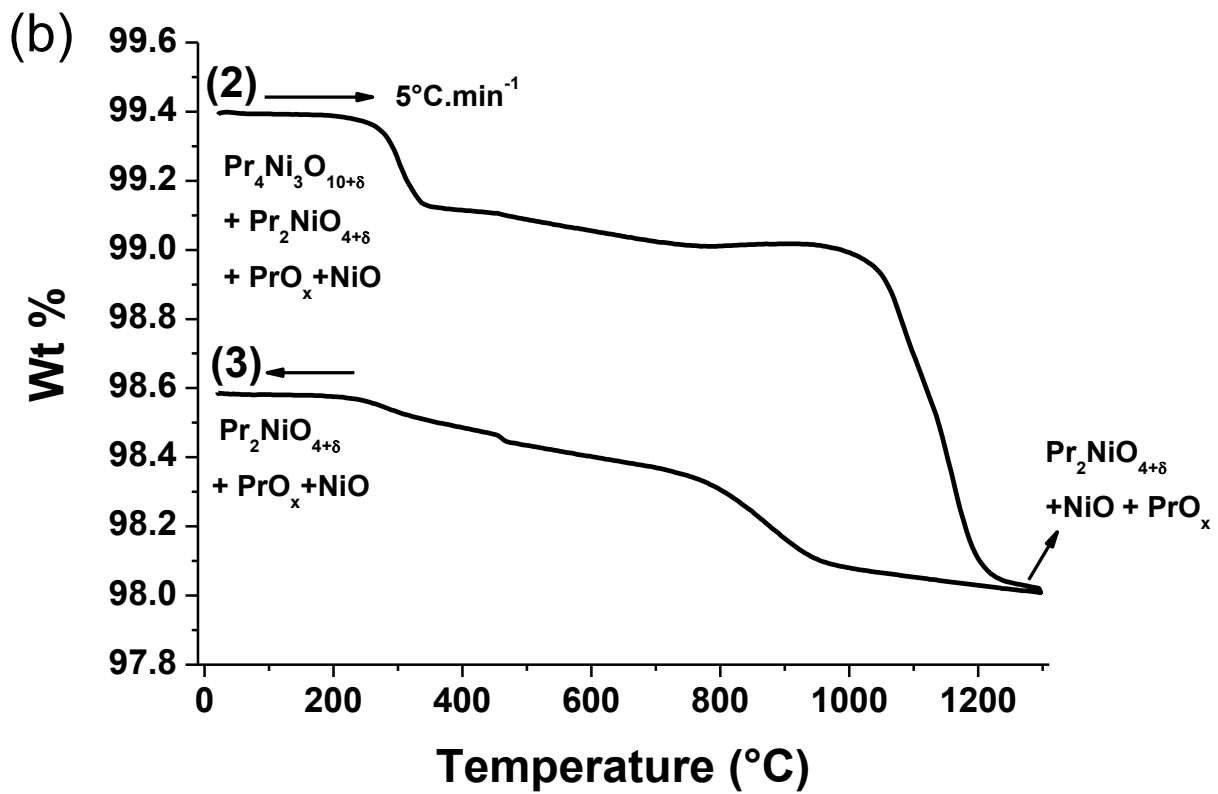


Figure 1: Variation of weight loss with temperature for  $\text{PrNiO}_{3-\delta}$ , under oxygen with (a)  $2^{\circ}$ , (b)  $5^{\circ}$  and (c)  $1^{\circ}\text{C}\cdot\text{min}^{-1}$  heating and cooling rates.



## Chapter 6

---

*Vibhu et al., Journal of Power Sources, 317 (2016) 184-193.*

# **Pr<sub>4</sub>Ni<sub>3</sub>O<sub>10+δ</sub>: a new promising oxygen electrode material for Solid Oxide Fuel Cells**

**Vaibhav Vibhu, Aline Rougier, Clément Nicollet, Aurélien Flura, Sébastien Fourcade, Nicolas Penin, Jean-Claude Grenier and Jean-Marc Bassat\***

*CNRS, Université de Bordeaux, Institut de Chimie de la Matière Condensée de Bordeaux (ICMCB), 87 Av. Dr Schweitzer, F-33608 Pessac Cedex, France.*

## **Abstract**

The present work is focused on the study of Pr<sub>4</sub>Ni<sub>3</sub>O<sub>10+δ</sub> as a new cathode material for Solid Oxide Fuel Cells (SOFCs). The structural study leads to an indexation in orthorhombic structure with Fmmm space group, this structure being thermally stable throughout the temperature range up to 1000 °C under air and oxygen. The variation of oxygen content (10+δ) as a function of temperature under different atmospheres show that Pr<sub>4</sub>Ni<sub>3</sub>O<sub>10+δ</sub> is always oxygen over-stoichiometric, which further suggests its MIEC properties. The polarization resistance ( $R_p$ ) of Pr<sub>4</sub>Ni<sub>3</sub>O<sub>10+δ</sub> electrode is measured for GDC/co-sintered and two-step sintered half cells. The  $R_p$  for co-sintered sample is found to be 0.16 Ω·cm<sup>2</sup> at 600 °C under air, which is as low as the one of highest performing Pr<sub>2</sub>NiO<sub>4+δ</sub> nickelate ( $R_p = 0.15$  Ω·cm<sup>2</sup> at 600 °C). Moreover, an anode supported (Ni-YSZ//YSZ) single cell including GDC//Pr<sub>4</sub>Ni<sub>3</sub>O<sub>10+δ</sub> co-sintered electrode shows a maximum power density of 1.60 W·cm<sup>-2</sup> at 800 °C and 0.68 W·cm<sup>-2</sup> at 700 °C. Here, the work is emphasized on the very close electrochemical performance of Pr<sub>4</sub>Ni<sub>3</sub>O<sub>10+δ</sub> compared to the one of Pr<sub>2</sub>NiO<sub>4+δ</sub> with higher chemical stability, which gives great interests to consider this material as a very promising oxygen-electrode for SOFCs.

**Keywords:** SOFC, Nickelates, Chemical stability, Oxygen over-stoichiometry, OER

## **1. Introduction**

The decrease of the operating temperature of the SOFCs is a critical challenge for their commercialization. Currently, the main objective is to decrease it down to around 600 – 700°C, in an effort to decrease the device cost (for example, using stainless steel instead of ceramics as interconnects) and to improve the cell durability. However, since the electrode reactions as well as ion transport through the electrolyte are temperature-driven, the electrochemical performance drastically decreases with temperature. Hence, it is mandatory to improve the materials and architecture of the cell in order to reach reasonable performance

at intermediate temperatures (600–700 °C). It is well known that promising materials for cathodes are Mixed Ionic and Electronic Conducting (MIEC) oxides [1-7]. Several attempts were made to find the best MIEC material for SOFCs in last few decades.

Recently Ruddlesden-Popper (RP) phases  $\text{Ln}_{n+1}\text{Ni}_n\text{O}_{3n+1}$  ( $\text{Ln} = \text{La}, \text{Pr}$  or  $\text{Nd}$ ) have shown excellent transport and electrochemical properties [6, 8-9]. The crystal structure of these phases can be described by the stacking of a finite number ( $n = 1, 2, 3$  mainly) of perovskite-type  $\text{LnNiO}_3$  layers and one rock salt  $\text{LnO}$  layer along the crystallographic  $c$ -direction ( $(\text{LnO})_n(\text{LnNiO}_3)_n$ ) [10-11]. The first member of the RP family of nickelates,  $n = 1$ , is  $\text{Ln}_2\text{NiO}_{4+\delta}$ , which adopts the  $\text{K}_2\text{NiF}_4$ -type structure with one layer of corner-sharing  $\text{NiO}_6$  octahedra along the  $c$ -direction.

In the second member of RP nickelates,  $n = 2$  ( $\text{Ln}_3\text{Ni}_2\text{O}_{7\pm\delta}$ ), two infinite  $\text{NiO}_6$  sheets are connected in  $c$ -direction between the rock salt layers. For  $n = 2$ , the electrical conductivity is significantly enhanced compared to  $\text{Ln}_2\text{NiO}_{4+\delta}$  as the nickel oxidation state and electronic correlation along  $c$ -direction increase.

Similarly, the structure of  $\text{Ln}_4\text{Ni}_3\text{O}_{10+\delta}$  ( $n = 3$ ) is built with three infinite  $\text{NiO}_6$  sheets connected in  $c$ -direction between the rock salt layers. Greenblatt reported that the smallest rare earth ion able to still stabilize  $\text{Ln}_4\text{Ni}_3\text{O}_{10+\delta}$  is  $\text{Nd}$  [11]. A metallic conductivity is observed for all the  $\text{Ln}_4\text{Ni}_3\text{O}_{10+\delta}$  phases and a metal-to-metal transition is observed for the  $\text{Ln} = \text{Pr}$  and  $\text{Nd}$  at 145 and 165K, respectively [11, 12]. The  $\text{Pr}_4\text{Ni}_3\text{O}_{10+\delta}$  has higher conductivity value in the 25–300 K temperature range than  $\text{Nd}_4\text{Ni}_3\text{O}_{10+\delta}$ , but lower than  $\text{La}_4\text{Ni}_3\text{O}_{10+\delta}$ . Regarding  $\text{Pr}_4\text{Ni}_3\text{O}_{10+\delta}$ , Bassat *et al.* have previously shown that the material is metallic [12], the transport properties being highly dependent on the  $\delta$ -value. Depending on the synthesis technique the  $\delta$  varies from  $-0.1$  to  $+0.1$ .

The first member of RP family,  $\text{Ln}_2\text{NiO}_{4+\delta}$  ( $\text{Ln} = \text{La}, \text{Pr}$  and  $\text{Nd}$ ) compounds have already evidenced promising results when used as cathode materials for SOFCs due to their MIEC properties [13-15].  $\text{Pr}_2\text{NiO}_{4+\delta}$  has the best electrochemical properties among three nickelates, especially at intermediate temperature (600–700°C) [16]. We have recently reported the decomposition of  $\text{Pr}_2\text{NiO}_{4+\delta}$  into  $\text{PrNiO}_{3-\delta}$ ,  $\text{Pr}_4\text{Ni}_3\text{O}_{10+\delta}$  and  $\text{Pr}_6\text{O}_{11}$  at the operating temperature range (600 to 800 °C) during long term [17]. A very interesting point is that even after complete dissociation the electrochemical performance, at least under  $i_{\text{dc}} = 0$  condition, do not show significant change (*i.e.* the same polarization resistance ( $R_p$ ) values

are obtained before and after ageing). Therefore, it is our goal to study the behaviour of these new forming materials, and in this study we especially focused on  $\text{Pr}_4\text{Ni}_3\text{O}_{10+\delta}$ .

According to author's knowledge, the literature on  $\text{Pr}_4\text{Ni}_3\text{O}_{10+\delta}$  remains scarce and limited to non-stoichiometry, transport and magnetic properties [10, 12], whereas its use as oxygen electrode in the field of SOFCs has never been reported. An effort was then made to investigate the properties of  $\text{Pr}_4\text{Ni}_3\text{O}_{10+\delta}$ , mainly the non-stoichiometry, chemical stability under different  $p\text{O}_2$  and electrochemical activity under air for use as an oxygen electrode material of SOFCs.

## 2. Experimental

### Powder preparation

The  $\text{Pr}_4\text{Ni}_3\text{O}_{10+\delta}$  phase was synthesised using the Glycine Nitrate Process (GNP) [18]. The corresponding precursors were  $\text{Pr}(\text{NO}_3)_3 \cdot 6\text{H}_2\text{O}$  (Sigma Aldrich , 99.99%),  $\text{Ni}(\text{NO}_3)_2 \cdot 6\text{H}_2\text{O}$  (Acros Organics, 99%) and glycine (Sigma Aldrich , 99.9%). The final annealing was performed at 1000 °C for 48 h under oxygen leading to well crystallized phases. Intermediate grinding and annealing steps were performed three times.

### X-ray diffraction analysis

The powders were first investigated by X-ray diffraction (XRD) at room temperature using a PANalytical X'pert MPD diffractometer with  $\text{Cu-K}_\alpha$  incident radiation to check the purity of phase. The XRD vs T (*i.e. in situ* XRD) were performed to check the stability of phase with temperature under air. The data were recorded for both heating and cooling, from room temperature up to 1000°C, by steps of 100°C. The heating and cooling rate was fixed to 2 °C.min<sup>-1</sup>, the powder being thermally equilibrated for 2 h at each particular temperature prior to the XRD data recording. The X-ray diffractogram recorded on the powder during cooling is preferentially reported here thanks to a thermal equilibrium which is expected to be more easily reached in this case.

The ageing test of powder was performed under air. Green pellets were first prepared and then left into a furnace for 1 month at 600, 700 and 800 °C, before the XRD characterization. Each X-ray diffractogram was fitted by profile matching using the Fullprof software.

## SEM analysis

The microstructures of  $\text{Pr}_4\text{Ni}_3\text{O}_{10+\delta}$  powder and the electrodes morphology were observed by field emission Scanning Electron Microscopy (JEOL JSM 6330 A) equipped with an EDS detector.

## Thermo Gravimetric analysis (TGA)

TGA experiments were carried out using a TA Instrument TGA-Q50 device, with the aim *i)* to determine the delta value,  $\delta$ , at room temperature under air, *ii)* to investigate the thermal stability *vs.*  $p\text{O}_2$  and *iii)* to study the  $\delta$  variation *vs.*  $T$  under air and oxygen atmospheres. In the first case the powders were beforehand heated under air up to 1000 °C, then cooled down to room temperature with a slow rate (2 °C.min<sup>-1</sup>), this cycle being reproduced twice to ensure a stable state of the material, *i.e.* a reproducible oxygen content. Then, a second cycle was performed under Ar - 5% H<sub>2</sub> flux with a very slow heating rate of (0.5 °C.min<sup>-1</sup>), the decomposition of the material leading to the determination of the oxygen stoichiometry after cycling the sample down to room temperature (Pr<sub>2</sub>O<sub>3</sub> and metallic Ni being formed as checked by XRD after the thermal cycle). Secondly, the thermal stability of  $\text{Pr}_4\text{Ni}_3\text{O}_{10+\delta}$  was investigated as a function of  $p\text{O}_2$ , the variation of the oxygen stoichiometry of the materials being successively studied under air ( $p\text{O}_2 = 0.21$  atm) and oxygen ( $p\text{O}_2 = 1$  atm), using heating and cooling rates of 2 °C.min<sup>-1</sup>. For this purpose, the powders were first thermodynamically equilibrated under air in the TGA device as described above (*i.e.* two cycles were performed under air). The gas was changed at room temperature and again two cycles were performed under oxygen. During cycling, the powder was left for 1 h at 1000 °C and room temperature.

## Conductivity measurements

It was first expected to prepare dense pellets by sintering the green pellets at 1000 °C for 24 h under oxygen, which are mandatory conditions to ensure keeping the pure  $\text{Pr}_4\text{Ni}_3\text{O}_{10+\delta}$  phase. However, it is worth mentioning that we could not succeed probably because of such limitation of temperature, 70 % being the highest density value obtained. The electrical conductivity was then determined under air using the four-probe technique, in the temperature range 20 – 800 °C with the heating and cooling rate of 1 °C.min<sup>-1</sup>.

## Preparation of symmetrical half cells

For the electrochemical studies, symmetrical half cells (electrode//GDC//8YSZ//GDC//electrode) were prepared. Dense pellets of 8YSZ (8 mol.% yttria stabilized zirconia) with diameter  $\approx 18$  mm and thickness  $\approx 1.2$  mm (preliminarily sintered at  $T = 1400$  °C) were used. The symmetrical half-cells were prepared by screen printing using two ways, *i.e.* two-step or co-sintering of the GDC/electrode layers. Terpeneol-based slurries were prepared from as prepared  $\text{Pr}_4\text{Ni}_3\text{O}_{10+\delta}$  powder and commercial GDC powder (Rhodia-Solvay). In order to increase the electrochemical performance of the half-cells [16], a 2-3  $\mu\text{m}$  GDC bi-layer was initially screen printed on both sides of the 8YSZ electrolyte pellet. The main role of GDC is, a) to obtain good interface and b) to stop the reactivity, between electrode and electrolyte.

Regarding the two steps sintering way, the GDC layer was first sintered at 1375 °C for 1 h under air. The electrode layer was then screen printed on each side of the GDC//8YSZ//GDC. The sintering study of the electrodes will be detailed in the Results and Discussion part.

The symmetrical half cells were also prepared by co-sintering the GDC and electrode layers. For this purpose, in a first step a single GDC layer was deposited on both sides of 8YSZ pellet. After drying ( $T \sim 80$  °C), the electrode layer was deposited on both sides by screen printing technique and co-sintered with GDC layer at 950 °C for 2 h under air.

A single cell was fabricated starting from a commercial anode supported half cell (Elcogen ASC-10C type) made of a 500  $\mu\text{m}$  thick Ni-8YSZ anode and a 3  $\mu\text{m}$  thick 8YSZ electrolyte membrane ( $\varnothing = 50$  mm). A GDC layer ( $\varnothing = 25$  mm) was first deposited on Ni-8YSZ//8YSZ support and then dried at 80 °C. After the deposition and sintering of the cathode layer ( $\varnothing = 16$  mm, see Single Cell measurements part), a  $\text{LaNi}_{0.6}\text{Fe}_{0.4}\text{O}_{3-\delta}$  (LNF) layer ( $\varnothing = 16$  mm) was deposited to improve the current collection [19].

## Electrochemical measurements

The electrochemical properties of the symmetrical half-cells were characterized by Electrochemical Impedance Spectroscopy (EIS). The initial EIS measurements were carried out under air, in the temperature range 500 – 800 °C under zero dc conditions. Gold grids (1.024  $\text{cm}^{-2}$  meshes) were used as current collectors. The impedance diagrams were recorded at steady state under potentiostatic control with 50 mV ac amplitude, from  $10^6$  Hz down to

$10^{-1}$  Hz, using a frequency response analyser module Autolab FRA2, coupled with a potentiostat/galvanostat PGSTAT 302N. The polarization resistance ( $R_p$ ) values were obtained by taking the difference between the low frequency (LF) and the high frequency (HF) intercepts with the real  $Z'$ -axis of the Nyquist representation. The complex impedance diagrams were fitted using an equivalent circuit by means of the Zview<sup>®</sup> (Scribner Associates) to measure the  $R_p$  of different processes.

Prior to single cell measurements, the anode was reduced using the following procedure: after heating in  $N_2$  up to 800 °C, the anode side was flushed with hydrogen gas with a flow rate of 250 ml.min<sup>-1</sup>. On the cathode side, synthetic flowing air was supplied as oxidant with flow rate of 500 ml.min<sup>-1</sup>. The impedance diagrams were recorded at OCV, 0.9, 0.8 and 0.7 V, at the operating temperatures, namely 800 and 700 °C. The ageing of a single cell at 700 °C was performed at a current density of 0.3 A·cm<sup>-2</sup>, using a Frequency Response Analyzer module Autolab FRA2, coupled with a potentiostat/galvanostat PGSTAT 302N.

### 3. Results and discussion

#### 3.1. XRD analysis

The XRD characterization of as-prepared  $Pr_4Ni_3O_{10+\delta}$  phase shows that the material crystallizes in an orthorhombic structure with  $Fmmm$  space group. The full pattern profile matching refinement leads to determine the following lattice parameters:  $a = 5.3714(2)$  Å,  $b = 5.4611(2)$  Å and  $c = 27.5271(3)$  Å (**Figure 1a**), these values are in good agreement with the previously reported results [10, 12].

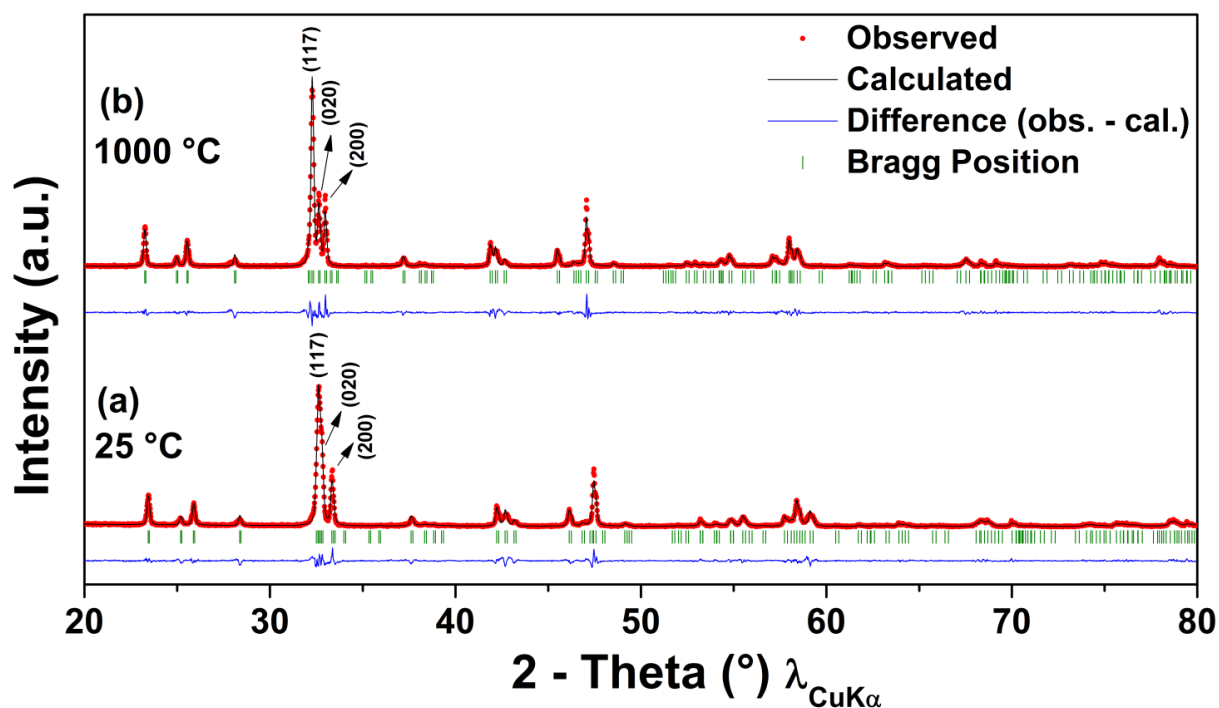


Figure 1: Fullprof refinement of the patterns of  $\text{Pr}_4\text{Ni}_3\text{O}_{10+\delta}$  at (a) 25 and (b) 1000 °C using  $Fmmm$  space group.

### 3.1.1. Thermal behaviour of the material with temperature under air (XRD vs. T)

The thermal variation of the X-ray diffractogram under air shows that the  $\text{Pr}_4\text{Ni}_3\text{O}_{10+\delta}$  phase remains stable up to 1000 °C; with increasing temperature, the structure keeps always the orthorhombic symmetry and is indexed with the  $Fmmm$  space group. An example is given in **Figure 1b**; at 1000 °C the refinement of the data leads to the following lattice parameters:  $a = 5.4300(4)$  Å,  $b = 5.4858(3)$  Å and  $c = 27.8910(3)$  Å. The absence of additional peaks with regard to the room temperature diagram confirms the stability of the material up to 1000 °C under air.

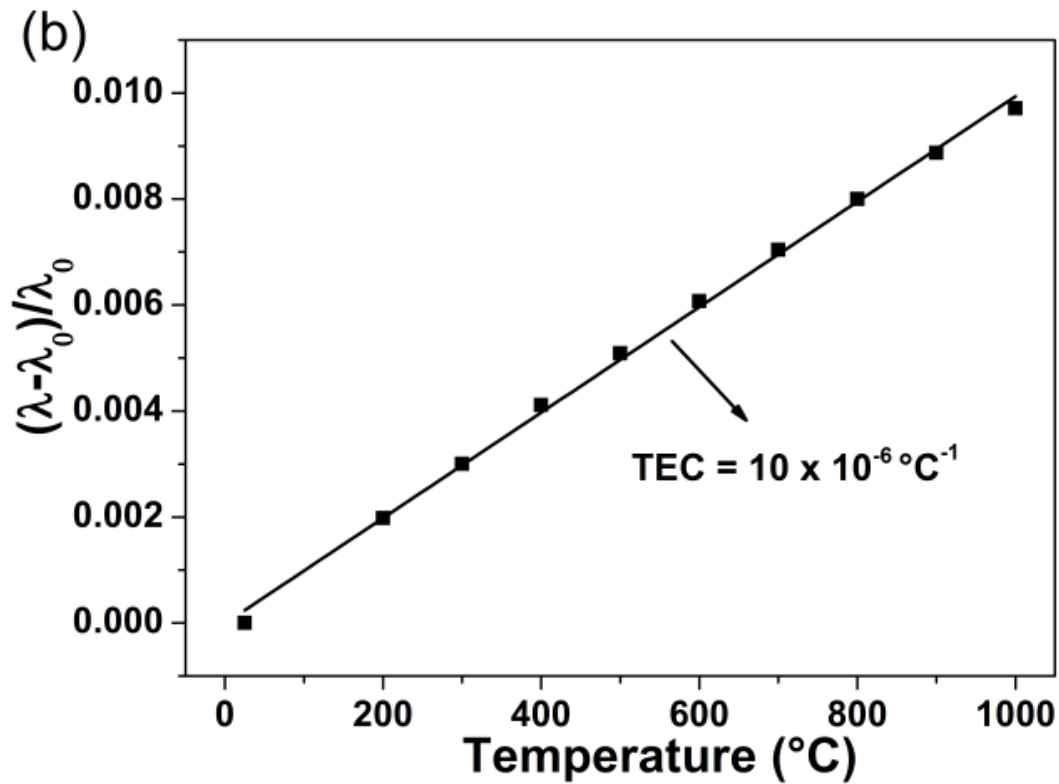
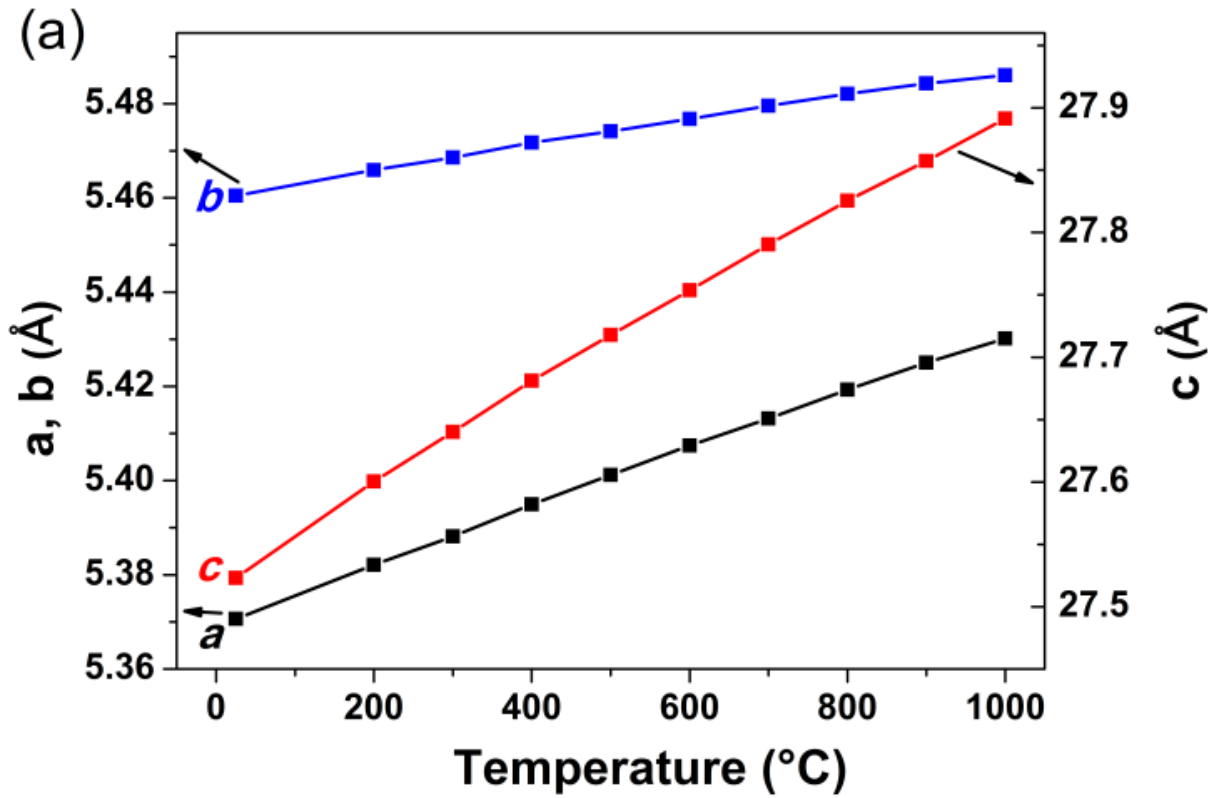


Figure 2: Variation of (a) lattice parameters and (b)  $(\lambda-\lambda_0)/\lambda_0$  of  $\text{Pr}_4\text{Ni}_3\text{O}_{10+\delta}$  under air as a function of temperature up to 1000 °C ( $\lambda$  and  $\lambda_0$  are cubic root of volume at particular temperature and room temperature respectively).

### 3.1.2. Variation of lattice parameters with temperature: determination of TEC

In **Figure 2a**, the variations of  $a$ ,  $b$  and  $c$  lattice parameters as a function of temperature are plotted. All of them show linear increase throughout the temperature range. The thermal expansion coefficient of  $\text{Pr}_4\text{Ni}_3\text{O}_{10+\delta}$  was calculated from the thermal variation of the lattice parameters *i.e.* the slope of  $(\lambda-\lambda_0/\lambda_0)$  vs  $T$  (**Figure 2b**), where  $\lambda$  and  $\lambda_0$  are cubic root of volume at particular temperature and room temperature respectively. The value of TEC is close to  $\sim 10 \times 10^{-6} \text{ }^\circ\text{C}^{-1}$  which is in the same order of those of the other components of SOFCs [20]. Following dilatometry measurements, a TEC value of  $12 \times 10^{-6} \text{ }^\circ\text{C}^{-1}$  was also determined; the observed discrepancy could be assigned to the fact that the pellet was not sufficiently dense.

## 3.2. TG analyses

Because the electrochemical behaviour of the material will be studied under air, we aim first to determine the over-stoichiometry value  $\delta$  after thermal equilibration under air, following the synthesis which is performed under oxygen. Later on, the evolution of  $\delta$  vs.  $T$  under air and oxygen will be recorded. Another part of this TGA study will aim to determine the thermal stability range of the material either under air or oxygen.

### 3.2.1. Determination of $\delta$ of material equilibrated under air

The  $\delta$ -value for  $\text{Pr}_4\text{Ni}_3\text{O}_{10+\delta}$  was calculated using TGA experiments performed under reducing conditions (5%  $\text{H}_2/\text{Ar}$  atmosphere, **Figure 3**). Two major weight losses occur: the first one at around  $400 \text{ }^\circ\text{C}$ , which corresponds to the reduction of  $\text{Ni}^{3+}$  into  $\text{Ni}^{2+}$  (corresponding plateau  $\text{Pr}_4\text{Ni}_3\text{O}_9$  is formed [21]), while the second weight loss corresponds to the complete reduction of  $\text{Ni}^{2+}$  into metallic  $\text{Ni}^0$ . Finally the total reduction of  $\text{Pr}_4\text{Ni}_3\text{O}_{10+\delta}$  into  $\text{Pr}_2\text{O}_3$  and  $\text{Ni}$  (within the appropriate ratio) is then evidenced, leading to the determination of  $\delta$ . The calculated value corresponding to the first plateau and after total reduction results in the almost same value,  $\delta = 0.10 \pm 0.01$  at room temperature.

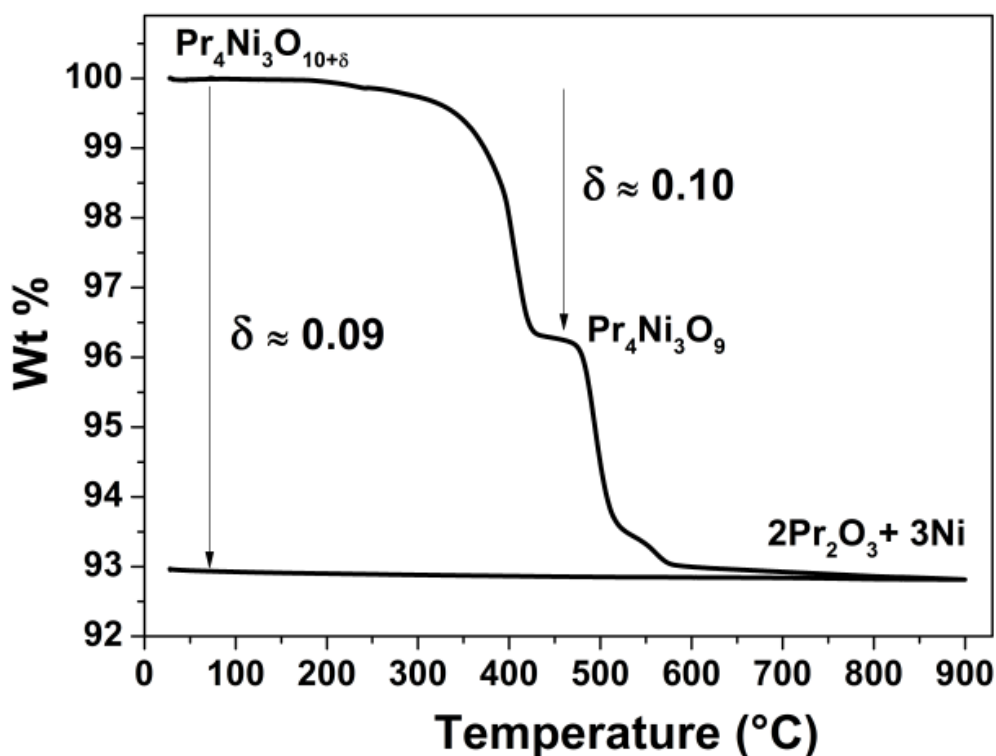


Figure 3: TGA plot under 5% Ar-H<sub>2</sub> for the determination of delta value.

### 3.2.2. Behavior under air and oxygen

TGA experiments were carried out under air and oxygen with the aim to investigate the chemical stability and to find the most appropriate temperature and atmosphere for the sintering of electrodes made of this material (refer to experimental part). **Figure 4a** and **4b** show the variation of the weight loss with temperature for  $\text{Pr}_4\text{Ni}_3\text{O}_{10+\delta}$  in air and in oxygen atmosphere, respectively; the results largely depend upon  $p\text{O}_2$ . Under air,  $\text{Pr}_4\text{Ni}_3\text{O}_{10+\delta}$  exhibits thermal stability up to  $\sim 1050$  °C. Above this temperature it starts decomposing and around  $T = 1140$  °C, it is completely decomposed into  $\text{Pr}_2\text{NiO}_{4+\delta}$  and NiO (**Figure 4a**). This decomposition was checked by XRD both on the powder at the end of this TGA cycle (**Figure 5a**) or after quenching another set of powder from 1200 °C to RT in a separate furnace (not reported). This decomposition is completely irreversible under air,  $\text{Pr}_2\text{NiO}_{4+\delta}$  phase being stable under air as confirmed by a second TGA cycle (not reported).

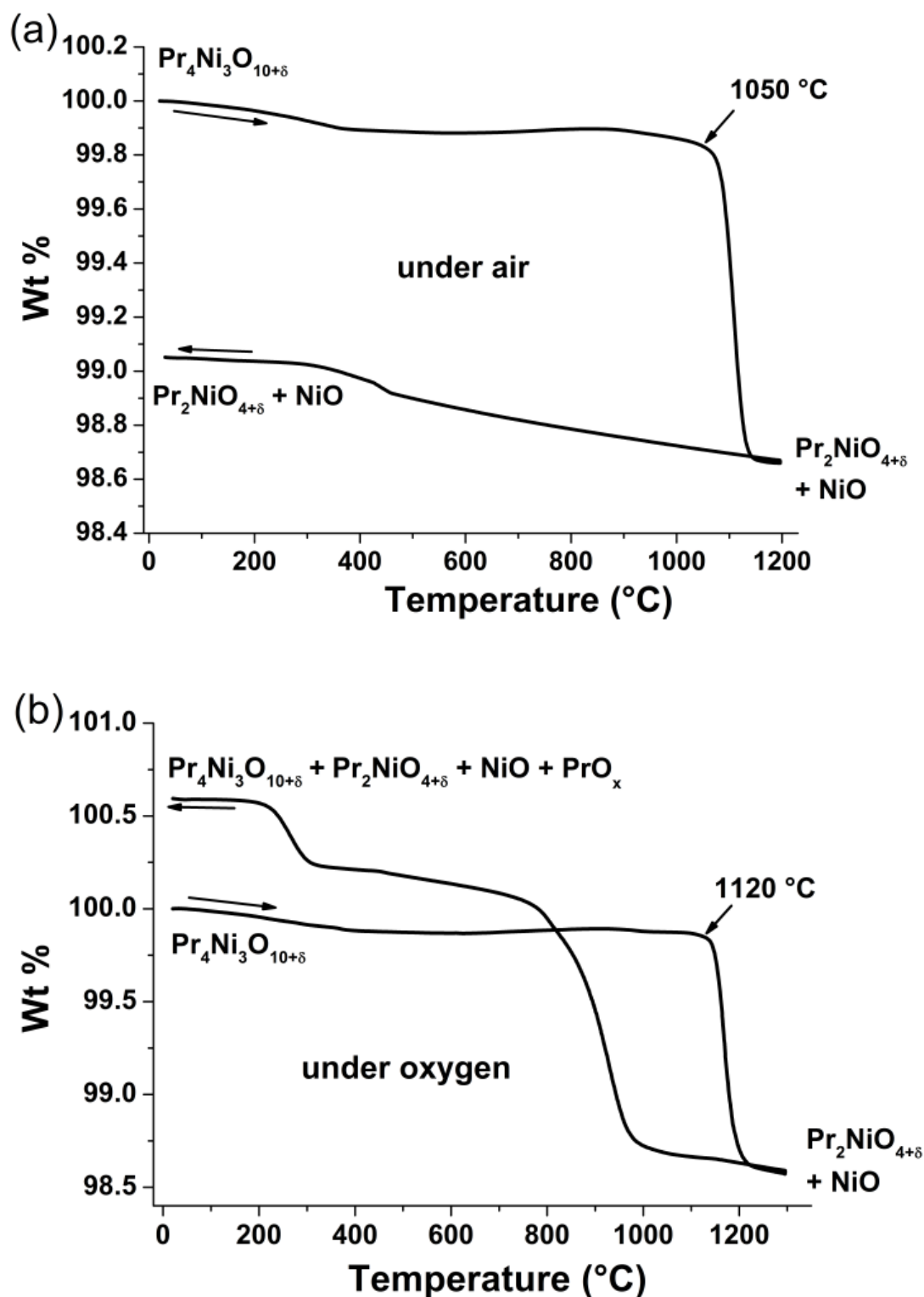
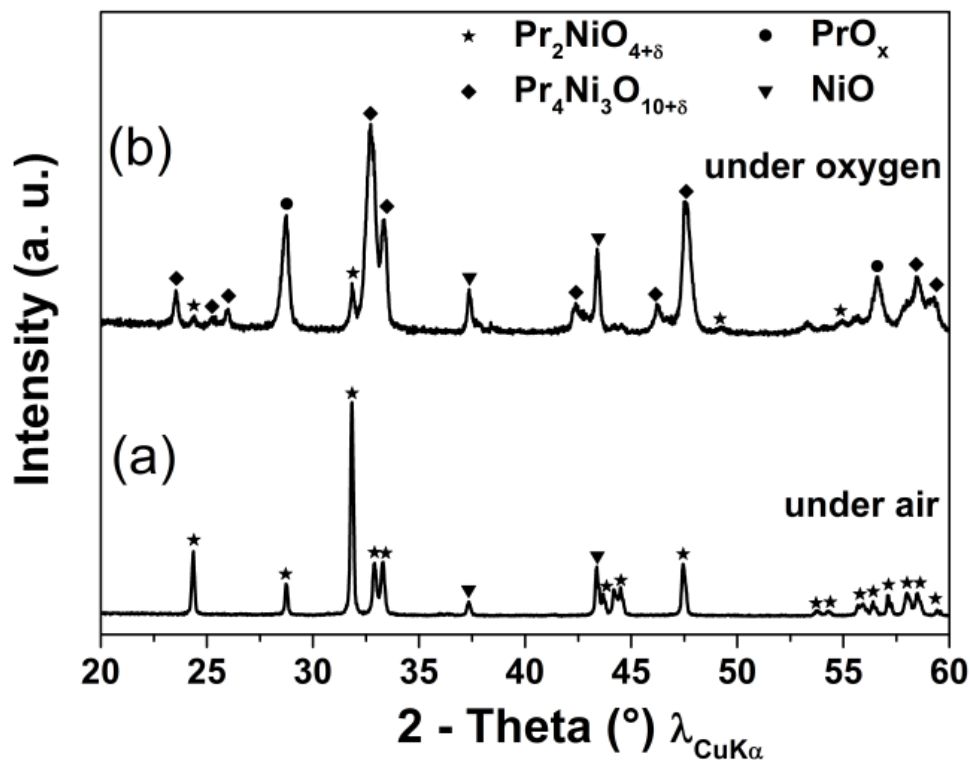


Figure 4: Thermal variation of weight loss with temperature for  $\text{Pr}_4\text{Ni}_3\text{O}_{10+\delta}$  under (a) air and (b) oxygen atmospheres.

Under oxygen,  $\text{Pr}_4\text{Ni}_3\text{O}_{10+\delta}$  shows higher stability than in air, up to 1120 °C (Figure 4b) and above this temperature, it decomposes again into  $\text{Pr}_2\text{NiO}_{4+\delta}$  and NiO (as checked by XRD again). However, the behaviour when cooling under oxygen is completely different than

what was previously observed under air. Indeed,  $\text{Pr}_2\text{NiO}_{4+\delta}$  starts again changing into  $\text{Pr}_4\text{Ni}_3\text{O}_{10+\delta}$  and  $\text{PrO}_x$  (around 950 °C). The XRD analysis at the end of cooling process shows the presence of mixture of  $\text{Pr}_4\text{Ni}_3\text{O}_{10+\delta}$ ,  $\text{Pr}_2\text{NiO}_{4+\delta}$ ,  $\text{PrO}_x$  and  $\text{NiO}$  (**Figure 5b**), which is in agreement with the previously reported results for  $\text{PrNiO}_{3-\delta}$  [22].



**Figure 5:** X-ray diffractograms after TGA performed on  $\text{Pr}_4\text{Ni}_3\text{O}_{10+\delta}$  powder under (a) air and (b) oxygen.

### 3.2.3. Variation of the oxygen content ( $\delta$ value) under air and oxygen

In the following, the thermal variation of the oxygen content was investigated over the stability domain of  $\text{Pr}_4\text{Ni}_3\text{O}_{10+\delta}$ , *i.e.* from room temperature up to 1000 °C (*cf.* **Figure 4**). Before starting the experiment, the powder was first equilibrated under air, ensuring the starting value of  $\delta \sim 0.10$ . For both atmospheres, two cycles were performed to reach the reversibility while the powder was kept for 1 hour at the 1000 °C before cooling. The thermal variation of the oxygen content,  $10+\delta$ , under air and oxygen is plotted in **Figure 6**. In air, a reversible behaviour is observed during both cycles.

Under oxygen, the material is up taking oxygen during first cycling, then, a reversible behavior is observed (2<sup>nd</sup> cycle is reported). One should point out that the material is always oxygen over-stoichiometric within the whole stability temperature range.

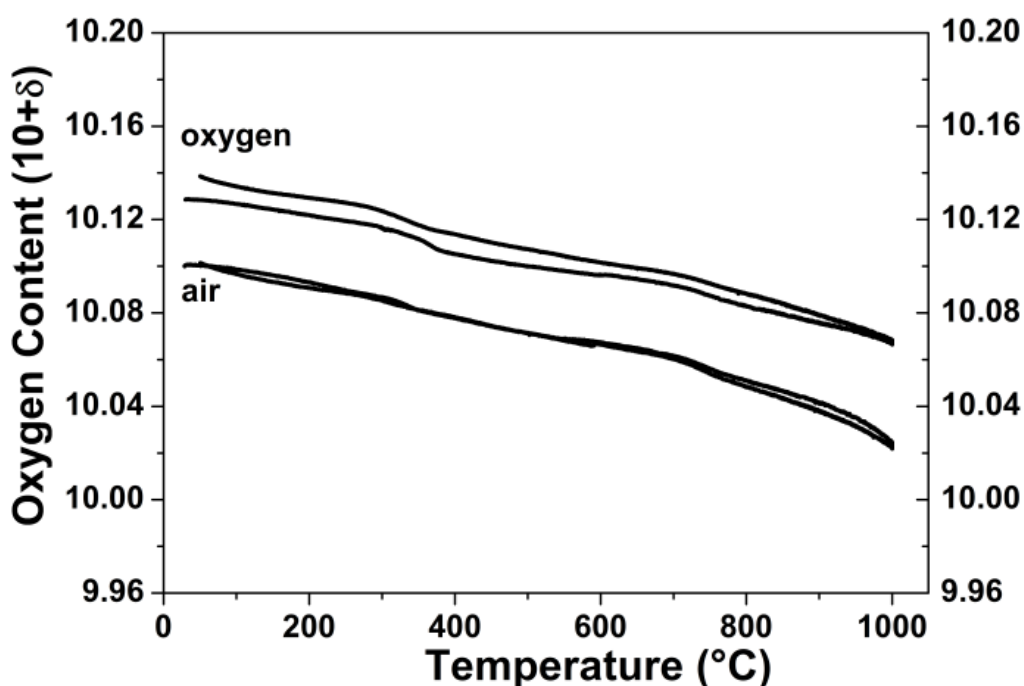


**Figure 6: Thermal variation of the oxygen content ( $10+\delta$ ) for  $\text{Pr}_4\text{Ni}_3\text{O}_{10+\delta}$ , (a) under air and (b) under oxygen at  $30\text{ }^\circ\text{C} \leq T \leq 1000\text{ }^\circ\text{C}$ .**

The cycling was also performed under argon up to  $800\text{ }^\circ\text{C}$  (*cf.* **Figure additional info. 1 and 2**), and as expected a small decrease in oxygen content is observed during first cycle while during second cycle a reversible behavior is observed. The calculated  $\delta$  values at room temperature after thermal equilibration under the considered atmospheres are 0.14 ( $\text{Ni}^{3+} \sim 76\%$ ), 0.10 ( $\text{Ni}^{3+} \sim 73\%$ ) and 0.07 ( $\text{Ni}^{3+} \sim 71\%$ ) under oxygen, air and argon, respectively. Furthermore it can be concluded that the material is “breathing” oxygen quite easily *i.e.* it is easy to include more interstitial oxygen under oxygen after equilibration under air, and it is also quite easy to remove the same amount of oxygen under argon ( $\sim 0.03$  in both cases).

As an intermediate conclusion, the above TGA study indicates that the thermal stability limit is  $1120\text{ }^\circ\text{C}$  and  $1050\text{ }^\circ\text{C}$  under oxygen and air, respectively, but we are aware that these observations are governed by kinetics. Moreover we checked that the long term thermal stability of the material is ensured at  $1000\text{ }^\circ\text{C}$  under oxygen, indeed this is the synthesis condition of  $\text{Pr}_4\text{Ni}_3\text{O}_{10+\delta}$ . It was also investigated that the material is stable under air at  $950\text{ }^\circ\text{C}$ . Such observations were further used as guidelines for the sintering of electrodes.

### 3.2.4. Long term chemical stability at operating temperatures

Following previous studies performed till high temperature, it's also mandatory to check the thermal stability of the material at the operating temperatures of SOFCs. Then the ageing of  $\text{Pr}_4\text{Ni}_3\text{O}_{10+\delta}$  powder was performed under air during one month at 600, 700 and 800 °C.

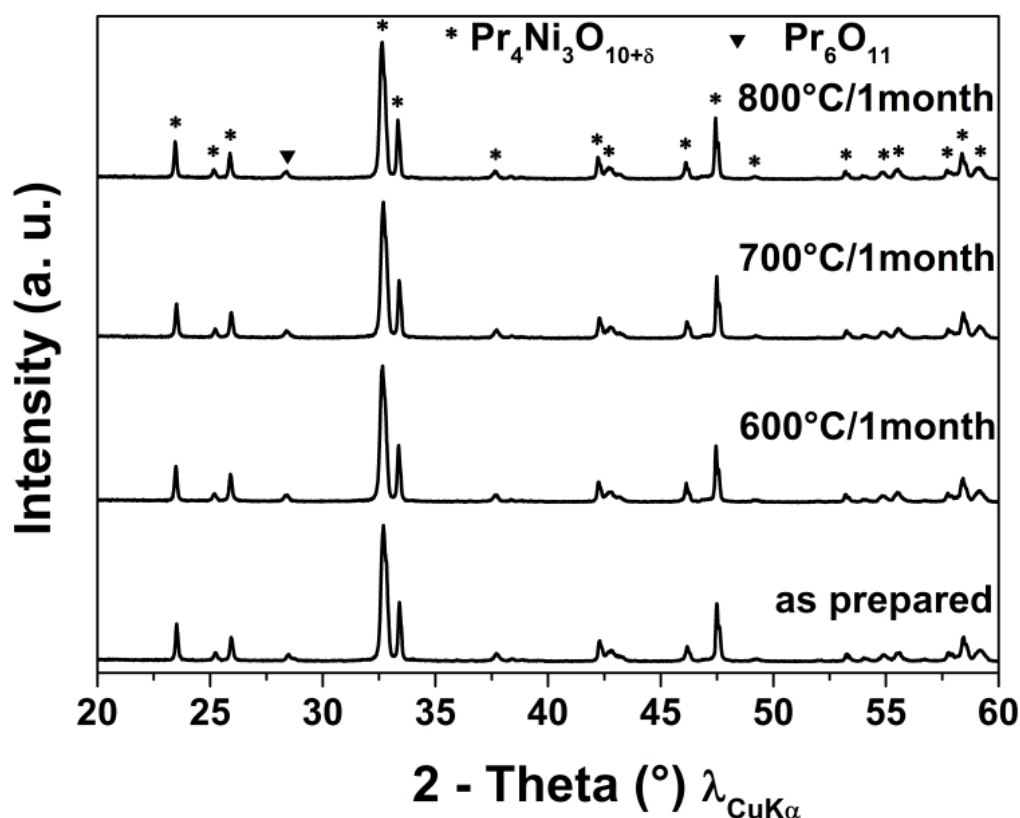


**Figure 7: X-ray diffractograms of  $\text{Pr}_4\text{Ni}_3\text{O}_{10+\delta}$  powder after ageing 1 month at 600, 700 and 800 °C under air.**

The corresponding XRD diffractograms along with as prepared powder are shown in **Figure 7**. The material is chemically very stable at these SOFCs operating conditions, indeed, only a very small peak of  $\text{PrO}_x$  is observed (however existing in the as-prepared powder as well). This long term stability indicates that this material is suitable to be used as oxygen electrode, which will be checked in the final part regarding electrochemical measurements.

### 3.3. Electrical Conductivity

The variation of the total electrical conductivity  $\sigma$  vs.  $1000/T$  for  $\text{Pr}_4\text{Ni}_3\text{O}_{10+\delta}$  is reported in **Figure 8**, and compared with the corresponding data for  $\text{PrNiO}_{3-\delta}$  and  $\text{Pr}_2\text{NiO}_{4+\delta}$ .

$\text{Pr}_4\text{Ni}_3\text{O}_{10+\delta}$  shows metal-like behaviour over the temperature range up to 20–800 °C under air, as  $\text{PrNiO}_{3-\delta}$  but unlike  $\text{Pr}_2\text{NiO}_{4+\delta}$  which shows semiconducting behaviour. The maximum conductivity value observed for  $\text{Pr}_4\text{Ni}_3\text{O}_{10+\delta}$  is close to  $200 \text{ S.cm}^{-1}$  (at room temperature) which is the highest value among  $\text{Pr}_4\text{Ni}_3\text{O}_{10+\delta}$ ,  $\text{PrNiO}_{3-\delta}$  and  $\text{Pr}_2\text{NiO}_{4+\delta}$  phases and is in agreement with the one earlier reported result [12]. The conductivity varies from  $\sim 85\text{--}200 \text{ S.cm}^{-1}$  from 800 °C to room temperature. At a typical operating temperature of 600 °C,  $\text{Pr}_4\text{Ni}_3\text{O}_{10+\delta}$  shows electrical conductivity,  $\sigma = 90 \text{ S.cm}^{-1}$ , similar to those of other Pr-based nickelates for ex.  $\text{PrNiO}_{3-\delta}$  ( $\sigma \sim 106 \text{ S.cm}^{-1}$ ) and  $\text{Pr}_2\text{NiO}_{4+\delta}$  ( $\sigma \sim 112 \text{ S.cm}^{-1}$ ) (**Figure 8**), meeting the requirement for a SOFC cathode material.

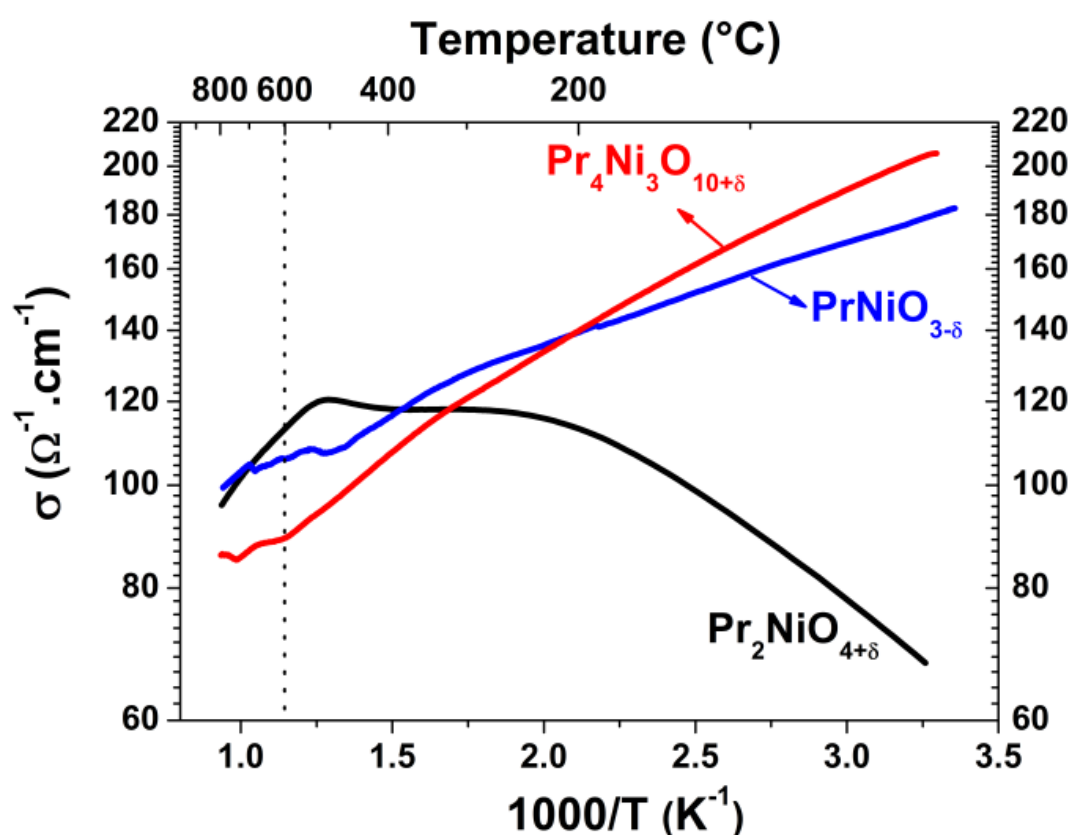


**Figure 8: Thermal variation of the electrical conductivity of  $\text{Pr}_4\text{Ni}_3\text{O}_{10+\delta}$  compared with  $\text{PrNiO}_{3-\delta}$  and  $\text{Pr}_2\text{NiO}_{4+\delta}$ , under air up to 800 °C.**

In general, in a material showing metallic behavior the decrease in conductivity observed with increasing temperature can be understood in terms of decrease of the charge carrier mobility while the charge carrier amount remains almost constant. Here, because the material exchanges oxygen with the surrounding atmosphere upon heating (**Figure 6**), one can wonder if the corresponding decrease of the holes amount ( $\text{Ni}^{3+}$ ) is large or not. As the  $\text{Ni}^{3+}$  percentage is not showing significant change with increasing temperature (73 to 70 %

from room temperature to 800 °C), it can be concluded that the decrease in the conductivity is due to a decrease of the charge carrier mobility as expected.

Considering the expected MIEC properties of the  $\text{Pr}_4\text{Ni}_3\text{O}_{10+\delta}$  phase, as in all atmospheres, the material remains always oxygen over-stoichiometric (see TGA part), the behavior should be MIEC whatever the  $p\text{O}_2$  throughout the temperature range of stability, however it would be to confirm experimentally measuring the ionic (oxygen) conductivity.

### 3.4. Electrochemical studies

In the second part of the work, we aimed first at the preparation of electrode ink using  $\text{Pr}_4\text{Ni}_3\text{O}_{10+\delta}$  powder prior to its shaping by screen-printing on 8YSZ//GDC supports. The sintering was performed using two different ways. The EIS vs. T measurements were performed and the results discussed comparing both sets of data obtained with the two kinds of half cells. Finally, single cells measurements ( $i$ - $V$  curves recording at the operating temperatures 800 and 700°C) were performed using the sintering way optimized in the previous step (at  $i_{dc}=0$ ).

#### 3.4.1. Morphology of as-prepared powder

Before the preparation of ink, the morphology of the as prepared powder was investigated by SEM and is shown in **Figure 9**. It evidences grains which are highly connected with each other. The high flame temperature which characterized the auto-combustion GNP process may explain this result. Therefore this powder was attrited with zirconia balls in ethanol medium for 1 h with the aim to obtain very fine powder, indeed a mean particle size of about 0.6  $\mu\text{m}$  (as checked using laser granulometry measurements) was finally obtained.

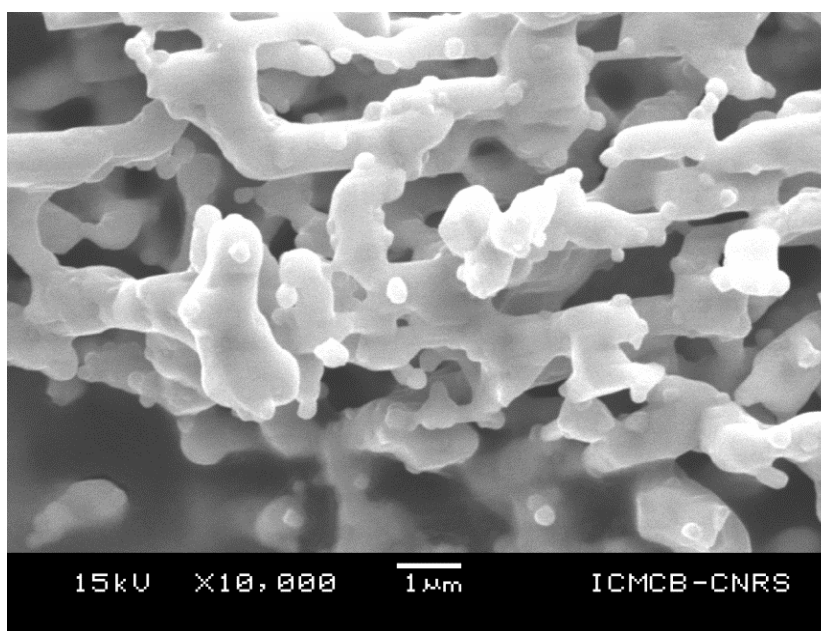


**Figure 9: Morphology of as-prepared powder after synthesis by GNP.**

#### **3.4.2. EIS characterization: symmetrical cell**

EIS measurements were carried out on  $\text{Pr}_4\text{Ni}_3\text{O}_{10+\delta}$ //GDC//8YSZ symmetrical half cells. These ones were prepared using two routes, either by a two-step process or co-sintering GDC and the electrode (detailed in experimental part). Then it will be possible to compare the polarization resistances,  $R_p$ , and the shape of impedance curves obtained in both cases.

#### **3.4.3. Optimization of the two-step sintering process**

The two-step sintering condition was first optimized using several sintering temperatures under oxygen. The sintering was first performed at the temperature corresponding to the phase stability limit, *i.e.* 1000 °C as discussed above. However one hour sintering is not sufficient from the mechanical point of view (confirmed by "tape test"); therefore 2 h of sintering is minimal. When the sintering was performed during 2 h at 1000 °C, the  $R_p$  value is very high ( $R_p = 2.7 \Omega\cdot\text{cm}^2$  at 600 °C, **Figure 10**). Hence for better electrochemical performance it is mandatory to sinter the electrode at higher temperature.

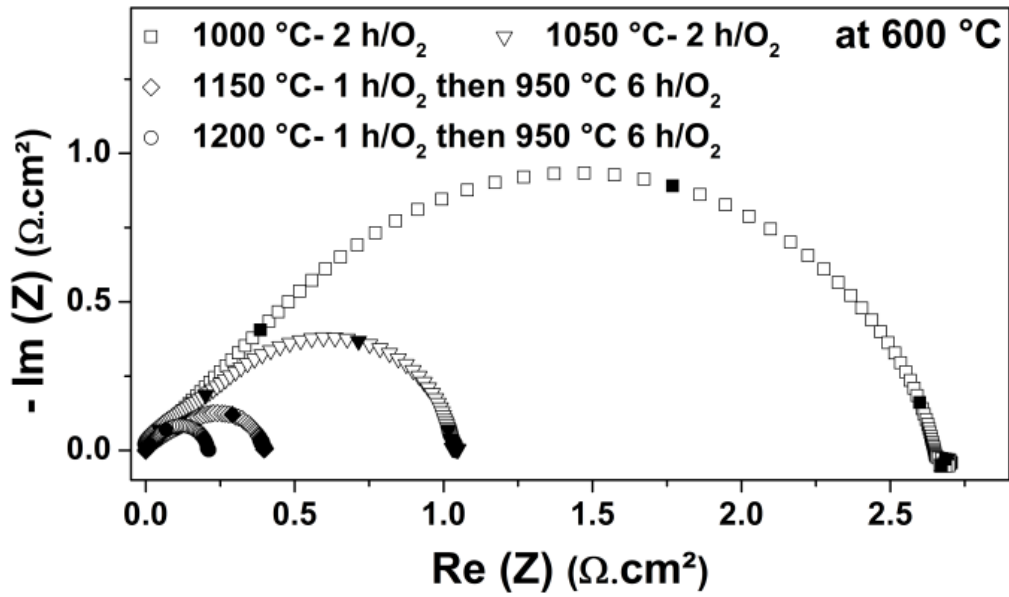


**Figure 10: Polarization resistances,  $R_p$ , measured at 600 °C under air on the half cells prepared by two-step sintering process at 1000°C/2h/O<sub>2</sub>, 1050°C/2h/O<sub>2</sub> (+ 950 °C/6h/O<sub>2</sub>), 1150°C/1h/O<sub>2</sub> (+ 950 °C/6h/O<sub>2</sub>) and 1200°C/1h/O<sub>2</sub> (+ 950 °C/6h/O<sub>2</sub>) and slowly cooled.**

**Pr<sub>2</sub>NiO<sub>4+δ</sub> is completely absent.**

The sintering at  $T > 1050$  °C/1h leads to partial decomposition into Pr<sub>2</sub>NiO<sub>4+δ</sub> and NiO, however, a slow cooling under O<sub>2</sub> leads to the re-formation of Pr<sub>4</sub>Ni<sub>3</sub>O<sub>10+δ</sub> (**Figure 4b**) [22]. The lowest the cooling rate is, the lowest the amount of Pr<sub>2</sub>NiO<sub>4+δ</sub> is expected. Then for preparing the electrodes, the half cells were cooled at 1°C/min from the sintering temperature ( $T = 1050, 1150$  and  $1200$  °C) and also kept at 950 °C for 6 h under O<sub>2</sub>, to make sure of the recovery of Pr<sub>4</sub>Ni<sub>3</sub>O<sub>10+δ</sub> phase. The corresponding X-ray diffractogram of the half cell sintered at 1150°C is shown in **Figure 11** as an example, in which Pr<sub>4</sub>Ni<sub>3</sub>O<sub>10+δ</sub> appears as major phase and no peak for Pr<sub>2</sub>NiO<sub>4+δ</sub> is observed.

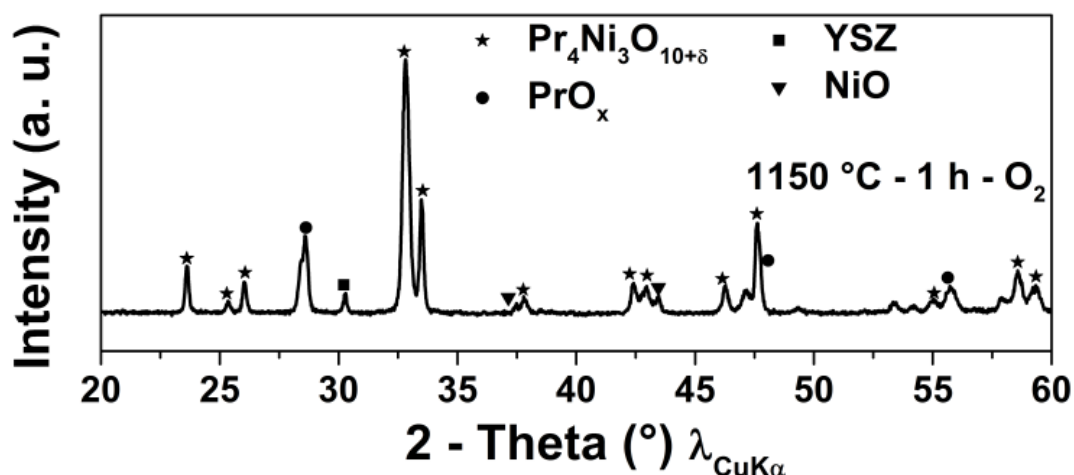


**Figure 11:** X-ray diffractogram of half cells after sintering at 1150 °C for 1 h under  $\text{O}_2$  (+ 950 °C/6h/ $\text{O}_2$ ).

Progressive increase of sintering temperature up to 1050 and 1150 °C leads to further decrease in the  $R_p$  values down to 1.05 and 0.25  $\Omega\cdot\text{cm}^2$  respectively at 600 °C. Further increase of the sintering temperature leads to small increase of  $R_p$ , up to 0.40  $\Omega\cdot\text{cm}^2$  when the sintering temperature is 1200 °C. Hence the sintering at 1150 °C for 1 h is obtained as an optimized condition, however it leads to the appearance of some additional phases ( $\text{PrO}_x$  and NiO) (*cf.* **Figure 11**). To avoid such additional phases, it's important to perform the sintering up to 1000 °C (thermal stability domain of  $\text{Pr}_4\text{Ni}_3\text{O}_{10+\delta}$ ). For this purpose, co-sintering of GDC and electrode was applied.

#### 3.4.4. Co-sintering of GDC and $\text{Pr}_4\text{Ni}_3\text{O}_{10+\delta}$ half cell

Aiming at favoring pure  $\text{Pr}_4\text{Ni}_3\text{O}_{10+\delta}$  phase, the symmetrical half cells were prepared by co-sintering GDC with the electrode at 950 °C for 2 h. The sintering condition was already optimized in our group. Air was chosen instead of oxygen for sake of simplicity. *In-situ* (in the electrochemical cell) and *ex-situ* (in the furnace) co-sintering experiments lead to similar  $R_p$  values of  $\approx 0.16 \Omega\cdot\text{cm}^2$  at 600 °C. Moreover after the co-sintering thermal cycle, no change is observed in the X-ray diffractogram of the electrode with respect to the starting  $\text{Pr}_4\text{Ni}_3\text{O}_{10+\delta}$  powder.

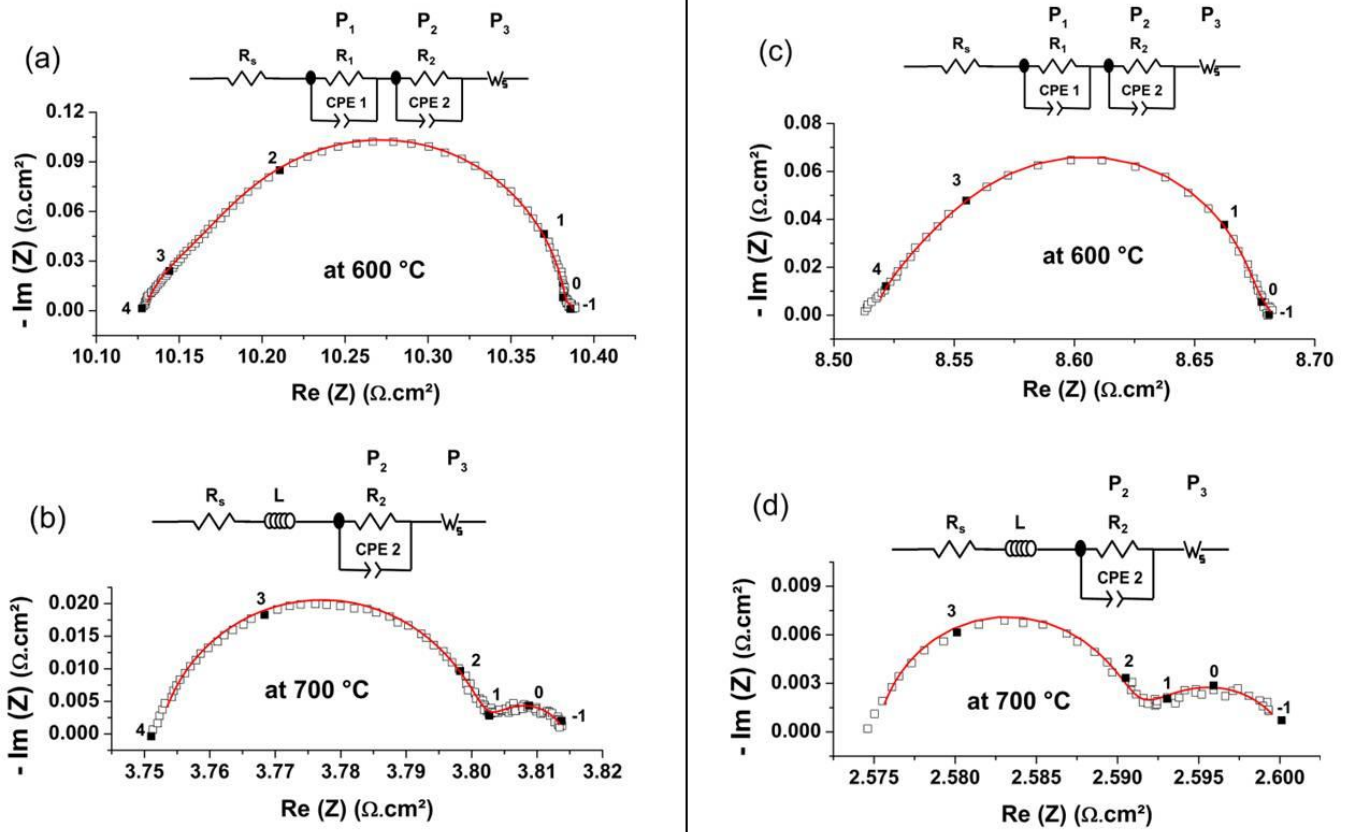


**Figure 12: Nyquist plots recorded for  $\text{Pr}_4\text{Ni}_3\text{O}_{10+\delta}$  electrode at 600 °C and 700 °C for both two-step sintered (1150 °C/1h) (a, b) and co-sintered (950 °C/2h) (c, d) half cells and fitted using  $R_s$  (series resistance),  $R//CPE$  and Warburg element ( $W_s$ ).**

### 3.4.5. Discussion

The EIS data were recorded between 500 and 800 °C. In **Figure 12 (a, b)** and **Figure 12 (c, d)** the Nyquist impedance diagrams are compared at 600 °C and 700 °C for two-step sintered and co-sintered half-cells, respectively. The different value of  $R_s$  at the same temperature is due to difference in the thickness of electrolyte support.

In both cases, three processes for  $T < 700$  °C ( $P_1$ ,  $P_2$  and  $P_3$ ) instead of two ( $P_2$  and  $P_3$ ) for  $T \geq 700$  °C are distinguished. At higher temperature,  $T \geq 700$  °C, as all processes are shifted toward higher frequencies, the process  $P_1$  is hidden by the inductance of the wires and hence could not be distinguished anymore. The processes  $P_1$  (appearing at high frequency ( $10^4 - 10^3$  Hz)) and  $P_2$  (appearing at middle frequencies ( $10^3 - 1$  Hz)) were fitted using two parallel  $R//CPE$  elements for the sake of simplicity, at 600 °C. The origin of process  $P_1$  is likely due to  $\text{O}^{2-}$  solid state diffusion in the interphase formed at the interface of GDC//electrode layer, as reported for  $\text{Pr}_2\text{NiO}_{4+\delta}$  [23]. Indeed, at the electrode//GDC interface

Pr-cations partly diffuse into the GDC layer forming Pr-doped ceria interphase, and the  $O^{2-}$  diffusion should occur on this new phase formed thanks to its MIEC properties [24, 25].

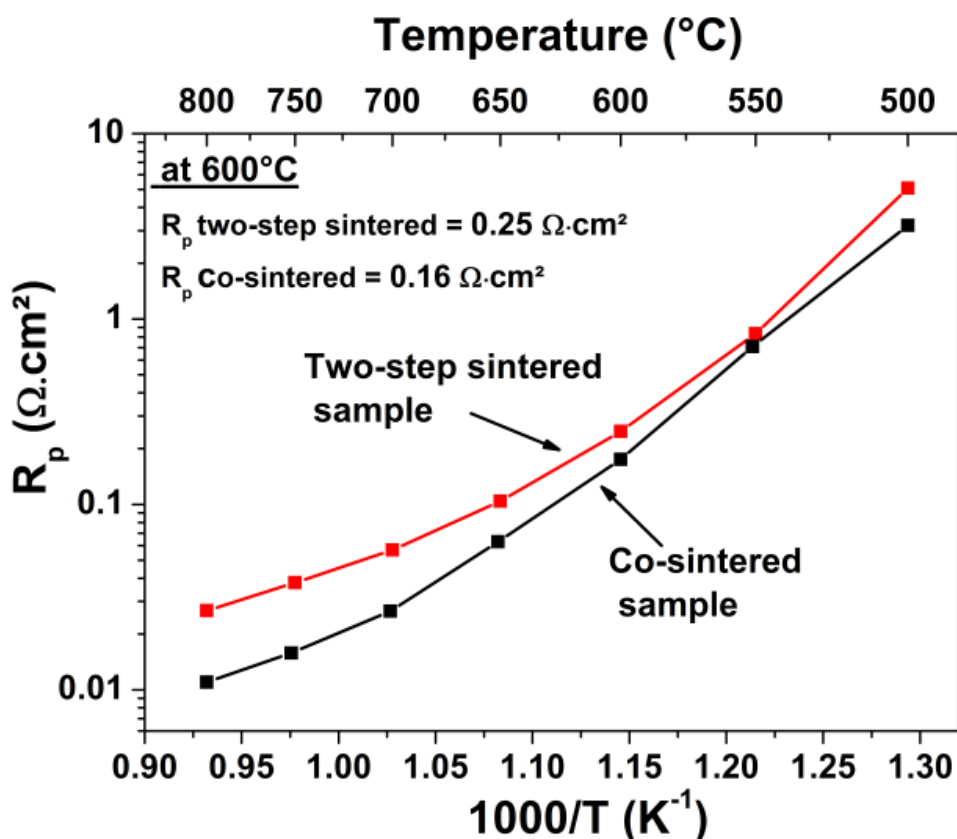


**Figure 13: Variation of  $R_p$  as a function of temperature for both two-step and co-sintered half cells.**

The process  $P_2$  is assigned to the oxygen electrode reaction (OER) at the  $Pr_4Ni_3O_{10+\delta}$  electrode (R//C shape), it is due to the relaxation of oxygen exchange reaction at the interface gas//electrode similar as  $Pr_2NiO_{4+\delta}$  [23]. The process  $P_3$  is due to gas diffusion impedance as already reported [26, 27], and usually fitted using one Warburg element  $W_s$ . The fit of the impedance data was carried out in order to extract only the  $R_p$  values. The total  $R_p$ , calculated for all temperatures (500–800 °C range) for the two-step sintered and co-sintered half cells under air, are plotted in **Figure 13**.

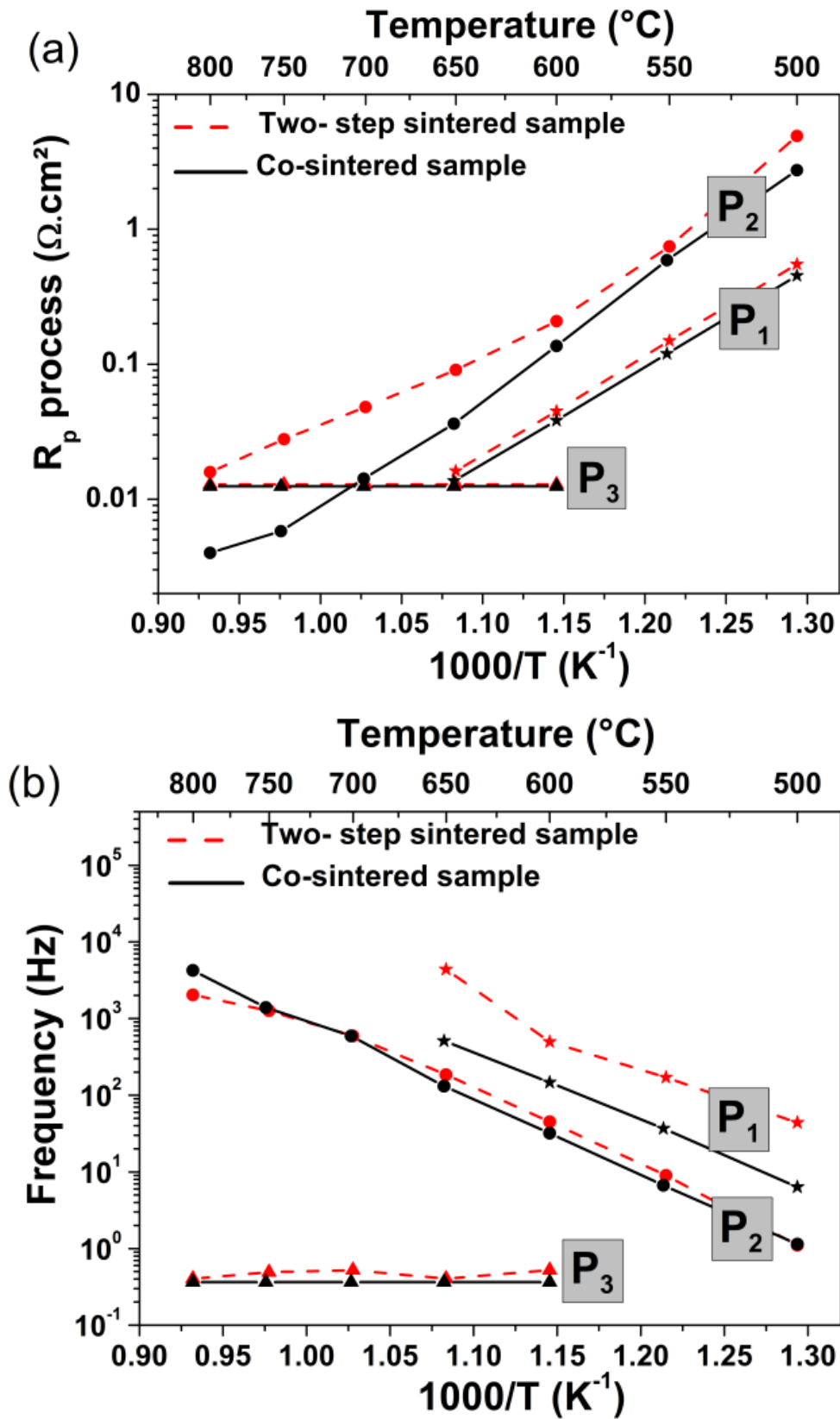


Figure 14: Variation of (a)  $R_p$  and (b) frequency of relaxation, of different processes with temperature, recorded under air for  $\text{Pr}_4\text{Ni}_3\text{O}_{10+\delta}$  electrode for both two-step and co-sintered half cells.

The  $R_p$  values obtained by co-sintering are slightly lower than those corresponding to the two-step sintering way, for ex. at 600 °C, the  $R_p$  for co-sintered and two-step sintered half cells are 0.16 and 0.25  $\Omega\cdot\text{cm}^2$ , respectively. However, these  $R_p$  values remain close to that of  $\text{Pr}_2\text{NiO}_{4+\delta}$  ( $R_p = 0.15 \Omega\cdot\text{cm}^2$  at 600 °C), which is currently the lowest value exhibited by nickelates [28]. In order to identify the origin of the difference in  $R_p$  values, the thermal variations of  $R_p$  related to the three processes namely  $P_1$ ,  $P_2$  and  $P_3$ , are plotted in **Figure 14a**.

Interestingly, the  $R_p$  values of the  $P_1$  and  $P_3$  processes for co-sintered and two-step sintered half cells are almost the same, however the differences are only observed for  $P_2$  process, depending on the sintering way. For the co-sintered half-cell, the  $R_p$  values are lower than that for the two-step sintered half cells. So it can be concluded that in both ways of sintering, the main difference is coming from the OER due to  $\text{Pr}_4\text{Ni}_3\text{O}_{10+\delta}$  electrode (process  $P_2$ ). The slightly higher value of  $R_p$  for  $P_2$  of two-step sintered half cells can either be related to the presence of additional phases ( $\text{PrO}_x$  and  $\text{NiO}$  (**Figure 11**)) or to the electrode microstructure. In general, at high sintering temperature, the particles coarsening should result in the decrease in active surface area that could affect the OER.

The frequency of relaxation of different processes involved in both fabrication processes are compared in **Figure 14b**. Only the  $P_1$  process shows some differences, which is likely related to the morphology of the interface (*cf.* **Figure 15**). Indeed, for the two-step sintered half cell, the GDC layer (sintered separately at 1375 °C for 1h) is much denser than the one of the co-sintered half cell (**Figure 15**), which leads to a higher relaxation frequency. It is worth noting that the frequencies of processes  $P_2$  (OER on  $\text{Pr}_4\text{Ni}_3\text{O}_{10+\delta}$  electrode) and  $P_3$ , (gas diffusion process), are logically almost identical for both processes.

#### 3.4.6. Morphology of half cells after EIS measurements

SEM observations of the  $\text{Pr}_4\text{Ni}_3\text{O}_{10+\delta}$  electrode were carried out after EIS measurements (**Figure 15**). The thicknesses of the electrodes are estimated to be  $\sim 10 \mu\text{m}$ . It can be noticed that all the layers show well adhesion with each other. From the SEM micrographs it seems that the GDC layers are different in both two-step and co-sintered half cells. The thickness of GDC is  $\sim 2 \mu\text{m}$  and  $3 \mu\text{m}$  respectively for two-step sintered and co-sintered half cells. A careful observation of the microstructure also suggests the morphology of the electrode is denser in case of two-step sintering. This can be linked to particles coarsening at high sintering temperature.

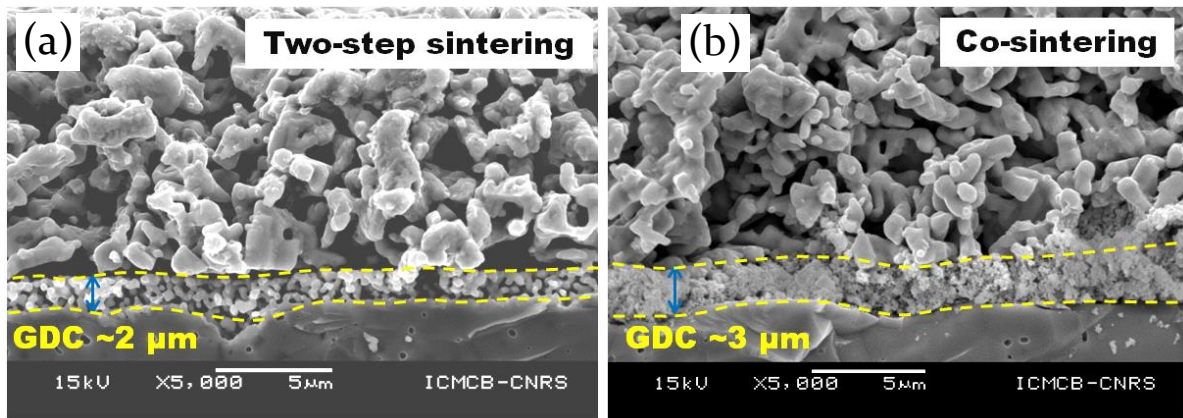


**Figure 15: SEM morphology of half cells after EIS measurements (a) two-step sintering and (b) co-sintering.**

### 3.4.7. Single cell measurements

The cathode sintering was performed using the previous optimized conditions determined for half cells, which is co-sintering together with the GDC layer at 950 °C for 2 h under air. The single cell was mounted into the measurement setup, with flows of air and N<sub>2</sub> on the cathode and anode sides, respectively. The cell was heated at 800 °C and N<sub>2</sub> at the anode side was progressively replaced by dry hydrogen (H<sub>2</sub>) to reduce NiO into metallic Ni. The open circuit voltage (OCV) was around 1.1 V as expected. The *i*-*V* characteristic was measured from OCV down to 0.4 V, and the impedance diagrams were recorded at OCV, 0.9, 0.8, and 0.7 V (not reported). Then the temperature was decreased down to 700 °C to measure again the *i*-*V* characteristic and impedance diagrams.

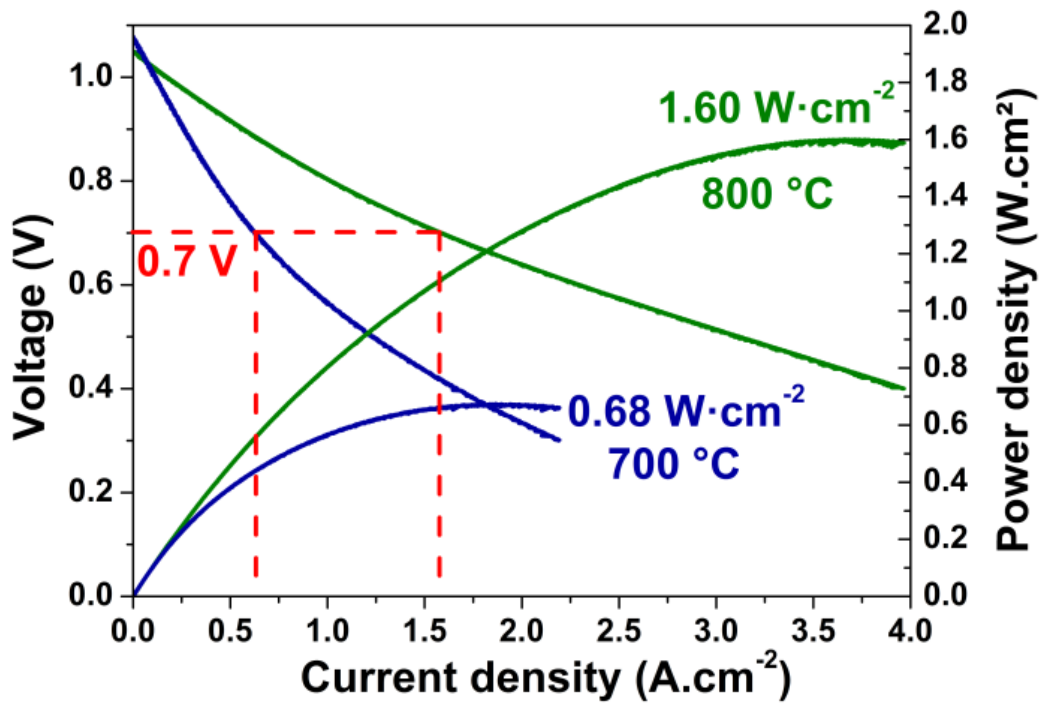


Figure 16: *i*-*V* curves and resulting power densities of a single cell made of a commercial half-cell and  $\text{Pr}_4\text{Ni}_3\text{O}_{10+\delta}$  as cathode.

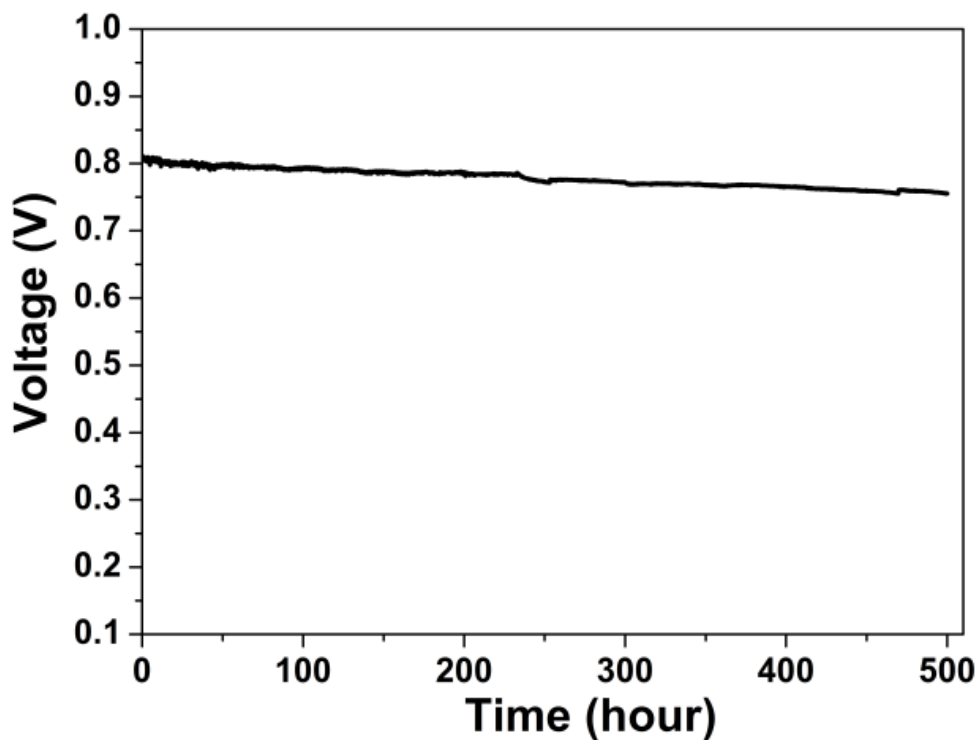


Figure 17: Ageing of the single cell at 700 °C, with a current density of  $0.3 \text{ A}\cdot\text{cm}^{-2}$ , for 500 h.

**Figure 16** shows the cell voltage as a function of the current density, as well as the resulting power density at 800 °C and 700 °C. The cell performance is high, reaching maximum power densities of 1.6 W·cm<sup>-2</sup> at 800 °C and 0.68 W·cm<sup>-2</sup> at 700 °C. For a potential of 0.7 V, the current density is 1.6 A·cm<sup>-2</sup> at 800 °C and reaches 0.64 A·cm<sup>-2</sup> at 700 °C.

Following the measurements at 800 and 700 °C, the cell was aged at 700 °C for 500 h at a current density of 0.3 A·cm<sup>-2</sup>. **Figure 17** shows the cell voltage as a function of time; the potential started at around 0.80 V, then a slight decrease is observed and after 500 h the potential is around 0.76 V.

## 4. Conclusion

This work reports the structural, stability and electrochemical studies of Pr<sub>4</sub>Ni<sub>3</sub>O<sub>10+δ</sub> as a new promising cathode material for SOFCs. Pr<sub>4</sub>Ni<sub>3</sub>O<sub>10+δ</sub> was successfully synthesized via glycine-nitrate route under normal oxygen flow (*p*O<sub>2</sub> ~ 1 atm). It crystallizes in orthorhombic structure with *Fmmm* space group. The XRD vs. temperature experiment under air shows a stable phase throughout the temperature range up to 1000 °C.

An over-stoichiometry, delta value δ = 0.10 is obtained under air. The measurement of oxygen content vs. T shows that the material is always over-stoichiometric whatever the *p*O<sub>2</sub> is, which should indicate that this material is MIEC-type under oxygen and air up to 1000 °C. Pr<sub>4</sub>Ni<sub>3</sub>O<sub>10+δ</sub> phase is stable maximum for 2 h under air and fully stable under oxygen at 1000 °C. Further increase of temperature leads to decomposition into Pr<sub>2</sub>NiO<sub>4+δ</sub> and NiO, under air and oxygen.

The half cell prepared by co-sintering process shows lower *R*<sub>p</sub> value (*R*<sub>p</sub> = 0.16 Ω·cm<sup>2</sup> at 600°C) than the one made by two-step sintering (*R*<sub>p</sub> = 0.25 Ω·cm<sup>2</sup> at the same temperature), which is almost same as Pr<sub>2</sub>NiO<sub>4+δ</sub>. A single cell with Pr<sub>4</sub>Ni<sub>3</sub>O<sub>10+δ</sub> electrode produced high power density of 1.60 W·cm<sup>-2</sup> at 800 °C and 0.68 W·cm<sup>-2</sup> at 700 °C.

Endly, the Pr<sub>4</sub>Ni<sub>3</sub>O<sub>10+δ</sub> phase is highly stable during long term up to 1 month under air at different SOFC operating temperatures: 600, 700 and 800 °C, contrarily to Pr<sub>2</sub>NiO<sub>4+δ</sub> which forms PrNiO<sub>3-δ</sub>, Pr<sub>4</sub>Ni<sub>3</sub>O<sub>10+δ</sub> and Pr<sub>6</sub>O<sub>11</sub> in the same conditions [17]. It can be then concluded that the electrochemical behavior of Pr<sub>4</sub>Ni<sub>3</sub>O<sub>10+δ</sub> is similar to that of Pr<sub>2</sub>NiO<sub>4+δ</sub>, but with a quite higher stability, which gives great interest to consider this material as a very promising oxygen electrode.

## Acknowledgements

The authors wish to gratefully acknowledge the Agence Nationale de la Recherche (A.N.R., France) for financial support. The authors also acknowledge Eric Lebraud for XRD and Dominique Denux for thermal measurements.

## References

- [1] A. Aguadero, L. Fawcett, S. Taub, R. Woolley, K.-T. Wu, N. Xu, J. A. Kilner, S. J. Skinner, *Journal of Materials Science*, 47 (2012) 3925-3948.
- [2] S. Peng, Y. Wei, J. Xue, Y. Chen, H. Wang, *International Journal of Hydrogen Energy*, 38, (2013) 10552-10558.
- [3] H. Zhao, Q. Li, L. Sun, *Science China Chemistry*, 54 (2011) 898-910.
- [4] A. J. Jacobson, *Chemistry of Materials*, 22 (2010) 660-674.
- [5] C. Sun, R. Hui, J. Roller, *Journal of Solid State Electrochemistry*, 14 (2010) 1125-1144.
- [6] A. Tarançon, M. Burriel, J. Santiso, S. J. Skinner, J. A. Kilner, *Journal of Materials Chemistry*, 20 (2010) 3799-3813.
- [7] D. J. L. Brett, A. Atkinson, N. P. Brandon, S. J. Skinner, *Chemical Society Reviews*, 37 (2008) 1568-1578.
- [8] G. Amow, S. J. Skinner, *Journal of Solid State Electrochemistry*, 10 (2006) 538-546.
- [9] S. Choi, S. Yoo, J.-Y. Shin, G. Kim, *Journal of the Electrochemical Society*, 158 (2011) B995-B999.
- [10] Z. Zhang, M. Greenblatt, *Journal of Solid State Chemistry*, 117 (1995) 236-246.
- [11] M. Greenblatt, *Current Opinion in Solid State and Materials Science*, 2 (1997) 174-183.
- [12] J.-M. Bassat, C. Allançon, P. Odier, J. P. Loup, M. Deus Carvalho, A. Wattiaux, *European Journal of Solid State and Inorganic Chemistry*, 35 (1998) 173-188.
- [13] A. Aguadero, J. A. Alonso, M. J. Martinez-Lope, M. T. Fernandez-Diaz, M. J. Escudero, L. Daza, *Journal of Materials Chemistry*, 16 (2006) 3402-3408.
- [14] E. Boehm, J.-M. Bassat, P. Dordor, F. Mauvy, J.-C. Grenier, P. Stevens, *Solid State Ionics*, 176 (2005) 2717-2725.
- [15] C. N. Munnings, S. J. Skinner, G. Amow, P. S. Whitfield, I. J. Davidson, *Solid State Ionics*, 176 (2005) 1895-1901.
- [16] C. Ferchaud, J.-C. Grenier, Y. Zhang-Steenwinkel, M. M. A. van Tuel, F. P. F. van Berkel, J.-M. Bassat, *Journal of Power Sources*, 196 (2011) 1872-1879.
- [17] V. Vibhu, J.-M. Bassat, A. Flura, C. Nicollet, J.-C. Grenier, A. Rougier, *ECS Transaction*, 68 (2015) 825-835.
- [18] L. A. Chick, L. R. Pederson, G. D. Maupin, J. L. Bates, L. E. Thomas, G. J. Exarhos, *Materials Letters*, 10 (1990) 6-12.
- [19] M. C. Tucker, L. Cheng, L. C. Dejonghe, *Journal of Power Sources*, 196 (2011) 8313-8322.
- [20] A. Flura, S. Dru, C. Nicollet, V. Vibhu, S. Fourcade, E. Lebraud, A. Rougier, J.-M. Bassat, J.-C. Grenier, *Journal of Solid State Chemistry*, 228 (2015) 189-198.
- [21] P. Lacorre, *Journal of Solid State Chemistry*, 97 (1992) 495-500.

- [22] V. Vibhu, J.-M. Bassat, A. Flura, C. Nicollet, N. Penin, J.-C. Grenier, A. Rougier, *Submitted in Journal of Material Chemistry A*, 2015.
- [23] A. Flura, C. Nicollet, S. Fourcade, V. Vibhu, A. Rougier, J.-M. Bassat, J.-C. Grenier, *Electrochimica Acta*, 174 (2015) 1030-1040.
- [24] P. Shuk, M. Greenblatt, *Solid State Ionics*, 116 (1999) 217-223.
- [25] R. Chockalingam, A. K. Ganguli, S. Basu, *Journal of Power Sources*, 250 (2014) 80-89.
- [26] S. Primdahl, M. Mogensen, *Journal of the Electrochemical Society*, 146 (1999) 2827-2833.
- [27] T. Jacobsen, P. V. Hendriksen, S. Koch, *Electrochimica Acta*, 53 (2008) 7500-7508.
- [28] V. Vibhu, A. Rougier, C. Nicollet, A. Flura, J.-C. Grenier, J.-M. Bassat, *Solid State Ionics*, 278 (2015) 32-37.

## Additional Information: Chapter 6

### 1. TGA experiments under argon atmosphere

TGA experiments were carried out under argon on  $\text{Pr}_4\text{Ni}_3\text{O}_{10+\delta}$  with the aim to investigate its chemical stability. **Figure 1** shows the corresponding variation of the weight change with temperature. Under argon,  $\text{Pr}_4\text{Ni}_3\text{O}_{10+\delta}$  exhibits thermal stability only up to  $\sim 900$  °C. Above this temperature it starts decomposing and around  $T = 1000$  °C, it is completely decomposed into  $\text{Pr}_2\text{NiO}_{4+\delta}$  and NiO (**Figure 1**). This decomposition was checked by XRD both on the powder at the end of this TGA cycle or after quenching another set of powder from  $1000$  °C to RT in a separate furnace. This decomposition is completely irreversible,  $\text{Pr}_2\text{NiO}_{4+\delta}$  phase being stable under argon as confirmed by a second TGA cycle.

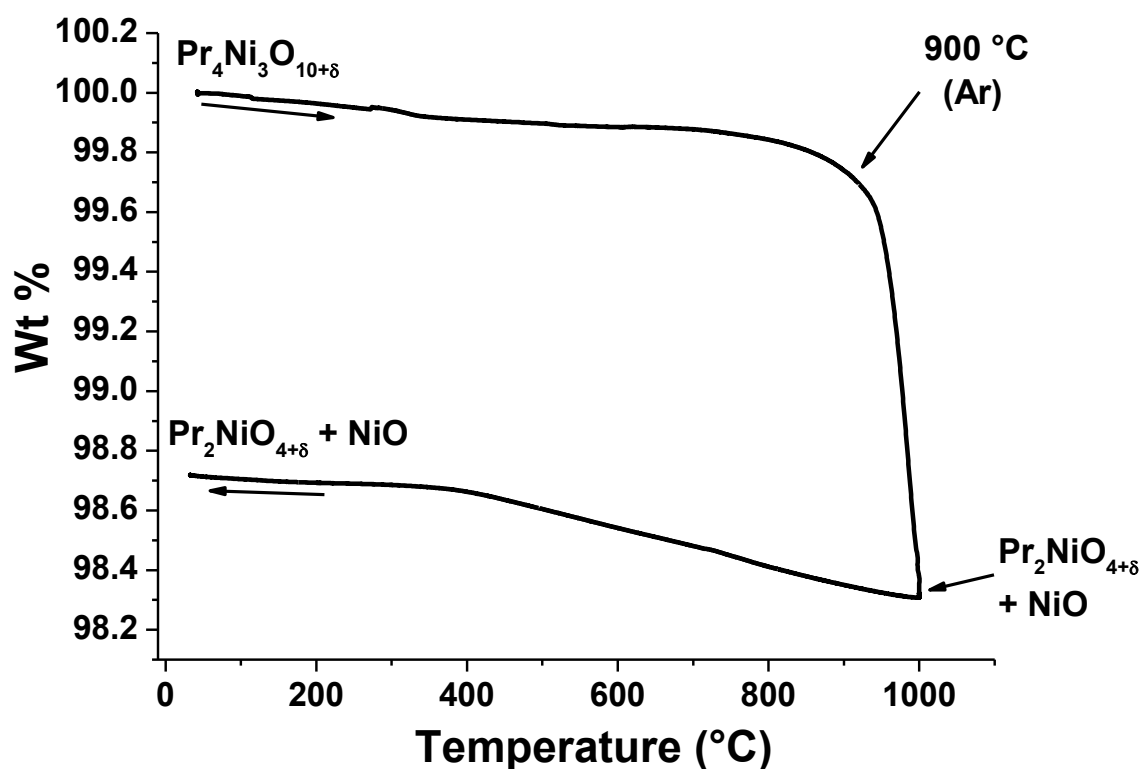


**Figure 1:** Thermal variation of weight for  $\text{Pr}_4\text{Ni}_3\text{O}_{10+\delta}$  recorded under argon atmosphere.

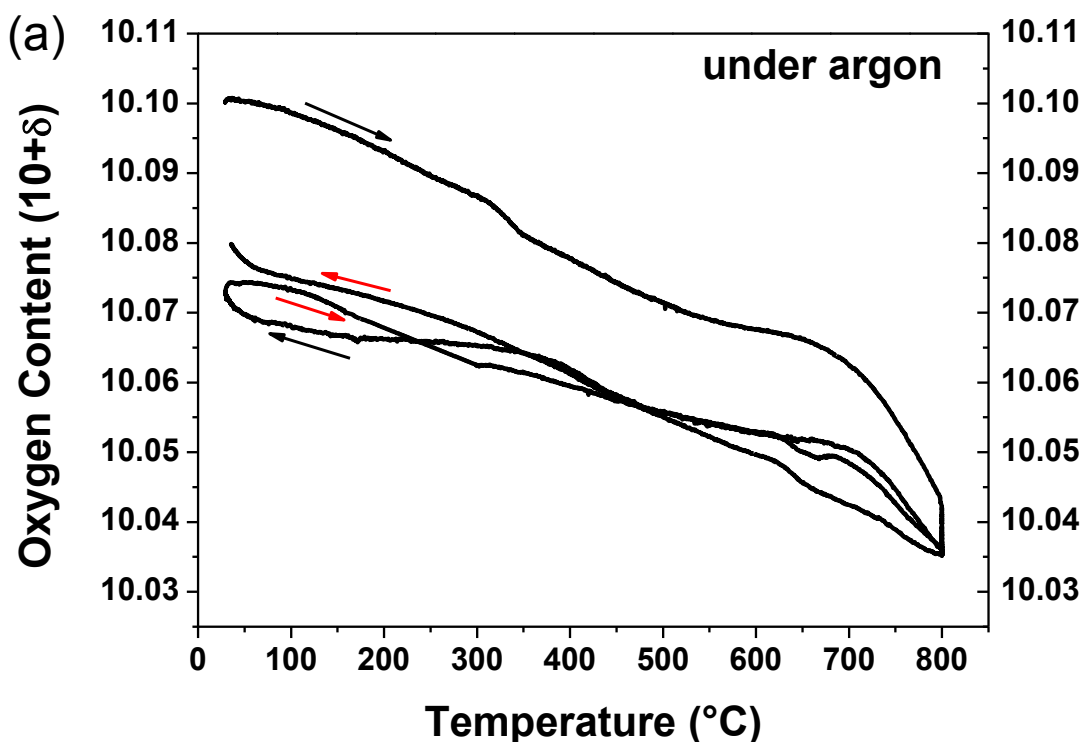


**Figure 2: Thermal variation of the oxygen content ( $10+\delta$ ) for  $\text{Pr}_4\text{Ni}_3\text{O}_{10+\delta}$  under argon ( $30\text{ }^\circ\text{C} \leq T \leq 800\text{ }^\circ\text{C}$ ).**

The thermal variation of the oxygen content was also investigated over the stability domain of  $\text{Pr}_4\text{Ni}_3\text{O}_{10+\delta}$  under argon, *i.e.* from room temperature to  $800\text{ }^\circ\text{C}$ . Before starting the experiment, the powder was first equilibrated under air, ensuring the starting value of  $\delta \sim 0.10$ . The thermal variation of the oxygen content,  $10+\delta$ , is plotted in **Figure 2**. During the first cycle, a weight loss upon heating is observed while in the second cycle an almost reversible behavior is noticed.

## 2. Preparation of dense pellets of $\text{Pr}_4\text{Ni}_3\text{O}_{10+\delta}$

It is very difficult to prepare dense pellet of  $\text{Pr}_4\text{Ni}_3\text{O}_{10+\delta}$  due to its restricted thermal stability range ( $<1000\text{ }^\circ\text{C}$  under air and oxygen). Nevertheless, we tried in somewhat different way following the results of the earlier TGA experiments. Above  $T > 1120\text{ }^\circ\text{C}$   $\text{Pr}_4\text{Ni}_3\text{O}_{10+\delta}$  is decomposed into  $\text{Pr}_2\text{NiO}_{4+\delta}$  and NiO. But if the resulting mixed phases is cooled slowly, the  $\text{Pr}_4\text{Ni}_3\text{O}_{10+\delta}$  phase is recovered, only containing small amounts of impurities ( $\text{PrO}_x$  and NiO). Pellets of  $\text{Pr}_4\text{Ni}_3\text{O}_{10+\delta}$  were prepared using this strategy. The schematic of heating and cooling is summarized in **Figure 3**. After cooling the relative density was found to be higher than 96 %.

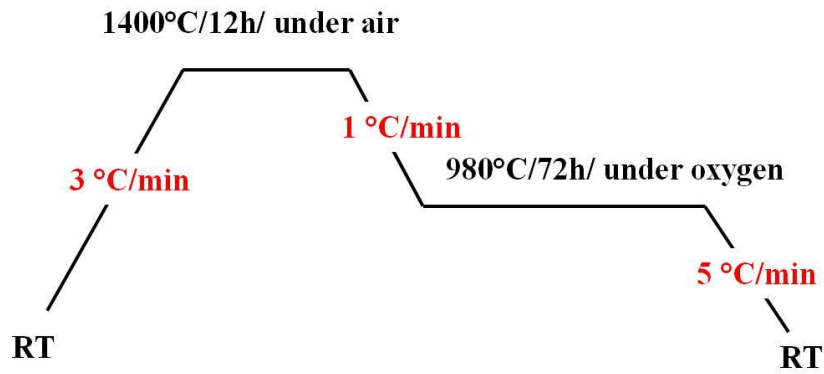


Figure 3: Schematic of heating and cooling rates to prepare dense pellets of  $\text{Pr}_4\text{Ni}_3\text{O}_{10+\delta}$ .

### 3. XRD analysis after the preparation of the dense pellets

The X-ray diffractogram of dense pellet is shown in **Figure 4**. The major phase is  $\text{Pr}_4\text{Ni}_3\text{O}_{10+\delta}$ , few peaks of  $\text{PrO}_x$  and  $\text{NiO}$  are also observed.

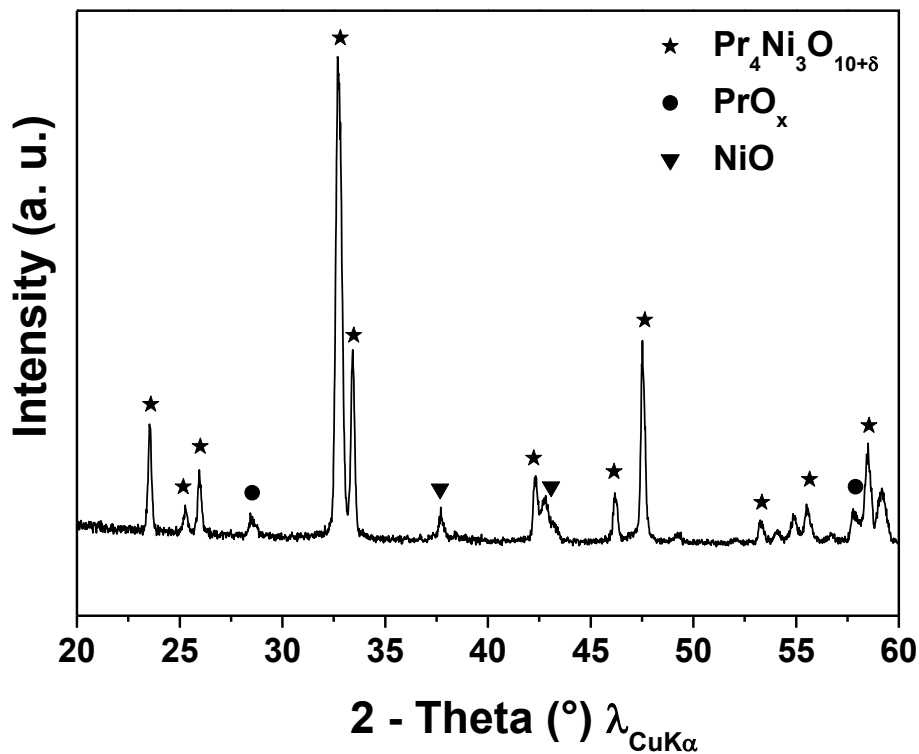
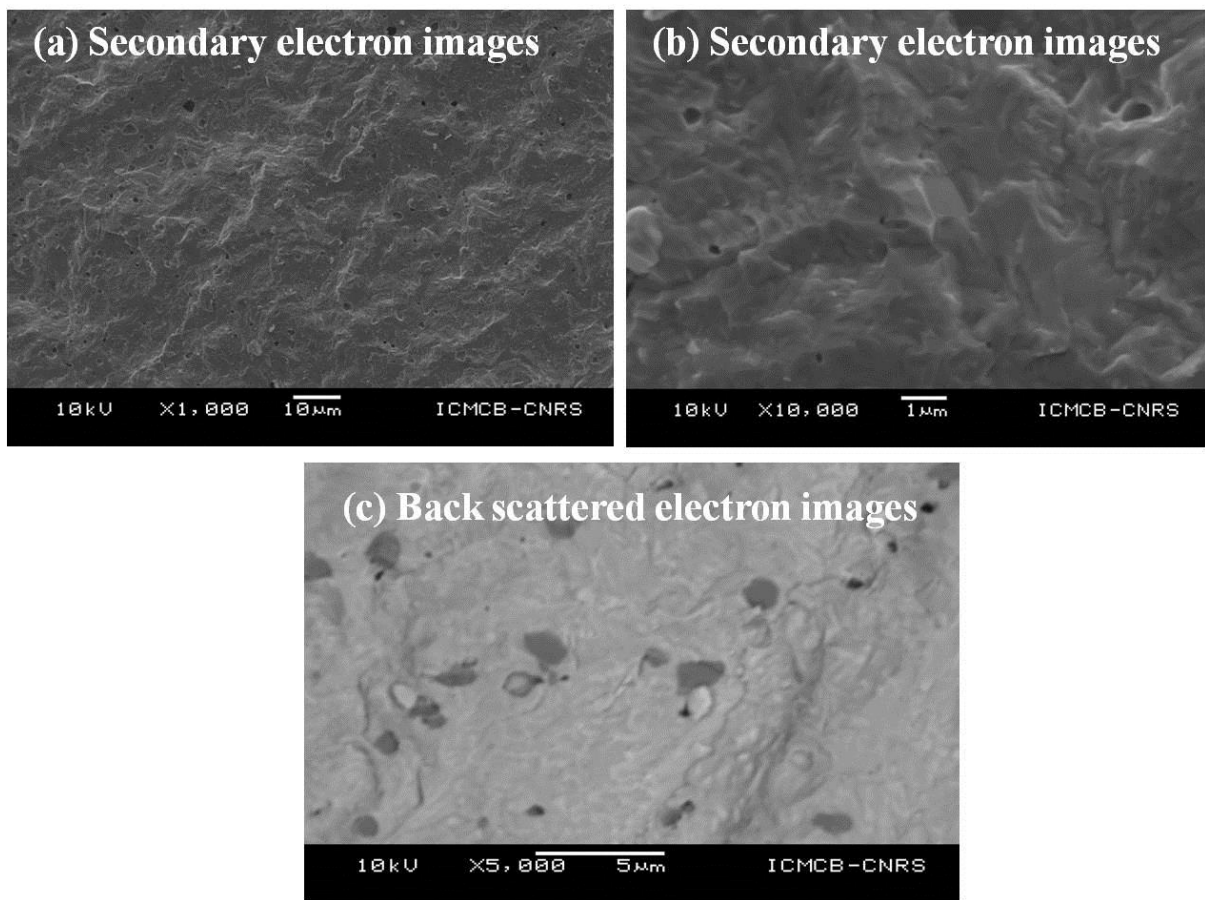


Figure 4: X-ray diffractogram recorded on the dense pellets of  $\text{Pr}_4\text{Ni}_3\text{O}_{10+\delta}$ .

#### 4. SEM-EDS Analysis on dense pellets

SEM images of the cross section of dense pellets are shown in **Figure 5**, which confirm quite high density of pellets without any porosity. **Figure 5a** and **b** corresponds to secondary electron images with different magnification while **Figure 5c** is a back scattered electron image. Some grey spots are visible on **Figure 5c**. EDS analysis was performed on the grey spots, confirming the presence of NiO (**Figure 6**).



**Figure 5: SEM images of the cross section of dense pellets of  $\text{Pr}_4\text{Ni}_3\text{O}_{10+\delta}$ .**

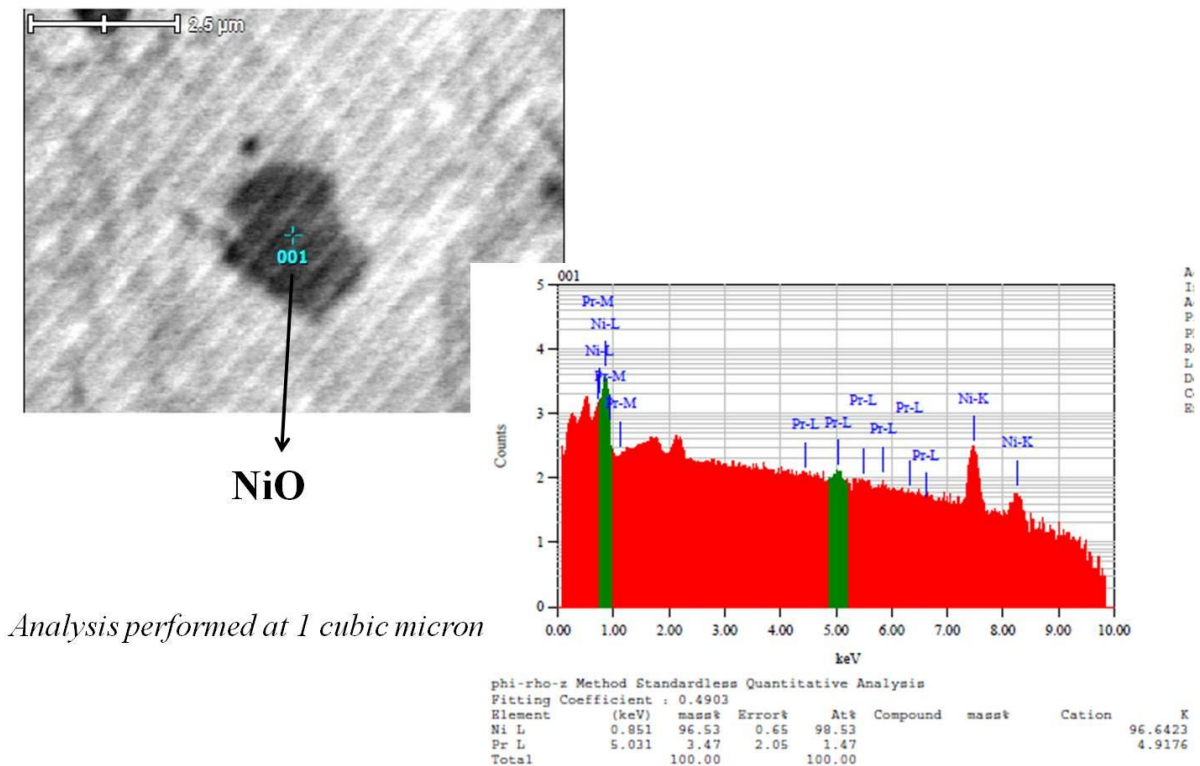


**Figure 6: SEM-EDS analysis on a grey spot present on a  $\text{Pr}_4\text{Ni}_3\text{O}_{10+\delta}$  dense pellet.**

### 5. Isotopic Exchange Depth Profiling – SIMS Experiments

The oxygen diffusion coefficient  $D^*$  and surface exchange coefficient  $k^*$  were determined by the so-called isotopic exchange depth profile (IEDP) technique combining isotopic exchange of  $^{18}\text{O}$  (used as an oxygen tracer) for  $^{16}\text{O}$  then secondary ion mass spectrometry (SIMS) analyses. The dense pellets were first abraded with silicon carbide papers of successive grades, and then polished with diamond paste down to a roughness close to  $0.3\ \mu\text{m}$ . The samples were annealed at a pressure of 210 mbar in an  $^{18}\text{O}$  enriched atmosphere (97%, Eurisotop) at 600 and 700 °C. Later on the experiment was also performed at higher oxygen partial pressure *i.e.* at 1000 mbar at 600 °C. The  $^{18}\text{O}$  penetration profiles, *i.e.* normalized  $^{18}\text{O}$  isotopic fraction ( $^{18}\text{O} / (^{16}\text{O} + ^{18}\text{O})$ ), were recorded as a function of the analyzed depth using a Cameca<sup>®</sup> IMS 6F SIMS apparatus with a  $\text{Cs}^+$  ions source. The profiles were then fitted using an appropriate solution to the diffusion equation given by Crank, for a solution of the second Fick's law of gas diffusion in solids. The fits of depth profiling at 700 and 600 °C are reported in **Figure 7**.

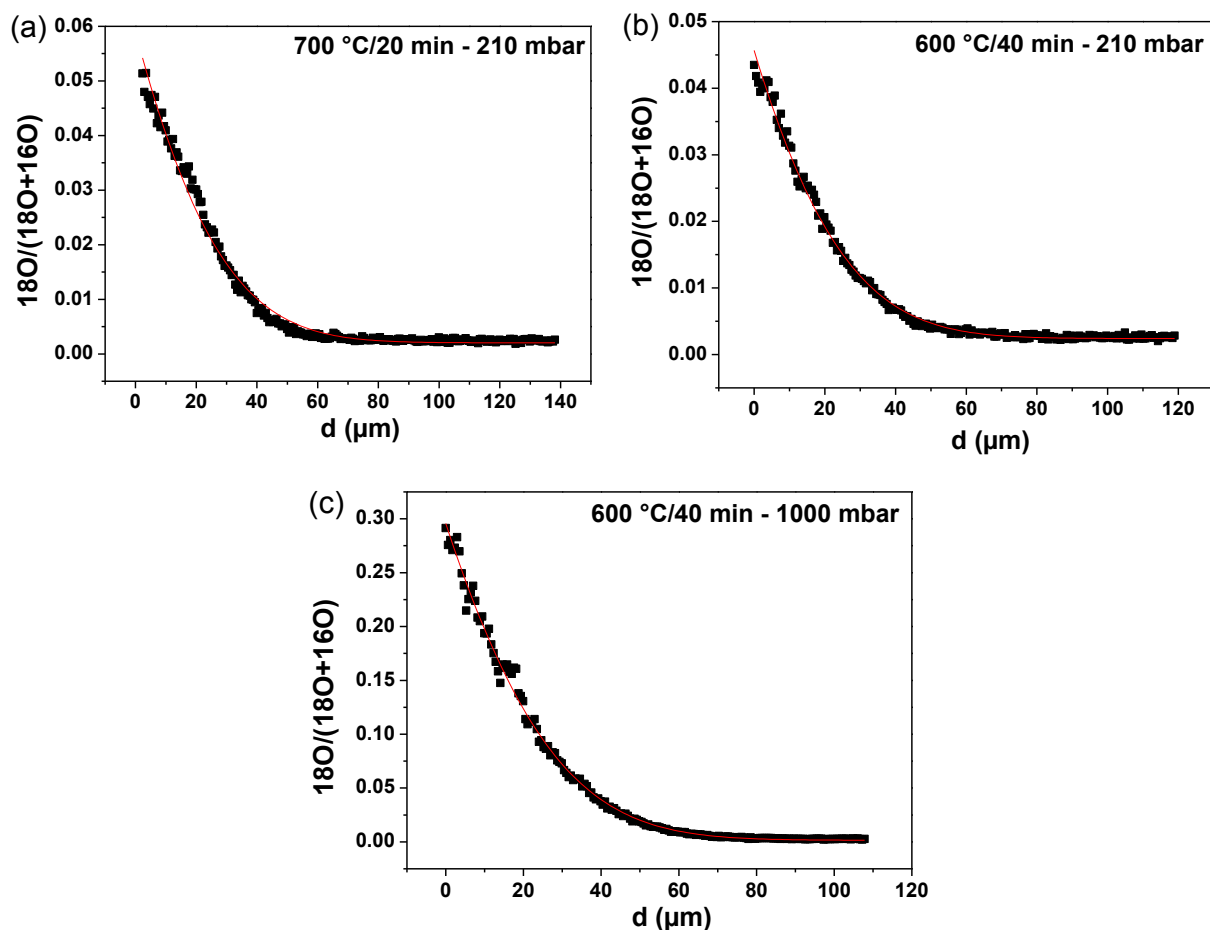


**Figure 7: Oxygen diffusion depth profiling for  $\text{Pr}_4\text{Ni}_3\text{O}_{10+\delta}$ .**

**Table:  $D^*$  and  $k^*$  values deduced from above depth profiles**

Condition	$D^*$ ( $\text{cm}^2.\text{s}^{-1}$ )	$k^*$ ( $\text{cm}.\text{s}^{-1}$ )
700 °C/20 min – 210 mbar	$4 \times 10^{-9}$	$1 \times 10^{-7}$
600 °C/40 min – 210 mbar	$2 \times 10^{-9}$	$4 \times 10^{-8}$
600 °C/40 min – 1000 mbar	$2 \times 10^{-9}$	$3.4 \times 10^{-7}$

The diffusion coefficient ( $D^*$ ) obtained from above depth profiling is around one order magnitude lower for  $\text{Pr}_4\text{Ni}_3\text{O}_{10+\delta}$  ( $D^*$  at 600 °C =  $2 \times 10^{-9} \text{ cm}^2.\text{s}^{-1}$ ) compared to  $\text{Pr}_2\text{NiO}_{4+\delta}$  ( $D^*$  at 600 °C =  $2.5 \times 10^{-8} \text{ cm}^2.\text{s}^{-1}$ ). Interestingly the  $D^*$  is the same at 210 and 1000 mbar pressure of  $^{18}\text{O}$  despite the slightly higher value of oxygen over-stoichiometry when the material is equilibrated under oxygen (**Chapter 6, Figure 6**)

The surface exchange coefficient ( $k^*$ ) at 600 °C is  $4 \times 10^{-8}$  cm.s<sup>-1</sup> which is also approximately one order magnitude less than Pr<sub>2</sub>NiO<sub>4+δ</sub> ( $k^*$  at 600 °C  $5 \times 10^{-7}$  cm.s<sup>-1</sup>). Under higher oxygen partial pressure, the  $k^*$  value increases.

The lower values of  $D^*$  and  $k^*$  in Pr<sub>4</sub>Ni<sub>3</sub>O<sub>10+δ</sub> compared to Pr<sub>2</sub>NiO<sub>4+δ</sub> can be understood in terms of presence of impurities in the material.

# Conclusion

---

## Conclusion

The initial objective of this PhD thesis was mostly twofold: 1) to focus on alternative oxygen electrodes for IT-SOFCs prepared in MSC-type conditions *i.e.* at sufficiently high temperature, which is a mandatory requirement with respect to the sintering of the electrode on an electrolyte substrate, but under low  $pO_2$  ( $10^{-4}$ - $10^{-5}$  atm) and 2) to investigate their long term chemical stability and electrochemical performance in the operating conditions of the SOFCs. To achieve our goals, the lanthanide based nickelates, which have been well known in our group at ICMCB-CNRS Bordeaux for several years, appear as good candidates due to their MIEC properties. In this context, the preparation of new compositions was considered at the starting point of our study. The understanding of the possible degradation mechanisms of these materials at the operating condition of SOFCs was also addressed.

The properties of the scarcely explored  $La_{2-x}Pr_xNiO_{4+\delta}$  (LPNO) series were investigated with the aim to find the best compromise between chemical stability and electrochemical performance. Indeed  $Pr_2NiO_{4+\delta}$  (PNO) shows excellent electrochemical properties at intermediate temperature while  $La_2NiO_{4+\delta}$  (LNO) exhibits higher chemical stability. Belonging to the  $K_2NiF_4$  -type structure, the **LPNO nickelates were successfully synthesized** by the citrate nitrate route. Their initial structural characterization by XRD shows two main domains of solid solutions depending on the La/Pr ratio with orthorhombic structure. One is related to La-rich phases, from ( $0.0 \leq x \leq 0.5$ ), with the *Fmmm* space group while the other one, Pr-rich phases, from ( $1.0 \leq x \leq 2.0$ ), crystallize with *Bmab* space group. The ( $0.5 < x < 1.0$ ) range corresponds to a biphasic domain. In addition, a careful investigation of PNO using laboratory XRD reveals the splitting of some reflections indicating some distortion in the structure.

For a deeper understanding of the structural properties of the LPNO series, synchrotron and neutron diffraction measurements were performed on several compositions. Joint refinements converged and confirmed the existence of three domains depending on  $x$  value (*i.e.* Pr content). One is related to La-rich phases with *Fmmm* orthorhombic structure ( $0.0 \leq x < 0.5$ ), the second one being related to **Pr-rich phase ( $1.1 < x \leq 2.0$ ) with *C2/m* monoclinic structure at room temperature**. Till now, this result has never been reported in the literature. In between  $0.5 \leq x \leq 1.1$ , a third region corresponding to a biphasic domain was confirmed. For Pr-rich compositions, both the monoclinic unit cell distortion and additional weak unindexed reflections were found to be dependent on both interstitial oxygen content ( $\delta$ -value) and even more strongly on A-site cation substitution.

The LPNO phases are oxygen over-stoichiometric in the whole temperature range either under air or argon. The  $\delta$  value increases with increasing  $x$ . The physico-chemical properties including TECs, electrical conductivity, oxygen diffusion and surface exchange coefficients indicate the **suitability of LPNO for MS-SOFCs application**. Regarding the electrochemical performance, the polarization resistance ( $R_p$ ) progressively decreases from LNO ( $0.28 \text{ } \Omega \cdot \text{cm}^2$  at  $700 \text{ } ^\circ\text{C}$ ) to PNO ( $0.03 \text{ } \Omega \cdot \text{cm}^2$  at  $700 \text{ } ^\circ\text{C}$ ) by increasing Pr content. Besides, the decrease in  $R_p$  as a function of  $x$  confirms that the Pr-rich compounds are more efficient for the oxygen electrode reaction than the La-rich ones.

The thermal ageing of the powders was carried out under air during one week and one month at  $600 \text{ } ^\circ\text{C}$ ,  $700 \text{ } ^\circ\text{C}$  and  $800 \text{ } ^\circ\text{C}$ . La-rich nickelates, *i.e.* LNO and  $\text{La}_{1.5}\text{Pr}_{0.5}\text{NiO}_{4+\delta}$  are chemically stable, contrarily to the Pr-rich nickelates *i.e.*  $\text{La}_{0.5}\text{Pr}_{1.5}\text{NiO}_{4+\delta}$ ,  $\text{LaPrNiO}_{4+\delta}$  and PNO. The extent of the decomposition of LPNO decreases with La content leading to a complete decomposition of PNO into  $\text{PrNiO}_{3-\delta}$ ,  $\text{Pr}_4\text{Ni}_3\text{O}_{10+\delta}$  and  $\text{Pr}_6\text{O}_{11}$ .

The long-term electrochemical measurements were performed at  $i_{dc}=0$  conditions on LPNO//GDC//YSZ half cells under air. Despite various degrees of chemical stability, and even for a complete decomposition of the end member PNO, the  $R_p$  values for all LPNO phases do not show significant change after ageing. A different behaviour is observed under current ( $i_{dc} = \pm 300 \text{ mA} \cdot \text{cm}^{-2}$ ) with a fast degradation (*i.e.* large increase in  $R_p$ ) in SOFC (cathodic) mode. For PNO and LNO, a large increase in  $R_p$  is observed after 1000 h of ageing up to 1800 h, while for  $\text{La}_{1.5}\text{Pr}_{0.5}\text{NiO}_{4+\delta}$ , the increase of  $R_p$  is very small. Contrarily, in SOEC (anodic) mode for all LPNO electrodes the  $R_p$  values remain almost constant up to 1800 h, whatever the composition. The electrochemical performance of  $\text{La}_{1.5}\text{Pr}_{0.5}\text{NiO}_{4+\delta}$  under current is far better than the one of PNO and LNO in SOFC mode. So finally  **$\text{La}_{1.5}\text{Pr}_{0.5}\text{NiO}_{4+\delta}$  appears to be the best compromise as cathode** in terms of combining chemical stability and electrochemical performance among all LPNO nickelates. Furthermore, the chemical stability of the material may be not an issue for the degradation, the major problem arising from the interface between the electrode and GDC. In case of LNO, an additional interphase appears between both layers, after 1800 h ageing at  $700 \text{ } ^\circ\text{C}$  under current, which leads to fast degradation even though the material itself was stable. It is concluded that the **new forming interphase in between GDC and electrode, plays a key role in the electrode performance**, despite the high chemical stability of the electrode material. To achieve long term performance, the interphase should be conductive and not be oxide ion blocking in nature.

**PrNiO<sub>3-δ</sub>** and **Pr<sub>4</sub>Ni<sub>3</sub>O<sub>10+δ</sub>** phases (being the main decomposition products of PNO) were fully investigated as suitable cathode materials for SOFCs. Firstly, **PrNiO<sub>3-δ</sub>** was **successfully synthesized** via citrate-nitrate route under oxygen flow ( $pO_2 \sim 1$  atm). The XRD vs. temperature study showed a phase transition from room temperature (*Pbnm* space group) orthorhombic to rhombohedral structure at  $\sim 600$  °C. Whatever the atmosphere is, PrNiO<sub>3-δ</sub> always remains oxygen sub-stoichiometric. The delta value  $\delta \approx 0.05$  is obtained at room temperature in air and it varies depending on  $pO_2$  (studied in argon, air and oxygen). In all atmospheres and temperature, PrNiO<sub>3-δ</sub> decomposes into Pr<sub>2</sub>NiO<sub>4+δ</sub> and NiO as end products while intermediate Pr<sub>4</sub>Ni<sub>3</sub>O<sub>10+δ</sub> is formed under air and oxygen. Electrochemical characterizations as SOFC oxygen electrode show that the half cells prepared by a two-step sintering process (being the GDC layer sintered in a first step, and then the sintering of the electrode in a second step) exhibits lower  $R_p$  value ( $R_p = 0.46 \Omega \cdot \text{cm}^2$  at 600°C) than the co-sintered (at the same time than the GDC layer) half cell ( $R_p = 0.91 \Omega \cdot \text{cm}^2$  at 600°C). However, the  $R_p$  values remain always higher than the one of Pr<sub>2</sub>NiO<sub>4+δ</sub> ( $R_p = 0.15 \Omega \cdot \text{cm}^2$  at 600 °C), limiting the interest of the perovskite phase as SOFC cathode.

The properties of high order Ruddlesden-Popper **Pr<sub>4</sub>Ni<sub>3</sub>O<sub>10+δ</sub>** phase were also studied. The nickelate, successfully synthesized via glycine-nitrate route under normal oxygen flow ( $pO_2 \sim 1$  atm), crystallizes in orthorhombic structure with *Fmmm* space group. The XRD vs. temperature experiment under air evidences a stable phase throughout the temperature range up to 1000 °C. An over-stoichiometry delta value  $\delta = 0.10$  is obtained under air at room temperature. The measurement of oxygen content vs. T shows that the material remains always over-stoichiometric whatever the  $pO_2$  is, which should indicate that this material is MIEC-type under oxygen and air up to 1000 °C. Pr<sub>4</sub>Ni<sub>3</sub>O<sub>10+δ</sub> phase is stable for about 2 h under air and fully stable under oxygen at 1000 °C. Further increase of temperature leads to decomposition into Pr<sub>2</sub>NiO<sub>4+δ</sub> and NiO, under air and oxygen. The half cell prepared by co-sintering process (with GDC layer) shows lower  $R_p$  value ( $R_p = 0.16 \Omega \cdot \text{cm}^2$  at 600 °C) than the one made by two-step sintering ( $R_p = 0.25 \Omega \cdot \text{cm}^2$  at the same temperature). This value is almost same as Pr<sub>2</sub>NiO<sub>4+δ</sub>. At the end, the Pr<sub>4</sub>Ni<sub>3</sub>O<sub>10+δ</sub> phase is highly stable during long term up to 1 month under air at different SOFC operating temperatures: 600, 700 and 800 °C, on the contrary to Pr<sub>2</sub>NiO<sub>4+δ</sub> which decomposes in the same conditions. A single cell with Pr<sub>4</sub>Ni<sub>3</sub>O<sub>10+δ</sub> electrode produced high power density of  $1.60 \text{ W} \cdot \text{cm}^{-2}$  at 800 °C and  $0.68 \text{ W} \cdot \text{cm}^{-2}$  at 700 °C for duration up to 500 h showing that **Pr<sub>4</sub>Ni<sub>3</sub>O<sub>10+δ</sub> is very promising as cathode material**.

## Major achievements in my PhD work

- $\text{La}_{2-x}\text{Pr}_x\text{NiO}_{4+\delta}$  ( $0.0 \leq x \leq 2.0$ ), LPNO series were successfully synthesized.
- $\text{Pr}_2\text{NiO}_{4+\delta}$  and Pr-rich phases are reported for the first time as monoclinic structure at room temperature.
- LPNO phases are suitable for MSCs. The best compromise between stability, performance and ageing is  $\text{La}_{1.5}\text{Pr}_{0.5}\text{NiO}_{4+\delta}$ .
- Chemical stability of the cathode material itself is not the main parameter upon ageing in operation conditions. The interface/interphase in between the GDC barrier layer and the electrode is a key issue.
- Among  $\text{PrNiO}_{3-\delta}$ ,  $\text{Pr}_2\text{NiO}_{4+\delta}$  and  $\text{Pr}_4\text{Ni}_3\text{O}_{10+\delta}$ ,  $\text{Pr}_4\text{Ni}_3\text{O}_{10+\delta}$  (n = 3 term of Ruddlesden-Popper series) is the most stable (chemically as well as structurally) and appears as the most promising cathode material.

This work opens some future perspectives.

- In order to validate the main achievements during this work, single cell measurements involving the mixed  $\text{La}_{1.5}\text{Pr}_{0.5}\text{NiO}_{4+\delta}$  nickelate as cathode need to be performed.
- Aiming at the determination of the origin of the unindexed extra peaks that might be attributed to modulation or superstructure in PNO and Pr-rich phases, HR-TEM experiments should be further carried out.
- A critical point remains the nature of the interface located in between the electrode and electrolyte support, requiring the most appropriate “couples” and to favour the formation of conductive interphase. For instance, recent result in our group demonstrates the benefit using Pr-doped ceria //LNO<sup>6</sup> instead of GDC, in terms of stable performance at operating conditions.

---

<sup>6</sup> A. Flura, C. Nicollet, V. Vibhu, A. Rougier, J. M. Bassat, J. C. Grenier, “Cerium doped with praseodymium instead of gadolinium as interface layer for lanthanum nickelate electrode in SOFC application”, *To be submitted*.



# Annexure

---

## Annex 1

### Impedance spectroscopy

The Electrochemical Impedance Spectroscopy (EIS) is a method of electrical measurements used with the aim to determine the various contributions of a given electrochemical system (such as for instance the symmetric half-cell electrode/electrolyte/electrode shown on **Figure 1**). It is based on the point by point analysis of the alternating current response to a sinusoidal voltage.

The electrical impedance  $Z(\omega)$  of a circuit is the ratio of the sinusoidal voltage applied  $U(\omega)=U_0 \text{Exp}(j\omega t)$  over the resulting current  $I(\omega)=I_0 \text{Exp}(j\omega t+\varphi)$ .

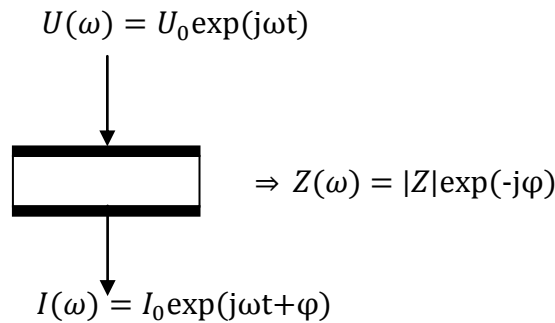


**Figure 1: Principle of the impedance spectroscopy (U: applied voltage, I: response current, Z: impedance,  $\omega$ : angular frequency with  $\omega= 2\pi f$  (where f: frequency and  $\varphi$ : phase shift))**

$Z(\omega)$  is a complex number that can be represented in polar coordinates by its modulus  $|Z|$  and phase  $\varphi$  or in Cartesian coordinates by:  $Z(\omega) = \text{Re}(Z)+j\text{Im}(Z) = Z'+jZ''$ .  $\text{Re}(Z)= Z'$  and  $\text{Im}(Z)= Z''$  represent the real and imaginary parts of the impedance, respectively. The relations between the different quantities are as follows:

$$|Z|^2 = \text{Re}^2(Z) + \text{Im}^2(Z) = (Z')^2 + (Z'')^2 \quad (1)$$

$$\varphi = \tan^{-1}(Z''/Z') \quad (2)$$

$$Z' = |Z| \cos \varphi \text{ and } Z'' = |Z| \sin \varphi \quad (3)$$

If the angular frequency  $\omega$  varies, the end of vector  $\overline{OM}$  of the impedance  $Z$  describes the complex plane (**Figure 2**).

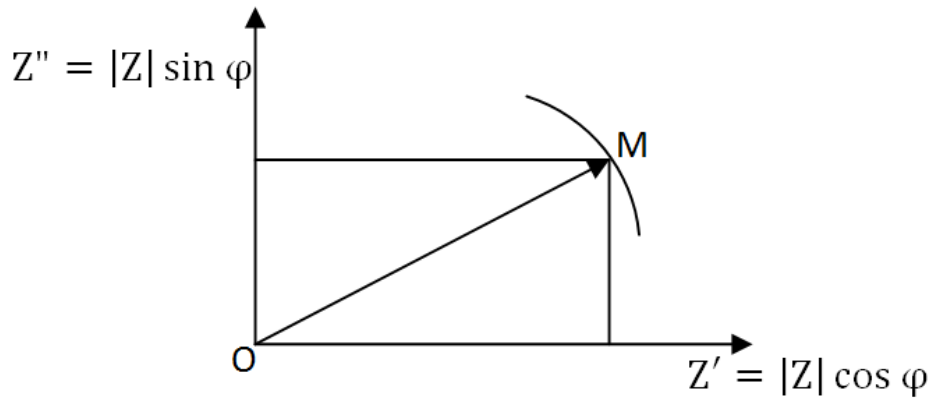


**Figure 2: Real ( $Z'$ ) and imaginary ( $Z''$ ) component of the impedance vector in the complex plane**

The impedance is generally represented by two ways:

- In the complex plane using Nyquist plot; in which  $-\text{Im}(Z) = f[\text{Re}(Z)]$ .
- Bode plot; in which  $|Z| = f[\log(\omega)]$  and  $\varphi = f[\log(\omega)]$ , are plotted.

### Instrumentation

The instrument of Impedance spectroscopy consists of two devices:

- Solartron Modulab, which can operate in the range of frequency  $10 \mu\text{Hz}$  to  $1 \text{MHz}$  and deliver a sinusoidal voltage amplitude which is adjustable between  $0$  and  $1 \text{V}$ .
- Autolab PGSTAT30, which is capable to operate in the frequency range  $10^{-3} \text{Hz}$  to  $1 \text{MHz}$  and deliver a sinusoidal voltage amplitude which is adjustable between  $0$  and  $300 \text{mV}$ .

The measurement setup were designed and built at ICMCB-CNRS. It consists of alumina tubes, gold grids are used as current collector and various contacts are made of platinum.

In the Nyquist plot showing the answer of a symmetrical cell, the negative of imaginary part of impedance;  $Z'' = -\text{Im}[Z(\omega)]$  is plotted as a function of real part of impedance;  $Z' = \text{Re}[Z(\omega)]$ . The theoretical diagram is shown in **Figure 3**.

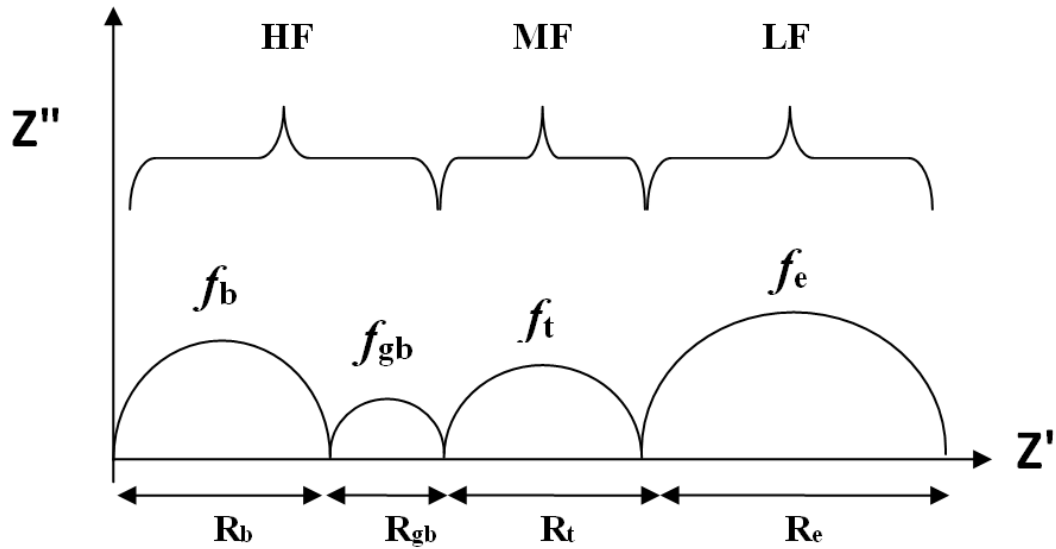


**Figure 3: Theoretical impedance diagram of the cell composed of electrolyte and electrode.**

The theoretical diagram is a combination of various arcs of circle, ranging from high frequency (HF, on the left part of the  $Z'$  axis) to low frequency (LF, right part of the  $Z'$  axis). The first arc is related to the diffusion of  $O^{2-}$  through the bulk of electrolyte (being the corresponding resistance labeled  $R_b$ ). The second arc is related to the diffusion of  $O^{2-}$  through grain boundaries of the electrolyte (with resistance  $R_{gb}$ ). These two arcs come under high frequency region. In the medium frequency (MF) range, a contribution related to the transfer of  $O^{2-}$  ions at the interface between cathode and electrolyte is often evidenced (with resistance  $R_t$ ). The arc located at low frequency (LF) is related to the electrode processes (adsorption of  $O_2$ , dissociation of  $O_2$ , charge transfer-diffusion ( $O^{2-}$ ) in the electrode, with resistance  $R_e$ ). As there is several processes involved in the electrode reaction, the contribution is usually more complex than one simple  $R/C$ . The frequencies  $f$  at the top of these arcs are different and constitute a signature enabling to identify each of the electrochemical phenomenon previously considered.

The capacity  $C_0$  of the circuit can be calculated in terms of angular frequency ( $\omega_0$ ) or frequency ( $f_0$ ) at the top of semicircle by using the following relation:

$$C_0 = \frac{1}{\omega_0 R} = \frac{1}{2\pi f_0 R} \quad (4)$$

It is then possible to determine the resistance of the electrolyte ( $R_b$  and  $R_{gb}$ ) and the polarization resistance ( $R_p$ ) of the electrode by using the complex impedance diagram.

$$R_p = R_t + R_e \quad (5)$$

By calculating the polarization resistance ( $R_p$ ), one can calculate the area specific resistance (ASR).

$$ASR = (R_p) \cdot S \cdot (1/2) \quad (6)$$

The surface area (S) of the electrodes is expressed in cm<sup>2</sup> and the coefficient 1/2 is introduced due to symmetry of the cell. The same normalization accounts for the capacitance C (in F.cm<sup>-2</sup>).

$$C = \frac{2 \cdot C_{measured}}{S} \quad (7)$$

The measurements were performed under ambient air, in a two electrode configuration with signal amplitude ( $E_{ampl}$ ) 50 mV and no DC voltage was applied. The frequency range was scanned from 1MHz to 10<sup>-2</sup> Hz with 71 points.

## Annex 2

### PUBLICATIONS

1. **V. VIBHU**, A. ROUGIER, C. NICOLLET, A. FLURA, N. PENIN, J.C. GRENIER and J.M. BASSAT, "*Pr<sub>4</sub>Ni<sub>3</sub>O<sub>10+δ</sub> : a new promising oxygen-electrode material for Solid Oxide Fuel Cells*", submitted to Journal of Power Sources 317 (2016) 184-193.
2. **V. VIBHU**, A. ROUGIER, C. NICOLLET, A. FLURA, J.C. GRENIER and J.M. BASSAT, "*La<sub>2-x</sub>Pr<sub>x</sub>NiO<sub>4+δ</sub> as suitable cathodes for Metal Supported SOFC's*", Solid State Ionics 278, 32 (2015).
3. C. NICOLLET, A. FLURA, **V. VIBHU**, A. ROUGIER, J.M. BASSAT and J.C. GRENIER, "*La<sub>2</sub>NiO<sub>4+δ</sub> infiltrated into gadolinium doped ceria as novel solid oxide fuel cells cathodes: Electrochemical performance and impedance modelling*", Journal of Power Sources 294, 473 (2015).
4. C. NICOLLET, A. FLURA, **V. VIBHU**, A. ROUGIER, J.M. BASSAT and J.C. GRENIER, "*An innovative efficient oxygen electrode for SOFC: Pr<sub>6</sub>O<sub>11</sub> infiltrated into Gd-doped ceria backbone*" In press, International Journal of Hydrogen Energy (2016).
5. FLURA, C. NICOLLET, **V. VIBHU**, B. ZEIMETZ, A. ROUGIER, J.M. BASSAT and J.C. GRENIER, "*Application of the Adler-Lane-Steele Model to Porous La<sub>2</sub>NiO<sub>4+δ</sub> SOFC Cathode: Influence of Interfaces with Gadolinia Doped Ceria*" Journal of The Electrochemical Society 163 (2016) F523-F532.
6. C. NICOLLET, A. FLURA, **V. VIBHU**, S. FOURCADE, A. ROUGIER, J.M. BASSAT and J.C. GRENIER, "*Preparation and characterization of Pr<sub>2</sub>NiO<sub>4+δ</sub> infiltrated into Gd-doped ceria as SOFC cathode*" Journal of Solid State electrochemistry, 20 (2016) 2071-2078.
7. T. BROUX, C. PRESTIPINO, M. BAHOUT, S. PAOFI, E. ELKAIM, **V. VIBHU**, J.C. GRENIER, A. ROUGIER, J.M. BASSAT and O. HERNANDEZ, "*Structure and reactivity with oxygen of Pr<sub>2</sub>NiO<sub>4+δ</sub> : an in situ synchrotron X-ray powder diffraction study*", Dalton Transactions 45 (2016) 3024-3033.
8. FLURA, C. NICOLLET, S. FOURCADE, **V. VIBHU**, A. ROUGIER, J.M. BASSAT and J.C. GRENIER, "*Identification and modelling of the oxygen gas diffusion impedance in SOFC porous electrodes: application to Pr<sub>2</sub>NiO<sub>4+δ</sub>*", Electrochimica Acta 174, 1030 (2015).
9. FLURA, S. DRU, C. NICOLLET, **V. VIBHU**, S. FOURCADE, E. LEBRAUD, A. ROUGIER, J.M. BASSAT and J.C. GRENIER, "*Chemical and structural changes in Ln<sub>2</sub>NiO<sub>4+δ</sub> (Ln=La, Pr or Nd) lanthanide nickelates as a function of oxygen partial pressure at high temperature*", Journal of Solid State Chemistry 228, 189 (2015).

## PROCEEDINGS

1. **V. VIBHU**, J.M. BASSAT, A. FLURA, C. NICOLLET, J.C. GRENIER and A. ROUGIER, “*Influence of La/Pr ratio on the ageing properties of  $La_{2-x}Pr_xNiO_{4+\delta}$  as cathodes in IT- SOFC’s*”, ECS Transactions 68(1), 825 (2015).
2. C. NICOLLET, A. FLURA, **V. VIBHU**, A. ROUGIER, J.M. BASSAT, J.C. GRENIER “*Lanthanum nickelate infiltration into porous Gd-doped ceria as cathode for Solid Oxide Fuel Cells*”, ECS Transactions 68(1), 837 (2015).
3. FLURA, A. ROUGIER, C. NICOLLET, **V. VIBHU**, F. FOURCADE, E. LEBRAUD, J.M. BASSAT, J.C. GRENIER “ *$La_2NiO_{4+\delta}$  ( $Ln=La, Pr$ ) as suitable cathodes for metal supported cells*”, ECS Transactions 68(1), 817 (2015).
4. ROUGIER, A. FLURA, C. NICOLLET, **V. VIBHU**, S. FOURCADE, J.-M. BASSAT, J.-C. GRENIER, A. BREVET and J. MOUGIN, “*Advanced cathode materials for metal supported cells: the lanthanide nickelates  $Ln_2NiO_{4+\delta}$  ( $Ln = La, Pr$ )*”, 11<sup>th</sup> European SOFC and SOE Forum, EFCF (2014) Chapter 10, B810, 138-144 (ISBN: 978-3-905592-16-0).
5. **V. VIBHU**, A. FLURA, C. NICOLLET, S. FOURCADE, A. ROUGIER, J.-M. BASSAT, J.-C. GRENIER, “*Preliminary Ageing Study of Praseodymium-Lanthanum Nickelates  $Pr_{2-x}La_xNiO_{4+\delta}$  as Cathodes for Metal Supported SOFCs*”, 11<sup>th</sup> European SOFC and SOE Forum, EFCF (2014) Chapter 13, B903, 18-25 (ISBN: 978-3-905592-16-0).
6. J.C. GRENIER, A. FLURA, S. DRU, C. NICOLLET, **V. VIBHU**, S. FOURCADE, A. ROUGIER, J.M. BASSAT, A. BREVET, and J. MOUGIN, “*Lanthanide nickelates  $Ln_2NiO_{4+\delta}$  ( $Ln = La, Pr$  or  $Nd$ ):promising cathode materials for metal supported SOFC’s*”, ECS Transactions, 57(1), 1771-1779 (2013).
7. **V. VIBHU**, A. ROUGIER, J.C. GRENIER and J.M. BASSAT, “*Mixed nickelates  $Pr_{2-x}La_xNiO_{4+\delta}$  used as cathodes in metal supported SOFC’s*”, ECS Transactions, 57(1), 2093-2100 (2013).

## List of publications under preparation

1. **V. VIBHU**, J.M. BASSAT, A. FLURA, C. NICOLLET, N. PENIN, J.C. GRENIER and A. ROUGIER, “*Structural and stability studies of  $PrNiO_{3-\delta}$* ”, to be submitted in Journal of Solid State electrochemistry (2016).
2. **V. VIBHU**, M. SUCHOMEL, N. PENIN, C. NICOLLET, A. FLURA, F. WEILL, J.C. GRENIER, J.M. BASSAT and A. ROUGIER, “*Structural characterization of Pr-rich phases in  $La_{2-x}Pr_xNiO_{4+\delta}$  series using Synchrotron and Neutron Powder Diffraction*”, to be submitted in Journal of Solid State Chemistry (2016).
3. **V. VIBHU**, A. ROUGIER, A. FLURA, C. NICOLLET, S. FOURCADE, T. HUNGRIA, J.C. GRENIER and J.M. BASSAT, “*Ageing Study of Praseodymium-Lanthanum Nickelates  $La_{2-x}Pr_xNiO_{4+\delta}$  as Cathodes for SOFCs*”, to be submitted in Journal of Power Sources (2016).





## Résumé

Ce travail de thèse est consacré à l'étude des nickelates  $\text{La}_{2-x}\text{Pr}_x\text{NiO}_{4+\delta}$ , comme nouveaux matériaux de cathodes pour piles à combustible haute température, SOFC, et en particulier à la caractérisation de leur stabilité chimique et leur comportement en fonctionnement. En effet, du fait de leur propriété de conduction mixte ionique et électronique, MIEC, les nickelates de structure type  $\text{K}_2\text{NiF}_4$ ,  $\text{Ln}_2\text{NiO}_{4+\delta}$  ( $\text{Ln} = \text{La}, \text{Pr}, \text{Nd}$ ), correspondant au terme  $n = 1$  de la série de Ruddlesden-Popper ( $\text{A}_{n+1}\text{M}_n\text{O}_{(3n+1)\pm\delta}$ ), sont des matériaux prometteurs pour des fonctionnements à température intermédiaire, IT-SOFC ( $T \leq 800$  °C). Compromis entre la stabilité chimique de  $\text{La}_2\text{NiO}_{4+\delta}$  et les très bonnes performances électrochimiques de  $\text{Pr}_2\text{NiO}_{4+\delta}$ , les phases  $\text{La}_{2-x}\text{Pr}_x\text{NiO}_{4+\delta}$ , ont été synthétisées et leurs propriétés physico-chimiques, de transport et électrochimiques ont été déterminées. L'étude approfondie des caractéristiques des électrodes par spectroscopie d'impédance en cellules symétriques a été réalisée à courant nul et sous polarisation anodique et cathodique sur des périodes d'un mois. De façon surprenante, même après la dissociation complète de  $\text{Pr}_2\text{NiO}_{4+\delta}$  en  $\text{PrNiO}_{3-\delta}$ ,  $\text{Pr}_4\text{Ni}_3\text{O}_{10+\delta}$  et  $\text{Pr}_6\text{O}_{11}$ , la résistance de polarisation ne montre pas de changement significatif. L'étude de  $\text{PrNiO}_{3-\delta}$  et  $\text{Pr}_4\text{Ni}_3\text{O}_{10+\delta}$ , comme matériau de cathode pour piles à combustible, démontre l'excellent comportement de la phase  $\text{Pr}_4\text{Ni}_3\text{O}_{10+\delta}$  et ceci en cellule symétrique ( $R_p(\text{Pr}_4\text{Ni}_3\text{O}_{10+\delta}) = R_p(\text{Pr}_2\text{NiO}_{4+\delta}) = 0.15 \text{ } \Omega \cdot \text{cm}^2$  à 600 °C) et cellule complète ( $1.6 \text{ W} \cdot \text{cm}^{-2}$  at 800 °C).

**Mots-clés:** Piles à Combustible Haute Température (SOFC), Nickelates, Conducteur ionique et électronique mixte (MIEC), Électrode à oxygène, Stabilité chimique, Vieillesse en fonctionnement, Spectroscopie d'impédance électrochimique (EIS)

## Summary

This PhD work is dedicated to stability and ageing studies of Praseodymium based nickelates as cathodes for Solid Oxide Fuel Cells (SOFCs). With this respect  $\text{Ln}_2\text{NiO}_{4+\delta}$  ( $\text{Ln}=\text{La}, \text{Pr}$  or  $\text{Nd}$ ) compounds with the  $\text{K}_2\text{NiF}_4$  type structure act as alternative cathode materials for IT-SOFC due to their mixed ionic and electronic conductivity (*i.e.* MIEC properties).  $\text{Pr}_2\text{NiO}_{4+\delta}$  shows excellent electrochemical properties at intermediate temperature (*i.e.* low polarization resistance  $R_p$  value,  $R_p = 0.03 \text{ } \Omega \cdot \text{cm}^2$  at 700 °C), while  $\text{La}_2\text{NiO}_{4+\delta}$  exhibits higher chemical stability. So, the properties of  $\text{La}_{2-x}\text{Pr}_x\text{NiO}_{4+\delta}$  nickelates were investigated with the aim to find best compromise between chemical stability and electrochemical performances. After synthesis, the physical and chemical properties as well as their transport and electrochemical properties have been determined. Measurements of the polarization resistance of symmetrical half-cells have been carried out by impedance spectroscopy. Then, the chemical stability and the electrochemical performance of the materials have been studied for duration up to one month. As an interesting point, even after complete dissociation of  $\text{Pr}_2\text{NiO}_{4+\delta}$  into  $\text{PrNiO}_{3-\delta}$ ,  $\text{Pr}_4\text{Ni}_3\text{O}_{10+\delta}$  and  $\text{Pr}_6\text{O}_{11}$ , the polarization resistance does not show significant change. So finally, two new materials  $\text{PrNiO}_{3-\delta}$  and  $\text{Pr}_4\text{Ni}_3\text{O}_{10+\delta}$  were investigated as SOFCs cathode showing very promising results for  $\text{Pr}_4\text{Ni}_3\text{O}_{10+\delta}$  in symmetrical cell ( $R_p(\text{Pr}_4\text{Ni}_3\text{O}_{10+\delta}) = R_p(\text{Pr}_2\text{NiO}_{4+\delta}) = 0.15 \text{ } \Omega \cdot \text{cm}^2$  à 600 °C) and complete cell ( $1.6 \text{ W} \cdot \text{cm}^{-2}$  at 800 °C).

**Key-words:** Solid Oxide Fuel Cell (SOFCs), Solid Oxide Electrolyzer Cell (SOECs), Mixed ionic and Electronic conductor (MIEC), Nickelates, Oxygen over-stoichiometry, Chemical stability, Ageing, Electrochemical Impedance Spectroscopy (EIS)